DEPARTMENT OF ELECTRONIC & ELECTRICAL ENGINEERING

University of Strathclyde Engineering

PLASMA-CLOSING SWITCH WITH CORONA ELECTRODES: DEVELOPMENT AND OPERATIONAL CHARACTERISTICS WHEN FILLED WITH DIFFERENT GASES

A thesis presented in fulfilment of the requirement for the degree of

Doctor of Philosophy

Yuan Yao

Department of Electronic and Electrical Engineering

University of Strathclyde

Glasgow, UK

2022

Declaration of Authenticity and Author's Rights

‘This thesis is the result of the author’s original research. It has been composed by the author and has not been previously submitted for examination which has led to the award of a degree.’

Signed:

Date:

Acknowledgements

I would like to acknowledge many people who have provided help and support throughout this PhD project. Firstly, I would like to acknowledge Dr. Igor Timoshkin for his supervision, support and guidance throughout this PhD project without whom this thesis would never have been completed.

I would also like to thank Prof. Scott MacGregor and the whole HVT Research Group for the opportunities and support. Thanks also should go to Dr Mark Wilson, who was always willing to take the time to help and support me in the lab and publishing. I also thank Dr. Martin Given for his continual help with technical discussions and writing.

Thanks to the High-Voltage Workshop for their assistance in producing the switch in this investigation and their assistance. Thanks to Maureen Cooper for her help over the years, especially in organising conference trips.

Finally, I would also like to thank my family, and in particular my wife Siyang, for all her support and understanding.

ABSTRACT

High voltage gas-filled plasma closing switches are critical components of pulsed power systems due to their capability to operate in wide voltage and current ranges (from tens of amperes to hundreds of kiloamperes). They can handle high rates of change in currents and voltages, *dI/dt*, and *dV/dt*, and provide a short switching time with low jitter when operating in a triggered mode.

The aims of this thesis are (i) to develop a novel, two-stage gas-filled plasma closing switch with corona electrodes and (ii) to investigate its operational performance in the self-breakdown and triggered operation regimes when filled with different environmentally friendly gases. The corona discharge electrodes used in the developed switch help to improve the switch's operational stability providing minimal standard deviation in the self-breakdown voltage and minimal jitter in the case of the triggered operational mode.

The operational performance of this plasma closing switch in both self-breakdown and triggered operation modes were investigated when the switch was filled with the selected gases ("Zero grade" air, N_2, CO_2, and a 90%/10% Ar/O_2 mixture) with pressures up to 12 bar (gauge). The obtained experimental data and their statistical analysis allowed for a comprehensive analysis of different operational parameters of the developed switch depending on the gas type, gas pressure and polarity of the applied voltage.

Experimental results have been used in the development of computational models. These analytical results contribute to a further understanding the dynamic characteristics of gas-filled spark-gap switches. The developed models can be used to optimise the parameters of a plasma closing switch filled with environmentally friendly gases to improve its operational performance.

CONTENTS

List of Symbols

V	Voltage (V)
C	Capacitance (F)
L	Inductance (H)
R	Resistance (Ω)
I	Current (A)
p	Gas pressure (bar)
d	Inter-electrode gap distance (cm)
E	Electric field strength (V/m)
α	Townsend's first ionisation coefficient (1/m)
γ	Townsend's second ionisation coefficient
α^*	The scale parameter in Weibull distribution (ns)
β^*	The shape parameter in Weibull distribution
C^*	Constant in equations for dynamic resistance
Q	Electric charge (C)
ε_r	The relative permittivity of dielectric gases
ε_0	Vacuum permittivity of free space (~8.85pF/m)
a_c	The radius of the current return path (cm)
$a(t)$	Temporal plasma radius of the plasma channel (cm)
l	Length of the plasma channel (cm)
σ	Electrical conductivity of the plasma-filled channel ($\Omega^{-1}\text{cm}^{-1}$)
ρ_0	Initial gas density (kg/m^3)
ξ	Constant in Braginskii equation

β	Non-uniformity parameter of the electric field

CHAPTER.1 INTRODUCTION

The pulsed power systems, used in scientific research and various practical applications, are based on the principle of energy compression. One of the critical components of pulsed power systems is gas-filled plasma closing switches.

The basic principle of operation of such switches is based on establishing a highly conductive plasma channel between the electrodes. When the applied voltage across the gas-filled gap formed by the switch electrodes exceeds the hold-off voltage, the gaseous medium will transform from a good insulator (with typical conductivity of $\sim 10^{-14} \Omega^{-1} m^{-1}$) to a good conductor, that is, a plasma channel with conductivity up to 10000's S/m will be formed between the electrodes. The channel resistance is low, and intense conductive current flows through the discharge channel providing the energy transfer to the load.

Plasma closing switches (PCSs) offer several advantages over other types of high voltage closing switches. They provide a high hold-off (operating) voltage (up to several MV) and can be accurately triggered, providing a low standard deviation in their time to breakdown (1-σ jitter). These switches can operate at high voltages and transfer high currents (from tens of amperes to hundreds of kiloamperes). They can handle high rates of change in currents and voltages, *dI/dt*, and *dV/dt* (Woodworth *et al.* 2009). Thus, these switches have been widely used in different pulse power systems.

In recent years, various gas-filled closing switches have been extensively studied to expand their practical applications including two or three electrode switches for low repetition-rate operation at high voltage (~100kV) and high peak current (~500kA) (Y.J. Chen et al. 2008; Cai et al. 2013). Another example is low-inductance gas-filled spark gap switches developed by R. E. Beverly III & Associates for high peak current (~1-500kA) and high voltage (2.5-75kV) pulsed power applications (Beverly 2001).

A range of low-inductance, low jitter, and high peak current gas-filled plasma closing switches have been developed for the use in in the linear transformer drivers (LTDs).

The plasma closing switches employed in LTD applications have been studied by (Jiang et al. 2015). However, the increasing demand for compact, small footprint pulsed power systems which can operate at high repetition rate put specific technical requirements on the design of the plasma closing switches (Gaudet et al. 2004). For example, a typical Marx generator used for a high-power microwave generation requires compact switches that operate at repetition rates up to 100 Hz and provide impulses with the peak voltage of ~100 kV and peak current of ~10 kA while having a long lifetime (A. Sharma et al. 2011).

The main aim of this thesis is to develop a novel, two-stage gas-filled plasma closing switch with corona electrodes and to investigate its operational performance in the self-breakdown and triggered operation regimes when filled with different environmentally friendly gases. This results in optimal operational parameters for applications that require compact , repetitive, and low-jitter design. The corona discharge electrodes used in the developed switch help to improve the switch's operational stability providing minimal standard deviation in the self-breakdown voltage and minimal jitter in the case of the triggered operational mode.

The developed compact plasma closing switch with corona electrodes was filled with the following gases: "Zero grade" air, N_2, CO_2, and a 90%/10% Ar/O_2 mixture. All tested gases were obtained from a commercial industrial gas supplier, BOC, a member of the Linde Group. "Zero grade" air is a 79%/21% N_2/O_2 mixture produced by mixing pure oxygen (99.6%) with pure nitrogen (99.998%). "Zero Grade" is a commercial name of this gas mixture produced by BOC. CO_2 purchased from BOC had purity of 99.8%, N_2 had purity of 99.998%. The 90%/10% Ar/O_2 mixture consisted of Ar with 99.999% purity and O_2 with 99.6% purity. The operational performance of this plasma closing switch in both self-breakdown and triggered operation modes was investigated when the switch was filled with the selected gases with pressures up to 12 bar (gauge). The obtained experimental data and their statistical analysis allowed for a comprehensive analysis of different operational parameters of the developed switch depending on the gas type, gas pressure and polarity of the applied voltage.

Based on the experimental results, analytical and computational models were developed and used to obtain the main characteristics of the post-breakdown transient plasma channels in different gases. These models take into account the transient properties of the plasma in the post-breakdown channel formed between PCS's electrodes. Therefore, the developed models can be used to study the dynamic inductance and resistance of the plasma channel formed in PCS in different pulse power systems. Also, these models allow for the analysis of the effect of plasma channel inductance and resistance on the parameters of the output HV impulses produced by the pulsed power system. The models can be used in the analysis of the transient resistance and power dissipation in the plasma closing switches.

In Chapter 2, a comprehensive literature review of different aspects of the pulsed power technology is presented, including the basic principles of the pulsed power systems, principles and mechanisms of gas discharge, breakdown mechanisms in plasma closing gas-filled switches, practical switching topologies and their operational characteristics. The switching topologies commonly used in the voltage build-up phase of pulsed power systems are reviewed, with an emphasis on gas-filled plasma closing switches, which are the main focus of the experimental research conducted in this project. The transient resistance of the post-breakdown plasma channels formed in different gases is discussed. This analysis includes different dynamic plasma resistance models presented in the literature. Chapter 2 also discusses different insulating gases used in the plasma closing switches, indicating that up to date, SF_6 is widely used in the plasma closing switches (PCS). Chapter 2 reviews the breakdown characteristics and reasons for using SF_6 in PCSs. However, growing environmental concerns have prompted the search for suitable alternatives to SF_6, and potential alternatives to SF_6 are presented and discussed. The literature review discusses the critical operational characteristics of spark switches, which form the basis and helps to develop the direction and main objectives of the present research project.

Chapter 3 presents and discusses the experimental systems developed throughout the present project. A high-pressure experimental test rig was designed and built to investigate the operating characteristics of the plasma-closed switch filled with

different gases: “Zero grade” (bottled) air, N_2, CO_2 and 90%/10% Ar/O_2 mixture. The main feature of this test setup is the developed two-stage triggered gas-filled plasma closing switch with corona electrodes that can withstand and operate at high gas pressures (up to 20 bar). Another novelty aspect associated with this test rig is the software (LabVIEW) environment developed to facilitate the computerized operation of the high voltage power supply (to provide consistent and repeatable charging voltage to test the plasma closing switch). This system also underpins automatic measurements during tests and computerized data acquisition. This software provides the required degree of control over the data acquisition devices, high voltage equipment and diagnostic systems, ensuring that the experimental conditions are the same in each test. The developed experimental set-up was used to obtain self-breakdown voltage values, voltage-current characteristics of corona discharges in the switch filled with different gases and impulse breakdown characteristics of the developed switch.

Chapter 4 presents the results of the systematic study of the operational characteristics of the switch in the self-breakdown mode. These characteristics include the self-breakdown voltage of the developed plasma closing switch filled with different gases (“Zero grade” (bottled) air, CO_2, N_2 and 90%/10% Ar/O_2 mixture) in the gas pressure range from 1 to 12 bar (gauge). The effect of the polarity of the applied voltage at different gas pressures on the self-breakdown performance of the switch was investigated. It was found that there is a crossover point between positive and negative breakdown voltages (obtained as functions of the gas pressure) at specific critical gas pressure when both negative and positive breakdown voltages have the same magnitudes (in the case of a single gap breakdown). For gas pressures lower than this critical value, the breakdown voltages for negative energization were higher than the positive breakdown voltages. The breakdown voltage for positive energisation is significantly higher than the negative breakdown voltage for gas pressures above this critical value. It was found that the gas type and gas pressure directly affect this critical gas pressure. In the case where the breakdown occurred in two sections (gaps) of the two-stage switch, no significant difference between positive and negative breakdown voltages are found for all tested gases, and the breakdown voltage increases as the gas

pressure increases. The self-breakdown voltage increases linearly with an increase in the gas pressure for air and N_2, thus making the operational performance of the switch filled with these gases highly predictable. However, for CO_2 and the 90%/10% Ar/O_2 mixture, the breakdown voltage demonstrates a noticeable corona stabilization region in the tested gas pressure range, typically observed in electronegative gases. The space charge generated by corona discharges weakens the electric field near the point electrode(s) while preventing streamer formation at the point electrode(s). Thus, it is important to investigate the space charge developed by the coronal discharges in the gases used in the present study.

Chapter 5 studies the pre-breakdown corona discharge in the multi-point-plane topologies filled with the tested gases in order to characterise its effect on the switching performance. This chapter investigates the DC corona-stabilized discharge behaviour in the multi-point-plane topology filled with all tested gases over the wide pressure range of 1-12 bar (gauge). The voltage-current characteristics of the corona discharges were obtained, and the effect of different factors such as polarity of the applied voltage, the gas type and pressure on the current-voltage characteristics were investigated.

Chapter 6 focuses on the impulse breakdown characteristics of the developed switch topology (two-stages PCS with a central trigger electrode with symmetrically located corona needles), filled with "Zero grade" air, CO_2, N_2, and 90%/10% Ar/O_2 mixture, the gas pressure was in the range from 1 to 12bar(gauge). The switch was triggered through a change of the electric field distribution by applying an external trigger HV pulse to the spark gaps already pre-energized below the self-breakdown voltage. This triggering causes the gas between the positive and negative electrodes to be broken down, and the switch closure is initiated. The time to breakdown and jitter were obtained and analysed. The effects of different factors such as polarity of trigger voltage, gas pressure and gas type in the switch, and the magnitude of DC voltage applied across the main electrodes have been investigated. The obtained results are essential for accurately controlling the operational performance and characteristics of the developed gas-filled plasma closing switch.

Chapter 7 developed a lumped-element *RLC* circuit to model the self-breakdown DC charged switch circuit and analyse the post-breakdown current waveforms in the plasma closing switch. This model was used to obtain the transient plasma resistance based on Kirchhoff's analysis of the circuit. By applying Kirchhoff's voltage law to this circuit, the equation for the transient post-breakdown resistance has been derived and solved using the experimental current waveforms. Therefore, different models and methods should be developed to establish the most reliable analysis method for the transient plasma channel resistance in PCSs. This analysis will help further optimise advanced gas-filled plasma closed switches for different pulsed power applications. At the same time, in this chapter, the analytical approaches based on the Braginskii and Kushner models were used to obtain the transient plasma characteristics, including the hydrodynamic radius of the expanding plasma channel and the post-breakdown transient plasma resistance in different gases.

Chapter 8 presents the results of the PSpice simulations in the RLC lumped element circuit, which models the transient process in the plasma closing switch. This PSpice model was developed to investigate the dynamic plasma resistance. The transient plasma resistance model developed in this chapter is based on the models available in the literature (Toepler 1927; Rompe and Weizel 1944; Braginskii 1958; Barannik 1975; Kushner, Kimura, and Byron 1985). The results obtained using the present model and the original experimental results have been compared and verified. The model which provides the most reliable results (transient plasma resistance) for the developed plasma closing switch has been identified.

Chapter 9 summarises and discusses the obtained results and provides recommendations for future research. The results show that the novel two-stage triggered gas-filled plasma closing switch developed in this work has advanced operating characteristics. It was shown that the polarity of the applied voltage does not affect the switch performance, which can be an advantage for different practical pulsed power systems. Furthermore, it was shown that the environmentally friendly gases

could be successfully used in the plasma closing switches developed in this work to minimize the use of SF_6 in the pulsed power systems.

CHAPTER.2 LITERATURE REVIEW

2.1 Introduction

This chapter reviews the literature and discusses the basic principles of pulsed power technology, the basic mechanisms of gas discharge and breakdown characteristics of different gases used in plasma closing switches (PCS). This chapter also discusses different gas-filled switching topologies and specific operating characteristics of the gas-filled PCSs described in the literature. Chapter 2 provides an in-depth analysis of different types of plasma closing switches used in different practical applications of pulsed power technology.

This chapter begins with a brief description of the basic principles of pulsed power technology and its practical aspects, including the defence-related, environmental and biomedical applications. The topologies of different PCSs used in these applications and their specific operational characteristics and parameters are reviewed and discussed, focusing on the electrode configuration and triggering mechanisms.

Then the Chapter proceeds with a review and discussion of the theoretical background of gas discharge, covering the Townsend discharge mechanism and development of plasma streamers, as Paschen's law which is essential for characterising the operational parameters of the plasma closing gas-filled switches is presented. The difference in the field distribution and operational characteristics of the PCSs with uniform and non-uniform electrode topologies is discussed. In addition, the transient plasma resistance models available in the literature for the self-breakdown DC charged switch circuit are reviewed and studied in-depth, and the operational parameters of the PCS are analysed.

Finally, the Chapter focuses on the discussion of different insulating gases used in the plasma closing switches. The insulating gases commonly used in the power and pulsed power industries are reviewed. One of the most used gases in the PCSs installed in the pulsed power systems is SF_6. Its advantages and the reason for its choice as the

dielectric gas in PCSs are discussed (Kline et al. 1979; Clough et al. 2005; D.K. Sharma et al. 2014). However, the growing environmental concerns have led to the search for suitable alternative gases for SF_6, and a brief review of the alternative environmentally friendly gases is provided in this Chapter.

2.2 Pulsed power technology

This section reviews the fundamentals of pulsed power systems and different switches. Due to the robustness, excellent operational capabilities and relatively low cost, gas-filled PCS are the critical component for different high-power pulsed systems. This section also discusses the operational characteristics of PCS in different topologies.

2.2.1 Basic principles of pulsed power technology

Pulsed power technology is based on the principle of energy compression, i.e. the electrical energy is accumulated in energy storage (capacitive or inductive) over a longer period and then releases over a significantly shorter time interval - in a short pulse (ps, μs duration) into a load (J.C. Martin 1995; Mesyats 2007). In this way, the pulsed power system can output pulses of ultra-high power, and its instantaneous power can be very high up to GW (H. Bluhm 2006a). Due to its capability to generate high peak power, the pulsed power technology has achieved great success in applications such as accelerators, high-power pulsed lasers and controllable fusion systems. In the 1930s, researchers and practitioners began using capacitive pulsed power systems to generate X-rays, the origin of the pulsed power technology (T.H. Martin 1969). Since 1964, after the successful development of the world's first high-current electron beam accelerator SMOG (5.4MV, 3.6kA, 30ns)(T.H. Martin, Williams, and Kristiansen 2014), major laboratories in the United States, Japan, the Soviet Union and Europe have successively developed and constructed high-power pulse systems. The pulsed power machine PBFA-II (12MV, 8.4MA, 40ns) developed by Sandia National Laboratories in 1986 is the first pulsed power system to exceed the impulsive power of 100TW (Cook et al. 1986). In defence applications, pulsed power technology is used to generate intensive X-rays for flash X-ray radiography, to generate intense pulsed microwaves, and to pump high-power excimer lasers (Tran et

al. 2015). In recent years the pulsed power technology has also been used in multiple civil, industrial, medical and environmental applications. For example, pulsed power systems are used to decompose CO_2, in electrostatic precipitator (Mizuno, Clements, and Davis 1986; Pokryvailo et al. 2004) and in pulsed field inactivation of microorganisms (Pedrow et al. 1997; Timoshkin, Mackersie, and MacGregor 2004; H.W. Lee et al. 2013; Qin et al. 2014).

A typical pulsed power system includes a power source, a primary energy storage system, a pulse forming line to produce the required pulse waveform, a switch and the load impedance matching network. Initial energy accumulated in the energy storage is released into the pulse forming line employing a closing switch. In the pulse forming line, the impulse is compressed and shaped. Finally, the impulse is delivered into the load (T.H. Martin, Williams, and Kristiansen 2014). Typical loads of pulsed power systems include induction accelerator cells, electrostatic accelerator electrodes, plasma sources, antennas, and microwave vacuum tubes. The pulsed power system is critical for obtaining intense current impulses and electron or ion beams and has been widely used in high-tech and defence fields (Driga and Fair 1991; Thomas G. Engel, Nunnally, and VanKirk 1999). The pulsed power systems are used to provide high energy, high voltage and high current impulses in the field of nuclear fusion, high-temperature and high-density plasma research, high-power laser research, intense beam physics research, and accelerator physics research (Smith 1991; J.L. Liu et al. 2009; Peng et al. 2014; Ju et al. 2017).

A typical diagram of the pulsed power system is shown in Figure 2.1.

Figure 2.1 The general scheme of the pulsed power system

Different energy storage systems can be employed in pulsed power devices, including capacitor energy storage (energy stored in the electric field), inductive energy storage (energy stored in the magnetic field), and chemical energy storage. The pulse forming system may include pulse transformer(s) and pulse forming line(s), and pulse shaping capacitor(s).

Another critical component of a typical pulsed power system is a switch, which allows the accumulated energy to be released into the pulse forming line in a short time interval to generate a high-power output impulse. It is one of the main components determining the energy transfer into the load and the rate of the energy transfer. The switch's operational characteristics affect the waveshape of the output pulse (its rise time and amplitude).

Depending on the energy storage methods, pulsed power systems can be equipped with closing switches (capacitive energy storage) (Schaefer, Kristiansen, and Guenther 2013) or opening switches (inductive energy storage) (Humphries 1987). Most high-power generators with capacitive storage devices commonly require closing switches (Burkes et al. 1979; Dougal and Morris 1992). Depending on the type of operation and the insulating medium used in the switches, pulsed power switches can be categorised into gas and liquid-filled plasma closing switches and solid-state switches, for example, produced by Behlke (Germany).

A pulsed power system based on capacitive energy storage is shown in Figure 2.2. This diagram shows a system with a gas-filled spark (plasma closing) switch. When the switch, *SW*, is open, capacitor *C* is charged by the DC voltage supply V_{DC} through the charging resistor R_{CH}. When the PCS is closed (by means of self-breakdown as shown in Figure 2.2 or by a triggered breakdown in the case of a 3-electrode switch), the capacitor rapidly transfers the stored energy to the load, generating a voltage impulse with the same polarity as the supply voltage across the load.

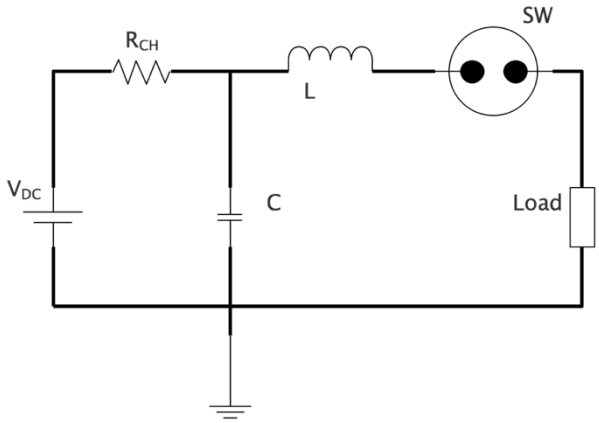

Figure 2.2 Schematic of a pulsed power system based on capacitive energy storage method, generating a voltage impulse with the same polarity as the supply voltage across the load.

If the positions of the capacitor and the switch are changed, when the switch is closed, the left terminal of the capacitor is grounded, and a voltage impulse with the polarity opposite to the supply voltage is generated across the load, as shown in Figure 2.3. The DC power supply is effectively decoupled from the load in this case, and the circuit can be grounded.

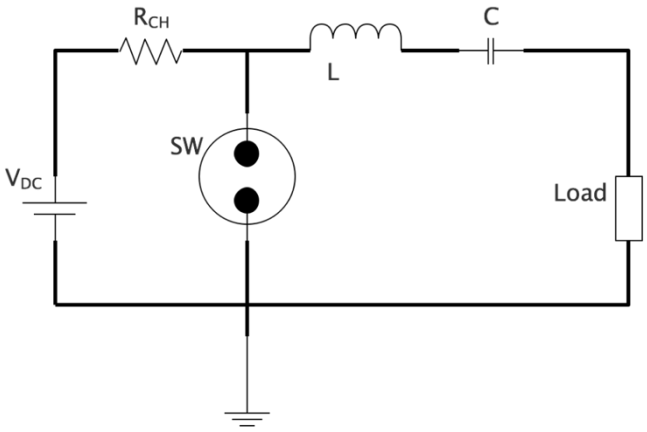

Figure 2.3 Schematic of a pulsed power system based on capacitive energy storage method, generating a voltage impulse with the opposite polarity as the supply voltage across the load

The circuit discussed in Figure 2.2 and Figure 2.3 is based on capacitive energy storage. The peak output voltage of the impulse generated by this circuit is equal to the

charging voltage of the power supply. In practical applications, voltage multiplication can be achieved by charging multiple capacitors in parallel and then discharging them in series (Marx voltage multiplication approach).

The inductances associated with the switch and with the transmission cables that connect the switch to the load are included in these circuit diagrams.

These inductances will affect the magnitude of the current transmitted to the load, the rate of current and voltage change ($\frac{dI}{dt}, \frac{dV}{dt}$) and thus rise time and duration of the output impulse. Therefore, it is required to minimise the switch inductance and resistance in the pulsed system to reduce energy loss.

2.2.2 Characteristics of plasma closing gas-filled switches

The switch is one of the critical components of the pulsed power system, and the characteristics of the switch directly affect the performance of the pulsed power device. In the case of the pulsed power system based on the capacitive energy storage, during the charging phase of its operation, the switch is open and acts as an insulator, isolating the energy storage part (a capacitor bank) from the load. After the completion of the charging process, the switch is closed and the electrical energy stored in the capacitor bank is transferred into the load over a short time interval (much shorter than the charging time).

There is a number of critical characteristics which should be considered for optimisation of the operational performance of plasma closing switches used in different pulsed power devices and systems. These characteristics include:

- **Hold-off voltage**: the DC voltage which is applied to the HV electrode(s) of the switch until breakdown occurs. The time to breakdown is called hold-off time. It reflects the dielectric properties of the insulating medium (gas) between the switch electrodes. .

- **Peak current**: the maximum current that passes through the switch.

- **Switching time**: the time interval during which the resistance of the plasma channel(s) formed between the switch electrodes significantly reduces . .

- **Delay time**: the time interval between the application of trigger impulse and formation of the breakdown conductive plasma channel(s). This time is governed by the processes of generation of charge carriers, development of the ionisation front, and establishment of the plasma conduction channel(s) between the electrodes.

- **Jitter**: time variance in the switching time. It is an important parameter which defines the reliability of switching operations. Typically, in the pulsed power applications, the jitter is obtained as a standard deviation in the time to breakdown (1-σ jitter).

- ***dV/dt***: the maximum rate of change of the applied voltage.

- ***dI/dt***: the rate of change of current passing through the switch

- **Recovery time**: the time required for the dielectric medium to regain its full dielectric strength

- **Pulse repetition rate:** the rate of generation of high voltage impulse.

- **Lifetime**: the maximum number of impulses which the switch can withstand without affecting its operational performance.

- **Cost**

Other important parameters which affect the operational performance of the pulsed power systems include the resistance and inductance of the plasma channel(es)

formed in the plasma closing switch. The resistance of the plasma channel is determined by the length of the gap, type of gas and gas pressure and parameters of the pulsed power circuit. The geometry of spark gap switches determines the inductance of the plasma channel. Modelling and evaluation of these two parameters will be discussed in the later sections.

Figure 2.4 shows the relationship between voltage and current when the trigatron (triggered plasma closing switch) is during operation. For efficient operation, closing switches should operate at significant breakdown voltage V_b and should have very low forward voltage drop V_F. Typically, there is a time lag between a trigger signal and switch closure. This time interval includes different phases. Each phase requires a specific time to be completed, and the closure time is typically referred to as the switching time. Initially, at time $\tau < \tau_b$, the switch is open. When $\tau = \tau_b$, the switch is closed and starts to conduct electric current (breakdown phase); the voltage across the switch drops rapidly, and the current increases. When $\tau = \tau_c$ the voltage drops to the value of the forward drop voltage, V_F, the forward voltage drop (V_F) across the switch electrodes during the conducting stage is much lower than breakdown voltage V_b, and the switch is closed.

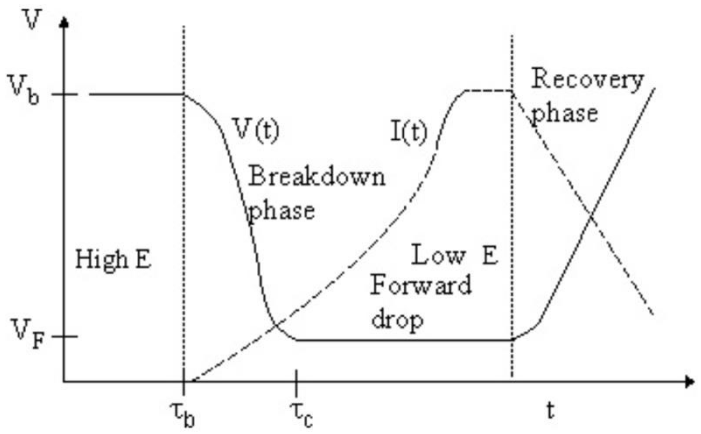

Figure 2.4 Voltage and current as functions of time during the triggered operation of plasma closing switch (spark gap) (Christophorou, McCorkle, and Hunter 1987).

The generation of initial charge carriers and subsequent propagation of the ionisation front in gas inside the switch results in the establishment of the conducting plasma channel(s) between the switch's electrodes. Once the initial stage of switch closure, which lasts up to $\tau = \tau_b$ is completed, i.e., a seed electron appears in the gap; the ionisation front(s) start to propagate in the gas-filled switch, and it takes a specific time for these ionisation front(s) to cross the gap, which is $\tau f = \tau c - \tau_b$. This time is called the formative time and is affected by various factors, including the electric field strength, nature of the gas(es), gas pressure and temperature, etc.

The switching voltage in the 'on' state (forward drop) is important for determining the overall switching efficiency. The forward conduction voltage is determined by a complex gas discharge process. It is known that the plasma temperature in the channel formed between the switch electrodes is typically ~(2,000K-10,000K) (Bondiou and Gallimberti 1994; Koutoula et al. 2016). Thus, the plasma conductivity could be significantly lower than the specific conductivity of metal, resulting in energy dissipating in the channel.

The switch's recovery time refers to when the dielectric strength of the gas inside the switch recovers due to the recombination and/or attachment of electrons. This recovery process is governed by the plasma kinetic properties, i.e., charge carrier's density, mobility, plasma temperature, recombination/attachment rates and other parameters.

2.2.3 Gas-filled plasma closing switches

Different types of plasma closing switches have been developed for different operation modes, including vacuum switches, ignitrons, thyratrons, gas-filled spark gaps, and solid-state switches. The dielectric media in the plasma closing switch can be vacuum, gas(es), liquid, or solid media (Burkes et al. 1979; Dougal, Morris, and Volakakis 1991; Cong et al. 2013). Each switch type has different operational characteristics and limitations, including switching time, maximum pulse repetition rate, jitter, hold-off voltage, peak current, the rate of voltage and current changes. Table 2.1 shows typical

characteristics of different plasma closing switches used in high voltage pulsed power applications.

Table 2.1 A summary of various switch parameters for pulsed power applications.(Burkes et al. 1979; Chu and Scott 1999)

Switch type	*Switching time*	*Hold-off voltage*	*Peak current*	*Jitter*	*repetition rate (Hz)*	*Lifetime*	*Cost*
Vacuum tube	~10s ns	~0.15MV	~0.5kA	~ns	-	~10^4 *hours*	High
Spark gaps	<~ns	~kV to MV	~10s A to MA	<~ns to ~us	1 shot - ~kHz	<10^4 *shots*	Commercially available
Thyratron	~ ns	~ 10s kV	~ 10s kA	<~ns	high	limited	Commercially available
Ignitron	~10s ns	~ 10s kV	Greater than ~ 100s kA	~10s ns	2 shots/min		Low
Solid-state switches	~ns to 100s µs	-	-	~ns	Very high	long	High

Due to high hold-off voltage and peak current capability, gas-filled plasma closing switches are usually employed in high-voltage and high-power pulsed power systems and apparatuses. Dielectric strength of the gas(es) used in PCSs, gas pressure and electrode topology determine the breakdown voltage of each particular PCS. When the switch is triggered, the current starts to flow through the plasma channel developed between the electrodes of the switch. Such Plasma closing switches can achieve fast switching times and deliver high power impulses into the load with low energy loss. The spark gap is one of the most commonly used gas-filled plasma closing switches (Gundersen 1991). Figure 2.5 shows different gas-filled closing switches and the range of gas operating pressures.

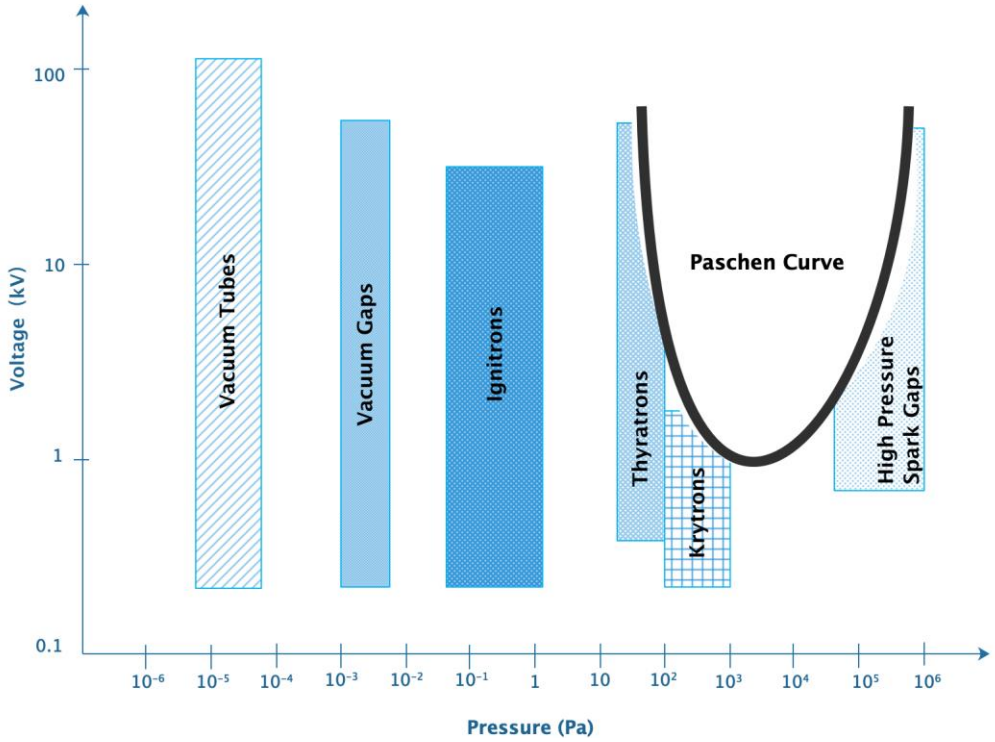

Figure 2.5 Different types of gas-filled closing switches in the range of gas pressures and operation voltages(Hansjoachim Bluhm 2006b).

Gas-filled plasma closing switches are acknowledged as one of the most used gas closing switches in different high-power pulse applications. Compared with other types of switches, gas-filled closing switches have the following advantages: (i) they are simple in their structure, (ii) they provide straightforward operation, (iii) they can be accurately triggered, and (iv) they can withstand significant voltage and current: conductive current from 10s A to 100s kA, and hold-off voltage up to several MV.

The basic principle of the plasma closing switch operation can be described as follows: when the applied voltage across the switch gap exceeds the hold-off voltage or an external source is used to ionise the gas medium in the switch, the gas breakdown results in the development of highly conductive channel(s) in the switch. Thus, a spark is generated between the electrodes and the plasma channel(s) resistance reduces sharply, resulting in the high current flow through the plasma discharge channel. Gases are considered self-healing dielectrics; thus, they can recover their dielectric strength after each breakdown. Gas-filled plasma closing switches are frequently employed in

pulsed power systems to protect expensive high-voltage equipment such as ignitrons and thyratrons. In this case, the PCS is open during normal operation of the high voltage system. However, if the applied voltage exceeds the threshold voltage or the load is abnormally short-circuited, the switch will immediately break down, and the fault current will bypass the high-voltage equipment as it will be diverted to the ground through the switch.

Another application of the gas-filled plasma closing switches is shaping the output waveforms in the pulsed power system. Such as pulse forming lines, gas-filled plasma closing switches are used to change or compress the output waveform.

The electrodes of gas-filled plasma closing switches can be designed as symmetric or asymmetric electrodes. Figure 2.6 presents three conventional topologies often employed in gas-filled closing switches. There is a quasi-uniform electric field in the plane-plane and sphere-sphere configurations of the electrode gaps. There is a highly non-uniform electric field distribution in the point-plane electrode gap. In a uniform electric field, the breakdown voltage can be predicted by Paschen's law for a given gap spacing-pressure product. In a non-uniform electric field, the data obtained by Paschen's curve can be used as the initial reference value. The breakdown voltage can be predicted by applying the scaling coefficient or using empirical data to define the actual gap operating behaviours. Plasma closing switches operate with highly non-uniform electric fields to utilise pre-breakdown to stabilise switching performance. Pre-breakdown corona discharges improve the performance of repetitive plasma closing switches, where the corona discharge can help to reduce pre-fire rates(Harrower, MacGregor, and Tuema 1999; Beveridge 2009; L. Li, Huang, and Yang 2020).

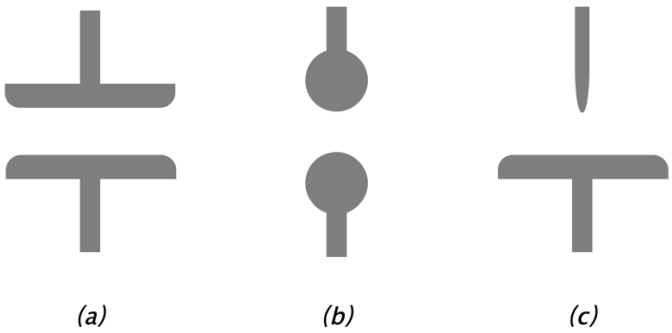

Figure 2.6 Typical geometry designs of gas-filled plasma closing switches. (a) plane-plane configuration; (b) sphere-sphere configuration; (c) point-plane configuration.

Figure 2.7(a) shows the electric field distribution in the plane-plane electrode system. This electrostatic field has been modelled using COMSOL software. It can be seen from Figure 2.7(a) that the electric field between two parallel plane electrodes is uniform. The electric field is enhanced at the electrode edges (fringe effects). Rounding the edges of the plane electrodes can effectively reduce the fringing effect, thereby improving the withstand voltage of the gap. The Rogowski profile of electrodes is used to generate the uniform field in the main gap and to avoid the field enhancement (as compared with the field in the main gap) at the electrode edges (Rizk and Trinh 2018).

Figures 2.7(b) and (c) show the field distribution in the sphere-sphere and point-plane electrode topologies. The electric field in the sphere-sphere electrode topology can be quasi-uniform (Turnbull, MacGregor, and Harrower 1997). Compared with the plane-plane structure, the electric field at the poles of the spherical electrodes is enhanced. The enhanced field stimulates the development of breakdown events on the poles of the spherical electrodes.

The point-plane electrodes produce an extremely non-uniform electric field. The maximum electric field in the gap is achieved at the tip of the point electrode. The electric field decreases rapidly with the distance away from the tip of the point electrode.

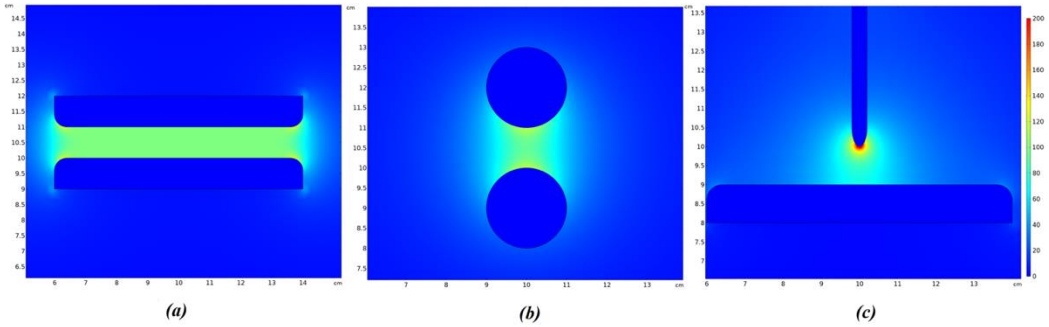

Figure 2.7 Electric field distributions(V/m) of typical geometry of gas spark gaps, simulated by COMSOL with a 1cm gap between electrodes and a 1V energisation. (a) plane-plane; (b) sphere-sphere; (c) point-plane.

In practice, most switches employ electrode configurations that produce non-uniform electric fields. To quantitatively analyse the degree of non-uniformity of the electric field, the coefficient of non-uniformity of the electric field β can be used:

$$\beta = \frac{E_{max}}{E_{av}} \tag{2.1}$$

where E_{max} is the maximum electric field strength; E_{av} is the mean electric field strength. β will be used in Chapter 4 and Chapter 7 in the equation for breakdown voltage in order to take into account the field non-uniformity. The average field is obtained as:

$$E_{av} = \frac{V}{d} \tag{2.2}$$

where V is the applied voltage on the electrode; d is the shortest distance on the gap.

For the point-plane topology, Coelho and Debeau provided an analytical expression for the field along the central axis, assuming that the point electrode is a confocal hyperboloid (Coelho and Debeau 1971):

$$E_{max} = \frac{2V}{a \ln\left(\frac{4d}{a}\right)} \tag{2.3}$$

where V is the applied voltage on the point electrode, a is the radius of the point electrode, and d is the distance between the point electrode and the plane electrode.

Due to its specific topology and operation, accurate triggering, ability to withstand significant voltages and transfer high currents, to operate at fast *dV/dt* and *dI/dt* and with low jitter, the gas-filled closing switches are widely used in different pulsed power applications.

This section will discuss the different methods of triggering the gas-filled closing switches and the switches currently used in the pulsed power industry. The gas-filled closing switches can be divided into the following categories in accordance with their triggering mechanisms: self-breakdown gaps, trigatron spark gaps, and field distortion spark gaps.

I. Self-breakdown PCSs

Self-breakdown plasma closing switches are commonly used in nanosecond and microsecond pulse generators. These switches are triggered by the voltage applied to their electrodes. In the self-breakdown topology, typically, two electrodes are used, and the gap between them is filled by an insulating gas (Mesyats 2007). The spark breakdown occurs when the electric field E between the electrodes exceeds the breakdown electric field E_b.

The electrode geometries of self-breakdown PCSs can be represented by three basic structures introduced above (plane-plane configuration, sphere-sphere configuration, and point-plane configuration.).

In practical applications, physical dimensions and geometric topologies of the plasma closing switches will be selected according to specific requirements.

Plane-plane or sphere-sphere configuration topologies can be used if a stable discharge voltage is required.

Self-breakdown PCSs typically have two operation modes. If the applied voltage increases slowly, the breakdown can be considered a static self-breakdown. If the breakdown is caused by transient voltage, the breakdown is called a pulse-charged self-breakdown. High-pressure self-breakdown PCSs are widely utilised in pulse generators with voltages up to 1MV at an average power of ~100kW with pulse repetition rates (PRR) of a few hundred Hz (Kristiansen 1993; J.-l. Liu et al. 2008). In addition, high-pressure self-breakdown PCSs provide high current handling capabilities (up to MA) and short closing times with low jitters at a relatively low cost.

Due to the relatively high inductance of the discharge channel and high current density, self-breakdown PCSs cannot operate at high repetition frequencies. The multi-channelling regime in Self-breakdown PCSs can be used to reduce the inductance and current density to address this obstacle (Kim et al. 1997).

II. Trigatron closing switches

The trigatron topology was first proposed by Craggs in 1946 (Craggs, Haine, and Meek 1946). It was initially used as a high voltage switch for a high-power modulator in radar. Since then, trigatrons have been widely utilised in pulsed power technology. As trigatron belongs to the gas spark gap category of switches, it provides many advantages, such as a wide voltage operating range, which can be from several kV (Wilkinson 1946) to several MV (Broadbent 1957; Markins 1971), with excellent triggering characteristics, a wide triggering range and a relatively simple structure.

As shown in Figure 2.8, the typical trigatron is composed of two main electrodes. The trigger electrode is inserted coaxially into an adjacent electrode and isolated by an insulating layer. However, because the trigger electrode is

located inside the adjacent electrode, electrode erosion will inevitably occur during its operation, especially under high current density discharge. The electrode erosion affects the triggering characteristics of the trigatron, ultimately affecting the overall operation stabilities and lifetime of this switch (L. Wang et al. 2014).

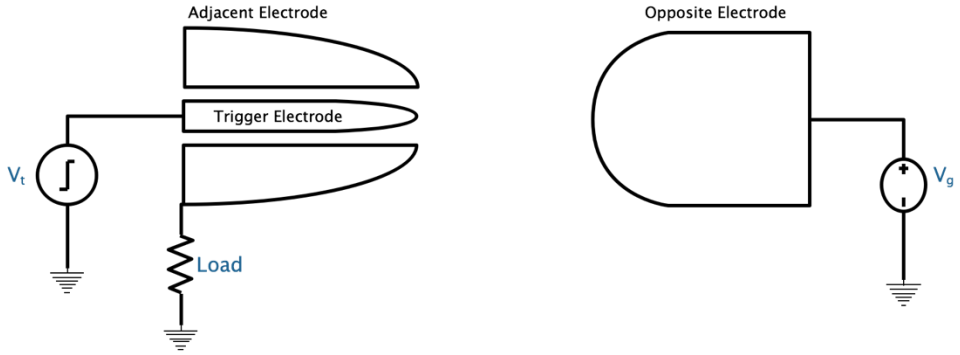

Figure 2.8 Schematic of a typical trigatron spark gap(Williams and Peterkin 1989)

It has been shown that there are two triggering mechanisms of trigatrons. The first mechanism is the trigger electrode and the opposite electrode discharge first, and then the trigger electrode and the adjacent electrode break down under the overvoltage. Under normal circumstances, the time to breakdown and jitter achieved by this triggering method is relatively short. Due to high electric field requirements, the trigger electrode is generally made as a pin. A large discharge current flows through the trigger electrode, which causes the erosion of the trigger electrode surface, resulting in a relatively short lifetime of trigatrons. Triggering also can be provided by the trigger electrode: the adjacent electrode discharge first, and then a breakdown occurs across the main gap under a fast-rising trigger pulse, which is somewhat similar to the self-breakdown spark gap. The time to breakdown and jitter of this triggering mode is relatively long. However, this method helps to reduce the discharge current which flows through the trigger electrode. Thereby it helps to reduce the trigger electrode erosion and effectively extend the lifetime of trigatrons (Peterkin and Williams 1989).

III. Field distortion three-electrode spark gaps

Field distortion three-electrode spark gaps are commonly used in the pulsed power system with fast switching time, low jitter and high performance. The switch is mainly composed of two gaps in series, separated by main electrodes and a trigger electrode located in the centre. The change in the electric field distribution triggers the switch by applying an external trigger pulse to spark gaps already pre-energised below the self-breakdown voltage. In the conventional topology, the main electrodes are designed to produce a reasonably uniform field so that substantial hold-off voltage can be generated across the main gap (Hussain and Zakaullah 2007; Wei et al. 2012).

Figure 2.9 shows the electrostatic field distribution in the switch with the central trigger electrode. Before triggering, as shown in Figure 2.9 (a), the trigger electrode is floating, and the electric field distribution in the main gap is virtually uniform. The is minimum distortion of the equipotential lines as compared with the case of no trigger electrode in the switch. When the trigger electrode is stressed with a trigger voltage (which typically has an opposite polarity to the applied voltage) the electric field between the upper and trigger electrodes is significantly increased, as shown in Figure 2.9 (b).

If the field strength is sufficiently high to cause the breakdown in the upper gap, a conducting plasma channel between the upper and trigger electrode is formed and both of these electrodes are now at the same potential and the lower gap becomes overvolted. This leads to an increase in the electric field in the lower gap of the switch, Figure 2.9(c) ,which results in the breakdown of this gap and closure of the switch.

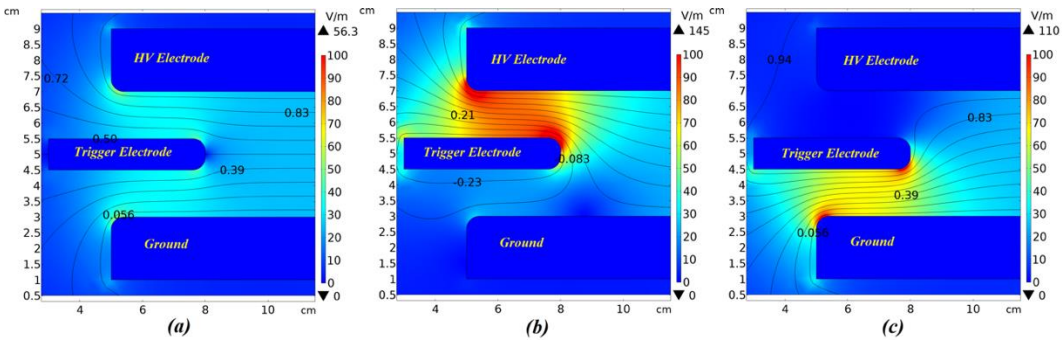

Figure 2.9 Electrostatic simulations of the field distribution in the field distortion triggered spark gap. A 1cm thick trigger electrode is placed in the middle of a 4 cm gap; nominal voltage of 1V is applied to the upper electrode. Electrostatic field distribution and equipotential lines when: (a) the trigger electrode is at floating potential (no trigger impulse applied); (b) -0.3V is applied to the trigger electrode; (c) the trigger and upper electrodes are at the same potential (this configuration models the breakdown event in the upper gap, when the plasma conductive channel links these two electrodes.

Other triggering mechanisms, including UV triggering, electron beam triggering and laser triggering, are all based on external ionising radiation sources (McDonald et al. 1980; LeChien et al. 2010; Larsson et al. 2014).

Ionising initiatory electrons, generated by an external source trigger, lead to the development of ionisation fronts in the switch, which result in the formation of a highly conductive channel, completing the breakdown process in the whole gap. The advantages of these triggering methods are high reliability and excellent switching performance. However, its limitations include the requirement of external sources.

2.3 Transient characteristics of PCSs

A typical PCS can be represented by an equivalent circuit shown in Figure 2.10 using the *RLC* lumped element circuit model. When the switch is open, the PCS is characterised by the equivalent capacitance C_s. At the switch closure, the capacitance C_s becomes connected in series with the plasma channel inductance $L_s(t)$ and plasma channel resistance $R_s(t)$, and these parameters are used to simulate a spark discharge.

During the formation and development of the conductive plasma channel, its inductance $L_s(t)$ and resistance $R_s(t)$ are transient in their nature.

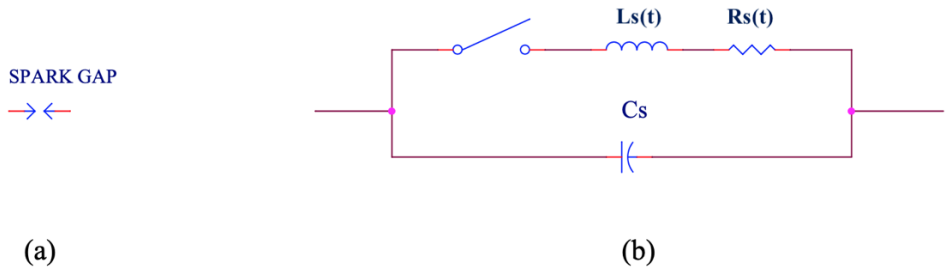

Figure 2.10 The equivalent circuit of a PCS in which C_s, $L_s(t)$ and $R_s(t)$ represent the self-capacitance, plasma channel inductance and plasma channel resistance, respectively.

Minimising plasma channel resistance can effectively minimise the energy dissipation in plasma closing switches. A considerable amount of research work about the transient resistance of plasma channels in gases has been conducted in the past few decades. The primary purpose of several papers published in the period from 1944 to 1999 by a group of researchers was to establish a model that could accurately describe the plasma channel resistance (Popovic, Popovic, and Platisa ; Toepler 1927; Rompe and Weizel 1944; Braginskii 1958; Vlastós, R., and W. 1972; Barannik 1975; Kushner, Kimura, and Byron 1985; Akiyama 1988; T. G. Engel, Donaldson, and Kristiansen 1989; Greason 1999; Hussey et al. 1999).

i. The capacitance of PCSs

When the gas-filled PCS is open and charged to voltage V, the electric charge, Q, on its electrodes is held by dielectric gas, and the capacitance of plasma channel is given by:

$$C_s = \frac{Q}{V} \tag{2.4}$$

where Q is the charge on electrodes; V is the applied voltage. For switches with different electrode geometries, the capacitance is also different. In the case of parallel plane electrodes, the self-capacitance is:

$$C_s = \frac{\varepsilon_r \varepsilon_0 A}{d} \ (F) \tag{2.5}$$

where ε_r is the relative permittivity of dielectric gases; ε_0 is the vacuum permittivity of free space (~8.85pF/m); A is the area of the electrode in [m^2]; d is the gap spacing in [m]. Typically, the self-capacitance of PCS switches is very small, <10s pF.

ii. The transient inductance of plasma channel

It is challenging to obtain the transient inductance of the plasma channel. When the streamer crosses the interelectrode gap and a conductive channel is established, the inductance of the plasma channel can be approximated by the inductance of a single conducting wire (Grover 2004):

$$L_s(t) = l\frac{\mu_0}{2\pi}\ln\left(\frac{a_c}{a(t)} - \frac{3}{4}\right) = 2l\ln\left(\frac{a_c}{a(t)} - \frac{3}{4}\right) \tag{2.6}$$

where l is the length of the plasma channel; a_c is the radius of the current return path; $a(t)$ is the temporal plasma radius of the plasma channel. The temporal plasma radius can be estimated by the Braginskii model, which will be introduced in detail in the following chapter. Based on the PCSs developed topology, theoretical analysts show that the plasma channel inductance is small (several nHs). The multichannel plasma closing switches can effectively reduce the inductance of plasma so that the rise time of the current pulse becomes faster.

iii. Transient resistance of plasma channel

All the plasma channel resistance models found in the literature and discussed in this section assume that the current in the plasma channel is related to its resistance. This is because the mobility of charged particles in the gas or plasma determines the resistivity of the gas (plasma). Therefore, if the mobility of the charged particles increases, the resistivity of plasma in the channel drops. Since resistivity determines the resistance, the plasma channel resistance drops. Moreover, the resistivity also determines the current density in the electric field, so the current flowing through the plasma channel rise.

In the ideal discharge process, according to Ohm's law, the transient resistance of the plasma channel drops from infinity (open circuit resistance) to very small (from several mΩ to tens mΩ) instantaneously as the current in the plasma channel reaches the maximum. However, the plasma resistance depends on the conduction current and is governed by the length and diameter of the plasma channel and the conductivity of plasma in the channel. The plasma channel expands as the energy delivered into the channel increases; this process is essential for investigating plasma resistance. The plasma channel has only a minimal radius at the initial stage of its expansion, and this radius significantly increases during the energy deposition stage. This process directly affects the resistance of the plasma channel. If it is assumed that the cylindrical plasma channel is formed between two electrodes, the time-dependent resistance of this channel will be expressed as

$$R(t) = \frac{l}{\sigma \pi a(t)^2} \tag{2.7}$$

where l is the length of the plasma channel in [cm]; σ is the electrical conductivity of the plasma-filled channel in [$\Omega^{-1} c\mathrm{m}^{-1}$]; $a(t)$ is the plasma channel radius in [cm]. Braginskii proposed to use a hydrodynamic approach to investigate the plasma channel radius (Braginskii 1958). This model assumes that as the conduction current flows through the plasma channel, the

Joule heating rapidly increases its temperature and pressure within the channel. Thus, the channel expands with a strong shock wave into the surrounding gas.

The theoretical value of the channel radius obtained from the Braginskii model agrees with the experimental data obtained by Maas (Maas 1985). The time-dependent plasma radius of the channel is expressed as:

$$a(t)^2 = \left(\frac{4}{\pi^2 \rho_0 \xi \sigma}\right)^{\frac{1}{3}} \int_{t0}^{t} I(t)^{\frac{2}{3}} dt \tag{2.8}$$

where σ is the electrical conductivity of the plasma-filled channel; ρ_0 is the initial gas density (the model assumes that σ and ρ_0 are constant during this energy deposition stage); ξ is the constant which depends on the gas properties.

Analysing plasma resistance equations proposed by Braginiskii, Toepler, Rompe and Weizel, Barannik, Popovic, Demenik and Kushner were used to study the plasma channel resistance. It can be concluded that most investigators are mainly focused on the energy balance equation and principles of thermodynamics (Popovic, Popovic, and Platisa ; Toepler 1927; Rompe and Weizel 1944; Braginskii 1958; Demenik 1968; Vlastós, R., and W. 1972; Barannik 1975; Kushner, Kimura, and Byron 1985). However, all these models require a phenomenological constant obtained experimentally or theoretically calculated. This constant is used to fit the analytical data under specific experimental conditions to the experimental results (i.e., type of gases, pressure, and plasma length). Rompe et al. obtained this constant through theoretical analysis (Rompe and Weizel 1944). In other models, the constant was obtained empirically based on the experimental data. Finally, it normalised the resistance curve, which only shifts without changing the shape.

Toepler first proposed the plasma resistance equation (Toepler 1927). The equation was empirically based on experimental data:

$$R_s(t) = \frac{C^* l}{\int I(t)\, dt} \tag{2.9}$$

where $R_s(t)$ is the time-dependent plasma resistance in [Ω]; C^* is a proportionality constant that depends upon gases; l is the plasma channel length in [cm] and $I(t)$ is the dynamic current in [A]. Under the experimental condition of a plasma channel length between 9 mm and 17.5 mm in the air with an initial pressure of 10^5 Pa, Toepler obtained the empirical expression of plasma resistance using experimental data. The Toepler's constant depends on the gases in the plasma channel. Engel reports a normalised constant of $C^* = 4.5 \times 10^{-2}$ at the pressure of $0.86 \times 10^5 Pa$. (T. G. Engel, Donaldson, and Kristiansen 1989)

Rompe and Weizel developed the plasma resistance equation in 1944 (Rompe and Weizel 1944). The equation was derived from an energy balance equation:

$$R_s(t) = \sqrt{\frac{p_0 l^2}{2C^* \int I(t)^2\, dt}} \tag{2.10}$$

where p_0 is the initial gas pressure (in Pa). Rompe and Weizel obtained the plasma resistance equation using a unipolar pulse with a width of 50ns at an initial pressure of 1.6×10^5 Pa for a plasma channel length of $l \leq 35$ mm. Mesyats have verified these test conditions. However, this model ignores the effects of thermal and radiation losses and the plasma radius. Engel reports a normalised constant of $C^* = 9.7$ at the pressure of 0.86×10^5 Pa in air, and Mesyats suggested $C^* = 11.5$ at the pressure of 10^5 Pa in air (Vorobev and Mesyats 1971).

Demenik *et al.* published the plasma resistance equation in 1968 (Demenik 1968), which took the plasma radius into account:

$$R_s(t) = \frac{C^* l}{a(t)^{\frac{10}{11}} I(t)^{\frac{6}{11}}} \tag{2.11}$$

where $a(t)$ is the plasma channel radius in [cm]. The equation was obtained for xenon by using a unipolar pulse with a width of 1.5ms at an initial pressure of $p_0 \leq 0.5 \times 10^5$Pa for a plasma channel length from 6mm to 300mm. Engel suggests a normalised constant of $C^* = 0.3$ at the pressure of 0.86×10^5Pa.

In 1972 Vlastós developed its plasma resistance equation (Vlastós, R., and W. 1972) which is given as :

$$R_s(t) = \frac{C^* l a(t)^{2/5}}{\int I(t)^2 \, dt^{3/5}} \tag{2.12}$$

This equation was obtained for the plasma channel with a length of 130mm and under the exploding wire restrike conditions. Engel suggested a constant C^* value of 876 for air at a pressure of 0.86×10^5Pa.

In 1974, Popovic presented another empirical plasma resistance equation (Popovic, Popovic, and Platisa):

$$R_s(t) = \frac{C^* l}{[\int I(t)^2 \, dt]^n} \tag{2.13}$$

where n is a constant. This equation was derived based on the experimental results obtained for different gases (air, oxygen, argon and xenon) by using unipolar pulses at an initial pressure of $p_0 \leq 0.5 \times 10^5$Pa and for the plasma channel with a length of 20mm. Engel has suggested using $C^* = 30$ and $n = 0.33$ for these gases.

Barannik *et al.* developed a new model for investigating plasma resistance (Barannik 1975), which also takes into account the plasma radius. The Barannik resistance was derived from the energy balance equation:

$$R_s(t) = \frac{C^* l {\rho_0}^{1/3}}{\int I(t)^{2/3}\, dt} \tag{2.14}$$

where ρ_0 is the initial gas density in [kg/m^3]. Barannik's model was developed based on the unipolar pulse with a width of 100ns, and for the plasma channel with a length of $l \leq 400$mm. Equation (2.33) was obtained for air, sulphur hexafluoride and nitrogen at the initial pressure of $p_0 \leq 12 \times 10^5$ Pa. The model assumes that the conductivity and the temperature of the plasma are constant in the channel. Barannik recommended the following value of C^*= 0.7×10^{-3} at the pressure of 10^5 Pa while Engel suggested using $C^* = 1.7 \times 10^{-3}$ at the pressure of 0.86×10^5Pa.

The Kushner model for the dynamic resistance of the plasma breakdown channel assumes that the plasma in the breakdown channel is in local thermodynamic equilibrium during its expansion phase (Kushner, Kimura, and Byron 1985). The expression for the resistance of the plasma channel given by Kushner *et al.* is:

$$R_s(t) = C^* l \left(\frac{{p_0}^3}{A(t)^2 I(t)^6} \right)^{\frac{1}{5}} \tag{2.15}$$

where A(t) in [cm^2] is the plasma channel cross-sectional area, which can be calculated from the temporal plasma channel radius using Braginskii's equation, $A(t) = \pi a(t)^2$. The model was developed based on the following test conditions: unipolar pulse with a width of 100ns, the current density of $2 \times 10^4 \mathrm{MA/cm^2}$, and a plasma channel length of $l = 12$mm. The equation was obtained for hydrogen, nitrogen, sulphur hexafluoride, methane and xenon

at an initial pressure of $p_0 = 0.5 \times 10^5 \text{Pa}$. Engel provided a normalised constant of $C^* = 24.7$ at the pressure of $0.86 \times 10^5 \text{Pa}$.

All the above models are compared in detail by using the transient plasma resistance models. In most of these models, the energy balance equation is solved, and the plasma resistance is proportional to the inverse integral of the conductive current. Since the models only consider the inverse integral of the current and ignore the energy balance condition, the empirical equations proposed by Toepler and Popovic *et al.* provide a maximum error compared with the experiment results. It has been shown that, in the early stage of breakdown, the models developed by Demenik *et al.*, Kushner *et al.*, Rompe and Weizel, and Vlastos provided more accurate values of plasma resistance. However, these models provide significant discrepancy (order of magnitude) in the resistance on a longer time scale. The Kushner model demonstrates the least accumulated error in the predicted plasma resistance compared to the experiment results. The Braginskii model is also based on the energy balance equation and assumes that the conductivity of plasma in the channel remains constant during the transient post-breakdown process. Thus, its resistance changes due to the hydrodynamic expansion of the conductive plasma channel. These transient plasma resistance models will be compared in detail in this work (Chapter 7) to understand the dynamic characteristics of PCSs further.

2.4 Insulation Properties of gases

Gases may be considered the most common and abundant insulating medium. Gases are widely used as insulating media in gas-insulated equipment in high-voltage power transmission and transformation systems: gas-insulated transformers, gas-insulated transmission lines, circuit breakers, etc.

Since SF_6 gas was discovered, its application has promoted the expeditious development of different high-voltage gas-insulated systems. However, SF_6 gas has a high global warming potential. Therefore, it is crucial to find environmentally friendly

alternatives to SF_6, and this search has become an important research topic in recent years.

2.4.1 Basic properties of SF_6

The insulating gases widely used as gaseous insulators are dry air and sulphur hexafluoride (SF_6) gas (Kline et al. 1979; Clough et al. 2005; D.K. Sharma et al. 2014). At atmospheric pressure, SF_6 has a high dielectric strength: ~2.5 times than that of air (Mardikyan, Seker, and Ayaz 2000). So, the SF_6 gas is widely used in power systems as a gaseous dielectric. SF_6 gas has excellent physical and chemical properties as insulating gas: it is a colourless, odourless, non-toxic and non-inflammable gas (Kawamura et al. 1998). Due to its exceptional chemical stability, it does not react with other substances, and its liquefaction temperature is low. Notably, it has high dielectric strength and excellent arc-quenching capability.

The molecule of SF_6 gas is a molecule with a high electron affinity value which makes SF6 strong electronegative gas. Figure 2.11 shows an SF6 molecule schematically. Moreover, its significant molecular weight and large cross-section shorten the mean free path of electrons and lower the ion mobility ratio of SF_6. Thus, the ionization process is weakened, and the recombination process is enhanced. SF_6 gas is non-corrosive, but it will decompose under high-temperature conditions during the discharge, forming low fluoride. When the gas contains moisture, these low fluorides will also produce a secondary reaction with water, converting into acidic substances such as HF and H_2SO_4 that are highly corrosive to insulating materials and metal materials, thereby causing damage to the equipment and operation failure.

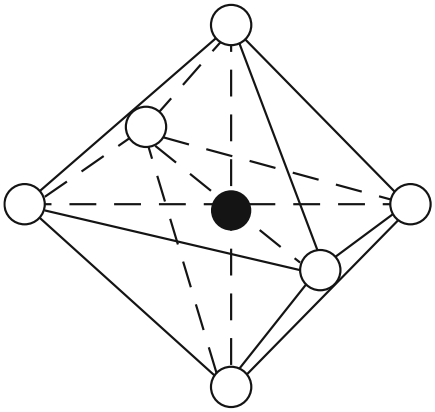

Figure 2.11 The SF_6 molecule structure(Xiao 2016)

In 1997, to prevent global warming, the Kyoto protocol classified SF_6 gas as a greenhouse gas (Protocol 1997). Unlike other greenhouse gases, SF_6 is difficult to degrade in the atmosphere. Therefore, the greenhouse effect of SF_6 is cumulative, even permanent. SF_6 gas molecules have the highest global warming potential (GWP) among other insulating gases. The GWP of SF_6 is about 22,800 times of that of CO_2. Therefore, SF_6 has become one of the most restricted greenhouse gases in the world. Therefore, the most crucial method to reduce the impact of SF_6 on the environment is to diminish the consumption of SF_6 and find an environmentally friendly alternative to SF_6 gas (Rabie and Franck 2018).

2.4.2 Alternatives to SF_6

So far, many theoretical and experimental studies have been on potential alternative gas to SF_6. However, there is still no single gas that can completely replace SF_6 gas as an insulation medium for HV applications. The alternative gas(es) must satisfy the following conditions to replace SF_6 gas:

- Strong electronegativity, excellent arc-quenching properties;
- high dielectric strength;

- low liquefaction temperatures, high vapour pressure, and high thermal conductivity characteristics;

- stable physical and chemical properties, non-toxic, and non-flammable;

- environmentally friendly low global warming potential (GWP) value;

- Low cost and secure storage;

For the above requirements, the research of alternative gas to SF_6 has two main methods. One is mixing SF_6 with other environmentally friendly gases while maintaining the insulation performance with the reduced proportions of SF_6. For many studies (Malik and Qureshi 1979; Kline et al. 1979; Mahdy 2011; Can et al. 2017), using natural gas (air, nitrogen or CO_2) as the mixed gas at a 20%-40% mixing ratio, the gas mixtures have the same insulation characteristics as pure SF_6. Furthermore, its economic impact is also considerable. The partial replacement of SF_6 is just an interim solution which cannot eliminate the usage of SF_6. The other is a complete replacement for SF_6 gas, that is, finding a new insulating medium and its mixed gas to eliminate the use of SF_6 gas. Research shows that some gases have the potential to replace SF_6 as an insulating medium in high-voltage equipment, such as CF_3I, c-C_4F_8, HFO1234ze or C_3F_8 (E. E. Kunhardt, Sutton, and Danner 1984; Ngoc et al. ; Katagiri et al. 2008; Koch and Franck 2015; Xian-qin et al. 2017; Beroual 2017). As a synthesis gas, CF_3I has been found to be the most potential alternative gas to SF_6 in recent years (L. Chen et al. 2017; P. Widger, Griffiths, and Haddad 2018). CF_3I with buffer gas is outstanding in terms of dielectric strength, arc extinguishing, heat conduction and environmental protection. CF_3I gas is a strongly electronegative gas. Global warming potential (GWP) is low, and the lifetime in the atmosphere is only two days. However, the high liquefaction temperature makes CF_3I gas challenging to use directly in high-voltage equipment, which usually needs to mix with other buffer gases (L. Chen et al. 2017).

Currently, theoretical and experimental studies have shown that it is difficult to find a gas or gas mixture that is better than SF_6 in terms of their dielectric strength, vapour pressure, liquefaction temperature, toxicity, physicochemical stability, compatibility and cost. However, the potential alternative gas with better characteristics can be found in specific applications for different purposes. For example, in the gas-filled spark gap of pulsed power generators, dry air, CO_2, nitrogen, hydrogen, argon and many mixtures of gases are widely used as the insulating medium to improve some performances (Crull et al. 2004; Rokunohe et al. 2005; S. Liu, Fan, and Shi 2008; Singhasathein et al. 2013; Hösl, Häfliger, and Franck 2017). The dry air, an insulation medium in the gas switch, exhibits excellent dielectric strength in different pressure regimes. The argon can provide faster switching times in the high-power pulse generator and improve the multichannel ability (Jiasen et al. 2011).

Table 2-2 Dielectric Strength of the gases used within this investigation (Rabie and Franck 2018).

Gas	***Insulation strength related to SF_6***	***Boiling points (℃)***	***GWP***	***Lifetime in the atmosphere (Year)***	***Electron-attaching***
SF_6	1	-63	22800	3200	Strongly
C_3F_8	0.96	-37	7000	2600	Strongly
c-C_4F_8	1.3	-6	8700	3200	Strongly
CF_3I	1.23	-22.5	0	2/365	Strongly
CO_2	0.3	-78.5	1	50-200	Weakly
Air	0.3	-183	0		Weakly
N_2	0.36	-196	0		Weakly
Argon	0.07	-185.7			Not

2.5 Aim of this study

This chapter discusses the relevant literature and provides the background for the current research project. In Chapter 2, the following aspects are reviewed and discussed: basic mechanisms of gas discharges, the breakdown mechanism relevant to the operation of plasma closing switches, the switching topologies and their operating characteristics and the basic operational principles of the pulse power systems. A detailed discussion of different types of plasma closing switches used in different practical applications is presented.

The basic theory of the gas discharge is reviewed, covering the Townsend and streamer discharges, as well as Paschen's breakdown law. The dynamic plasma resistance models available in the literature are reviewed and discussed in detail, and the operating parameters of plasma closing switches are also analysed.

Finally, the operating characteristics of plasma closing switches filled with different gases are discussed, and the gases used in such applications are reviewed. Growing environmental concerns have prompted the search for suitable alternatives to SF_6 (environmentally friendly gases), which are reviewed in the present Chapter.

High voltage gas-filled plasma closing switches (PCSs) are widely used in pulsed power systems due to their capability to operate in wide voltage and current ranges, their ability to cope with high rates of change of voltage and current and to provide short switching time with low jitter when operating in a triggered mode. The low resistance and inductance of plasma channel in these switches also mean they can be used in pulsed power systems that operate at high voltage and produce fast-rising current and voltage impulses. Although the solid-state switching technology gains popularity as a potential replacement for the gas-filled PCSs in some pulsed power systems and applications, the plasma closing switches remain essential components for different practical high voltage high power impulsive systems due to their robustness, exceptional operational capabilities and characteristics, relatively simple technical process and a relatively low cost. Researchers and engineers continue to invest significant efforts in the design and development of novel switch topologies in order to improve their operational performance and switching characteristics.

One of the critical aspects which should be addressed is the use of environmentally friendly gases as working fluids in the plasma closing switches. Therefore, the present study is focused on an experimental investigation of the breakdown behaviours of plasma closing switches filled with different gases and gas mixtures (air, N_2, 90%/10% Ar/O_2, and CO_2) which can be used as a potential substitution for SF_6 in PCSs.

The other aspect addressed in this study is the improvement of the operating characteristics of the PCSs and the development of compact PCSs that will facilitate reduced footprint of practical pulsed power systems. Gas-filled plasma closing switches with higher breakdown voltage and lower jitter are required for practical pulsed power applications. The key characteristics and parameters should be investigated, including the self-breakdown voltage, time to breakdown and jitter of the switches. The operating parameters of PCS filled with different environmentally friendly gases require further optimisation and investigation to find the optimal solution for specific practical applications of gas-filled PCSs.

The present work is focused on developing a two-stage triggered gas-filled PCSs with corona electrodes, which can provide low spread in the self-breakdown voltage and low jitter when filled with environmentally friendly gases. The proposed gas-filled switching topology includes a trigger electrode and multiple corona discharge needle electrodes, which are required for the stabilization of the operational performance of the switch. The operational (the self-breakdown and triggered) characteristics of the PCSs have been investigated over a wide range of gas pressures, 1-12 bar (gauge) in order to establish potential phenomenological relationships between the operating voltage, the standard deviation in the self-breakdown voltage, pre-breakdown delay time and jitter and the gas pressure in the switch. These phenomenological relationships will help further optimise and develop gas-filled PCSs filled with environmentally friendly gases.

Based on the models presented in the literature and the experimental results, a new analytical and computational model was developed and used to obtain the main characteristics of the transient post-breakdown plasma channel formed during the breakdown process in the multi-electrode plasma closing switching topology. This analysis can help in the further development and optimisation of advanced gas-filled plasma closing switches for pulsed power applications.

CHAPTER.3 EXPERIMENTAL SET-UP AND PROCEDURES

3.1 Introduction

A gas-filled plasma closing switch is an essential component of high voltage, high-power impulsive system(s). PCSs have been used in such systems for several decades due to their robustness, excellent operational characteristics and relatively low cost. Significant efforts have been undertaken by researchers and engineers working in the field of pulsed power to develop novel PCS topologies that improve their operational characteristics. Numerous research reports and papers on PCSs topologies developed for different practical pulsed power applications have been published since the 1960s. However, there are gaps in understanding the operation principles of complex PCSs topologies, and there is an urgent need to improve further the operational performance of the plasma closing switches filled with environmentally friendly gases.

This chapter focuses on developing the experimental set-up, designing and constructing a switch topology, and improving the control and measurement methods and test procedures. First, developing a novel two-stage triggered gas-filled PCS with corona electrodes that can withstand high gas pressure and provide low spread in the self-breakdown voltage and low jitter when filled with environmentally friendly gases is explained. Then the designed and developed pneumatic and voltage charging control systems used in the tests are described. After that, the diagnostic system with the in-house developed data processing software is introduced. Finally, the test procedures are presented and discussed in sections 3.5-3.7.

3.2 Design and Development of the Switch Topology

A dedicated two-stage PCS with a highly divergent electric field has been designed and developed. The cross-section of the switch is shown in Fig 3.1.

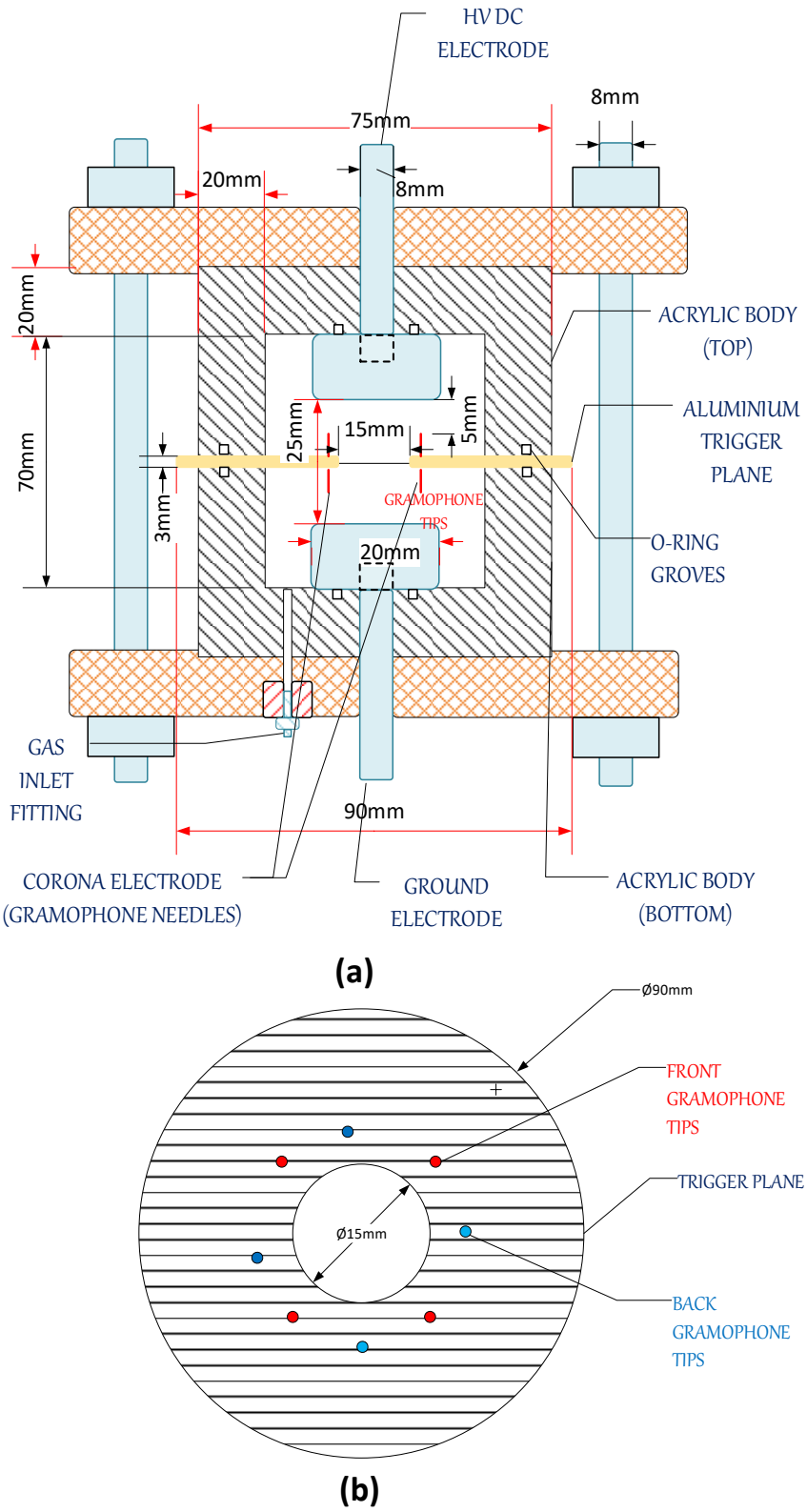

Figure. 3.1. (a) A cross-section of the developed PCS with four needle electrodes on each side of the central plate. (b) central trigger electrode with needles.

As shown in Figure. 3.2, the proposed gas-filled switch topology is axisymmetric. The PCS consists of three major components: (i) the acrylic switch body, (ii) the main plain electrodes and (iii) the central trigger electrode. The switch body is composed of upper and lower cup-shaped parts made of clear acrylic (Perspex). The wall thickness of the cup-shaped part is 20mm, with an internal diameter of 35mm. There is an 8 mm diameter through-hole in the centre of the bottom of the cup-shaped part to locate the main(plane) electrode. The internal space height of the switch is 70 mm. It was found experimentally that the switch made of Perspex with wall thickness of at least 20mm (as discussed above) can withstand gas pressures up to 20 bar (gauge) for at least 1 hour. Two stainless steel cylindrical electrodes with a height of 22.5mm and a diameter of 20 mm are fixed on the top and bottom of the switch by two stainless steel rods. An aluminium trigger plate electrode with an internal aperture of 15mm is located in the centre of the two main(plane) electrodes. Four sharp needle electrodes (gramophone needle) with a diameter of 0.072mm are symmetrically installed around the internal aperture on each side of the trigger electrode to generate a highly non-uniform electrical field distribution. The gap distance between the tips of the needles and the plane electrodes is fixed at 5mm, with an accuracy of $\pm$0.5mm. The sealing of the switch topology is accomplished by O-rings embedded in the slots. A gas inlet with threads that can withstand pressure up to 20bar is employed on the switch body. Four nylon bolts fix the top and bottom glass-reinforced nylon covers to enhance the mechanical strength of the switch.

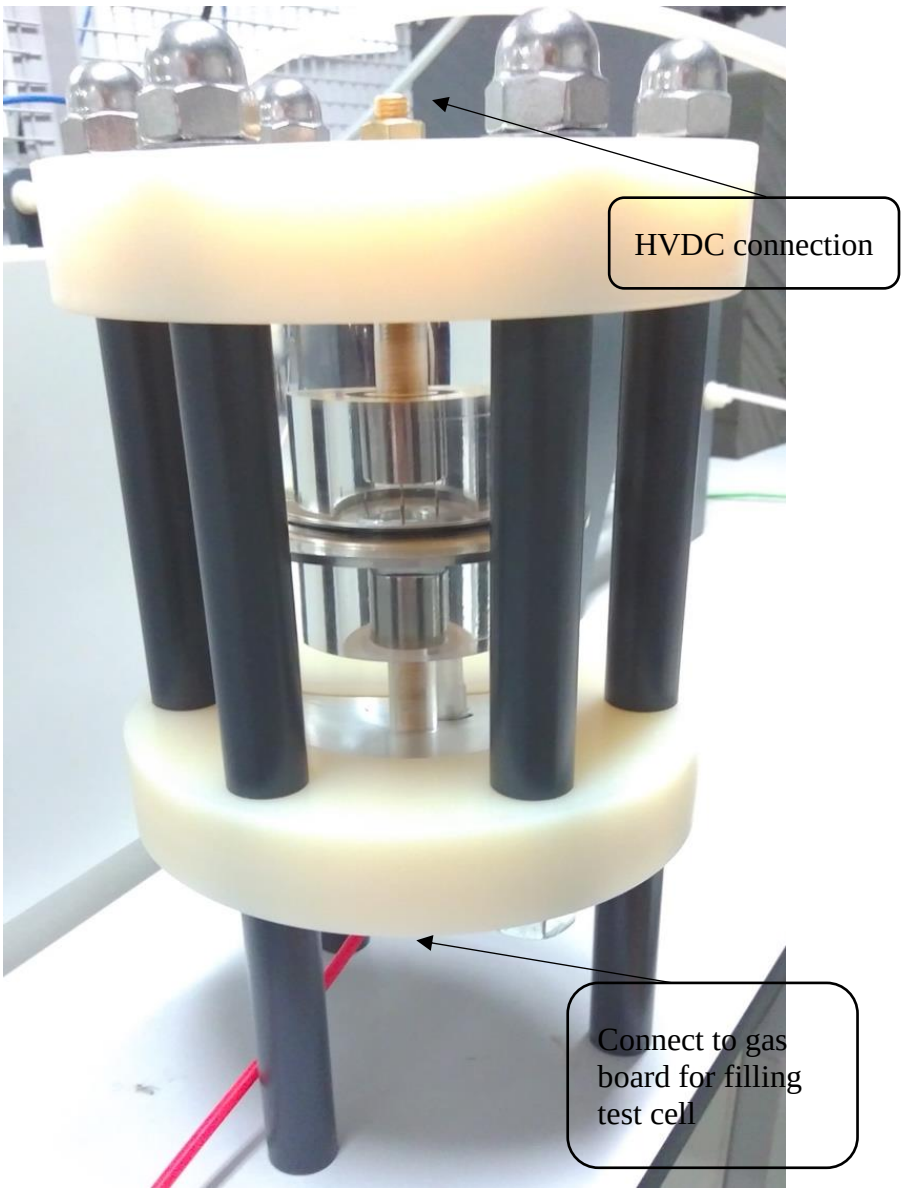

Figure. 3.2 Photograph of the developed PCS.

3.3 Pneumatic Control System

In order to enable accurate operation of the PCS filled with different gases, a gas control system has been employed to control gas pressure in the switch ranging from atmospheric pressure up to 20bar (gauge).

The gas handling and control system includes gas cylinder(s), a designed pneumatic control board equipped with a precision digital gas pressure regulator, ball valves and

a vacuum pump. Four different gases were used in the tests, including "Zero grade" air, CO_2, and 90%/10% Ar/O_2 mixture and N_2. Each gas cylinder with individual gas was connected to the digital pressure regulator through a ball valve at the entrance of the pneumatic control board. The digital pressure regulator, Alicat PC-1500PSIG-D, was used to set and control the pressure in the switch. The accuracy of the digital pressure regulator is $\pm$0.25%. The pressure regulator outlet is connected to a vacuum pump and the PCS via a tee adaptor. The rotary vacuum pump was used to evacuate to less than 0.9bar (gauge) before filling with the test gas to ensure no other impurity gas was mixed. The gas control system was used in each series of tests conducted in the research project. The gas control system is indicated in Figure 3.3.

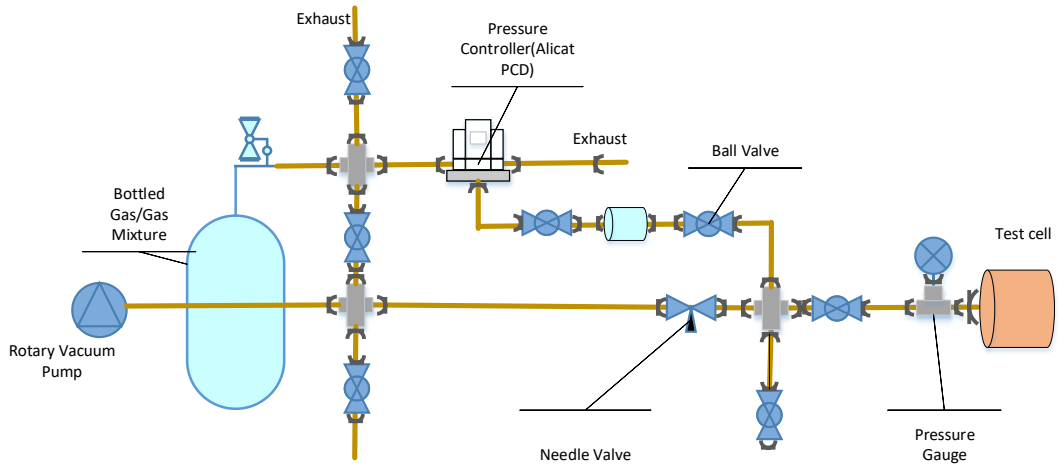

Figure. 3.3. Pneumatic pressure control system.

3.4 High-voltage Control and Data Acquisition System

A LabVIEW program, shown in Figure 3.4, is compiled to control a ramp increase of voltage across the switch, enable interlock protection of high-voltage power supply, and obtain data by connecting an oscilloscope.

The computer is connected to a digital acquisition board, National Instruments DAQ USB-6008, in which the corresponding input signal is 0-5V through an RS232 interface. The maximum output signal of the data acquisition card is expanded to 15V

through a designed isolation amplifier. In order to reduce the instability caused by electromagnetic interference during operation, the amplifier circuit uses an optocoupler circuit to achieve the isolation of the combined external circuit and the internal circuit.

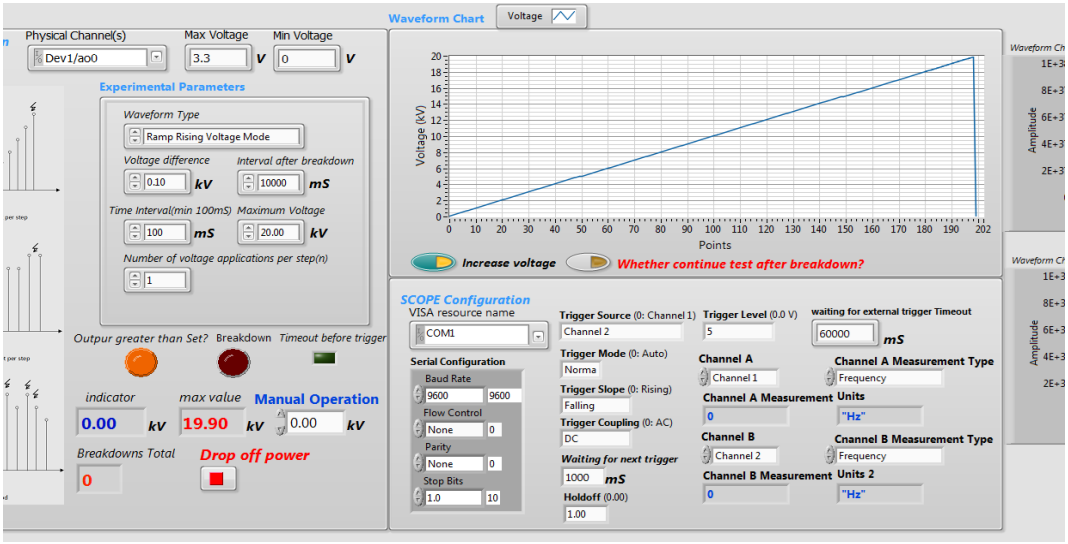

Figure. 3.4. The interface of the LabVIEW control program

The power-on mode of the controlled power supply is set to automatic and manual voltage application modes. In the manual mode, the step size of each step can be set, and then gradually increased voltage by pressing the keyboard keys. In the automatic mode, the program can raise the applied voltage from 60kV/100ms to 60V/100ms, which was mainly limited by the HVDC power supply. To measure the breakdown voltage and corona inception voltage, the rising rate was typically set to 100V/100ms. This rate of rising of the applied voltage is sufficiently long. Thus, these stress conditions can be considered DC energisation. When a breakdown occurs, the program promptly reduces the power supply's output to 0V.

In order to realise the automated experiment process, the program allows for continuous breakdown tests. Setting how many shots to take for each experiment and the interval between every two shots can make the experiment more convenient. The

data obtained in each experiment can be directly transmitted to the computer for display and processing through the serial communication port of the oscilloscope.

In order to ensure the safety of operators and high-voltage equipment, the program included a Man-Machine Protection interface. The UI can set the maximum output voltage. When the voltage output reaches the set value, the test PCS does not discharge, and then the program will automatically reduce the output to 0. When the output voltage of the monitored power supply is not applied according to the settings, the program will automatically stop running and will reduce the voltage to zero to allow the operator to check the fault.

The complete LabVIEW code used for this project is listed in Appendix A. The following sections will discuss the experimental set-ups and methodologies utilised during this research project.

3.5 Experimental Set-up and Methodology for Static Self-breakdown

In order to study the breakdown characteristics for both polarities of the switching topology filled with air, N_2, CO_2 and a mixture of 90%/10% Ar/O_2, an experimental set-up of self-breakdown voltages is performed. Figure 3.5 shows the experimental set-up used for the static self-breakdown voltages measurements.

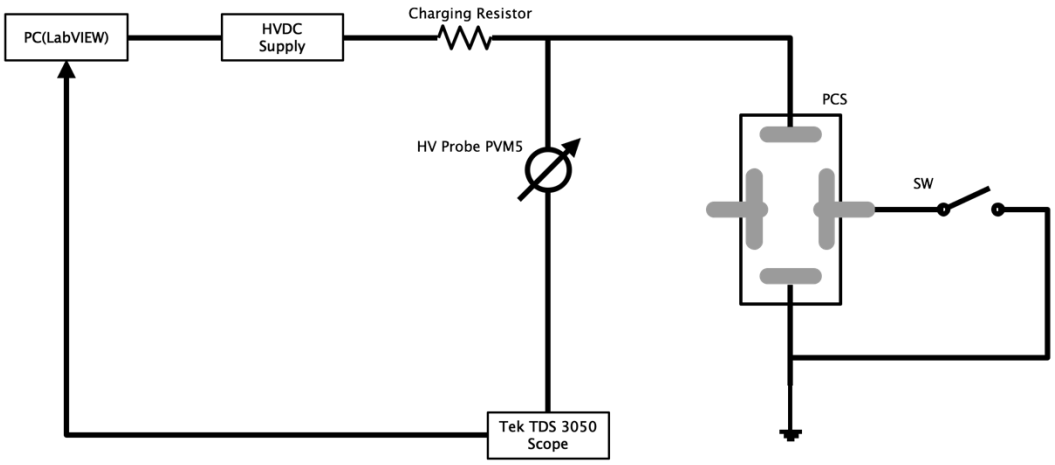

Figure. 3.5. Schematic of the experimental set-up used for static breakdown measurement.

A Glassman high voltage DC power supply (EH series, 0-60 kV) was used to stress the upper plane electrode through a 1MΩ charging resistor. The PC controlled the voltage output of the power supply via an RS232 interface using a National Instruments DAQ USB-6008 digital acquisition card. The control programme is compiled with the LabVIEW programme. The ramp rate of the applied voltage controlled by the PC was variable. The voltage across the switch was monitored using a North Star PVM-5 high voltage probe (60kV impulse/100 kV DC, 80 MHz bandwidth, 400 MΩ input resistance, and 12 pF input capacitance) was connected to the upper plane HV electrode. The switch which was series connected between PCS and ground controls the connection mode of the trigger electrode. When only the self-breakdown voltage in the upper gap was measured, the switch is closed and the central trigger electrode of the switch with the corona needles was connected to the ground. When the switch is open, the central trigger electrode was disconnected from the ground and remained at a free-floating potential during measurements of the static self-breakdown voltage in the complete PCS (upper and lower gaps). The high voltage signals were observed and recorded by a Tektronix TDS 3050 digitising oscilloscope (500 MHz bandwidth, 5 GS/s sampling rate).

Breakdown tests were conducted for all gases over the pressure range from 1 to 12bar (gauge) in 1bar increments. The upper plane electrode was stressed with both positive and negative DC voltage. The self-breakdown voltage was recorded for 30 breakdown events in each set of measurements. The mean self-breakdown voltage value and its standard deviation, representing the spread in the self-breakdown voltage, were obtained for each set of tests.

After each set of breakdown tests, the PCSs was evacuated and filled with a fresh portion of the gas under the test.

3.6 Experimental Set-up and Methodology for Pre-breakdown Corona Current Measurements

In order to study the corona discharge in the switching topology filled with air, N_2, CO_2 and a mixture of 90%/10% Ar/O_2, a designated experimental set-up was developed, shown in Figure 3.6.

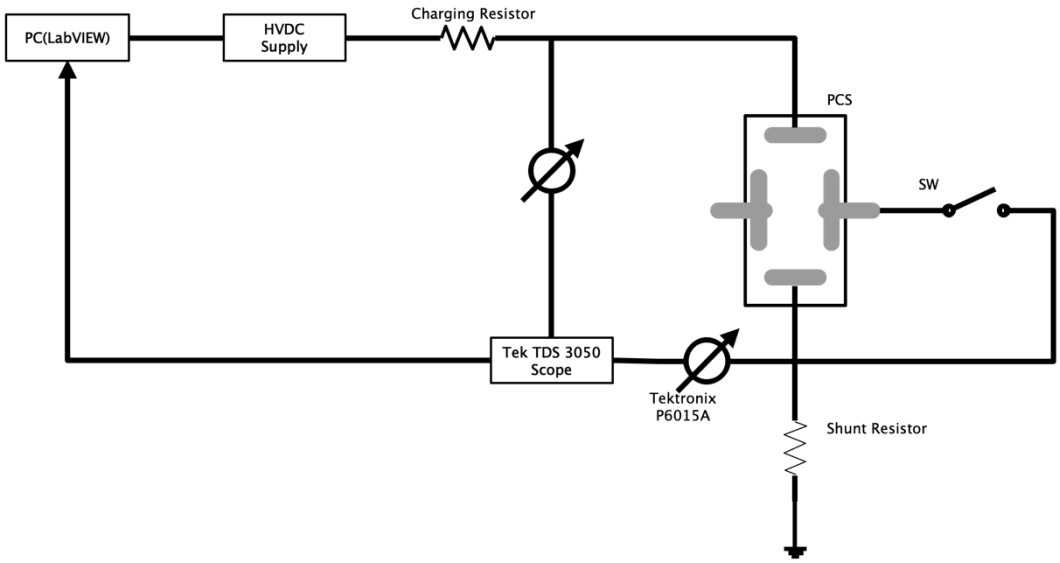

Figure. 3.6. Schematic of the experimental set-up used for corona discharge measurement.

In the set-up shown in Figure 3.6 switch SW is open and the PCS is grounded through a shielded low inductance 10kΩ shunt resistor. The corona current flowing through the PCS can be obtained by measuring the voltage drop across the shunt resistor and dividing this voltage by the value of the shunt resistor according to the Ohm's law. The voltage across the shunt resistor was measured by the HV Tektronix P6015A probe (1:1000 voltage division ratio, 75 MHz bandwidth), low voltage signal from the probe was recorded by the Tektronix TDS 3050 digital oscilloscope (500 MHz bandwidth, 5 GS/s sampling rate). The reason for choosing the HV Tektronix P6015A probe is to protect the test equipment when the switch break down. When measuring only the corona inception voltage in upper gap, switch SW was closed and the central triggering electrode of the switch with the corona needles was connected to the ground via the 10kΩ shunt resistor. When monitoring the corona inception voltage in the PCS, the central electrode was disconnected from the shunt resistor and left at a floating potential.

The upper plane electrode was stressed with both positive and negative polarity DC voltage. The applied voltage was controlled via a LabVIEW programme interfacing with a National Instruments DAQ (USB6008).

The test procedure involves a steady increase of the voltage until breakdown occurs. Analysis of the voltage and current waveforms at the moment of the initial rise of current and the corresponding voltage value gives the corona inception voltage.

Corona discharges were investigated in the PCS filled with all gases over the pressure range from 1 to 12bar (gauge) in 1bar increments. The corona inception voltage was recorded for 30 events in each set of measurements. The corona inception voltage and the corresponding standard deviation were calculated for each test set.

After each set of experiments, the test gas in the PCS was refreshed. Several minutes before proceeding to the next set of experiments were allowed in each series of tests.

3.7 Experimental Set-up and Methodology of Triggering with Fast Impulses

The previous experiments focused on studying the self-breakdown voltage and corona discharge initiation voltage in the PCS topology. However, in many pulsed power applications, the operational parameters of the switch are also essential. In order to investigate the triggered behaviour, including the time to breakdown and associated jitter of the switch filled with bottled air, N_2, CO_2 and 90%/10% Ar/O_2 mixture, a triggering impulse needs to be applied to the central electrode.

In order to generate the triggered HV impulses with defined pulse width and shape, an inverting Blumlein pulse generator was employed. The Blumlein pulse generator provides a ~30kV voltage impulse with a duration of ~280ns and a rising rate of ~1kV/ns, as shown in Figure 3.7.

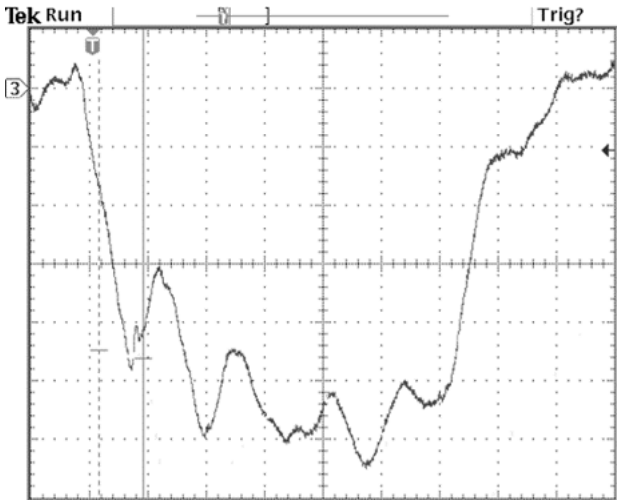

Figure. 3.7. Trigger impulse voltage waveform generated by the Blumlein pulse generator. Vertical scale: 5kV/division; horizontal scale: 40ns/division.

The set-up diagrammatically shown in Figure 3.8 was employed for the measurements of the triggered operational characteristics of the PCS. The upper plane electrode was stressed by the high voltage supplied by a Glassman HVDC power supply (0-60kV) via a 1MΩ charging resistor. The central electrode was connected to an inverting Blumlein pulse generator by a decoupling capacitor (2.2pF). The trigger impulse voltage waveforms were monitored using an HV probe, Tektronix P6015A (75MHz bandwidth, 100MΩ input resistance, and 3pF input capacitance, at higher frequencies, the input resistance reduces down to 1kΩ for 100MHz signal), connected to the central trigger plane of the switch. The voltage across the switch was monitored using a NorthStar PVM-5 high-voltage probe (1000:1 division ratio, 80MHz bandwidth); and a Tektronix TDS 3050 digitising oscilloscope (500MHz bandwidth, 5GS/s sampling rate).

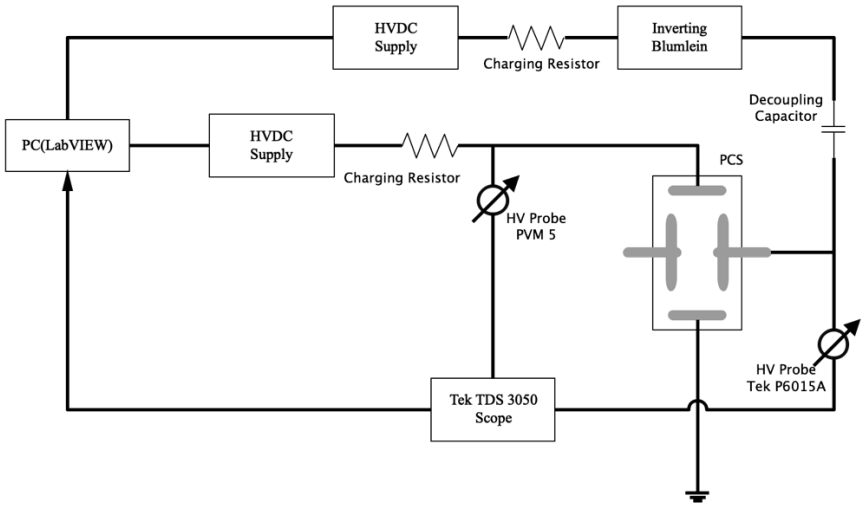

Figure. 3.8. Schematic of the experimental set-up used to investigate triggered operational characteristics.

The upper plane electrode was stressed with both positive and negative polarity DC voltage at two stress levels, 70% and 90% of the self-breakdown voltage, which was previously measured in section 3.5 with the same test gas at the same pressure. The applied voltage was controlled via a LabVIEW program interfacing with a National Instruments DAQ (USB6008).

The test gas within the PCS was refreshed before each change of the gas pressures tested from 1 to 12 bar (gauge) in 1 bar increments or when the DC stress applied voltage level was changed.

3.8 Conclusion

This chapter introduced the design of a novel plasma closing switch topology and discussed different experimental set-ups and methodologies for investigating the operational characteristics of the developed PCS. This two-stage triggered gas-filled PCS with corona electrodes can operate at high gas pressures (it has been tested up to 20bar). This chapter developed and discussed the diagnostic and measurement system with the data acquisition software. In order to facilitate the control of high-voltage power supplies and automatic measurement and acquisition of data, a set of

LabVIEW-based codes has been developed to control the HV power supply and collect data with the help of a National Instruments DAQ (USB6008).

The following chapters will investigate the breakdown behaviour of the developed switch stressed with HV voltage of both polarities and filled with four different gases, this selection of gases includes three electronegative gases ("Zero grade" air, CO_2, and 90%/10% Ar/O_2 mixture) and one electropositive gas, N_2. A comprehensive study of the effects of different DC voltage levels, gas pressures, and other conditions on the switch's breakdown characteristics has been conducted, and the obtained results will be presented and discussed in Chapter 4.

CHAPTER.4 SELF-BREAKDOWN CHARACTERISTICS OF A HIGH-PRESSURE PLASMA CLOSING SWITCH FILLED WITH DIFFERENT GASES

4.1 Introduction

Chapter 3 introduced the design of the two-stage triggered gas-filled PCS with multiple corona discharge needle electrodes and discussed the different experimental set-ups and methodologies for investigating PCSs operational characteristics.

The system developed and discussed in Chapter 3 was used aim to investigate the behaviour of the breakdown voltage in a developed topology for both positive and negative applied voltages. Chapter 4 presents the results of this study.

Chapter4 investigates the breakdown voltage when the PCS is stressed with both polarities when filled with four different gases: three electronegative gases ("Zero grade" air, CO_2, and 90%/10% Ar/O_2 mixture) and one electropositive gas, N_2. The breakdown characteristics were obtained for the pressure range from 1 bar to 12 bar (gauge). The results of this comprehensive investigation of the effects of different operating voltages, gas pressures, and other conditions on the switch's breakdown characteristics are presented and discussed in Chapter 4. The obtained results will help in developing compact, high-performance plasma closing switches and pulsed power systems in practical applications.

4.2 Experimental Methodology

The gases selected for this study are gases which are present in the atmosphere (gases with low global warming potential, GWP, as compared with SF_6) and which potentially can replace SF_6 in plasma closing switches.

Although SF_6 is one of the widely used insulating gases, plasma closing switches in the pulsed power generators may also be filled with dry air, nitrogen, or other gases with low GWP.

Another candidate to replace SF_6 in gas-filled PCSs is argon (argon/oxygen mixtures) which can provide faster switching times in the high-power pulse generator and support the development of multiple breakdown channels (multichannel effect), which will help to reduce the switch inductance.

Recently it was suggested that CO_2 (Phillip Widger et al. 2020) could be used as a replacement gas (instead of SF_6) in some practical gas insulating lines (GIL's). Also, the arc quenching characteristics demonstrated by CO_2 allow for consideration of this gas as a potential replacement for SF_6 in medium voltage circuit breakers. (Uchii et al. 2007; W.-Y. Lee et al. 2020).

Thus, four gases were selected for the present study: "Zero grade" air (BOC bottled), CO_2 (BOC Ltd), and 90%/10% Ar/O_2 mixture (BOC Ltd) and N_2(99.9% N_2, BOC Ltd).

The pressure range, from 1 bar to 12 bar (gauge), used in this study is limited by the maximum pressure the test cell can withstand and the maximum output voltage of the power supply. (The maximum pressure may be different for different tested gases).

A ramped voltage with a rising rate of 600 V/s was used to stress the switch electrodes and measure the self-breakdown breakdown voltage. The self-breakdown voltage was recorded for 30 breakdown events in each set of measurements (without a change of gas in the switch). In order to avoid the residual space charge and the products from the discharge affecting the next shot, the interval between the two shots is set to 1 minute. After each measurement set (after 30 breakdown events), the gas in the PCS s was removed: the PCS was evacuated and filled with a fresh gas portion. The mean breakdown voltage and its standard deviation were calculated for each set of measurements (30 breakdown events).

4.3 Self-Breakdown Voltage: Results and Analysis

This section presents the experimentally obtained results for all four tested gases: the breakdown behaviour of the switch filled with these gases was investigated, and the mean value of breakdown voltage was obtained. It was shown that the breakdown parameters obtained in this study depend on the gas pressure, gas type, the polarity of the applied voltage and electrode topology. The breakdown performance of the switch filled with the tested gases is presented and discussed in the following sections.

4.3.1 Self-Breakdown Voltage of Air

This section presents the breakdown voltage of the single and double gaps of the switch filled with air. The upper plane electrode was stressed with positive and negative polarity ramped DC voltage, respectively. In each test, the self-breakdown voltage was recorded for 30 breakdown events without refreshing the gas in the switch. The mean breakdown voltage value and its standard deviation, representing the spread in the self-breakdown voltage, were calculated for each test set. Figure 4.1 shows the breakdown voltage as a function of the gas pressure for the air-filled switch.

The experimentally obtained breakdown data have been fitted with linear empirical functions using the best fit procedure in OriginPro 2017 graphing software. The breakdown voltages, $V_{br}(p)$ (kV), as a function of pressure, p (bar), are presented in Figure 4.1. It can be seen that in the case of both switch topologies: single gap and double gap configurations of the switch, the linear dependence of the breakdown voltage on the pressure for both positive and negative energisation is observed.

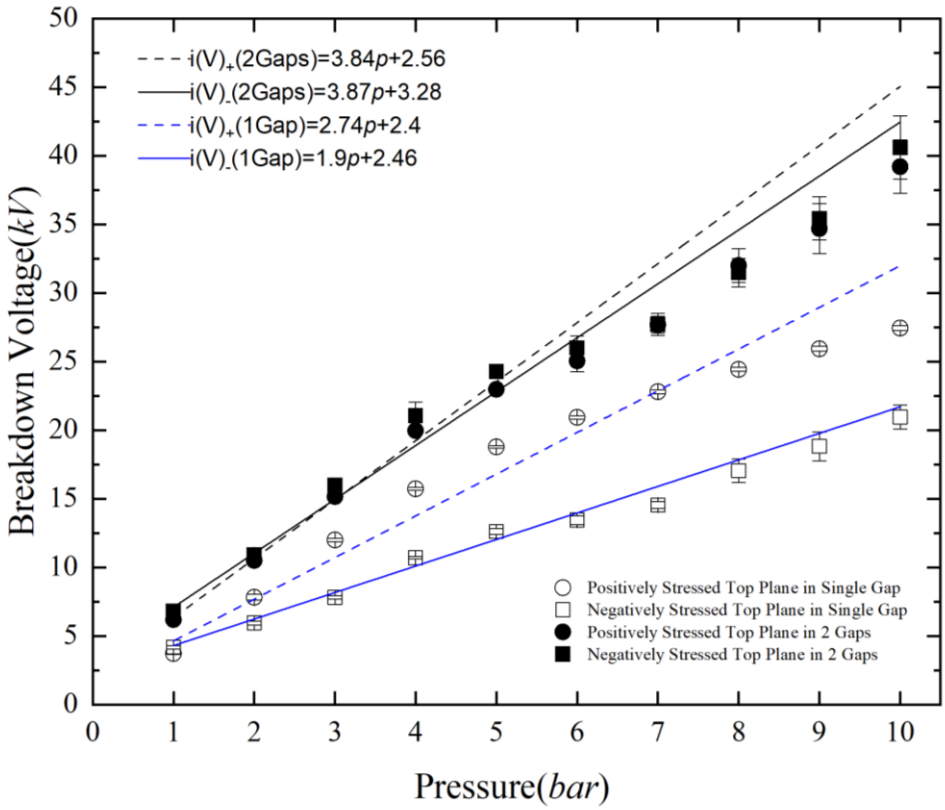

Figure 4.1 Self-breakdown voltage as a function of gas pressure for an air-filled switch was calculated for 30 breakdown measurements for each gas pressure; Solid symbols: discharge within the single gap, and open symbols: discharge within both gaps.

As can be seen from the results in Figure 4.1, the self-breakdown voltages increase almost linearly as the pressure increases. If breakdowns occur only in the upper gap, the breakdown voltage for negative energisation is higher than the positive breakdown voltage for 1 bar. When the gas pressure exceeds 2 bar, the positive breakdown voltage becomes higher than the negative breakdown voltage. It was found that there is a critical pressure at which positive and negative breakdown voltages have the same absolute value. This pressure is between 1 bar and 2 bar. The maximum difference between positive and negative breakdown voltages is found at 7 bar. At this pressure, the positive breakdown voltage is ~40% higher than the negative breakdown voltage. Compared with negative energisation, the rate at which the breakdown voltage increases with pressure is faster than positive energisation.

In the case of a breakdown occurring in both gaps, the breakdown voltages for positive and negative energisation are similar, i.e., there is no considerable difference between positive and negative breakdown voltages. This is due to the symmetry in the geometry of the central floating electrode. The corona (gramophone needles) electrodes are evenly distributed on each side of the central floating electrode and placed in the middle of the switch's main electrodes. When the HV electrode is positively stressed, the needle's potential on the centre electrode of the upper gap's side will be lower than that of the HV electrode. Therefore, the space charge generated by the corona discharge on the streamer head weakens the electric field strength and inhibits its propagation, which will lead to an increase in the breakdown strength in this gap. In the lower gap, the needle's potential on the centre electrode of the lower gap's side will be higher than the ground electrode. The space charge generated by the corona discharge on the streamer head enhances the electric field strength and develops its propagation. Therefore, the breakdown strength of this gap will be lower than that of the upper gap. When the HV electrode is negatively stressed, the potential of the needles on the upper side of the centre electrode (which forms the upper gap in the switch) will be higher than the potential of the HV electrode. In the lower gap, the potential of the needles located on the lower side of the centre electrode (which forms the lower gap in the switch) will be lower than the potential of the ground electrode. Therefore, the breakdown strength of the lower gap will be higher than that of the upper gap. Due to the symmetry of electrodes, there will always be one electrode with a breakdown voltage lower than the other, independent of the polarity of the applied voltage. This breakdown voltage will define the breakdown behaviour of the switch. Therefore, the breakdown voltages for positive and negative energisation are similar when a breakdown occurs in both gaps in this switch.

As shown in Figure 4.2 (a), the standard deviation in the breakdown voltage is relatively small, in the range of (0.05 -0.22) kV (or 0.9% -1%) and does not increase with an increase in the gas pressure when the HV electrode is positively stressed. The standard deviation in the self-breakdown voltage fluctuates in the tested pressure range. When the HV electrode is negatively stressed, the standard deviation for gas pressures lower than 7 bar is relatively stable. There is a significant increase in the standard

deviation, from 0.28kV to 0.87kV (1.8% to 4.9%), as the gas pressure increases from 7 bar to 8 bar and the breakdown voltage values show a larger spread for the gas pressures over 8 bar. It can be found that the standard deviation in the breakdown voltage in the case of positive stress is smaller as compared with negative energisation, as all breakdowns occur in the upper gap of the switch filled with air.

In the case of breakdown events in both gaps (two-gap switch configuration), it was found that the standard deviation in the breakdown voltage linearly increases with an increase in the gas pressure across the tested pressure range from 0.08kV to 2.31kV (1.3% to 5.6%), figure 4.2 (b)

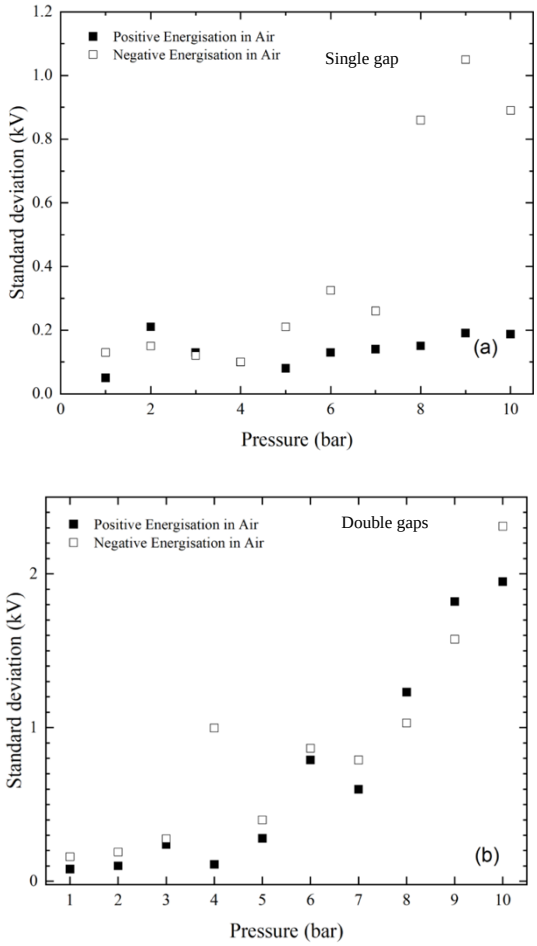

Figure 4.2 Standard deviation in the self-breakdown voltage as a function of gas pressure. Solid symbols, positive energisation and open symbols, negative energisation. Standard deviation was calculated for 30 breakdown measurements for each gas pressure. (a) within a single gap. (b) within double gaps.

4.3.2 Self-Breakdown Voltage of CO_2-filled switch

This section presents the obtained breakdown voltages (single gap and double gap configurations) when the switch is filled with CO_2. The experimental procedure was the same as described in section 4.3.1. The obtained results, i.e., the self-breakdown voltage as a function of the gas pressures, are presented in Figure 4.3.

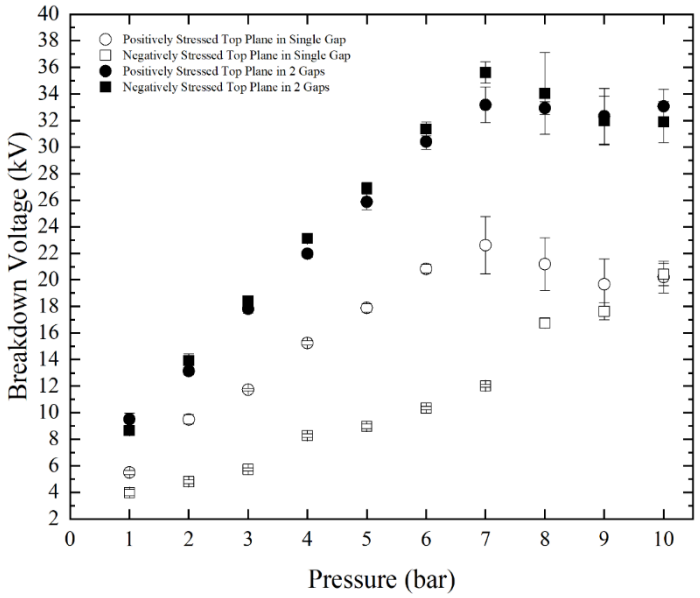

Figure 4.3 Self-breakdown voltage as a function of gas pressure for the CO_2-filled switch, calculated for 30 breakdown measurements for each gas pressure. Solid symbols: discharge within the single gap, and open symbols: discharge within both gaps.

As can be seen from Figure 4.3, when breakdowns occur in both gaps, the breakdown voltages for positive and negative energisation are similar across the tested pressure range. There is no noticeable difference between positive and negative breakdown voltages. The self-breakdown voltage demonstrates a non-linear behaviour with the gas pressure above 7 bar.

The CO_2-filled switch demonstrates corona stabilisation behaviour. The space charge generated by corona discharges weakens the electric field near the point electrode(s), thus preventing the formation of streamers at these point electrode(s). The self-

breakdown voltage is higher than the corona ignition voltage within this specific pressure range. This phenomenon depends on several parameters, including the gap geometry, gas composition and gas pressure, which will be discussed in the following Chapter. Due to the symmetry of electrodes, the breakdown voltages for positive and negative energisation are similar as breakdown events occur in both upper and lower gaps in this developed switch topology.

When a breakdown occurs only in the upper gap of the CO_2-filled switch, in the case of positive energisation, the self-breakdown voltage exhibits a non-linear behaviour. It starts to reduce at pressures above 7 bar. However, the self-breakdown voltage starts to rise again when gas pressure increases above 9 bar. On the contrary, in the case of negative energisation, the self-breakdown voltage increases almost linearly with the gas pressure. It becomes similar to the positive breakdown voltage at pressures above 10 bar.

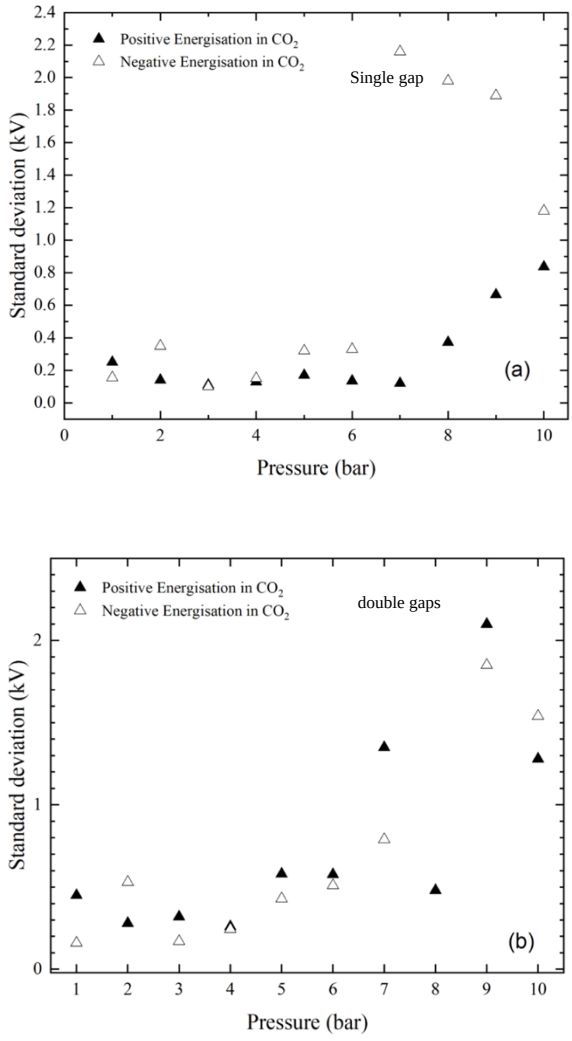

Figure 4.4 Standard deviation in the self-breakdown voltage as a function of gas pressure for the CO_2-filled switch. Solid symbols, positive energisation and open symbols, negative energisation. Standard deviation was calculated for 30 breakdown measurements for each gas pressure. (a) within a single gap. (b) within double gaps.

As shown in Figure 4.4 (a), when the HV electrode is negatively stressed, the standard deviation is in the range of 0.12kV – 0.83kV (1.1% -3.9%). The standard deviation of the self-breakdown voltage fluctuates for gas pressure up to 7 bar and starts rising for pressures above 8 bar. When the HV electrode is positively stressed, the breakdown voltage standard deviation fluctuation is relatively stable as the gas pressure below 6 bar is from 0.1 kV to 0.32 kV (0.9% to 2.6%). There is a significant increase in the standard deviation from 0.32kV to 2.16kV (2.6% to 9.5%) as the gas pressure increases from 6 bar to 7 bar. It can be found that the standard deviation of the

breakdown voltage in the case of negative stress is smaller as compared with positive energisation as breakdowns occur in the upper gap filled with CO_2.

In the case of breakdown events in both gaps, shown in Figure 4.4 (b), it was found that the standard deviation in the breakdown voltage is similar for both positive and negative energisation. It should be noted that there is a significant increase in the standard deviation at 8 bar for positive energisation. It may be caused by the change of self-breakdown voltage characteristics under this pressure. The breakdown voltage reaches the maximum value at 7 bar and then drops at 8 bar. The standard deviation notably rises at 7 bar.

4.3.3 Self-Breakdown Voltage of N_2 -filled switch

This section presents the obtained breakdown voltages (single gap and double gap configurations) when the switch is filled with N_2. The obtained results, i.e., the self-breakdown voltage as a function of the gas pressures, are presented in Figure 4.5.

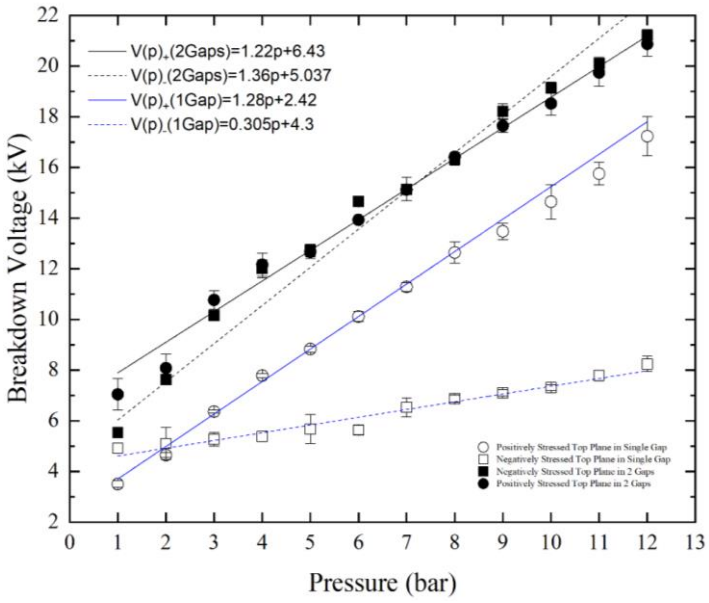

Figure 4.5 Self-breakdown voltage as a function of gas pressure for the N_2-filled switch, which was calculated for 30 breakdown measurements for each gas pressure. Solid symbols: breakdown within the single gap, and open symbols: breakdown within both gaps.

As shown in Figure 4.5, the self-breakdown voltage increases linearly as the pressure increases for both configurations: single and double gaps. When a breakdown occurs only in the upper gap, the breakdown voltage for negative energisation linearly rises from 5 kV to 8.2 kV as the gas pressure increases. In the case of positive energisation, the self-breakdown voltages increase linearly from 3.5 kV to 17.2kV with an increase in gas pressure. The negative breakdown voltage is higher than the positive breakdown voltage for the gas pressure up to 2 bar. When the gas pressure increases above 3 bar, the upper gap's breakdown voltage is higher for positive energisation than that for negative energisation. There is a critical pressure at which breakdown voltages are similar for both energisations. This critical pressure is found to be in the range from 2 bar to 3 bar. The critical pressure is mainly determined by complex processes in the ionization and transport regions in the electrode gap, including formation of the sheath and space charge barrier (Hogg et al. 2015). The maximum difference is observed at 12 bar. The positive breakdown voltage is ~52% higher than the negative breakdown voltage. The rate at which the breakdown voltage increases with pressure is faster for positive energisation than for negative energisation.

When a breakdown occurs in both the upper and lower gaps, the breakdown voltages for positive and negative energisation are similar across the tested pressure range. There is no statistically significant difference between positive and negative breakdown voltages. The self-breakdown voltage also exhibits an increasing linear trend with increased gas pressure.

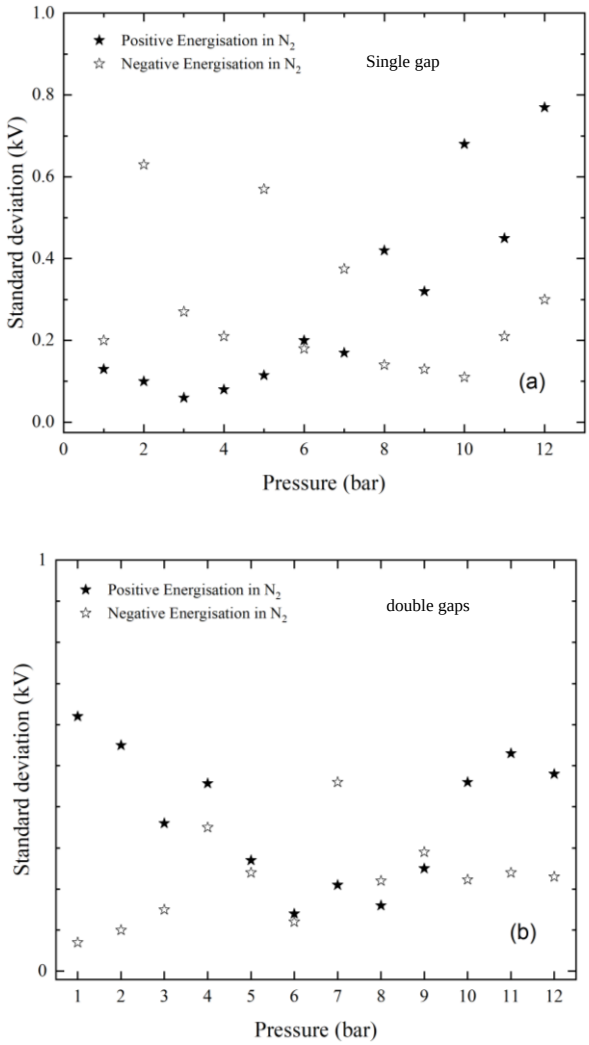

Figure 4.6 Standard deviation in the self-breakdown voltage as a function of gas pressure for an N_2-filled switch. Solid symbols, positive energisation and open symbols, negative energisation. Standard deviation was calculated for 30 breakdown measurements for each gas pressure. (a) within a single gap. (b) within double gaps.

Figure 4.6 (a) shows no distinct trend for the standard deviation in the breakdown voltages for both negative and positive energisations. When the HV electrode is negatively stressed, the standard deviation ranges from 0.13 kV - 0.63 kV (1.7% - 12.1%). When the HV electrode is positively stressed, the breakdown voltage standard deviation fluctuation is relatively stable for the gas pressure below 7 bar: 0.07 kV to 0.21 kV (1.1% to 2.1%). The standard deviation started to increase from 0.33 kV to 0.78 kV as the gas pressure was increased above 8 bar.

In the case of breakdown events in both gaps, it was found that for both positive and negative energisation, the standard deviation in the breakdown voltage does not demonstrate any apparent trends with the gas pressure, Figure 4.6 (b). When the HV electrode is negatively stressed, the standard deviation is in the range from 0.07 kV to 0.46 kV (1.4% - 3%). When the HV electrode is positively stressed, the standard deviation is within the range of 0.14 kV-0.62 kV (1.8% - 8.7%). Therefore, the developed switch could provide the most stable operational performance when filled with N_2.

4.3.4 Self-Breakdown Voltage of the Switch Filled with a Mixture of 90%/10% Ar/O_2

This section presents the obtained breakdown voltages (single gap and double gap configurations) when the switch is filled with a mixture of 90%/10% Ar/O_2. Figure 4.7 shows the self-breakdown voltage as a function of the gas pressure for the developed switch topology filled with this 90%/10% Ar/O_2 mixture.

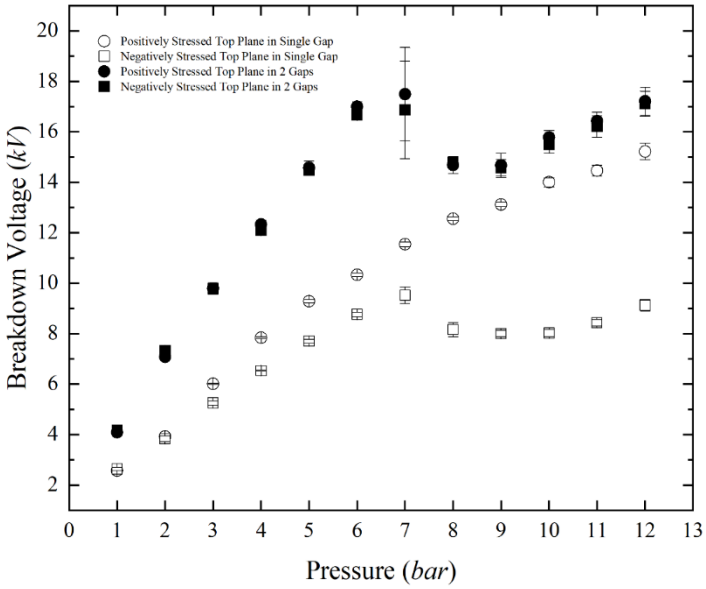

Figure 4.7 Self-breakdown voltage as a function of gas pressure for the developed switch topology when filled with a 90%/10% Ar/O_2 mixture, calculated for 30 breakdown measurements for each gas pressure. Solid symbols: discharge within the single gap, and open symbols: discharge within both gaps.

Figure 4.7 shows that the positive and negative energisation breakdown voltages are similar across the tested pressure range when a breakdown occurs in both the upper and lower gaps. Negative breakdown voltages are identical to the breakdown voltages in the positive energisation case due to the electrodes' symmetrical geometry. The self-breakdown voltage demonstrates a non-linear behaviour with the gas pressure above 7 bar. For this developed switch topology filled with a 90%/10% Ar/O_2 mixture, the self-breakdown voltage reaches the maximum value at 7 bar and then decreases at 8 bar. When the gas pressure is 9 bar, the breakdown voltage reaches its lowest value, which rises gradually as the gas pressure increases.

When a breakdown occurs only in the single (upper) gap of the switch (when the central ring electrode of the switch is grounded), the self-breakdown voltage of the switch filled with the 90%/10% Ar/O_2 mixture exhibits an increasing linear trend across the tested pressure in positive energisation. In the case of negative energisation, the self-breakdown voltage for a 90%/10% Ar/O_2 mixture linearly rises to the highest value at 7 bar. The self-breakdown voltage starts to decrease at 8 bar and reaches its lowest value at 9 bar, and then it continues to rise gradually again as the gas pressure increases. The negative breakdown voltage is higher than that for positive energisation for 1 bar. When the gas pressure increases and rises above 2 bar, the single upper gap's breakdown voltage is higher for positive energisation than that for negative energisation. There is a critical pressure at which breakdown voltages are the same for positive and negative energisations. This pressure is found to be in the range between 1 bar and 2 bar.

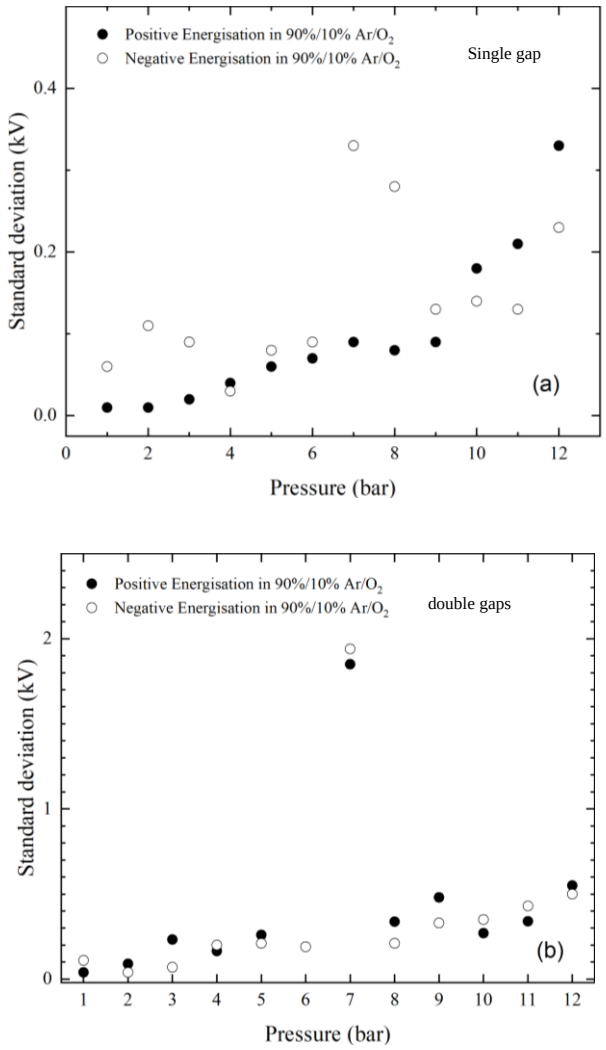

Figure 4.8 Standard deviation in the self-breakdown voltage as a function of gas pressure for the developed switch topology when filled with a 90%/10% Ar/O_2 mixture. Solid symbols, positive energisation and open symbols, negative energisation. Standard deviation was calculated for 30 breakdown measurements for each gas pressure. (a) within a single gap. (b) within double gaps.

As shown in Figure 4.8 (a), there is no distinct trend for the standard deviation in the breakdown voltage for negative energisation. The standard deviation was found to be in the range from 0.03 kV - 0.33 kV (0.4% -3.4%). When the HV electrode is positively stressed, it was found that the standard deviation linearly increases with increasing gas pressure across the tested pressure range from 0.01kV to 0.33kV (0.3% to 2.1%).

In the case of breakdown events in both gaps, shown in Figure 4.8 (b), it was found that in the case of positive energisation, the standard deviation in the breakdown voltage is not significantly different from the standard deviation in the case of negative energisation. The standard deviation demonstrates a slight increase with an increase in gas pressure. It should be noted that there is a significant increase in the standard deviation at 7 bar due to the change of self-breakdown voltage characteristics under this pressure.

4.3.5 Comparison of Self-Breakdown Voltages for all gases

This section compares the breakdown voltage capabilities of all tested gases. The obtained average self-breakdown voltages for all tested gases are shown in Figure 4.9 as functions of the gas pressure in the developed switch for both positive and negative energisation.

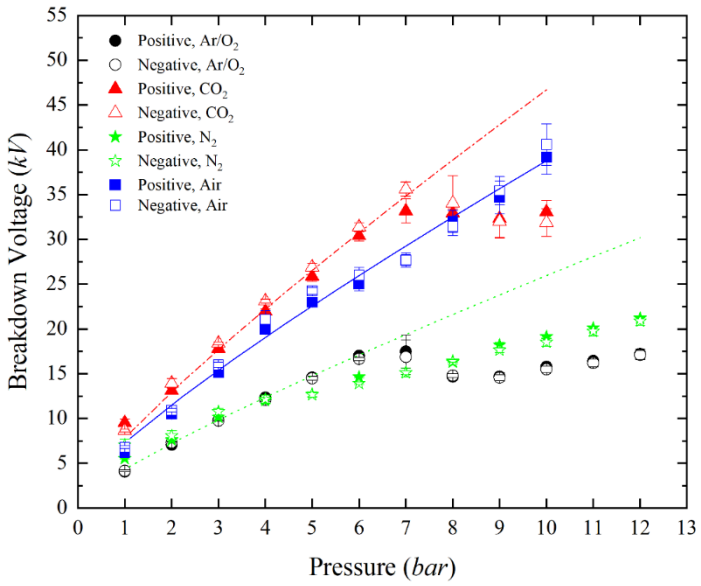

Figure 4.9 Self-breakdown voltage as a function of gas pressure for the developed switch topology filled with all tested gases. Each symbol represents an average value of 30 measurements: blue squares, air; green stars, N_2; red triangles, CO_2; and black circles, 90%/10% Ar/O_2. Solid symbols, positive energisation and open symbols, negative energisation. Self-breakdown voltages are obtained by equation (4.1): solid blue line, air; dash-dotted red line, CO_2; and dotted green line, N_2.

It can be seen from Figure 4.9 that the obtained self-breakdown voltage shows that all tested gases can be divided into two groups: N_2 and Ar/O_2 mixture have lower self-breakdown voltages in the developed switching topology compared with air and CO_2. For higher pressures, this difference is more remarkable. The self-breakdown voltages for CO_2 were higher than that for all other tested gases within the pressure range from 1 bar to 7 bar. Nevertheless, the self-breakdown voltage for CO_2 exhibits a non-linear increasing trend and starts to decline for pressures above 7 bar. In contrast, the breakdown voltage of air increases linearly with the gas pressure for all tested pressures range and this increase is more pronounced compared with the self-breakdown voltage of CO_2 for pressures above 7 bar. The breakdown voltage of the switch filled with the Ar/O_2 mixture also demonstrates a non-linear behaviour with the gas pressure above 7 bar.

Furthermore, Figure 4.9 shows no statistically significant difference between positive and negative self- breakdown voltages for all tested gases. The reason for this has been discussed in section 4.3.1. Due to the electrodes' symmetry, there will always be one electrode whose breakdown voltage is lower than the other electrode and independent of polarity, which will dominate the system's breakdown behaviour. Therefore, breakdown voltages for positive and negative energisation are similar when a breakdown occurs in both gaps in this 2-gap topology switch.

Generally, when a breakdown occurs in a gas-filled plasma closing switch in a uniform electric field, the breakdown voltage is a function of the product of the gas pressure and inter-electrode gap, i.e., the breakdown voltage in the uniform electric field topology can be presented as a function of the *pd* product. It can be obtained by equation (2.30). In this case, the calculated breakdown voltage agrees with the experimental results. However, Paschen's law cannot be used to describe the breakdown voltage in the strongly non-uniform electric field. Therefore, to describe the experimental breakdown voltage $V_{br}(p)$ of all tested gases in this non-uniform electric field case, the following equation is introduced, which is based on the Townsend breakdown theory:

$$V_{br} = \frac{\beta Bpd}{\ln Apd - k} \tag{4.6}$$

where p is the gas pressure, d is the inter-electrode gap distance, the constants A ($\times 10^2/(mm \cdot bar)$) and B ($(kV/(mm \cdot bar))$) describe the primary ionisation coefficient, k is a gain coefficient (in Townsend theory, k is a function of the secondary ionisation coefficient). The coefficient β is introduced in equation (4.6) to account for the non-uniformity of the electric field, which is described in (2.1). It is the ratio between the mean electric field strength in the uniform field in a parallel-plane topology and the maximum electric field strength at the point electrode in a point-plane topology. The developed switch topology design provides the field non-uniformity factor $\beta \sim 1/10$, obtained in QuickField electrostatic software by modelling the point-plane topology.

The analytical fitting to the experimentally obtained breakdown voltage data was conducted using the best fit procedure in the Origin Pro software package. The analytical fitting lines are shown in Figure 4.9. The parameter k was a fitting parameter, and the constants A and B were given (Raizer, Kisin, and Allen 2011). The constants A, B and the parameter k with their standard errors are shown in Table 4.1. As the 90%/10% Ar/O_2 mixture has not previously been investigated for its suitability as an insulation gas within switching devices, there is no classic A and B for this specific mixture. Therefore, the breakdown voltage for the 90%/10% Ar/O_2 mixture did not fit (4.6).

Table 4.1 Coefficients A, B, and fitting parameter k used in analytical fitting (4.6) for each tested gas

Gas	A $(\times 10^2/(mm \cdot bar))$	B $((kV/(mm \cdot bar))$	k
Air	**11.0**	**26.9**	**7.0±0.1**
N_2	**6.7**	**20.9**	**4.5±0.1**
CO_2	**15.2**	**35.4**	**6.5±0.1**

The standard deviation in the self-breakdown voltage, σ_{Vbr}, for all tested gases (air, CO_2, N_2, and the 90%/10% Ar/O_2 mixture) is shown in Figure 4.10(a)-(d) as a function of the gas pressure in the developed switch topology. The standard deviation in the self-breakdown voltage indicated the stability of the switch operational performance. It was found that the standard deviation in the self-breakdown voltages in the developed switch filled with air and CO_2 is higher than the standard deviation in the self-breakdown voltages in the developed switch filled within N_2 and the Ar/O_2 mixture. The standard deviation increases with an increase in the gas pressure across the tested pressure range for air and CO_2, as shown in Figure 4.10 (a) and (b). Figure 4.10 (d) shows that the standard deviation for the 90%/10% Ar/O_2 mixture demonstrates a slight increase with an increase in the gas pressure. It should be noted that there is a significant increase in the standard deviation at 7 bar and above.

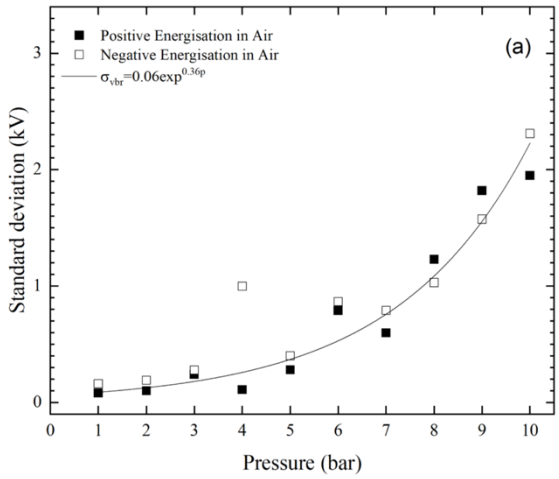

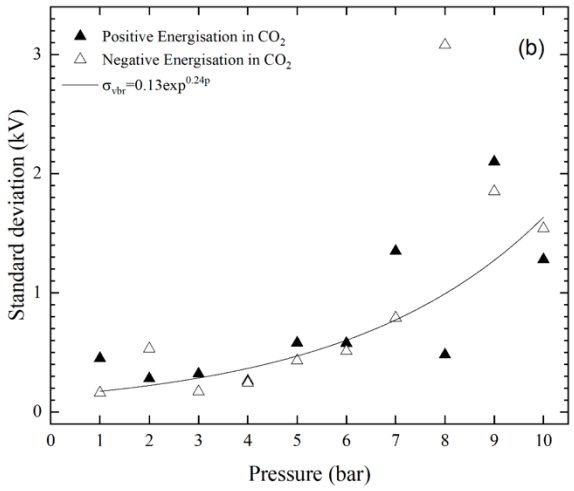

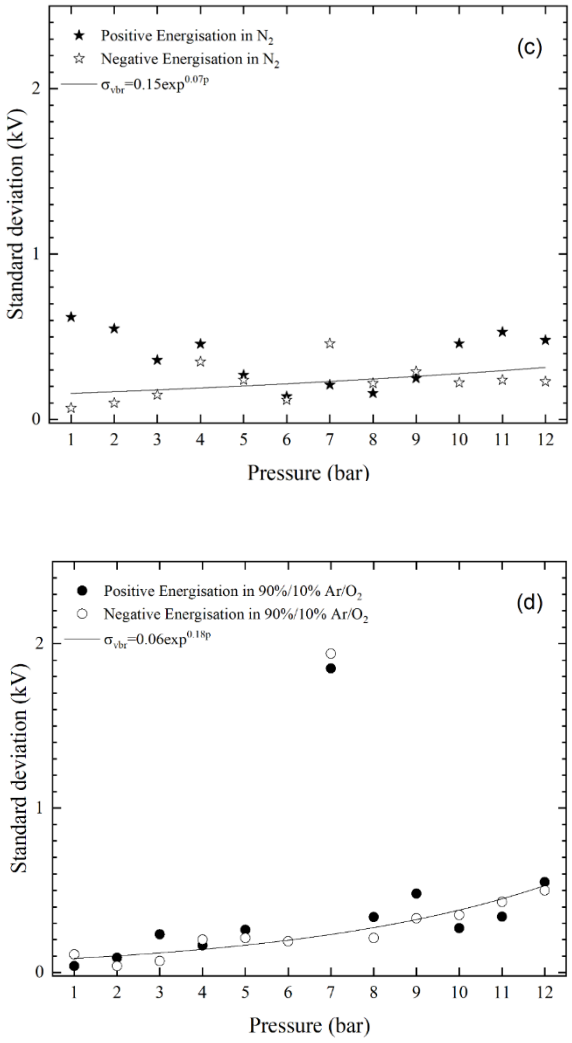

Figure 4.10 Standard deviation of self-breakdown voltage as a function of gas pressure for the developed switch topology when filled with all tested gases. Each symbol represents an average value of 30 measurements: Solid symbols: positive energisation, and open symbols: negative energisation. (a) Synthetic air. (b) CO_2. (c) N_2. (d) 90%/10% Ar/O_2.

In this work, an exponential function (4.7) has been introduced to fit the standard deviation in Figure 4.10 by using the Origin Pro software package. This exponential equation describes the standard deviation for all gases as a function of experimental data.

$$\sigma_{Vbr} = Ce^{Dp} \tag{4.7}$$

where C (kV) and D (bar^{-1}) are fitting coefficients extracted from the experimental data; these coefficients and the standard errors are given in Table 4.2.

Table 4.2 Coefficients C and D used in fitting (4.2) for each tested gas

Gas	C (***kV***)	D(Bar^{-1})
Air	**0.06±0.01**	**0.36±0.02**
N_2	**0.15±0.01**	**0.07±0.05**
CO_2	**0.13±0.01**	**0.24±0.04**
Ar/O_2	**0.06±0.01**	**0.18±0.03**

It was found in Table 4.2 that coefficient D has a close relationship with the rising rate of the trend curve. The greater the coefficient D is, the faster the standard deviation rises with increased gas pressure in the switch.

4.4 Conclusion

This Chapter presents the results of the investigation of the self-breakdown performance of the switch filled with different gases (air, CO_2, N_2, and the 90%/10% Ar/O_2 mixture). The breakdown voltage and its standard deviation were obtained as functions of the gas pressure in the switch. These values were obtained using the upper gap and both gaps within the developed switch topology.

In the case of a breakdown occurring in the upper gap, it was found that there is a point of intersection between positive and negative breakdown voltages at specific, critical gas pressure. For the gas pressures lower than this critical pressure, all breakdown voltages for negative energisation were found to be higher than in the case of positive energisation. For pressures above this critical pressure, the breakdown voltages for positive energisation are higher than those for negative energisation. The critical gas pressure at this convergence point is defined. It was found that the gas type and gas pressure directly impacted the critical gas pressure. For positive and negative energisation, the self-breakdown voltages increase linearly as the pressure of air and N_2 increases.

When breakdown events occur in both upper and lower switch gaps, it was found that there is no significant difference between positive and negative breakdown voltages for all tested gases and the breakdown voltage increases as the gas pressure increase for all tested gas pressures.

The self-breakdown voltage exhibits a linear trend as the gas pressure increases in the case of air and N_2. This trend is highly predictable when the switch is filled with these gases. However, for CO_2 and the 90%/10% Ar/O_2 mixture, the breakdown voltage demonstrates a significant corona stabilisation region within the tested gas pressure range, which is typically observed in electronegative gases. The space charge generated by corona discharges weakens the electric field near the point electrode(s), preventing streamer formation at the point electrode(s).

The standard deviation in the self-breakdown voltage for all tested gases is a critical parameter that describes the switch operation's stability. It was found that the standard deviation increases with an increase in gas pressure, from 0.08kV to 2.31kV (1.3% to 5.6%) for air; from 2.3% to 5% for CO_2; from 1.4%-8.7% for N_2; and For the Ar/O_2 mixture, this range is from ∼1% to ∼3% (except the standard deviation obtained at 7 bar). It can be seen from the comparison that N_2 and Ar/O_2-filled switch has the relatively lowest standard deviation in the self-breakdown voltage. Therefore, N_2 and the Ar/O_2 gas mixture could provide the most stable breakdown characteristics in the developed switch topology.

Through a large number of experimental observations, when the switch was filled with a fresh portion of the gas, the first 100s of the experimental data points showed that the stability of the switch is not sufficiently good. Significant variation was observed in the first 100s of breakdown voltage values.

Potential cause of this undesirable phenomenon is the presence of impurities and burrs on the electrode surface which may appear after each discharge.

However, due to electrode erosion, after several 100s of breakdown events, the electrode surface changes significantly. Burrs on the electrode surface are greatly reduced, and it is expected that impurities could vaporize at high temperatures. Moreover, the microstructure of the electrode also changes with increasing number of breakdowns, and the surface becomes uneven, forming multiple points of the electric field enhancement. This may improve the efficiency of initial electrons generation and reduce statistical variation in breakdown voltage which improves the operational stability of the switch.

This Chapter presented the results obtained in low current and low repetition-rate modes. The breakdown mechanism under high repetition-rate operation may be significantly different when compared with the low repetition-rate operation, including elevated electrode erosion. These aspects require further investigation in future.

The next Chapter of this thesis will investigate the pre-breakdown discharge characteristics in the developed switch filled with all tested gases, including the corona stabilisation phenomenon.

CHAPTER.5 CHARACTERISATION OF PRE-BREAKDOWN PROCESSES IN A PCS Filled WITH DIFFERENT GASES

5.1 Introduction

The corona discharge can be considered as a partial, non-complete discharge in the inter-electrode gas-filled gap. This discharge is formed by the ionisation of fluid in the region of a high electric field, in the vicinity of electrode(s) with a small radius of curvature, for example, needle, blade or thin wire electrode(s).

Corona discharge is a local self-sustained discharge initiated when the applied electric field at the conductor's surface exceeds its critical value. The ionisation starts in the vicinity of this sharp energised electrode. In this region, called the ionisation zone, ionised gas molecules and electrons form non-thermal plasma. This ionisation zone appears as a weak to bright glow (Loeb and Kip 1939).

Two zones are distinguished in the corona discharge: the ionisation zone described above and the transport zone in which the field is not strong enough to cause ionisation acts. Due to the rapid electric field reduction with the distance away from the sharp HV electrode, no ionisation acts occur in this transport zone.

The corona current is formed by the movement of ions in the transport zone. The polarity of the electrical potential defines the polarity of corona discharge onto the corona electrode. Suppose the corona electrode is stressed with positive potential. In that case, this corona discharge is called a positive corona discharge, and vice versa – if the corona electrode is stressed with negative potential, this discharge is called a negative corona discharge. In the case of the positive corona, positive ions move through the transport zone toward the opposite electrode (anode). In contrast, negative ions and electrons form the corona current in the case of the negative corona discharge.

The geometric configuration of the electrode plays a critical role in the formation of the corona discharge. The inhomogeneity of the electric field limits the primary

ionisation process to the vicinity of the sharp HV electrode due to the high local electric field.

As mentioned above, a positive corona discharge will be developed if a positive voltage is applied to the sharp HV electrode. As positive voltage increases, the discharge will take various forms. At first, random and non-regular current pulses appear. This regime is called the burst pulse corona. The short and faint streamers called the streamer corona would be developed away from the electrode. When the applied voltage is increased further, the discharge will be transformed into a glow corona discharge. Finally, the discharge transforms into a spark discharge (Chang, Lawless, and Yamamoto 1991). Negative corona discharge is different from positive corona discharge. A negative corona appears as a non-uniform corona glow around the sharp HV conductor, and its appearance and structure depend on the characteristics and irregularities of the sharp energised conductor. When the voltage gradually increases, periodic and stable current pulses with fast rise times and short duration appear. These current impulses are called Trichel pulses (Trichel 1939). When the magnitude of the applied voltage increases, the frequency of the Trichel pulses increases and their magnitude gradually decreases, and the discharge is transformed into a pulseless, glow corona (Lama and Gallo 1974; Morrow 1985). Finally, a spark discharge is formed as the applied voltage increases.

Corona discharges can be classified as steady state and pulse corona discharges. Corona discharge generated by energisation of the HV electrodes with high DC voltage is called DC corona discharge. Although the DC corona technology is mature, and DC corona systems are typically reliable and low in price, DC corona discharges provide relatively low discharge power density (with an applied voltage of 40kV releases a power of about 0.2W/cm of the discharge). The mean electron energy in such discharges is also low, which leads to its low efficiency in different plasma-chemical applications (i.e. plasma cleansing of gas and liquid streams) (Fridman, Chirokov, and Gutsol 2005). Therefore, DC corona discharge is not ideal for some practical applications, such as material surface treatment, chemical synthesis, etc. The pulse corona discharge can be developed when a sharp electrode is stressed with short

ns or μs high voltage impulses. In such a short time interval, the electrons are accelerated and gain sufficient energy to be classified as high-energy electrons. However, ions remain largely stationary due to their large mass and are not accelerated during the HV pulse. Therefore, most of the energy delivered into the discharge is spent to generate high-energy electrons with the mean energy of ~10eV (Gallimberti, Hepworth, and Klewe 1974; Spyrou and Manassis 1989; Veldhuizen and Rutgers 2002; Raizer 2017).

In the corona discharge, the non-uniformity of the electric field significantly affects the discharge characteristics. The non-uniformity of the electric field restricts the main ionisation processes near the electrode with the high local electric field. Therefore, the corona discharge characteristics are determined by the electrode's configuration, gas nature and pressure, and the distance between electrodes.

Corona discharges in the power industry and HV systems should be avoided because they can have many adverse effects, including power loss, audible noise, electromagnetic interference, UV light emission, ozone generation and insulation damage. Corona discharge is the major cause of power losses in the power system transmission lines, and it is also a typical sign of insulation deterioration. Therefore, power companies employ different methods to detect corona discharges on transmission and substation equipment to minimise their negative impact.

However, in the pulsed power technology, corona discharges are used in the corona stabilised switches to achieve their stable operation in repetitive operation modes.

Conventional gas-filled spark gap switches are generally used in pulsed power systems due to their simple structure, excellent capabilities to withstand high voltage and operate in high *dV/dt* and *dI/dt* regimes, their ability to conduct significant current, and short switching time. However, due to limiting voltage recovery characteristics, the pulse repetition rates of such switches are typically limited to a few 10s of pulses (Schaefer, Kristiansen, and Guenther 1990). The corona-stabilised plasma closing switches offer significant improvement compared to the traditional gas-filled spark

switches in terms of voltage recovery and other operational characteristics in the repetitive operation regime. A highly divergent electrical field developed in such switches results in the corona stabilisation effect, which improves their operational characteristics such as voltage recovery, pulse repletion rate and operation stability (Harrower, MacGregor, and Tuema 1999; Beveridge 2009).

Corona stabilisation is the operational characteristic of the plasma closing switches filled with electronegative gases (such as SF_6) and with a non-uniform electrode topology that generates a highly divergent electrical field.

Corona stabilisation occurs within a specific gas pressure range, depending on the electrode topology. In the corona stabilisation regime of operation, the corona discharge appears in the vicinity of the energised electrode before complete spark breakdown. Charged species produced by the corona discharge develop a volumetric space charge around the energised electrode with the same polarity as the polarity of the applied voltage. Thus, it results in the field re-distribution and its reduction in the vicinity of the HV electrode. This reduction of the field leads to stabilisation of the operating voltage, i.e., its full recovery after each breakdown. Thus, a higher pulse repetition rate and higher operational voltage stability (compared with switches with no corona stabilisation effect) can be achieved.

A typical schematic voltage-pressure characteristic curve for corona discharge in an electronegative gas is shown in Figure 5.1. The dashed straight line shows the corona inception voltage as a function of gas pressure. The breakdown voltage in the P_1-P_c pressure range is significantly higher than the corona inception voltage, leading to the well-pronounced corona stabilisation effect.

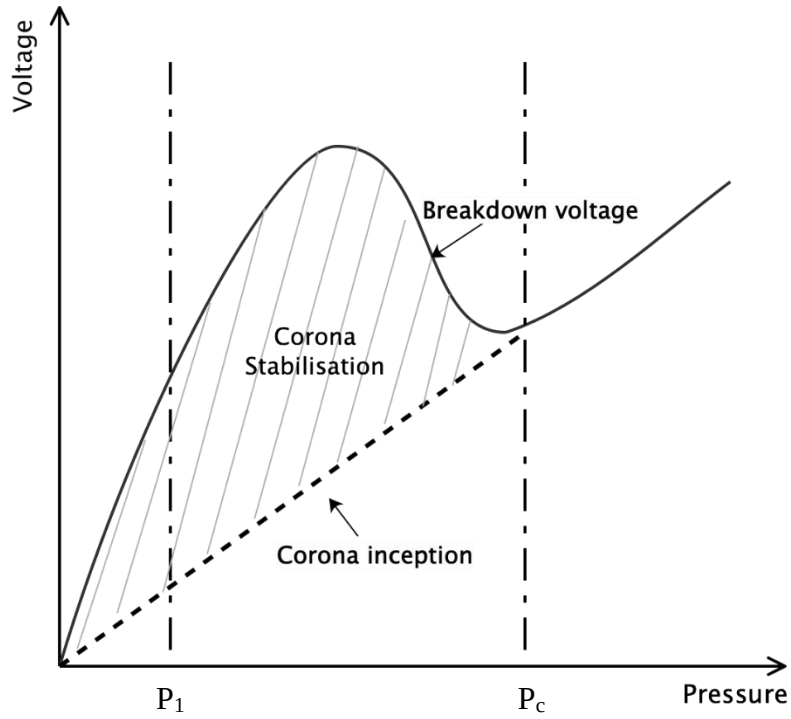

Figure. 5.1. The V-p characteristic of corona stabilised plasma closing switch with a highly divergent field. Picture based on (MacGregor et al. 1996)

Above the critical pressure P_c, no corona discharges are observed, i.e., spark breakdown occurs without prior ignition of corona discharge. The advantage of the generation of corona discharges in plasma closing switches is that it can prevent the breakdown in the gap until the applied voltage reaches its nominal operating value. Thus, the switch can fully recover its withstand voltage, allowing it to operate at a higher pulse repetition rate.

This work aims to optimise the operating performance of the developed switch topology. Therefore, studying the corona discharge characteristics in this topology filled with tested gases is necessary. The developed switch topology adopts a symmetrical arrangement of HV needles at each side of the central electrode. When the HV electrode is stressed with positive DC voltage, a negative corona discharge occurs at the needle electrodes located on the upper side of the trigger plate, i.e., in the upper gap of the switch. At the same time, a positive corona discharge occurs at the needle electrodes in the lower gap of the switch. On the other hand, when the HV electrode is negatively stressed, a positive corona discharge occurs at the needle

electrodes in the upper gap of the switch, and a negative corona discharge occurs at the needle electrodes in the lower gap of the switch. Therefore, regardless of the polarity of the HV electrode, both positive and negative corona discharges are generated in the switch, which helps to improve the switch's operational characteristics.

In this Chapter, the DC corona characteristics developed in the switch filled with all tested gases have been investigated over the pressure range of 1-12 bar(gauge). The voltage-current characteristics of the corona discharges in the developed configuration have been obtained and analysed, and the influence of main factors such as the polarity of the applied voltage, the gas pressure and the type of the gas on the voltage-current characteristics has been investigated.

5.2 Experimental Methodology

This study has been conducted using the developed two-stage triggered gas-filled switch topology with multiple corona discharge point electrodes. In order to study the performance of the corona stabilised switch, including its breakdown characteristics and corona-stabilised region, the corona discharges have been investigated using the multi-point electrode switch filled with four tested gases ("Zero grade" air, CO_2, 90%/10% Ar/O_2 mixture and N_2) over the gas pressure range 1-12 bar(gauge).

The HVDC power supply and measuring circuit are shown in Figure 3.5. A Glassman, 0-60 kV, 1.5 mA high voltage DC power supply was used to stress the upper plane electrode. The output polarity of the DCHV power supply is realised by changing the power output module. The output voltage was increased steadily at a rising rate of 500V/100ms until the breakdown occurred. The corona inception voltage was obtained by measuring the voltage drop across with a 10 kΩ current viewing resistor in series with the gap. The voltage across the current viewing resistor was observed by the HV probe, Tektronix P6015A (1:1000 division ratio, 75 MHz), connected to Tektronix TDS 3050 digitising oscilloscope (500 MHz bandwidth, 5 GS/s sampling rate). The corona inception voltage was recorded for at least 30 events for each set of experimental parameters. The average corona inception voltage and its standard deviation were calculated for each test.

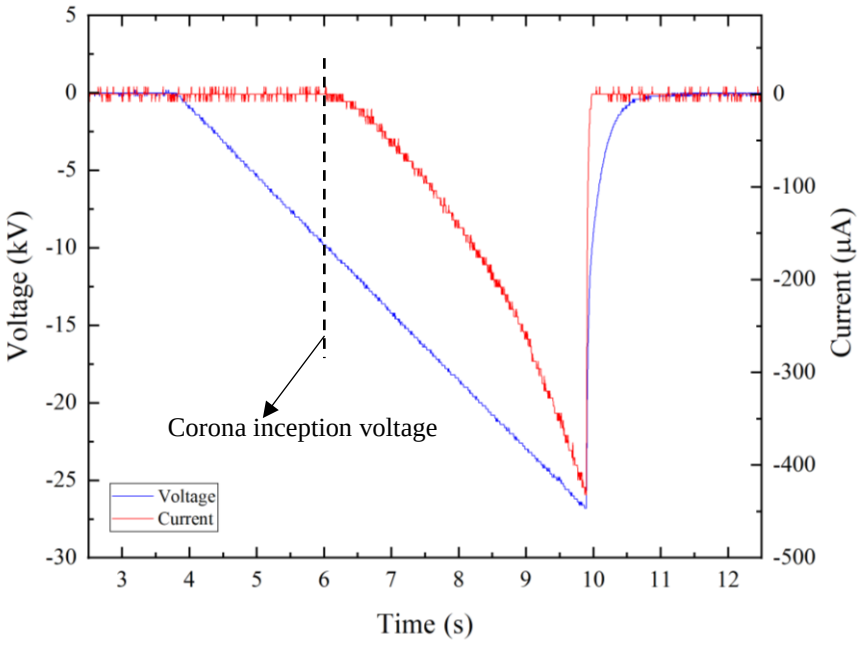

Figure. 5.2. Example waveforms of negatively stressed DC voltage, current, and the corresponding corona inception voltage at a pressure of 6 bar in the air.

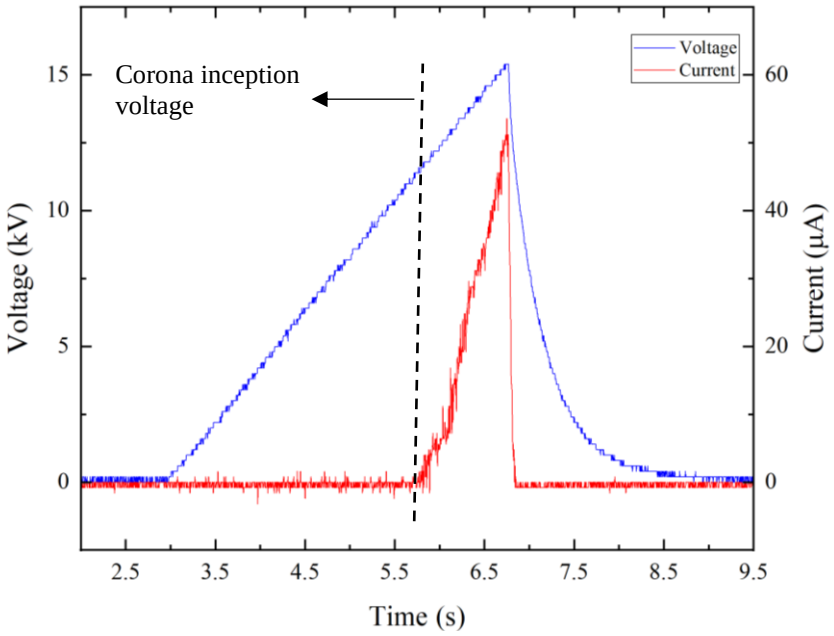

Figure. 5.3. Example waveforms of positively stressed DC voltage, current, and the corresponding corona inception voltage at a pressure of 6 bar in the air.

The upper plane electrode was stressed with both positive and negative polarity DC voltage to determine the corona inception voltage. The applied voltage was controlled

via a LabVIEW program interfacing with a National Instruments DAQ (USB6008) and was steadily increased. Figure 5.2 and Figure 5.3 show examples of the voltage and current waveform used to obtain the corona inception voltages for positively and negatively stressed corona electrodes. The voltage and current waveforms were used to obtain the voltage at the moment of initial rise of the corona current (corona inception voltage). In order to ensure the safety of operation, the maximum output voltages of the power supply was set at the level slightly lower than the previously obtained self-breakdown voltage. When the applied voltage reaches this specific (lower than the self-breakdown voltage) value, the program automatically reduces the voltage to 0 (as shown in Figure 5.3).

5.3 DC Corona Inception Voltage

In this section, the corona stabilisation effect was investigated, and the corona discharge inception voltage was obtained as a function of gas pressure. Corona discharges were analysed within single and double gap configurations using all tested gases over the pressure range from 1 to 12bar (gauge), 1bar increments. For each set of measurements, the corona inception voltage was recorded for at least 30 events. The mean value of the corona inception voltage and its standard deviation were calculated for each test. After each set of experiments, the test gas in the PCS was refreshed. Several minutes were allowed before proceeding to the next set of experiments. The obtained values of the corona inception voltage as a function of gas pressure were fitted with a linear function (5.1). The fitting coefficients obtained in this study only apply to the experimental conditions used in this work.

The experiment observed that the corona discharge only occurs in the air and 90%/10% Ar/O_2 mixture within the upper gap due to their strong electronegative characteristics.

Figure 5.4 shows the corona inception voltage as a function of the gas pressure for the upper gap in the developed switch topology filled with tested gases. It can be seen that the corona inception voltage has a linear dependence on the pressure for both positive and negative energisation. The experimentally obtained corona inception voltages have been fitted with linear empirical functions using the best fit procedure in

OriginPro *2017* graphing software. As a function of pressure, p (bar), the corona inception voltages, V_i (kV), presented in (5.1)

$$V_i = Ap + B \tag{5.1}$$

where *A(kV/bar)* and *B(kV)* are fitting coefficients extracted from the experimental data.

As shown in Figure 5.4, the corona inception voltage increases linearly proportionally as the pressure increases for both positive and negative energisation.

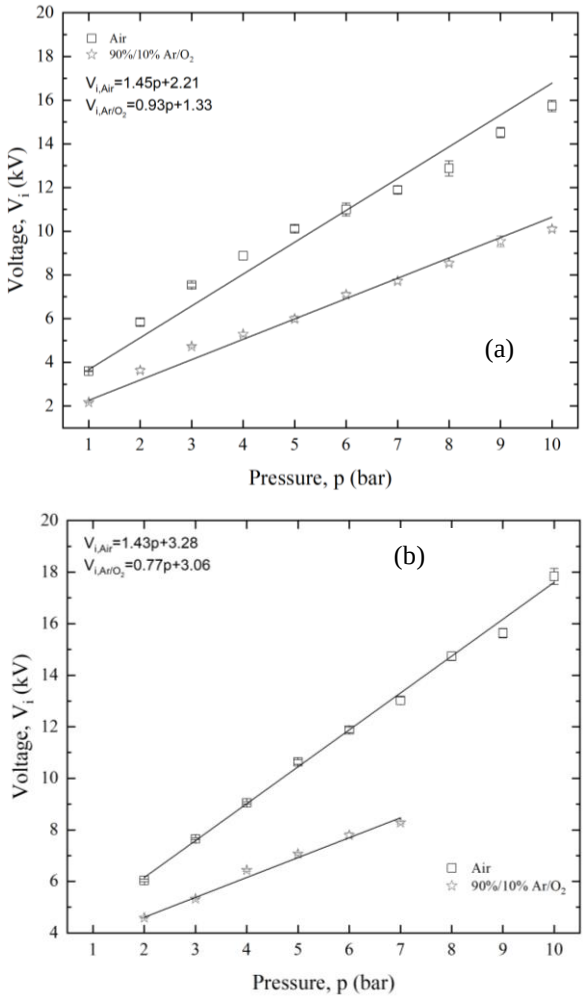

Figure. 5.4. Corona inception voltage, V_i, as a function of the gas pressure for the upper gap in the developed switch topology filled with air and Ar/O_2. (a) positively stressed HV electrode; (b) negatively stressed HV electrode.

The corona inception and self-breakdown voltages for the positively and the negatively stressed electrode are shown in Figure 5.5 for all tested gases: air and 90%/10% Ar/O_2. Figure 5.5 clearly shows that both the corona inception voltage and self-breakdown voltage increase with the increasing gas pressure of tested gases. The corona-stabilisation region for a positively stressed electrode is more comprehensive than a negatively stressed one. Therefore, the critical pressure for a positively stressed HV electrode is higher than for a negatively stressed one. Corona inception voltages for negatively stressed HV electrode were present for pressures above 2 bar for air and 90%/10% Ar/O_2. Over the corona stabilisation region, it was found that the critical pressure is 8 bar for negatively stressed HV electrode with 90%/10% Ar/O_2. Above 8 bar, no corona discharge occurs, and a spark discharge occurs directly at the onset.

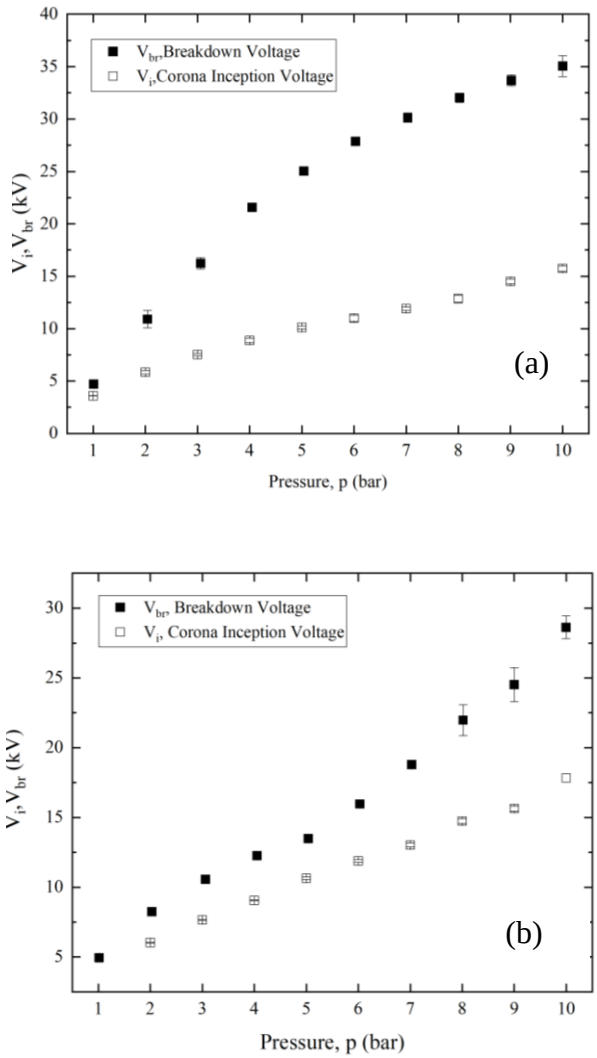

Figure. 5.5. Corona inception and breakdown voltages as functions of the gas pressure of the air-filled corona stabilised switch. (a) positive HV electrode; (b) negative HV electrode

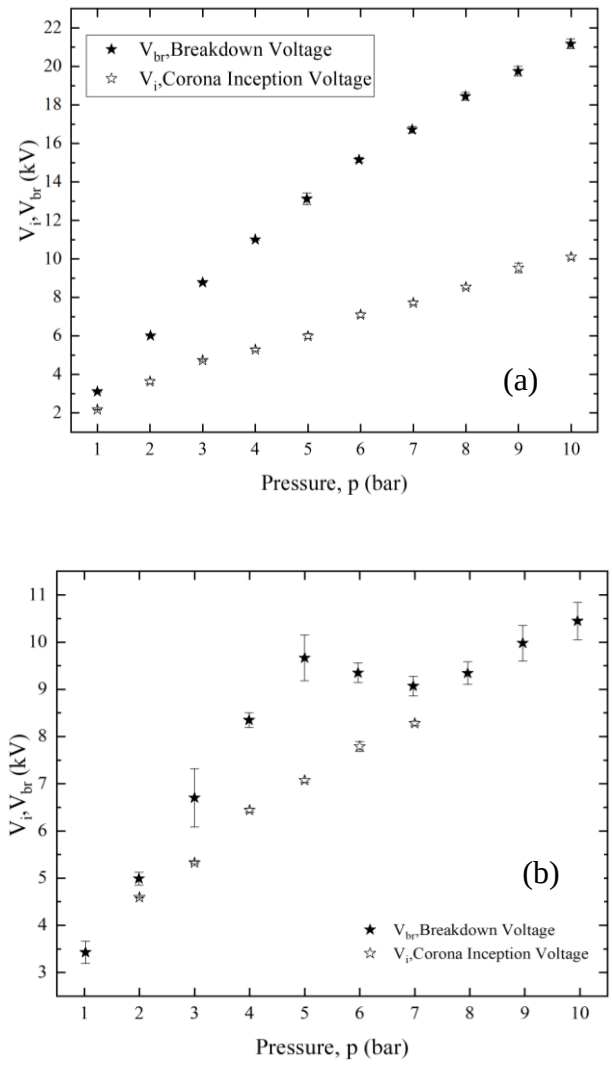

Figure. 5.6. Corona inception and breakdown voltages as functions of the gas pressure of the corona stabilised switch filled with 90%/10% Ar/O_2 mixture. (a) positive HV electrode; (b) negative HV electrode;

Figure 5.7 shows open shutter photographs of corona discharges at the needle electrodes. When the main HV electrode is stressed with negative voltage, the switch is filed with the 90%/10% Ar/O_2 at 5 bar. The corona discharge occurs only in the upper gap (5mm) as the central ring with the needle electrodes is grounded. As the voltage increases, the corona starts with the burst pulse corona is shown in Figure 5.6. The short and faint streamers appear away from the electrode. This regime is called the streamer corona. The repetitive current pulses occur at this time, and the current increases significantly compared to the initial stage. When the applied voltage

continues to increase further, the peak amplitude of the current pulses and their frequency increases, and the average current continues to grow until the moment when the discharge mode converts to glow corona. Finally, the gap is completely broken down, forming a spark discharge.

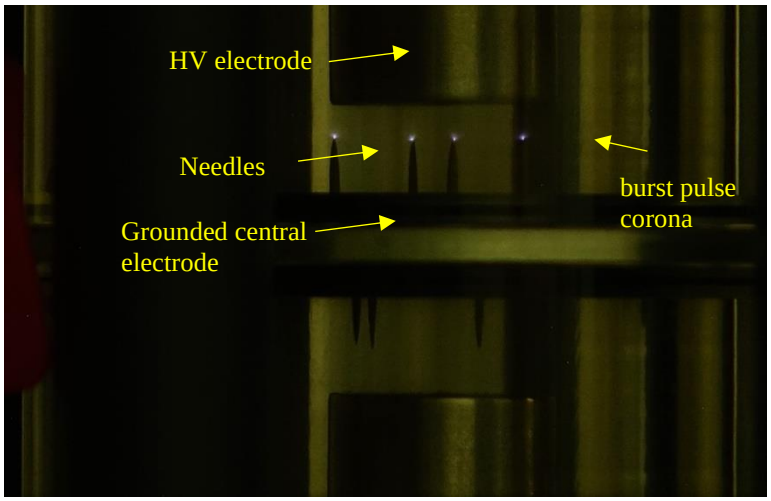

(a)

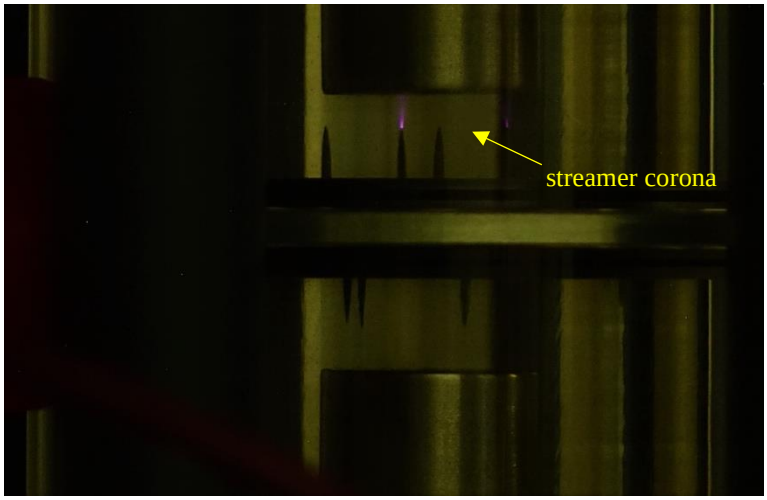

(b)

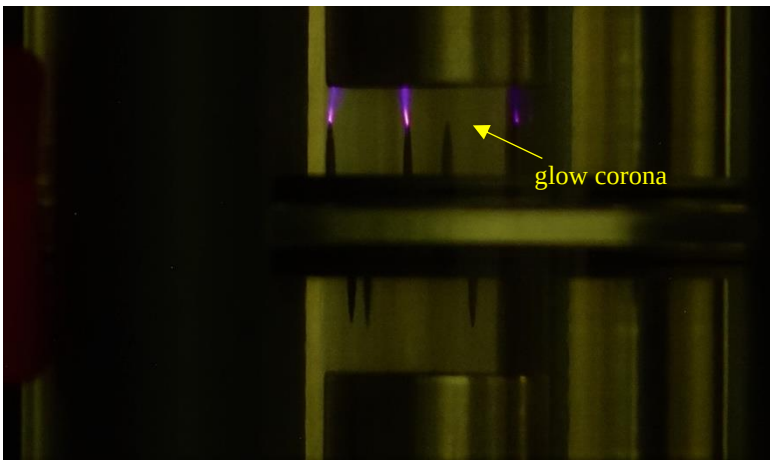

(c)

Figure 5.7 Open shutter photographs of positive corona discharge. Negatively stressed HV electrode with the 90%/10% Ar/O_2 at 5 bar in the upper gap(5mm) in the developed switch topology.

The experimental findings demonstrate that the corona discharge only occurs in the air within both the upper and lower gaps. As shown in Figure 5.8, unlike discharge occurring in a single gap, both positively and negatively stressed HV electrode breakdown characteristics are almost the same when discharge occurs in both upper and lower gaps. This is due to the symmetry of the electrode structure. Applying DC positive or negative high voltage to the HV electrode has no noticeable effect on the corona inception voltage or the self-breakdown voltage, which is different from the polarity effect observed in the point-plane structure. It was found that the corona stabilisation in air occurs up to the critical pressure of 7 bar for both polarities of high voltage. Above 7 bar, no corona discharges were observed, and breakdown occurs directly at the onset.

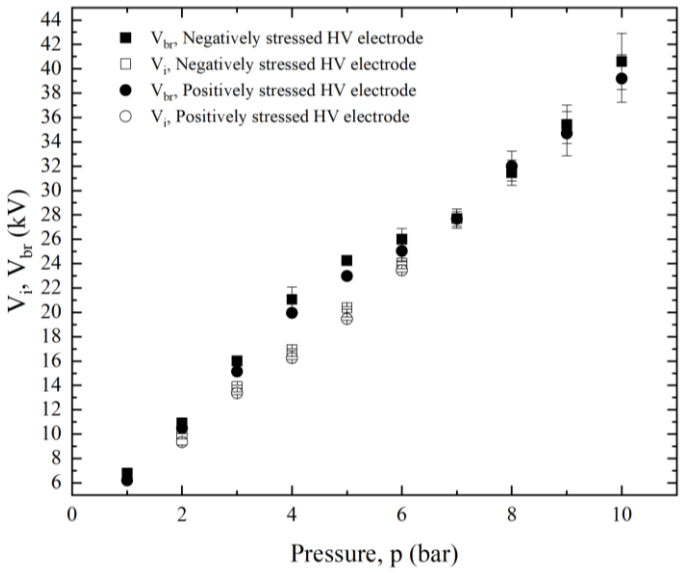

Figure. 5.8. Corona inception voltage and self-breakdown voltage as a function of the gas pressure with the corona stabilisation region for both the upper and lower gaps in the developed switch topology. Solid symbols, self-breakdown voltage; open symbols, corona inception voltage. Circles positively stressed HV electrode in the air; squares, negatively stressed HV electrode in the air. Each point is an average value of 10 measurements, and error bars represent the standard deviation.

Figure 5.9 shows open shutter photographs of corona discharge occurring in the developed switch topology. When the HV electrode is stressed with positive DC voltage, a negative corona discharge occurs at the needle electrode of the upper gap. At the same time, a positive corona discharge occurs at the needle electrode in the lower gap. In contrast, when the HV electrode is negatively stressed, a positive corona discharge occurs at the needle electrode in the upper gap, and a negative corona discharge occurs simultaneously at the needle electrode of the lower gap. Therefore, regardless of the polarity of the HV electrode, both positive and negative corona discharges are generated in the switch.

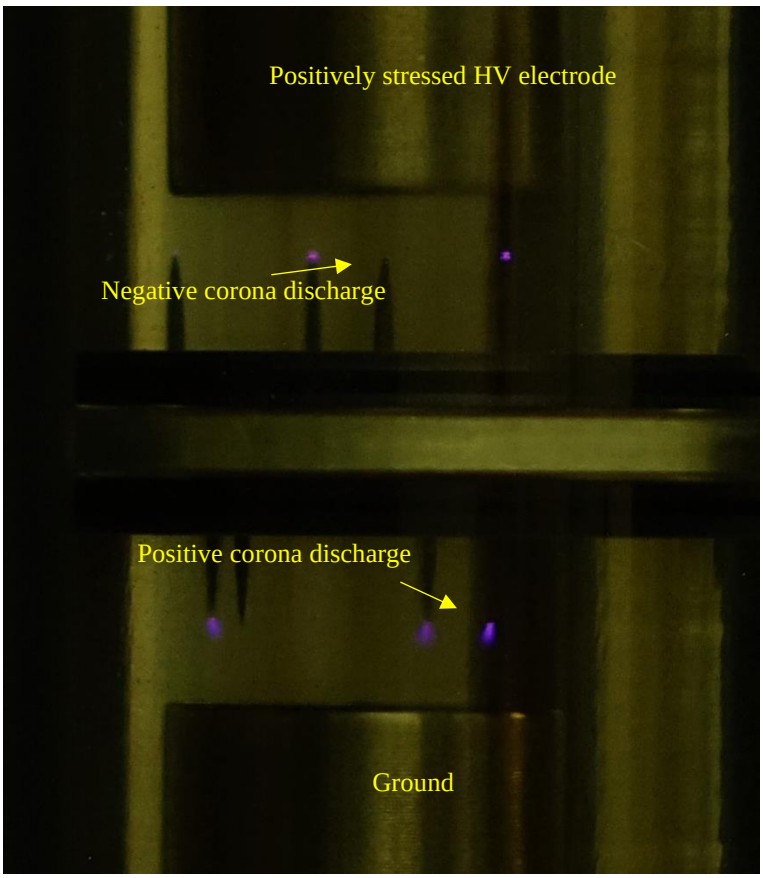

Figure 5.9 Open shutter photographs of corona discharge occurring in both gaps. Positively stressed HV electrode with the air at 4 bar in the developed switch topology.

In order to get a better understanding of the pre-breakdown corona discharge, further research into the relationship between the applied voltage and the corona current is necessitated.

5.4 Voltage-Current Characteristics in the Switch Topology

The qualitative description of the corona discharge process is relatively straightforward. However, due to the characteristics of the electrode configuration, the existence of the space charge in the gap, and difficulties with measuring microscopic parameters, quantitative analysis is challenging.

The voltage-current characteristics, presenting information about the space charge in the electrode gap, reflect the energy injected into the gap between the electrodes, thereby affecting the corona discharge. Many researchers studied corona discharge in

coaxial topologies or wire plate electrode structures, and voltage-current characteristics limited the related theoretical studies. Saverio (Cristina, Dinelli, and Feliziani 1991) obtained the voltage-current characteristic of corona discharge in DC electrostatic precipitators (coaxial topology). It is believed that the irregularity of the emitter surface makes the calculated corona initiation voltage slightly higher than the actual corona initiation voltage. At present, the empirical formula (6.2) (Robledo-Martinez 1993) is used to describe the voltage-current relationship of the discharge in different electrode configurations, and the values of *C* under other conditions are determined according to the experimental results (Raizer, Kisin, and Allen 2011).

$$I = CV(V - V_0) \tag{5.2}$$

where *I* is the corona current (μA), V_0 is a fitting inception voltage (kV), *V* is the applied voltage (kV), and *C* is a fitting coefficient (μA/(kV)^2) that depends on the geometry of the electrodes and which is, in most cases, a linear function of mobility.

In recent years, in many research publications on corona discharges, the DC energisation method was adopted, which uses needle-plates or other structures to form multiple discharges to increase the discharge current and the discharge energy. Through experiments, Yamada summarised the voltage-current characteristics of the negative corona discharge with a point-grid electrode system (Yamada 2004). Adamiak studied the summarised the voltage-current characteristics of a corona discharge in the point-plane configuration, simulated the extremely non-uniform electric field with the boundary element method, derived the electric field generated by the space charge with the finite element method and obtained the voltage-current characteristics of a corona discharge for the point-plane configuration (Adamiak 2004).

The V-I curves in Figure 5.10 present the relationship between the applied voltage and the corona current from the initial voltage until complete breakdown. Figure 5.10 shows that regardless of the polarity of HV voltage applied to the main HV electrode, the corona current within the upper gap in the developed switch topology increases nearly proportional to the increase in the applied voltage. The corona discharge current

was higher for the positively stressed HV electrode than for the negatively stressed HV electrode. The corona discharge current was higher in the air than in the 90%/10% Ar/O_2 mixture for both positive and negative applied voltages.

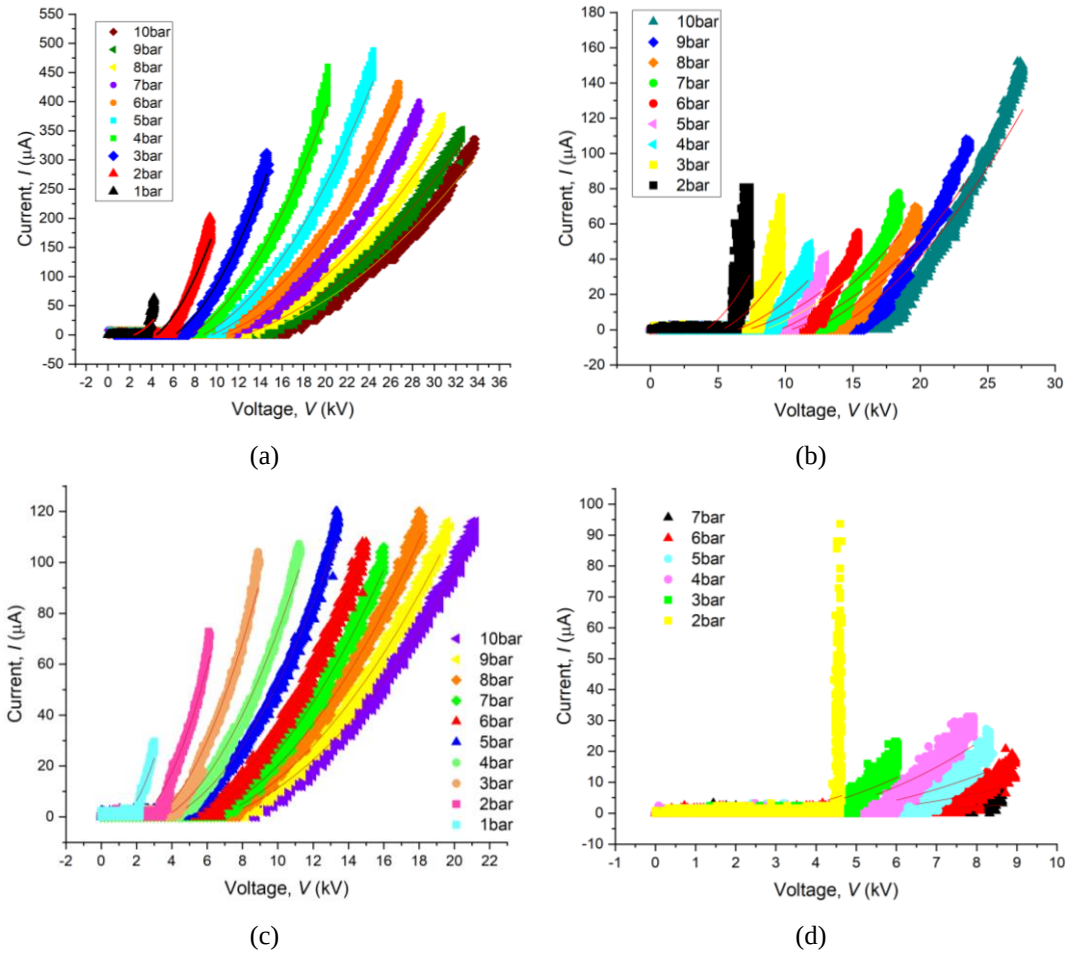

Figure. 5.10. Voltage-Current curves for corona discharge within the upper gap in the developed switch topology. (a) positively stressed HV electrode in the air; (b) negatively stressed HV electrode in the air; (c) positively stressed HV electrode in 90%/10% Ar/O_2; (d) negatively stressed HV electrode in 90%/10% Ar/O_2

The experimentally obtained corona current and voltage relationship have been fitted with the function given by equation (5.2) using the best fit procedure in OriginPro 2017 graphing software. The fitting coefficients, *C*, were determined by fitting (5.2) to the experimental data. The obtained *C* values are shown in Table 5.1 and Table 5.2.

Table 5.1. Fitting for Voltage-Current curves for corona discharge within the upper gap filled with air

	Positively stressed HV electrode		Negatively stressed HV electrode	
Pressure (Bar)	V_0 **(kV)**	C **(μA/(kV)^2)**	V_0 **(kV)**	C **(μA/(kV)^2)**
1	2.39	3.37		
2	4.52	3.52	4.14	1.31
3	6.24	2.26	5.38	0.80
4	7.73	1.56	6.49	0.47
5	8.77	1.14	7.44	0.32
6	9.56	0.86	8.59	0.32
7	10.36	0.69	9.76	0.31
8	11.24	0.58	10.36	0.28
9	12.56	0.50	12.16	0.30
10	13.22	0.44	14.35	0.32

Table 5.2. Fitting for Voltage-Current curves for corona discharge within the upper gap filled with 90%/10% Ar/O_2

	Positively stressed HV electrode		Negatively stressed HV electrode	
Pressure (Bar)	V_0 **(kV)**	C **(μA/(kV)^2)**	V_0 **(kV)**	C **(μA/(kV)^2)**
1	1.29	4.50		
2	2.40	2.72	2.69	0.63
3	3.21	1.78	3.14	0.67
4	3.65	1.14	3.94	0.69
5	3.89	0.86	4.35	0.40
6	5.02	0.67	4.78	0.23
7	5.59	0.57	4.94	0.07
8	5.97	0.50		
9	6.50	0.42		
10	6.87	0.36		

Figure 5.11 records the relationship between the applied voltage and the corona current for corona discharge within the developed switch topology's upper and lower gaps. Figure 5.11 shows that the corona discharge current is almost similar for the same gas pressure regardless of the polarity of the voltage applied to the HV electrode.

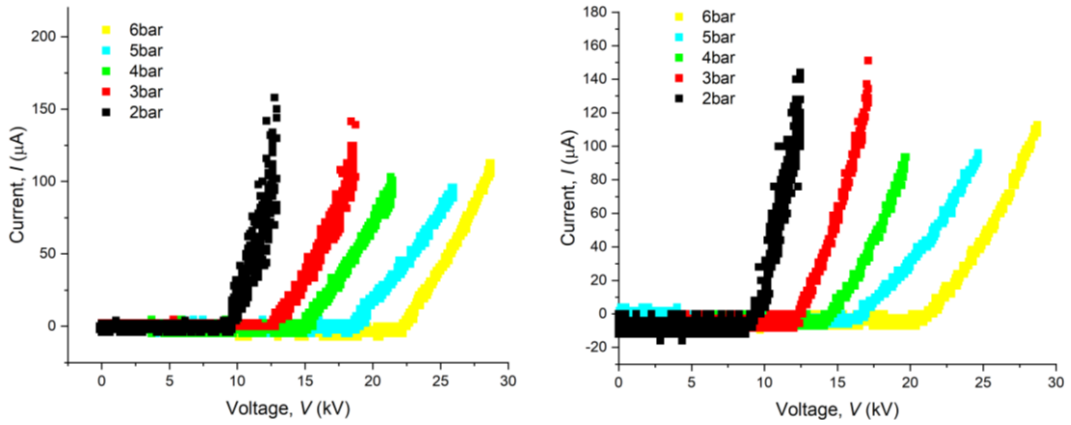

(a) (b)

Figure. 5.11. Voltage-Current curves for corona discharge within both the upper and lower gaps in the developed switch topology. (a) positively stressed HV electrode in the air; (b) negatively stressed HV electrode in the air.

5.5 Conclusion

The qualitative study of the pre-breakdown corona discharge characteristics in the multi-point-plane topologies filled with all tested gases in the pressure range of 1-12 bar(gauge) has been conducted in this Chapter. The experimental results demonstrate that the corona discharge only occurs in the air and the 90%/10% Ar/O_2 mixture due to their electronegative characteristics.

Because of the symmetry in the developed switch topology, a negative corona discharge occurred at the needle electrodes in the upper gap when the HV electrode was stressed with positive DC voltage. At the same time, a positive corona discharge occurs at the needle electrode located on the lower gap. On the other hand, when the HV electrode is negatively stressed, a positive corona discharge occurs at the needle electrode located in the upper gap, and a negative corona discharge occurs at the needle electrode located in the lower gap. Therefore, regardless of the polarity of the HV electrode, both positive and negative corona discharges are generated on both sides of the central electrode.

It was found that the voltage-current curves and characteristics of positive or negative corona discharges in the developed switch topology are similar, including the corona initiation voltage, corona discharge current and spark discharge voltage. The developed switch topology observed no polarity effects associated with the corona discharges.

CHAPTER.6 IMPULSE BREAKDOWN CHARACTERISTICS OF THE PLASMA CLOSING SWITCH FILLED WITH DIFFERENT GASES

6.1 Introduction

As discussed in Chapter 2, the gas-filled plasma closing switches can be divided into several categories depending on their operation principle/ triggering mechanisms: self-breakdown spark gaps, trigatron spark gaps, field distortion spark gaps, pneumatically triggered switches, and radiation-triggered switches. The time to breakdown and the standard deviation in the time to breakdown (jitter) are the critical parameters that affect the output pulse characteristics, especially in the case of pulsed power systems with multiple switches. Therefore, it is essential to investigate how the time to breakdown and jitter can be reduced.

A time interval from the moment of application of (high) voltage to the HV electrode of the gas plasma closing switch to the moment of formation of the conductive plasma channel in the switch is called total time to breakdown t_{br}. This time to breakdown is governed by many factors, such as gap distance, the area of electrodes and amplitude of the applied voltage, gas nature and its pressure, polarity and the rate of rising of the applied voltage. Typically it is assumed that this time lag comprises two parts: a statistical time lag and formative time lag (Alston 1968). The statistical time lag, t_s, is the time interval from the moment of the voltage applied to the appearance of seed electron(s) in the gap, which leads to the development of an electronic avalanche. The formative time lag, t_f, is a time interval required for developing the avalanche into a plasma streamer or the time required for a streamer to cross the gap.

The formative time lag is much shorter than the statistical time lag. In many practical cases, the total time to breakdown t_{br} is assumed to be approximately equal to the statistical time lag t_s.

The jitter describes the time variance (1-σ jitter) in the time interval between the application of the HV (trigger) impulse and the complete breakdown of gas in the switch (establishment of the conductive plasma channel).

During the development of the electron avalanches, the electric field of the space charge formed by the electron avalanche will be significantly enhanced. This space charge distorts the original electric field, intensifying the electric field at the head of the avalanche. When the number of electrons in the avalanche head reaches 10^8, the field ahead of the avalanche becomes so strong that it leads to significant intensification of the ionisation processes and the formation of a fast-moving ionisation wave – plasma streamer. Raether et al. proposed a criterion for the development of the electron avalanche into a streamer (Raether 1964). The number of electrons in the avalanche formed on the gap *d* is expressed by (2.20). The electric field in front of the electron avalanche (avalanche head) can be estimated as

$$E_r = \frac{e \cdot n_0 e^{\alpha d}}{4\pi\varepsilon_0 r^2} \tag{6.1}$$

where *r* is the radius of the head of the electron avalanche; *e* is the electron charge; *d* is the electrode gap; α is Townsend's first ionisation coefficient; n_0 is the initial number of electrons. It can be estimated from the diffusion process of electrons that the radius of the head of the electron avalanche, *r*, is

$$r \approx \sqrt{3Dt} \tag{6.2}$$

$$t = \frac{d}{v_e} = \frac{d}{\mu_e E} \tag{6.3}$$

where *D* is the electron diffusion coefficient; t is the time for electrons to migrate from *x=0* to *x=d*; v_e and μ_e are the drift velocity and mobility of electrons, respectively. *r* can be obtained as

$$r \approx \sqrt{\frac{3Dd}{\mu_e E}} \tag{6.4}$$

Using the Einstein relation in the kinetic theory of gases which links $D = \frac{\mu_e k T_e}{e}$, and the electron energy is $eV = \frac{3}{2} k T_e$; where T_e is the electron temperature in plasma (K); k is Boltzmann's constant; e is an electron. The diffusion coefficient, D, of electrons can be obtained.

$$D = \frac{2}{3} V \mu_e \tag{6.5}$$

The electric field in front of the avalanche head can be rewritten as

$$E_r = \frac{e \cdot n_0 e^{\alpha d}}{4\pi\varepsilon_0 (2Vd)} E \tag{6.6}$$

When the avalanche has its length longer than its critical distance x_{cr}, the critical number of electrons, n_{cr}, is reached in the avalanche head

$$n_{cr} = n_0 e^{\alpha x_{cr}} = \frac{4\pi\varepsilon_0 (2V x_{cr})}{e} \tag{6.7}$$

When $\alpha x_{cr} \approx 20$, and the number of electrons in the electron avalanche are more significant than 10^8, the streamer is formed (Dutton, Jones, and Palmer 1961; Erich E. Kunhardt 1980; McDonald et al. 1980). The critical avalanche time required to develop the streamer (avalanche-to-streamer transition) can be obtained by

$$\tau_{cr} = \frac{x_{cr}}{v_e} = \frac{\ln n_{cr}}{\alpha v_e} \tag{6.8}$$

Therefore, the main factor affecting the discharge formative time lag is Townsend's first ionisation coefficient, α, and the drift velocity of electrons; the discharge

formative time lag decreases with an increase in α and v_e. According to (2.22), increasing the gas pressure p and the electric field strength E in the spark gap will increase Townsend's first ionisation coefficient, α, and both factors can reduce the formative time lag of the discharge. The principal approach to increasing the electric field strength in the spark gap is to increase the voltage amplitude of the applied trigger impulse so that the field strength of the distorted electric field is higher when the spark gap discharges.

From the above analysis, it can be concluded that the formative time lag of discharge is related to Townsend's first ionisation coefficient of electrons. Increasing the gas pressure and the electric field strength in the spark gap can reduce the formative time lag of the switch. Specific methods to minimise the delay include increasing the amplitude of the applied trigger impulse, thus increasing the electric field intensity of electric field distortion. An increase in the gas pressure and the electric field strength in the switch leads to the ionisation coefficient growth. This reduces the formative time lag of the spark gap discharges.

This Chapter investigates impulse breakdown characteristics of the developed switch filled with all tested gases ("Zero grade" air, CO_2, N_2, and 90%/10% Ar/O_2 mixture) over the gas pressure range 1-12 bar(gauge). The triggered plasma closing switches are widely used in the pulsed power system with high operating voltage, high repetition rate, fast switching time, low jitter and high performance(Bernstein 1973; Mercer, Smith, and Martin 1976).

The switch is triggered by the change of the electric field distribution by applying an external trigger pulse. The time to breakdown and jitter of the PCS have been obtained, and the effect of different factors such as the discharge polarity, the pressure between electrodes and the amplitude of DC stress voltage applied across the main inter-electrode gaps have been investigated.

6.2 Experimental Methodology

The diagram of the experimental set-up used in this study is presented and discussed in chapter 3. The impulse breakdown characteristics of the developed switch filled with four tested gases ("Zero grade" air, CO_2, 90%/10% Ar/O_2 mixture and N_2) over the gas pressure range 1-12 bar(gauge), including total time to breakdown and its jitter have been obtained.

HV trigger impulses with a defined pulse shape were applied to a central switch electrode during the experimental procedure. In order to generate the triggered impulses, an inverting Blumlein pulse generator has been employed. The Blumlein pulse generator provides approximately voltage impulse with a magnitude of 30kV and duration of 280ns; the voltage rate of rising is ~1kV/ns.

The upper plane electrode of the switch was stressed by HVDC voltage generated by a Glassman HVDC power supply (0-60kV) via a 1MΩ charging resistor. The central electrode was connected to an inverting Blumlein pulse generator through a capacitor (2.2pF) which decoupled the Blumlein pulse generator and the test cell. The trigger impulse voltage waveforms were monitored using a high-voltage probe, Tektronix P6015A (75MHz bandwidth, 100MΩ input resistance, and 3pF input capacitance, at higher frequencies, the input resistance reduces down to 1kΩ for 100MHz signal), connected to the central trigger plane of the switch. The voltage across the switch was monitored and recorded using a North star PVM-5 high-voltage probe (1000:1) and a Tektronix TDS 3050 digitising oscilloscope (500MHz bandwidth, 5GS/s sampling rate). The upper plane electrode was stressed with both positive and negative polarity DC voltage for two stress levels, 70% and 90% of the self-breakdown voltage, at a rate of ~0.6kV/s. The applied voltage was controlled via a LabVIEW program interfacing with a National Instruments DAQ (USB6008).

Figure 6.1 shows the voltage waveforms obtained from Tektronix P6015A to monitor trigger impulse voltage which is connected to the central trigger plane of the switch, and the North Star PVM-5 probe to monitor the voltage across the main gap of the switch

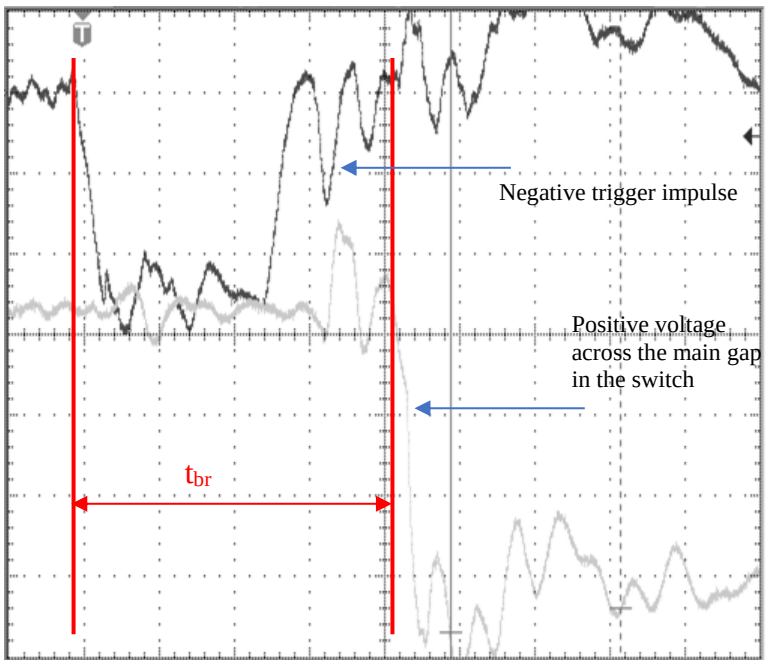

Figure. 6.1. Typical voltage waveform illustrating the measured time to breakdown in an air-filled switch at 9 bar with 90% V_{br} DC stress applied. Vertical scale: 10 kV/division; horizontal scale: 100 ns/division.

It is seen from Figure 6.1 that the breakdown time is measured from the moment of application of the negative trigger impulse. When a complete breakdown occurs in the switch, the voltage across the gap drops to zero. This time moment is defined as the end of the breakdown time interval, t_{br}. Figure 6.1 shows that in triggered operation, the top plane electrode of the switch was stressed by a positive DC voltage via a 1MΩ charging resistor, and a trigger generator applied an impulse trigger of -30 kV via a decoupling resistor to the central trigger electrode of the switch.

The time to breakdown was recorded for 20 consecutive breakdown events in each gas in each set of measurements. The average breakdown time and its standard deviation, defined as the jitter, were calculated for each set of tests. After each set of experiments, the gas in the PCSs cell needs to be evacuated and filled with the refreshed test gas (several minutes were allowed before proceeding to the next set of experiments).

6.3 Electrostatic Simulation of the field distribution in the PCS

Before experimental breakdown measurements, the electrostatic field distribution in the corona stabilised switch topology was obtained using the COMSOL Multiphysics package. A 2D electrostatic model of the PCS was developed. In this model, the upper plane electrode was stressed by 10 kV DC voltage, and the lower electrode was grounded. One situation is to simulate the electric field distribution for the switch when the central trigger electrode is at a floating potential. Another case includes an application of a -30kV voltage to the central trigger electrode.

Figure 6.2 shows the electric field distribution in the PCS. When the central trigger electrode is at a floating potential, the electric field in the switch is mainly concentrated around the tips of the corona needles on both sides of the central trigger electrode. As seen in Figures 6.3(a) and (b), the peak magnitude of the electric field is ~10.8MV/m in the region surrounding the needle tips located on the central trigger electrode.

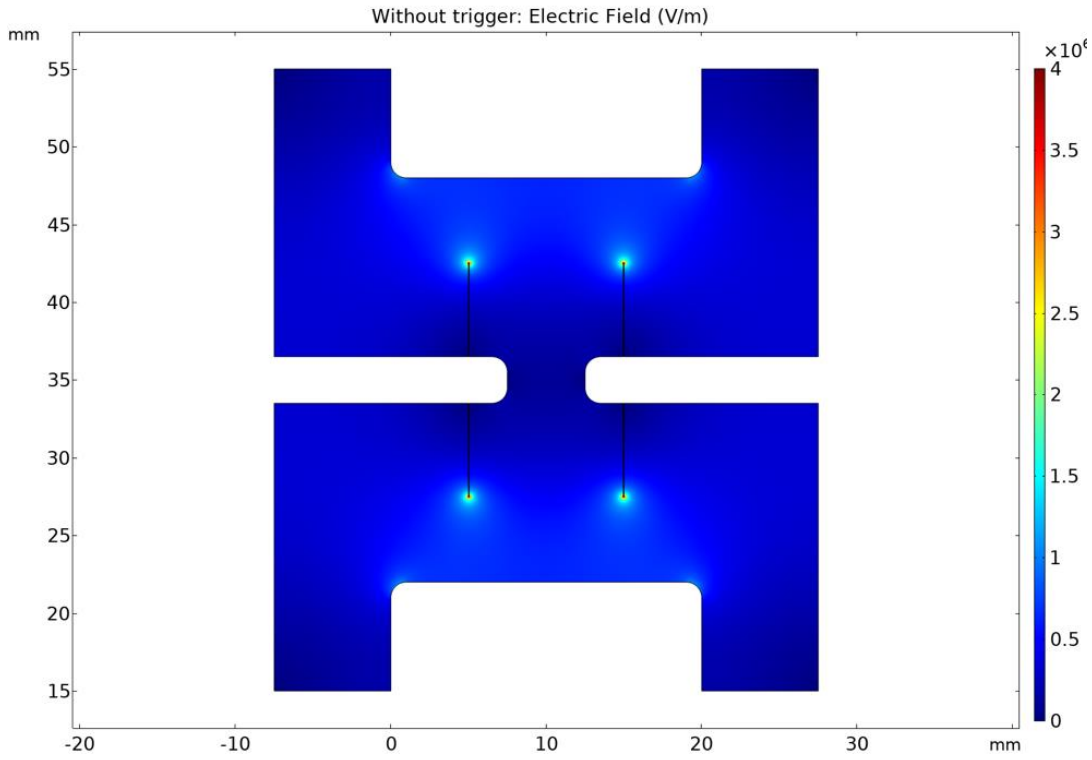

(a)

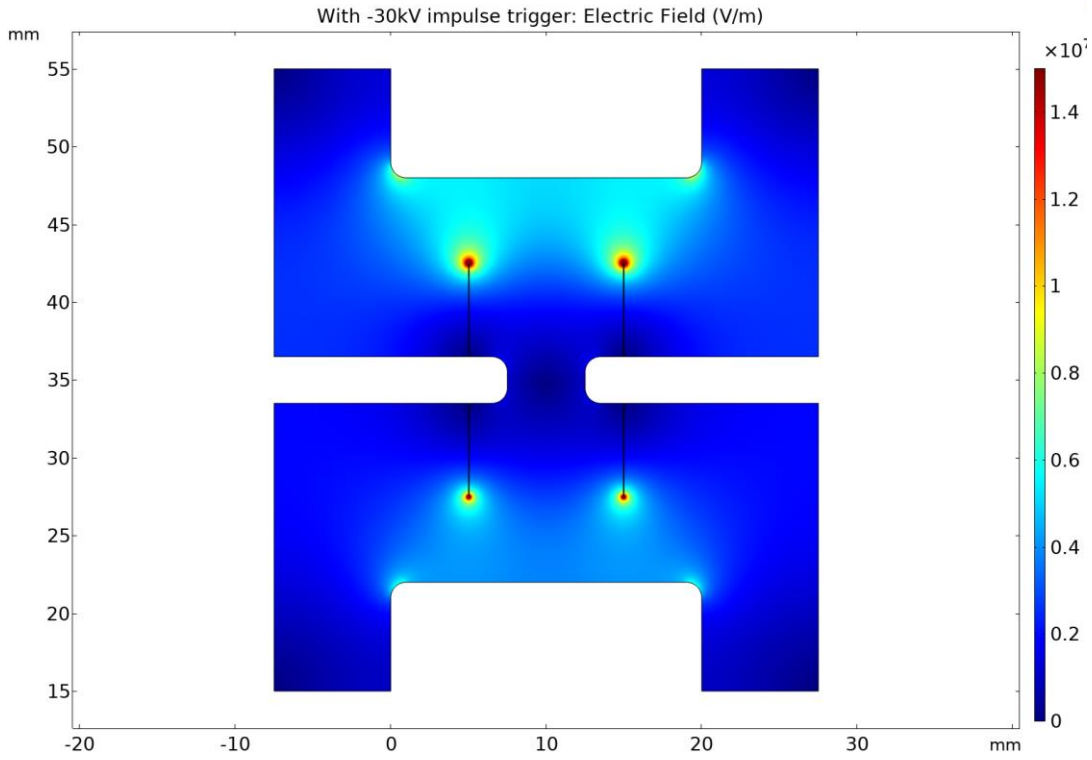

(b)

Figure. 6.2. The electrostatic field distribution in the field-distortion spark gaps. (a) The upper plane electrode is stressed by 10 kV DC voltage, the lower electrode is grounded, and the central trigger electrode is at a floating potential. (b) The upper plane electrode was stressed by 10 kV DC voltage, the lower electrode was grounded, and the -30kV trigger signal was applied to the central trigger electrode.

When a -30kV impulse voltage is applied to the central trigger electrode, the electric field is at its maximum in the region surrounding the tips on the central trigger electrode in the upper gap of the switch. Figure 6.3(c) shows that the maximum magnitude of the electric field, in this case, is ~88MV/m. Figure 6.3(d) shows that the electric field's peak magnitude in the region surrounding the needle tips on the central trigger electrode in the lower gap of the switch is ~66MV/m.

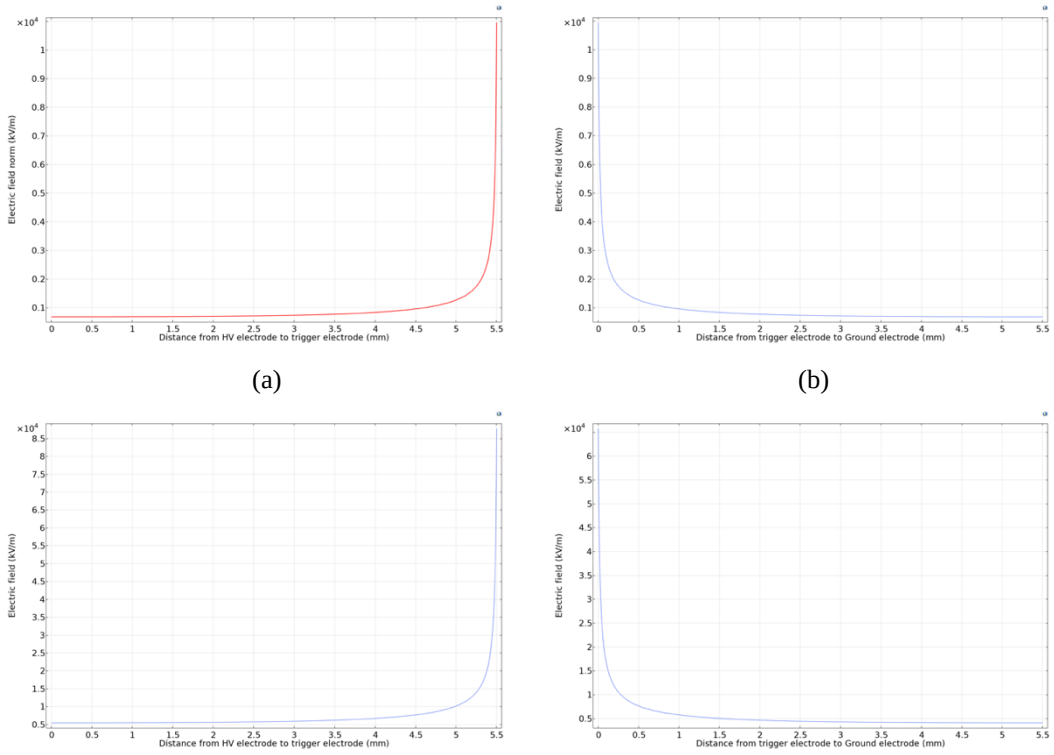

Figure. 6.3. (a) The electric field between the upper and central trigger electrodes is at a floating potential. The applied voltage is 10kV DC. (b) The electric field in the region between the central trigger electrode at a floating potential and the lower electrode is grounded. (c) The electric field in the region between the upper electrode is applied with 10kV DC and the central trigger electrode where -30kV is applied. (d) The electric field in the region between the central trigger electrode is applied with -30kV and the lower electrode is grounded.

The central trigger electrode significantly impacts the electric field distribution between the primary electrodes, whether at floating potential or energised with a trigger voltage. Moreover, it can be seen that when the trigger voltage is applied to the central trigger electrode, the strength of the electric field in the region surrounding the needle tips increases significantly. The maximum value of the electric field reaches ~88 MV/m, which is far greater than the electric field strength required for the breakdown of the air gap, which makes the gaps between the two primary electrodes quickly break down. When a -30 kV trigger voltage is applied to the central trigger electrode, the maximum electric field strength is ~8 times higher than the maximum voltage when the central trigger electrode is a floating potential, which reduces the switching delay time.

6.4 Triggered Operation of the PCS at different Pressures and different DC Stress Voltages

In the pulsed power industry, fast switching time and minimum jitter are critical parameters because they represent the stability of the operation of the plasma closing switch. On the other hand, the low jitter allows multiple pulsed power systems to be synchronised. Therefore, it is imperative to determine operating parameters to reduce both the time to breakdown and jitter.

In this section, the triggered switch was filled with the selected gases/gas mixture: bottled air, N_2, CO_2, and the Ar/O_2 mixture. The results of the triggered operation of the switch for each gas (i.e., the time to breakdown and jitter as a function of gas pressure and the level of energisation) are shown below. Using Origin Pro graphing software, an exponential fit is applied to the experimental data to compare the time to breakdown characteristics of the switches at different gas pressures for varying levels of DC stress voltage applied across the switch.

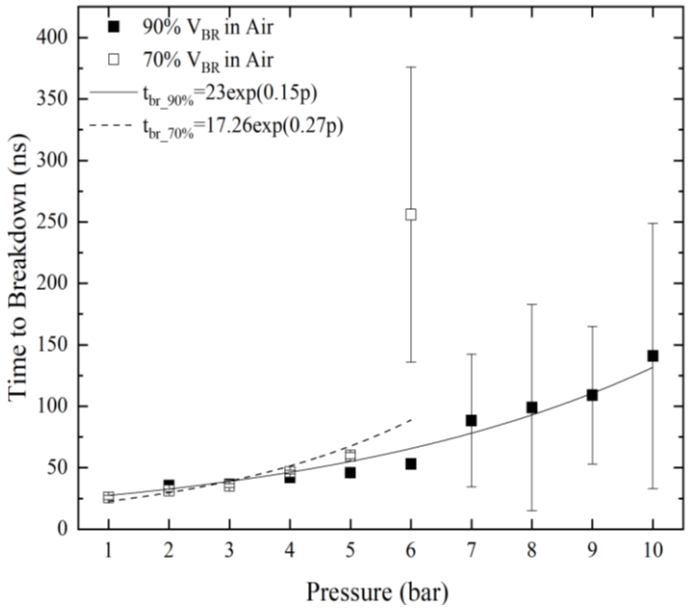

Figure. 6.4. Time to breakdown as a function of gas pressure for air for 70% and 90% self-breakdown voltage. Each point is an average of 20 measurements, and error bars represent the standard deviation values (jitter).

Figure 6.4 shows the obtained time to breakdown as a function of the gas pressure for the energisation levels equal to the 70% and 90% DC self-breakdown voltage energisation, i.e., the applied voltage is 70% and 90% of the self-breakdown voltage established in Chapter 4.

It was found that the time to breakdown increases with increasing gas pressure in the whole tested pressure range. When the switch was stressed with 70% of the self-breakdown voltage, there was a significant increase in the time, up to t ~ (130-370) ns for the pressure of 6 bar. No breakdown events were observed at this energisation level with gas pressure above 6 bar. When 90% of the DC self-breakdown voltage is applied across the air-filled switch, breakdown events can be observed in the entire test pressure range, up to 10 bar, and the breakdown time increases with the increase in the gas pressure.

By analysing the relationship between time to breakdown and gas pressure for 70% and 90% of the DC self-breakdown voltage applied across the switch, it can be found that the breakdown time and jitter increase as the gas pressure increases. This is mainly due to the rise in the operating pressure within the switch, which will increase the withstand voltage in the gap of the switch and increase the breakdown time and jitter of the switch.

When 90% of the dc self-breakdown voltage is applied across the switch, it was clearly observed that the breakdown time is shorter than under 70% dc self-breakdown energisation. The electric field strength in the switch gap increases under the applied dc self-breakdown voltage is increased. The ionisation process is intensified, and the electron avalanche and streamer develop faster, thus accelerating the breakdown process in the gas gap. As the stressed dc self-breakdown voltage increases, the time to breakdown and jitter is reduced, and the switch's performance becomes more stable.

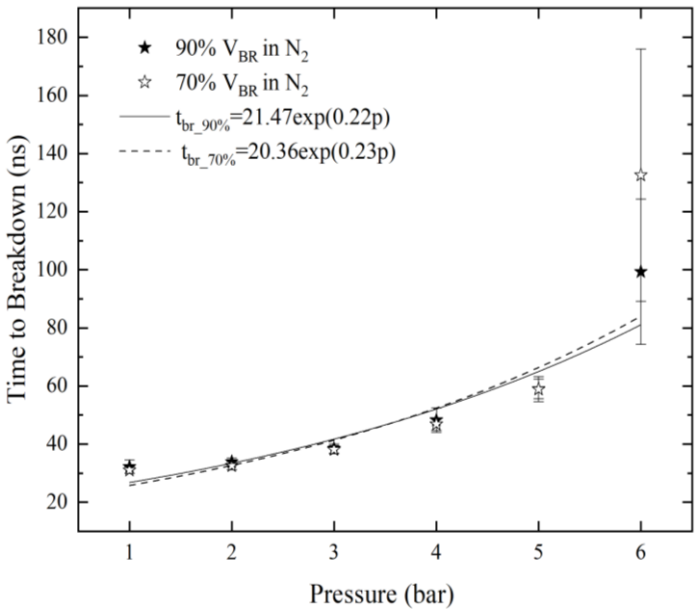

Figure. 6.5. Time to breakdown as a function of gas pressure for N_2 gas mixture for 70% and 90% self-breakdown voltage. Each point averages 20 measurements, and error bars represent the standard deviation values (jitter).

In the case of the N_2-filled switch, the time to breakdown also increases with an increase in the gas pressure in the tested pressure range for the energisation levels equal to the 70% and 90% self-breakdown energisation levels, as shown in Figure 6.5. Thus, for both energisation levels, the maximum pressure at which breakdown events can occur is 6 bar, and no breakdown events were observed for gas pressures higher than 6 bar. Furthermore, there is no apparent difference in time to breakdown for both energisation levels for gas pressures below 6 bar. However, when the gas pressure is at its maximum (6 bar), the time to breakdown and jitter increase significantly, and it is observed that the breakdown time for 90% of the dc self-breakdown voltage is considerably less than that under the condition of 70% of the dc self-breakdown voltage.

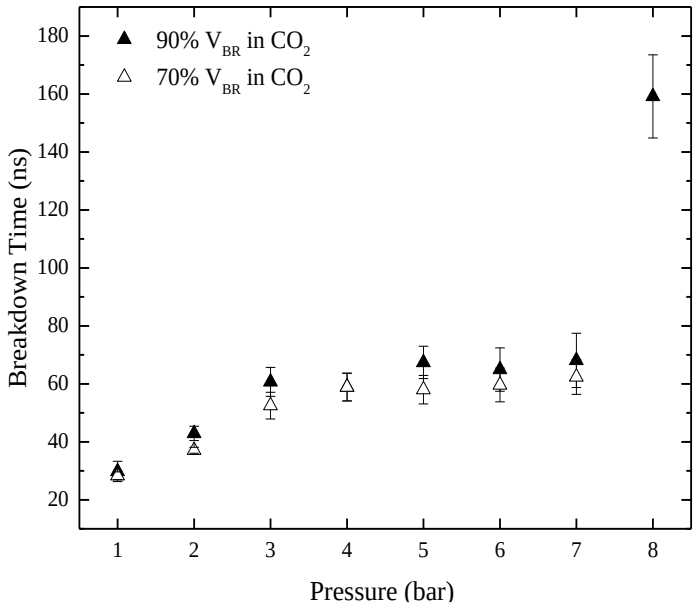

Figure. 6.6. Time to breakdown as a function of gas pressure for CO_2 gas mixture for 70% and 90% self-breakdown voltage. Each point is an average of 20 measurements, and error bars represent the standard deviation values (jitter).

When the switch was filled with CO_2, the time to breakdown demonstrated a non-monotonic increase with an increase in the gas pressure for the energisation levels equal to 70% and 90% of the dc self-breakdown voltage applied across the switch. The time to breakdown increased from ~30 ns to ~60 ns for pressures 1-3 bar and then soaked at ~ (60-67) ns for pressures 3-7 bar for both energisation levels. For 90% of dc self-breakdown energisation level, the time to breakdown rose distinctly to ~160 ns at 8 bar. For 90% self-breakdown energisation levels, the maximum pressure at which breakdown events can occur is 8 bar, and no breakdown events were demonstrated for higher gas pressures. Furthermore, there is no apparent difference in time to breakdown for both energisation levels as gas pressure under 8 bar, even the time to breakdown for 70% of dc self-breakdown energisation level is slightly shorter than that for 90% self-breakdown energisation level.

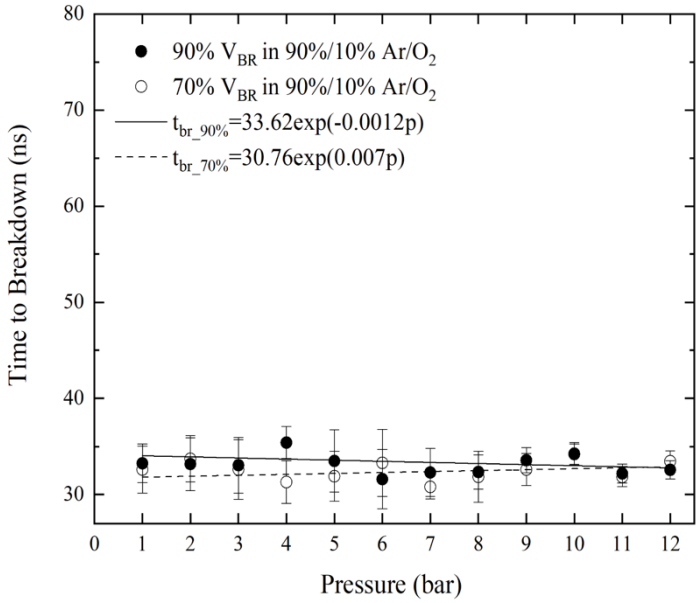

Figure. 6.7. Time to breakdown as a function of gas pressure for 90%/10% Ar/O_2 gas mixture for the energisation levels equal to the 70% and 90% self-breakdown voltage. Each point is an average of 20 measurements, and error bars represent the standard deviation values (jitter).

Figure 6.7 shows the obtained time to breakdown as a function of the gas pressure for 70% and 90% of the dc self-breakdown voltage applied across the switch filled with the Ar/O_2 mixture. The breakdown events were observed over the pressure range of 1 bar to 12 bar for both energisation levels. In this gas pressure range, the breakdown time does not change significantly, and it does not show any noticeable trends with a change in the gas pressure. The breakdown time fluctuates slightly and remains within ~ (31-35) ns for both energisation levels. As the gas pressure increases, the withstand voltage of the gap increases, and the breakdown time also increases. However, as the gas pressure and the withstand voltage increase, the electric field developed in the switch also increases, and the increase in the electric field reduces the breakdown time. Thus, both factors: the gas pressure and the electric field strength, provide an opposite effect on the time to breakdown. Therefore, the breakdown time does not change significantly due to the mutual influence of the gas pressure and electric field.

An exponential phenomenological function (6.9) has been used to fit the experimental data (the relationship between the time to breakdown and the gas pressure) using Origin Pro graphing software:

$$t_{br} = Mexp(Np) \tag{6.9}$$

where t_{br} is the time to breakdown, p is the gas pressure, M (ns) and N (bar^{-1}) are fitting coefficients. Using the best fit procedure in the Origin Pro graphing software, coefficients M and N have been obtained by fitting Equation (6.9) to the experimental data. Numerical values of the obtained coefficients M and N for both energisation levels and each gas are presented in Table 6.1.

Table 6.1 Coefficients M and N used in fitting (6.9) for each tested gas for both energisation levels

Gas	***70% DC stress***		***90% DC stress***	
	M (ns)	N (Bar^{-1})	M (ns)	N (Bar^{-1})
Air	**17.26±8.1**	**0.27±0.2**	**23±9.7**	**0.15±0.1**
N_2	**20.36±1**	**0.23±0.05**	**21.47±1.3**	**0.22±0.01**
Ar/O_2	**30.76±0.81**	**0.007±0.003**	**33.62±0.74**	**-0.0012±0.001**

It can be seen from Table 6.1 that for the experimental conditions where 90% of the dc self-breakdown voltage is applied across the switch, the gradient of the exponential fitting is larger than that value obtained when 70% self-breakdown voltage is applied to the switch. Furthermore, when the switch is filled with the Ar/O_2 mixture, the gradient of the exponential fitting is the largest compared to the switch filled with other tested gases. The power value of the exponential fit of the time to breakdown data is the smallest when the switch is filled with the Ar/O_2 mixture for both energisation levels. It shows that the fluctuation of the breakdown time is minimal in the entire gas pressure range, and it does not show a noticeable trend of increasing with the increase of gas pressure.

Another critical operating parameter for the PCS filled with all tested gases to be investigated is the jitter. Jitter is obtained by calculating the standard deviation (1-σ) of the time to breakdown. It represents the degree of consistency in the time to

breakdown. The jitter as a function of the gas pressure in the switch for both energisation levels was plotted in Figure. 6.8 - Figure. 6.11.

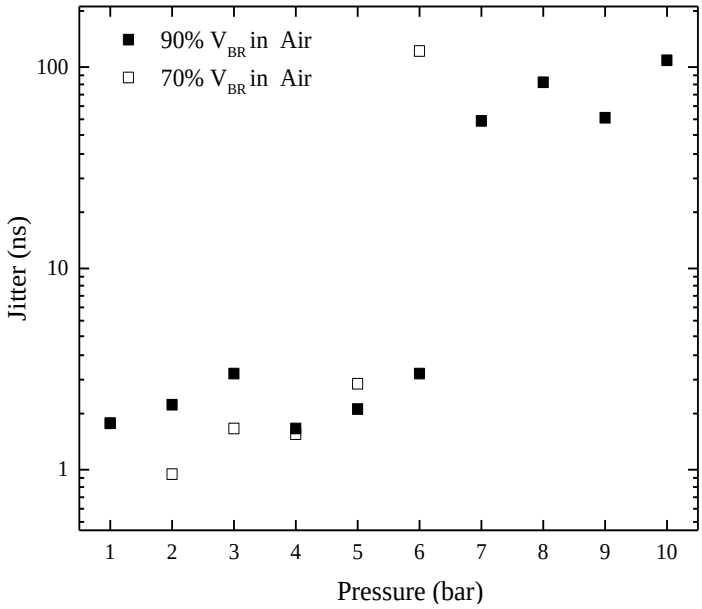

Figure. 6.8. Jitter as a function of the gas pressure for air for both 70% and 90% dc self-breakdown voltage levels.

As shown in Figure. 6.8, when the switch was filled with air, the jitter increased with increasing gas pressure across the tested pressure range for the energisation levels equal to 70% and 90% of the dc self-breakdown voltage applied across the switch as a dc stress voltage. In addition, for 90% of dc self-breakdown energisation levels, it was found that jitter increases in the range from ~1 ns to ~3.8 ns with increasing gas pressure up to 5 bar for both energisation levels. Then there is a significant surge to ~ (54-108) ns for pressure above 7 bar. When the 70% self-breakdown voltage is applied to the switch, the jitter sharply increases to ~120 ns for pressure above 6 bar, the maximum operating pressure for air at this energisation level.

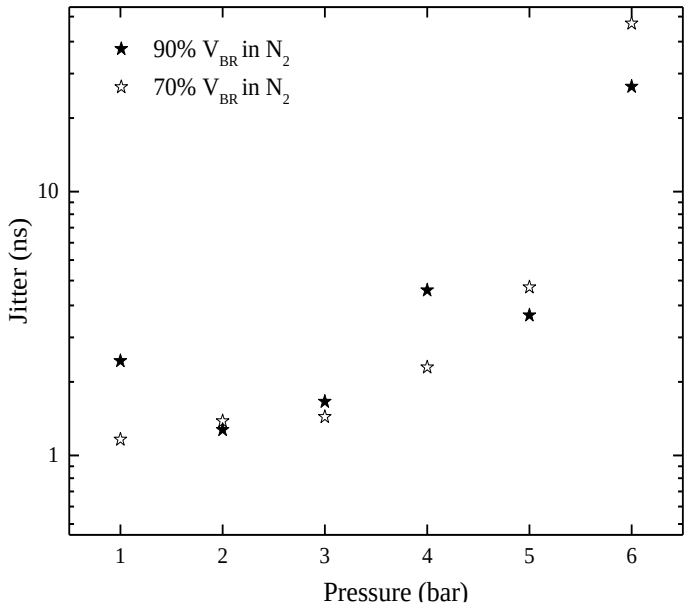

Figure. 6.9. Jitter as a function of the gas pressure for N_2 for both 70% and 90% dc self-breakdown voltage levels

When the switch was filled with N_2, the jitter demonstrated an upward tendency as the gas pressure rose for the energisation levels equal to 70% and 90% of the dc self-breakdown voltage, as shown in Figure 6.9. If the switch was stressed with 70% of the self-breakdown voltage, the jitter varies from ~1.2 ns to ~4.8 ns. When the gas pressure increases from 1 bar to 5 bar, there is a significant increase in the switch jitter, up to ~ 13.7 ns at the pressure of 6 bar. When 90% of the dc self-breakdown voltage is applied across the N_2-filled switch, the jitter varies from ~1.3 ns to ~4.8 ns when the gas pressure increases from 1 bar to 5 bar and then rises sharply to ~ 11.8 ns at the pressure of 6 bar. The pressure of 6 bar is the maximum operating pressure for N_2 for both energisation levels.

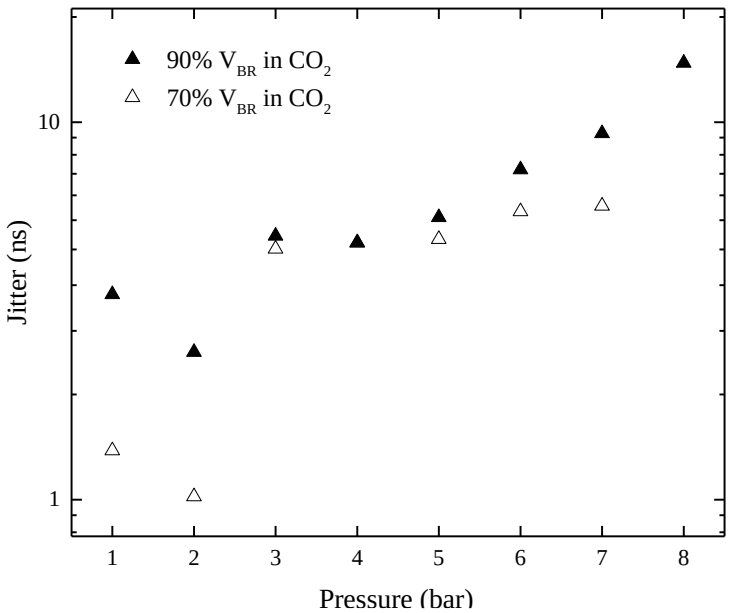

Figure. 6.10. Jitter as a function of the gas pressure for CO_2 for both 70% and 90% dc self-breakdown voltage levels

In the case of a CO_2-filled switch, the jitter increases with increasing gas pressure across the tested pressure range for both 70% and 90% self-breakdown energisation levels, as shown in Figure 6.10. When 90% of the dc self-breakdown voltage is applied across the CO_2-filled switch, the jitter demonstrates a linear rise with increased gas pressure. The jitter increases from ~2.6 ns to ~10.6 ns with an increase in the gas pressure from 1 bar to 8 bar. When the switch was stressed with 70% of the self-breakdown voltage, the jitter was relatively low to ~ (1.1-1.5) ns for low pressures, up to 2 bar, and then there was a significant increase to ~5ns at 3 bar. The jitter fluctuates from ~5 ns to ~5.8 ns with an increase in the gas pressure from 3 bar to 7 bar. The pressures of 7 bar and 8 bar were the maximum operating pressure for N_2 for 70% and 90% of self-breakdown energisation levels, respectively.

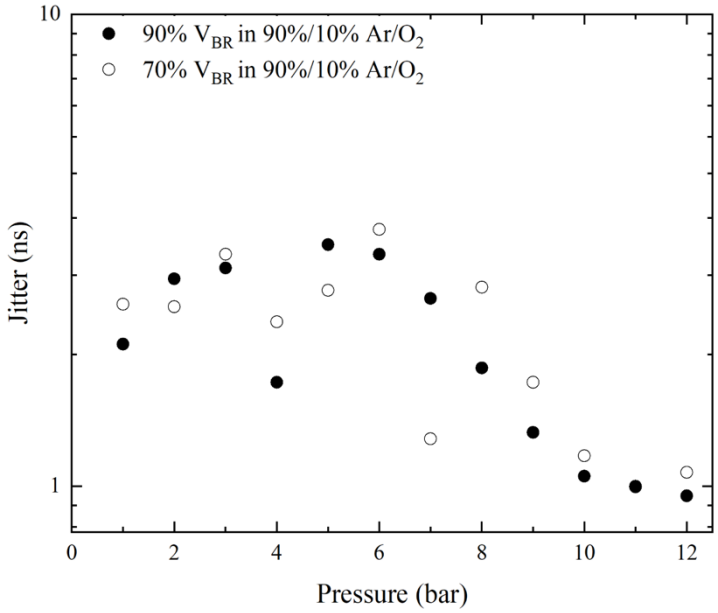

Figure. 6.11. Jitter as a function of the gas pressure for 90%/10% Ar/O_2 mixture for both 70% and 90% dc self-breakdown voltage levels.

Figure 6.11 shows the jitter as a function of the gas pressure for 70% and 90% of the dc self-breakdown voltage applied across the switch as a dc stress voltage filled with the Ar/O_2 mixture. It was found that the 90%/10% Ar/O_2 gas mixture provides the lowest jitter as compared with the other tested gases. The jitter remained within the range from ~1.6 ns to ~3.5 ns for pressures up to 6 bar for both energisation levels. It demonstrated a decreasing tendency for pressures above 6 bar, reaching the values of ~1.2 ns and ~1.1 ns at 10 bar for the 70% and 90% energisation levels, respectively. It is noted that the jitter reduced to a sub-nanosecond level for the gas pressures above 11 bar, when the switch was stressed with 90% of the self-breakdown voltage.

6.5 Weibull Statistical Analysis

Each set of time to breakdown data obtained and presented in the previous section has been statistically analysed using the Weibull statistical analysis (Kiyan et al. 2011) to compare the reliability of the switch when filled with different gases. The Weibull distribution is one of the fundamental distributions used in engineering reliability analysis (Weibull 1951).

The Weibull distribution can be used to find the probability of the closure switch at a specific time. The cumulative distribution function $F(t_{br})$ of the 2-parameter Weibull distribution is given by

$$F(t_{br}) = 1 - exp\left\{-\left(\frac{t_{br}}{\alpha^*}\right)^{\beta^*}\right\} \tag{6.10}$$

where t_{br} is the time to breakdown; α^* (ns) is the scale parameter representing the characteristic time to breakdown, i.e., the time at which breakdown probability is 63%; β^* is the shape parameter that presents the degree of dispersion of a random variable (time to breakdown in this case). The shape parameter is the slope of the regressed line in the Weibull distribution plot. The greater β^* is, the higher probability of breakdown events occurring with the specific time to breakdown. In the case of the 2-parameter distribution, the minimum time at which a breakdown event may occur is assumed to be zero (in the 3-parameter Weibull distribution, this time is used as the location parameter). The assumption that the location parameter is 0s is based on the statistical nature of gas discharge, i.e., it is assumed that a potential breakdown event in the switch may occur at a very short (~0s) time.

The fitting of the Weibull distribution (6.10) to the experimental data and obtaining the scale and shape parameters α^* and β^* of the Weibull distribution was conducted using the Origin Pro Graphing software. The Origin Pro graphing software fitting procedure also provided the upper and lower 95% confidence intervals for the obtained Weibull coefficients. A comparison of the Weibull statistical coefficients obtained for all gases and pressures under both energisation levels was conducted. All Weibull distribution graphs for the time to breakdown are presented in Appendix C.

Figures 6.12-6.15 present the Weibull parameters for the switch filled with air, N_2, CO_2, and Ar/O_2 mixture in the tested pressure range from 1 bar to 12 bar (gauge) for energisation levels equal to 70% and 90% of the dc self-breakdown voltage. Tables 6.2-6.5 present two Weibull parameters for the time to breakdown for all gas pressures and energisation levels equal to 70% and 90% of the DC self-breakdown voltage level.

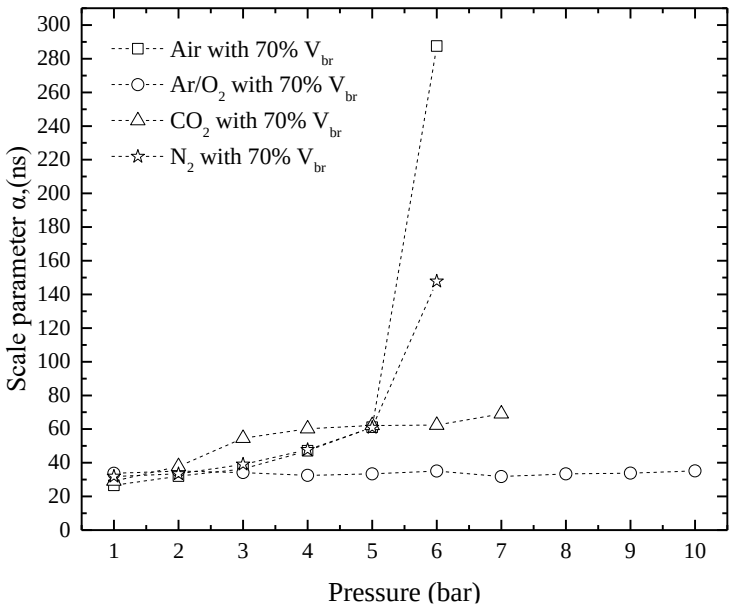

Figure. 6.12. The scale parameter as functions of the gas pressure for 70% (open symbols) of the dc self-breakdown energisation levels. Connection dashed lines are provided for visual guidance only.

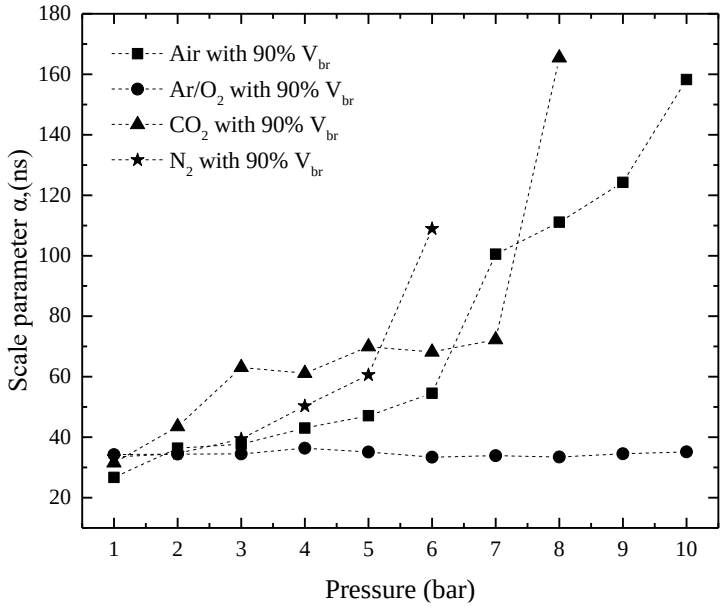

Figure. 6.13. The scale parameter as function of the gas pressure for 90% (solid symbols) of the dc self-breakdown energisation levels. Connection dashed lines are provided for visual guidance only.

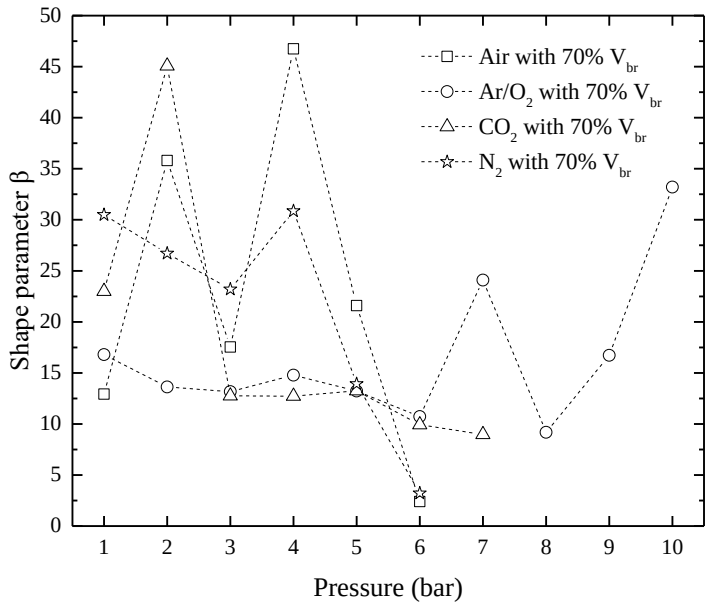

Figure. 6.14. The shape parameter as function of the gas pressure for 70% (open symbols) of the dc self-breakdown energisation levels. Connection dashed lines are provided for visual guidance only.

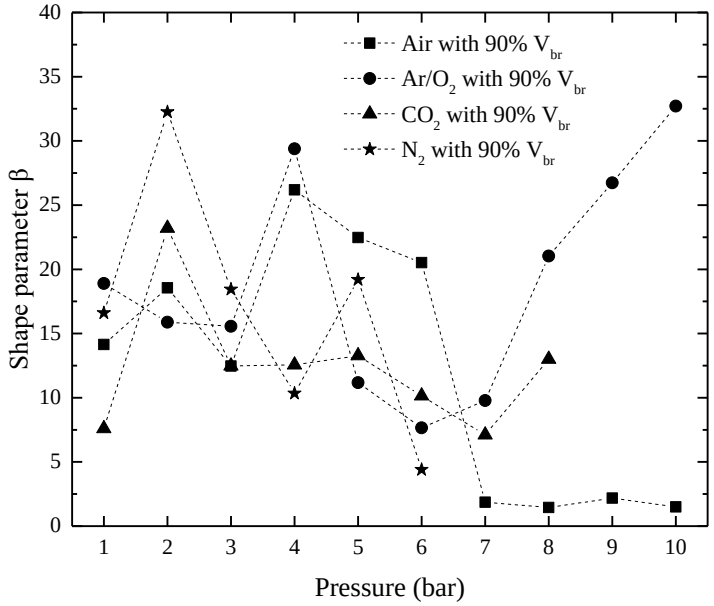

Figure. 6.15. The shape parameter as function of the gas pressure for 90% (solid symbols) of the dc self-breakdown energisation levels. Connection dashed lines are provided for visual guidance only.

Table 6.2 Weibull coefficients for time to breakdown events obtained for air for each tested pressure for both energisation levels

	70% DC stress		*90% DC stress*	
Pressure (bar)	α^*(ns)	β^*	α^*(ns)	β^*
1	26.60	12.93	26.70	14.15
2	32.08	35.80	36.35	18.56
3	36.27	17.54	37.70	12.47
4	47.10	46.75	43.02	26.18
5	61.11	21.60	47.08	22.46
6	287.50	2.40	54.54	20.52
7			100.50	1.85
8			111.12	1.45
9			124.23	2.17
10			158.26	1.50

Table 6.3 Weibull coefficients for time to breakdown events obtained for N_2 for each tested pressure for both energisation levels

	70% DC stress		*90% DC stress*	
Pressure (bar)	$\boldsymbol{\alpha}^*$(ns)	$\boldsymbol{\beta}^*$	$\boldsymbol{\alpha}^*$(ns)	$\boldsymbol{\beta}^*$
1	31.87	30.48	33.40	16.60
2	33.36	26.71	34.63	32.25
3	39.08	23.22	39.42	18.44
4	47.77	30.85	50.28	10.34
5	60.94	13.90	60.58	19.22
6	147.75	3.20	108.90	4.40

Table 6.4 Weibull coefficients for time to breakdown events obtained for CO_2 for each tested pressure for both energisation levels

	70% DC stress		*90% DC stress*	
Pressure (bar)	α^*(ns)	β^*	α^*(ns)	β^*
1	29.15	23	31.52	7.6
2	37.87	45.00	43.54	23.10
3	54.60	12.75	63.07	12.48
4	60.25	12.72	61.11	12.56
5	62.19	13.25	69.97	13.28
6	62.31	9.92	68.15	10.15
7	69.03	8.97	72.23	7.10
8			165.44	13.00

Table 6.5 Weibull coefficients for time to breakdown events obtained for Ar/O_2 mixture for each tested pressure for both energisation levels

	70% DC stress		*90% DC stress*	
Pressure (bar)	α^*(ns)	β^*	α^*(ns)	β^*
1	33.70	16.80	34.24	18.90
2	35.03	13.62	34.40	15.80
3	34.16	13.17	34.50	15.56
4	32.53	14.78	36.36	29.39
5	33.40	13.22	35.10	11.17
6	35.10	10.70	33.40	7.66
7	31.75	24.10	33.88	9.78
8	33.40	9.17	33.46	21.00
9	33.80	16.70	34.50	26.70
10	35.13	33.20	35.16	32.70

From the results in the above Figure and table, it can be seen that for air, N_2, and CO_2, for both energisation levels, the characteristic time to breakdown, α increases with an increase in the gas pressure in the switch.

Figure 6.12 shows that when the switch is filled with N_2 and CO_2, the characteristic time to breakdown rises significantly at the maximum operating pressure, which is the maximum pressure at which breakdown events can occur in these gases. For the Ar/O_2 mixture, the characteristic time to breakdown does not significantly increase with an increase in the pressure in the switch. As discussed in the previous section, for air, N_2, and CO_2, when the operating pressure in the switch increases, the withstand voltage in the gap also increases accordingly, thereby increasing the switching time. For the Ar/O_2 mixture, due to the mutual influence of the pressure and the electric field strength in the entire pressure range, the breakdown time does not show a pronounced tendency or change.

It can be seen from Table 6.2 that, in the case of an air-filled switch, when 70% of the DC self-breakdown voltage is applied across the switch, the characteristic time to breakdown α is different from this time obtained by applying 90% of the DC self-breakdown voltage across the switch. The reason for this is that air is an electronegative gas. When a DC self-breakdown voltage is applied, the electric field in the switching gap results in an intensive collisional ionisation process leading to the gap closure. As the DC voltage applied to the switch increases, the breakdown time /switch closure time decreases. When the switch was filled with other gases, there was no noticeable difference in the characteristic time of breakdown α for 70% and 90% of the DC self-breakdown voltage across the switch.

The shape parameter β^* defines the slope of the cumulative distribution function (6.10) of the Weibull probability distribution plot. A value of β^*, greater than 1, indicates that the switch demonstrates an increasing rate of breakdown events (switch closure events) with the time to breakdown. Tables 6.2-6.5 show that the shape parameters $\beta^* > 1$ have been obtained for all tested gases at all tested pressures for both energisation levels. Therefore, for these values of the shape parameter, the Weibull probability distribution

function is negatively skewed, indicating a higher probability of switch closure (breakdown) events with longer time to switch closure (longer time to breakdown). If the shape parameter $\beta^* = 1$, the rate of switch closure events doesn't depend on the switching time; there is a single combination of the gas pressure and energisation level (air, 10 bar, 90% DC self-breakdown voltage energisation) which provided the shape parameter close to 1 ($\beta^* = 1.5$, Table 6.2).

When the switch was filled with air, N_2 and CO_2, it was shown that for both energisation levels, the shape parameter β^* decreases with an increase in the pressure in the switch. This indicates a higher probability of breakdown (switch closure) events with a longer switching time. In the Ar/O_2 mixture used to fill the switch, for the energisation level equals 90% of the DC self-breakdown voltage, the shape parameter, β^*, shows a rising tendency for gas pressures above 6 bar.

6.6 Conclusions

This Chapter has presented a detailed and systematic investigation into impulse breakdown characteristics of the developed switch filled with all tested gases ("Zero grade" air, CO_2, N_2, and 90%/10% Ar/O_2 mixture) over the gas pressure range 1-12 bar (gauge). The switch was triggered by an external HV trigger impulse. The main electrodes of the switch were pre-energised below the self-breakdown voltage. The time to breakdown and the jitter were obtained, and the effect of different factors such as the gas pressure and the magnitude of DC voltage applied across the switch, was investigated.

The electrostatic field distribution in the switch with the corona electrodes was obtained using the COMSOL Multiphysics package. When the trigger voltage is applied to the central trigger electrode, the electric field strength in the region surrounding the needle tips increases significantly. The maximum value of the electric field is significantly greater than the breakdown field of the gap, which reduces the switching time.

The obtained results show that in the triggered operation regime of the switch, the time to breakdown increases with an increase in the gas pressure for air, N_2, and CO_2 in the complete pressure range for energisation levels of 70% and 90% of the DC self-breakdown voltage. The main reason for this increase in time is the increase in the operating pressure within the switch. For the 90%/10% Ar/O_2 mixture, the breakdown time doesn't change significantly, and it does not show any functional dependency with an increased gas pressure. The breakdown time fluctuates slightly and remains within ~ (31-35) ns for both energisation levels.

It has been shown that when the switch is filled with air, N_2, and CO_2, the jitter increases as the gas pressure increases within the complete gas pressure range for the energisation levels of 70% and 90% of the DC self-breakdown. It was found that the lowest jitter was achieved with the 90%/10% Ar/O_2 gas mixture as compared with the other tested gases: jitter was as low as ~1.2 ns and ~1.1 ns at 10 bar for the 70% and 90% energisation levels respectively. It was found that the jitter reduced to a sub-nanosecond level for the gas (Ar/O_2 gas mixture) pressure above 11 bar when the switch was stressed with 90% of the self-breakdown voltage. It was found that the switch jitter reduces as the gas pressure increases.

A two-parameter Weibull distribution was used to analyse the time to breakdown data to obtain the general tendencies of the Weibull distribution parameters as functions of the gas pressure. The scale parameter α^* represents the characteristic time to breakdown. It was shown that for all test gases except for the 90%/10% Ar/O_2 mixture, the characteristic time of breakdown α^* increases with an increase in the pressure in the switch. When the switch is filled with N_2 and CO_2, the characteristic time of breakdown rises significantly at the maximum operating pressure, which is the maximum pressure at which a breakdown event occurs in these gases. β^* is the shape parameter which defines the slope of the regressed line in the Weibull plot. The greater β^* is, the higher rate of breakdown events (switch closure events) with the time to breakdown (switch closure time). When the switch was filled with air, N_2 and CO_2, it was shown that, for both energisation levels, the shape parameter, β^*, decreases with an increase in the gas pressure in the switch. In the case of the Ar/O_2-mixture, for the

90% energisation level, the shape parameter, β^*, shows a rising tendency with a gas pressure for pressures above 6 bar.

CHAPTER.7 DYNAMIC CHARACTERISTICS OF THE PLASMA CHANNEL

7.1 Introduction

The plasma closing switch starts to transfer the energy after its closure, i.e., when a conductive path is established between its electrodes. The switch closure process can be described in two distinct phases.

(1) After the initial seed electron(s) appear in the gap, these electrons start moving away from the HV cathode, forming an electron avalanche. This avalanche may transform into the streamer before it reaches the opposite electrode. Thus, a weakly ionised discharge channel is established between the two electrodes.

(2) This weakly ionised channel starts to conduct current and very quickly (in less than a few ns) becomes a highly conductive plasma channel, the voltage across the switch collapses rapidly at this moment, and the charge is transferred through the switch into the load. In the case of the RLC circuit, the current which flow through the switch causes the expansion of the plasma channel and reduction of its resistance.

As discussed in Chapter 2, gas-filled PCSs with different topologies have been developed in the past several decades, and their operational characteristics have been analysed. Such analysis and thorough investigation of PCSs are essential for developing and optimising different pulsed power systems (Schaefer, Kristiansen, and Guenther 1990). In specific practical applications in which fast-rising current pulses are used, PCSs required to transfer high currents over a short period and withstand currents with a significant rate of rising, i.e., high *dI/dt*. Therefore, to achieve the optimal operational performance of the pulse power system, it is necessary to investigate further the transient plasma characteristics (the dynamic resistance and inductance) of the plasma channel in the gas-filled plasma closing switch after its closure.

Typically, in fast switching operations, the dynamic resistance and inductance of the plasma channel reduce the peak magnitude and its *dI/dt* (Dick et al. 2000). With the rapid expansion of the plasma channel, its resistance decreases rapidly, thus the conduction current increases rapidly. For the pulse power system to operate efficiently, the transient time for the plasma channel resistance should be reduced to its minimum value. For example, (Cary and Mazzie 1979) discussed transient times shorter than ~1 ns. Also, the dynamic resistance of the plasma channel may affect the voltage collapse time after switch closure, the energy deposition rate and the total energy deposited into the load, and the energy losses during the switching process (Sorensen and Ristic 1977; H. Wang et al. 2012). Therefore, it is desirable to minimise the plasma channel resistance and inductance to improve energy transmission efficiency and reduce power losses in PCS' s. to achieve ultra-fast rise-time (ns) and high peak current impulses (kA).

To summarise, the plasma channel formation phase is not considered here, since most of the energy is deposited during the high current flow into the newly formed conductive channel phase. The discharge is generated by a circuit that includes several components that can affect the deposition of energy into the plasma. The time-dependent resistance and the inductance of the plasma channel formed during the breakdown process are essential parameters to describe the operating performance of the PCS. They are also important parameters for establishing the computational model of the plasma closing switch.

The transient resistance of the plasma channel in gases has been studied for many years, and different models and approaches have been proposed. By analysing plasma resistance equations proposed by Braginiskii (Braginskii 1958), Toepler (Toepler 1927), Rompe and Weizel (Rompe and Weizel 1944), Barannik (Barannik 1975), Popovic (Popovic, Popovic, and Platisa), Demenik (Demenik 1968) and Kushner (Kushner, Kimura, and Byron 1985), it may be concluded that most of the investigators based their models on energy balance equation and principles of thermodynamics. However, a phenomenological constant(s) is required in all cases.

These constants can be obtained experimentally or theoretically. These constants can be obtained by fitting the analytical equation sot the experimental data obtained under specific conditions (i.e., type of gases, pressure, and plasma length).

Toepler first proposed his plasma resistance equation in 1927 (Toepler 1927). The equation was empirically derived from the experimental data. In Toepler's empirical model, the resistance of the plasma channel is proportional to the product of Toepler's coefficient, and the plasma channel length is inversely proportional to the integral of the conduction current. Toepler's coefficient is a proportionality constant that depends upon the nature of the gas and can be obtained by fitting the calculated resistance to the experimental data.

Rompe and Weizel (Rompe and Weizel 1944) proposed a theoretical relationship between the plasma resistance and the current in the circuit based on the energy balance equation with phenomenological constant(s) related to specific experimental conditions.

Braginskii's model (Braginskii 1958) is also based on the energy balance in the spark/plasma channel. Braginskii's method assumes that as the conduction current flows through the plasma channel, the Joule heating of the plasma results in a rapid increase in its temperature and pressure. Thus, the channel expands, driving a strong shock wave into the surrounding gas. Assuming that the pressure at the plasma-gas interface is proportional to the square of the expansion velocity of the plasma channel, the time-dependent radius and the resistance of the plasma channel can be obtained.

Kushner's model (Kushner, Kimura, and Byron 1985) is assumed that the plasma in the plasma channel is in local thermodynamic equilibrium, and the plasma channel expands hydrodynamically. If the time-dependent plasma channel radius is obtained, the dynamic resistance of the spark/plasma channel can be obtained.

In addition, in the studies by Akiyama et al. (Akiyama 1988), Engel et al. (T. G. Engel, Donaldson, and Kristiansen 1989) and Greason (Greason 1999), the transient

resistance of the plasma channel was obtained by using the experimental breakdown current and voltage waveforms. However, because it is difficult to separate the resistive and inductive components in the switch impedance (VanDevender 1978), it is challenging to accurately obtain the voltage drop across the switch and the transient current through the switch.

In this chapter, a lumped-element RLC circuit of the switch was developed and used to model the breakdown process to analyse the post-breakdown current waveform. The transient plasma resistance was obtained based on Kirchhoff's circuit analysis. By applying Kirchhoff's voltage law to this circuit, the equation for the transient post-breakdown resistance was derived and solved using the experimental current waveforms. At the same time, this study also used the Braginskii and Kushner methods to obtain the hydrodynamic radius of the extended plasma channel.

Different models and methods have been evaluated and compared with each other in this Chapter to establish a reliable analytical method for obtaining the plasma channel resistance in PCSs. This analysis can help further develop and optimise advanced gas-filled plasma closing switches for pulsed power applications.

7.2 Experimental Methodology

This section describes an experimental set-up which was used to obtain the post-breakdown current waveform flowing through the plasma channel in order to investigate the resistance of the plasma channel. The switch was filled with different gases: dry air, CO_2, N_2 and the 90%/10% Ar/O_2 mixture. Gas pressure was in the range from 1 bar (gauge) to 10 bar (gauge). Using the experimental data, the lumped element circuits can obtain the time-dependent plasma resistance using Kirchhoff's equation. The plasma resistance can also be obtained based on the transient radius of the plasma channel using the Braginskii model.

Also, the plasma resistance can be obtained using the improved Kushner's analysis approach, the analytical radius of the channel and the experimental breakdown current

waveform. The analysis of the resistances obtained by these methods allows for evaluating the applicability of each of these models for the analysis of the transient post-breakdown resistance and optimisation of the design and operational parameters of PCSs.

The experimental set-up has been developed (its schematic diagram is shown in Figure 7.1) to study the switch's post-breakdown characteristics. In order to obtain a larger discharge current, it is necessary to control the experimental circuit's stray parameters and shorten the connecting cables' length as much as possible.

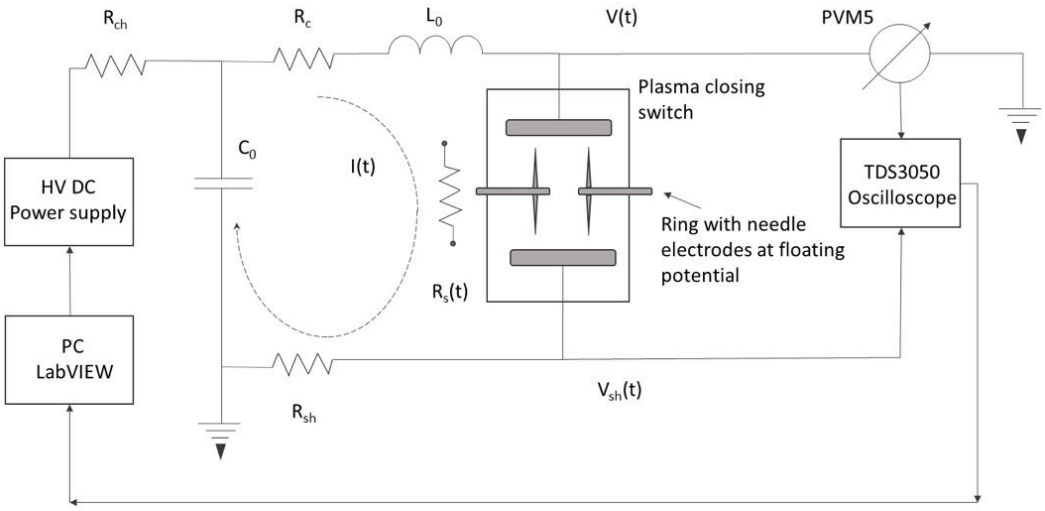

Figure. 7.1. A schematic of the experimental set-up to obtain the post-breakdown current waveforms

A Glassman high voltage DC power supply (EH series, 0-60 kV) was used to stress the upper plane electrode through a 1MΩ charging resistor, R_{ch}. The PC controlled the power supply voltage output via an RS232 interface using a National Instruments DAQ USB-6008 digital acquisition card. The control programme is compiled with the LabVIEW program. The ramp rate of the applied voltage controlled by the PC was 600 V/s. An 80nF high voltage capacitor (Maxwell Ltd), C_0, parallels the circuit's switch. The total inductance of the circuit is represented in Figure. 7.1. by an inductor L_0. A tubular low-inductance current shunt (29V/kA, Samtech Ltd, Scotland) was positioned in series with the spark switch to obtain the transient current. Thus, the post-breakdown circuit could be represented by a lumped RLC circuit, where $R_s(t)$ represents the time-dependent resistance of the PCS, R_c represents the resistance of

circuit components, and R_{sh} represents the resistance of the current shunt. As described in Chapter 3, the central electrode of the switch with corona discharge needles was at a floating potential.

The voltage drops, $V(t)$, across the switch were monitored using a North Star PVM-5 high voltage probe (60kV impulse/100 kV DC, 80 MHz bandwidth, 400 MOhm input resistance, and 12 pF input capacitance) which was connected to the upper plane HV electrode. The voltage drops across the current shunt, $V_{sh}(t)$, were used to obtain the post-breakdown current in the circuit: $I(t) = V_{sh}(t)/R_{sh}$. The post-breakdown current obtained by shunt resistor through the switch were monitored and recorded by a Tektronix TDS 3050 digitising oscilloscope (500 MHz bandwidth, 5 GS/s sampling rate) via a 10dB attenuator.

Breakdown tests were conducted using all gases in the pressure range from 1 to 10 bar (gauge) using 1bar increments. The breakdown voltage and current waveforms were obtained in each test and recorded for 10 consecutive breakdown events without changing the gas in the PCS. The gas control system used in the present work to manage the gas environment in the PCS includes a designed pneumatic control board via a precision digital pressure regulator and a rotary vacuum pump to evacuate the switch before filling it with a fresh portion of gas. A digital pressure controller, Alicat PC-1500PSIG-D, sets and controls the gas pressure in the switch. After each set of experiments, the gas in the PCSs cell was evacuated, and the switch was filled with the fresh portion of gas for the next test.

7.3 Analytical Model of Plasma Channel

When a breakdown occurs in the switch, the voltage collapses from its (pre-)breakdown value, V_{br}, to the voltage value across the thermalized plasma channel, V_{th}. At this moment, the conduction current starts to flow through the plasma, resulting in current and voltage oscillations due to the underdamped behaviour of the RLC circuit. A typical example of the transient current through the air-filled switch and the voltage collapse across this switch is shown in Figure 7.2.

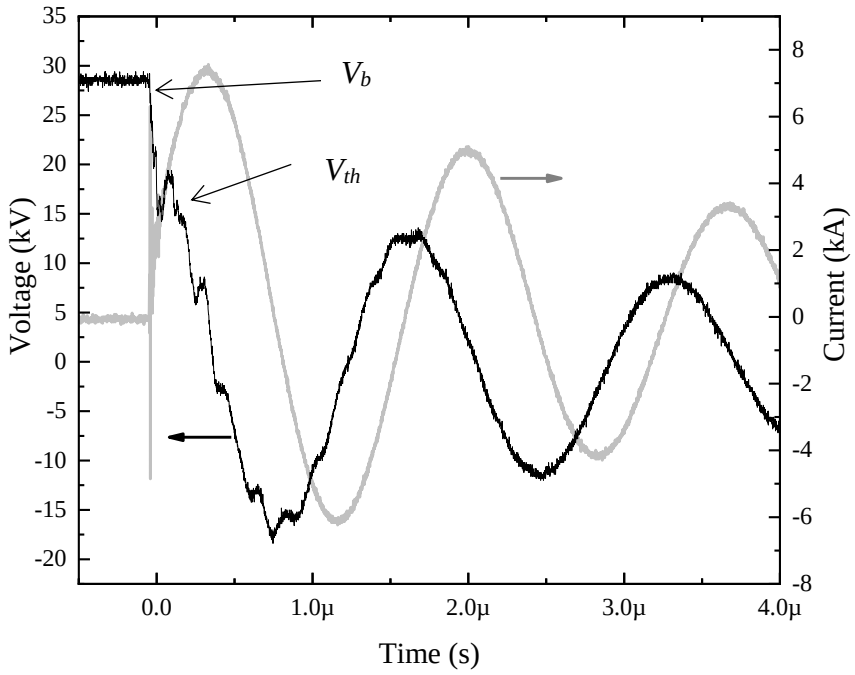

Figure. 7.2. Experimentally obtained post-breakdown current and voltage waveforms of the breakdown in the air-filled switch at 6 bar.

The transient process in the gas-filled plasma closing switch typically can be described as the transient process in the RLC circuit base on the capacitive discharge. When the final breakdown plasma streamer bridges the inter-electrode gap, the conduction current starts to flow through this plasma channel, resulting in its fast Joule heating. The post-breakdown circuit, which includes the current through the plasma channel and the pulse driving circuit, can be described using a lumped-element RLC equivalent circuit shown in Figure 7.3.

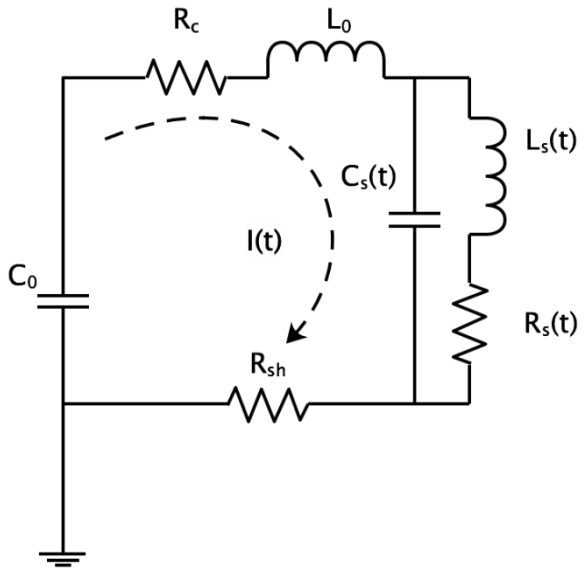

Figure. 7.3. Equivalent circuit during a breakdown event. R_c models the resistance of circuit components, R_{sh} represents the resistance of the current shunt, the inductance of the circuit is represented by an inductor L_0, C_s is the capacitance of the plasma channel, and the plasma channel is modelled by a resistance $R_s(t)$ and an inductance $L_s(t)$.

When the switch is open, the electric charge is stored in capacitance C_0 given by:

$$C_0 = \frac{Q}{V} \tag{7.1}$$

where Q is the charge stored in the capacitor; V is the voltage across the capacitor terminals.

The switch electrodes also form a capacitance, C_s which is typically very small, from several pF to 10s pF and can be neglected in the transient process analysis.

It is a challenging task to obtain the transient inductance of the plasma channel. When the streamer crossed the gap, and the conductive channel bridged the inter-electrode gap, the inductance of the channel can be approximated by the inductance of a conducting wire. This inductance can be calculated using the equation provided in (Grover 2004):

$$L_s(t) = l\frac{\mu_0}{2\pi}\ln\left(\frac{a_c}{a(t)} - \frac{3}{4}\right) = 2l\ln\left(\frac{a_c}{a(t)} - \frac{3}{4}\right) \quad (7.2)$$

where $L_s(t)$ is the transient inductance in the plasma channel (in nH); l is the length of the plasma channel (in cm); a_c is the radius of the current return path (in cm); $a(t)$ is the temporal plasma radius of the plasma channel (in cm). The temporal plasma radius is challenging to measure accurately. The plasma inductance is significantly smaller than L_0 and can be neglected. Multi-channelling (formation of multiple parallel breakdown channels) can effectively reduce the inductance of the plasma channel so that the rise time of the current pulse is faster.

The breakdown process takes place in two distinct phases. The plasma streamer is developed in the first phase and propagates across the gap between the electrodes. The second phase begins when the established plasma channel starts to conduct the current and expands into the surrounding gas. When the conductive plasma channel is formed between the energised and grounded electrodes, the transient pre-breakdown phase of the discharge process is completed. When the plasma channel in the gap between the electrodes forms a bridge, along with the rapid expansion of the plasma channel, the resistance of the channel decreases rapidly, and the conductive current flowing through this channel increases rapidly, resulting in intense Joule heating and thermalisation of the channel. The resistance of the plasma channel decreases rapidly during the first quarter of the current oscillation and reaches its minimum value when the current through the channel has its maximum value. Therefore, the post-breakdown dynamic resistance of the plasma channel in the PCS is affected by the post-breakdown oscillation of the charge in the circuit.

All plasma resistance models described in the literature assume that the current in the plasma channel is related to its resistance. This is because the mobility and drift velocity of the charged particles (electrons and ions) determines the resistivity of the plasma. Therefore, as the drift velocity of the charged particles increases, the resistance of the plasma channel drops, and the current flowing through the channel rise.

In the ideal discharge process, the transient resistance drops from a very high value to zero in a very short time interval as the current in the plasma channel reaches its maximum. However, the plasma resistance depends on the conduction current and has a close relationship with the size of the plasma channel, plasma temperature, and pressure. The radius of the plasma channel expands as the energy increases, which is the essential factor which affects the plasma resistance. The plasma channel has a minimum radius at the initial stage (which could be less than a millimetre), and this radius significantly increases during the energy deposition stage. This directly affects the resistance of the plasma channel.

There are several approaches to modelling the dynamic behaviour of the post-breakdown resistance. The Toepler approach is a phenomenological model in which the resistance of the plasma channel is proportional to the product of the Toppler's coefficient and the plasma channel length and inversely proportional to the integral of the transient current. Toepler phenomenological equation was empirically derived based on experimental data.

The Rompe-Weizel and Vlastós models are deduced from the energy balance equation for the plasma channel with a fixed channel radius. The Braginskii model assumes that the channel conductivity remains constant, but its resistance reduces during the hydrodynamic channel expansion. Kushner's model assumes that the plasma in the plasma channel is in its local thermodynamic equilibrium state, and the plasma channel expands hydrodynamically.

These approaches have mainly been used to model the transient plasma resistance in the case of overdamped current oscillation in the circuit. However, in some practical cases, to optimise the operational characteristics of plasma closing switches, it is required to have detailed information on the dynamic behaviour of the plasma channel resistance in the case of underdamped current oscillations in the post-breakdown circuit. This section investigates the applicability of the discussed approaches and the method based on Kirchhoff's voltage law to the transient underdamped process.

7.3.1 Analysis of Under-damped RLC Circuit

In the analysis conducted in this section, it was assumed that the resistance and inductance of the plasma channel are constant during the formation of the plasma channel. Therefore, the discharge initially propagates from the HV electrode toward the ground electrode when the plasma closing switch is triggered. The duration of the propagation phase is closely related to the streamer velocity. Therefore, the propagation phase typically lasts hundreds of nanoseconds, during which the conductive current flows through the newly formed channel. In the plasma channel expansion stage, the plasma channel expands rapidly. Thus, the resistance of the plasma channel decreases rapidly and reaches a stable value. The resistance of the plasma channel can be modelled using a constant resistance value. Therefore, the conductive current flowing through the plasma channel can be described by the following equation:

$$I(t) = I_0 \sin \omega t \, e^{-\alpha t} \tag{7.3}$$

where I_0 is the constant parameter which is related to the maximum current in the circuit (in A), α is the dampening constant (in 1/sec) and ω is the angular frequency (in rad/sec), all of which can be obtained from the experimental waveform. The post-breakdown current waveforms in the circuit were obtained using the voltage drop across the current viewing resistor. The current constant, I_0, in Equation (1) can be expressed as:

$$I_0 = \frac{U_{th}}{\omega L} \tag{7.4}$$

where U_{th} is the voltage across the plasma channel when the plasma becomes thermal; L is the total inductance of the discharge circuit loop, which is the sum of the inductance of the circuit and the inductance of the plasma channel. The dampening constant α and the angular frequency ω for this circuit are:

$$\alpha = \frac{R_{total}}{2L} \tag{7.5}$$

$$\omega^2 = \frac{1}{LC} - \left(\frac{R_{total}}{2L}\right)^2 \tag{7.6}$$

where R_{total} is a sum of the constant resistance of the circuit and the constant resistance of the plasma channel. According to the equation (7.3), the oscillation period of current in the circuit can be obtained as:

$$\Delta T = \frac{2L}{R_{total}} \ln \frac{I_0}{I_1} \tag{7.7}$$

where I_0 is the maximum peak current; I_1 is the second peak current after the first oscillation period. Substituting $\Delta T = \frac{2\pi}{\omega}$ into equation (7.7) can calculate the total inductance L in the circuit loop:

$$L = \frac{\Delta T^2}{\left[4\pi^2 + \left(\ln \frac{I_0}{I_1}\right)^2\right] C} \tag{7.8}$$

The total resistance R_{total} can be obtained from equation (7.7):

$$R_{total} = \frac{2L}{\Delta T} \ln \frac{I_0}{I_1} \tag{7.9}$$

In the present experimental system, the nominal capacitance of the capacitor in the circuit is 80 nF and the nominal inductance of the capacitor is ~30 nH. The inductance of electrodes is ~60 nH. This value was obtained using the equation for the inductance of a single conductor provided by (Grover 2004). The measuring circuit contains two stainless steel bars with a thickness of 3mm, the lengths of which are respectively 100mm and 200mm and two cables whose radius is 1.5mm with a length of 1500mm. The total inductance of the transmission line was calculated using equations provided

by (Grover 2004), with topological parameters obtained from the experimental set-up, and found to be ~750 nH.

The resistance of the plasma closing switch includes the structure resistance and the plasma channel resistance when the switch is discharged. The structure resistance can be calculated according to the electrode size and the resistivity of the electrode material. The structural resistance of the switch mainly includes the main electrode resistance and the resistance of the trigger electrode. The skin effect of the conductor needs to be considered when calculating the structural resistance of the switch. The skin depth, d, calculation equation of the metal conductor is:

$$d = \sqrt{\frac{\rho}{\pi \mu_0 \mu_r f}} \tag{7.10}$$

where μ_0 is the permeability of free space; μ_r is the relative magnetic permeability of the conductor; ρ (in $\Omega \cdot$ m) is the resistivity of the medium; f (in Hz) is the frequency of the current. The effective current-carrying area of the switch electrode is:

$$S_f = \pi(D - d)d \tag{7.11}$$

where D is the diameter of the electrode. The formula used for obtaining the resistance is:

$$R = \frac{l\rho}{S_f} \tag{7.12}$$

The resistance of the two electrodes was found to be ~0.1mΩ, so the structure resistance of the electrodes is very small and can be neglected.

The equivalent circuit resistance was obtained using the transient current oscillation with no plasma closing switch, i.e., the short-circuit current waveform. This equivalent circuit resistance was obtained by fitting the exponentially decaying sinusoidal

oscillation, Equation (7.3), to the experimental short-circuit current waveforms. This procedure used ten individual short-circuit current waveforms, providing 0.35Ω as an average value for the equivalent circuit resistance. Its standard deviation is 0.02 Ω.

When calculating the inductance and resistance of the plasma channel, the total inductance and resistance of the discharge circuit should be subtracted from the inductance of the capacitor and the inductance and resistance of the circuit.

The analysis in this section assumes that the resistance of the plasma channel is constant and does not change with time. However, the resistance of the plasma channel changes with time. The resistance at the beginning of the discharge is tremendous. It decreases with the increase of the current flowing through the plasma channel, finally tends to a minimum value, and then returns to the great extreme value after the discharge. Therefore, in the subsequent analysis, the resistance of the plasma channel will be considered a time-varying resistance.

7.3.2 The Braginskii Model for the Plasma Channel

Braginskii's model is based on the assumption that the Joule heating of the plasma channel takes place as the current flows through the initially very narrow plasma channel. During this process, its temperature, pressure and ionisation rise rapidly, expanding the channel with supersonic velocity and driving a robust cylindrical shock wave into the surrounding gas.

The plasma channel expands, and its radius increases which, according to (Braginskii 1958), can be obtained by:

$$a(t)^2 = \left(\frac{4}{\pi^2 \rho_0 \xi \sigma}\right)^{\frac{1}{3}} \int_{t0}^{t} I(t)^{\frac{2}{3}}\, dt \tag{7.13}$$

where σ is the electrical conductivity of the plasma-filled channel; ρ_0 is gas density (this model assumes that σ and ρ_0 have constant values during the energy deposition

stage); ξ is also approximately constant, which depends on the gas properties- it is related to the effective ratio of specific heats, $\bar{\gamma}$, assuming that the plasma in the breakdown channel can be considered to satisfy the ideal gas approximation. According to (Hussey et al. 1999), $\bar{\gamma}$ = 1.25 for common gases such as air and N_2. An expression for ξ was also obtained in (Braginskii 1958):

$$\xi = K_p\left(1 + \frac{1}{\bar{\gamma}-1}\frac{1}{\dot{a}^2}(\ddot{a}a + \dot{a}^2)\right) \cong K_p\frac{\bar{\gamma}}{\bar{\gamma}-1} \tag{7.14}$$

Braginskii assumed that K_p=0.9. Thus, for air and nitrogen, ξ=4.5; In the case of CO_2 and the Ar/O_2 mixture, ξ values are 6.9 and 2.26, respectively.

In the Braginskii approach, it is assumed that the conductivity of plasma is constant during the entire transient process. Although it is known that the plasma conductivity can vary during the transient current oscillation in the plasma channel, it was shown by (Braginskii 1958) that these differences are not significant. The plasma conductivity used in (7.13) could be considered to be constant.

The plasma temperature of the spark discharge is approximately ~(5000–6500)K (McGarvey 2017). Using the Spitzer model (Spitzer 2006), which associates the plasma temperature and the electrical conductivity of the plasma, the plasma channel conductivity was calculated to have a fixed value of ~5000 S/m for calculations conducted in the present work.

The time-dependent resistance of this channel, which is obtained by the Braginskii approach, is given as:

$$R_{sB}(t) = \frac{l}{\sigma\pi a(t)^2} \tag{7.15}$$

where *l* is the length of the plasma channel. When the plasma channel is established in the initial stage, current flows through the plasma channel. The channel radius at

this initial stage has little effect on the time-dependent resistance of the plasma channel obtained by the Braginskii method.

7.3.3 The Kushner Model for Plasma Resistance

In the Kushner model, the dynamic resistance of the plasma breakdown channel is calculated by assuming that the plasma in the breakdown channel is in the local thermodynamic equilibrium during the plasma channel expansion stage, and the channel expands hydrodynamically. Since the Kushner model assumes a high degree of ionisation in the plasma channel, it avoids the limitations of the Spitzer model. In (Kushner, Kimura, and Byron 1985), the Kushner equation of the time-dependent resistance of the plasma channel is expressed as:

$$R_{sK}(t) = \beta K l \left(\frac{p^3}{A(t)^2 I(t)^6} \right)^{\frac{1}{5}} \tag{7.16}$$

where l is the length of the plasma channel (in cm); p is the initial gas pressure (in Pa); $A(t) = \pi a(t)^2$ is the plasma channel cross-sectional area (in cm^2), where $a(t)$ was calculated using Braginskii's equation (7.13); The coefficient β is expressed as the non-uniformity of the electric field, which is described in (2.34). It is the ratio between the mean electric field strength in the uniform field in a parallel-plane topology and the maximum electric field strength at the point electrode in a point-plane topology. In (Santamaria and Román 2013), it was found that β is proportional to El/p, where E is the electrical field strength at the breakdown. The non-uniformity of the electric field, β, was derived in QuickField electrostatic software by modelling the point-plane topology and was found to be ~1/11. K is a Kushner constant. Values of K were obtained (Lister, Li, and Godyak 1996; Kushner, Kimura, and Byron 1985) for a quasi-uniform electric field and found to be ~24.7.

7.3.4 The RLC Post-Breakdown Circuit Model

When the plasma channel in the gap between the electrodes forms a bridge, along with the rapid expansion of the plasma channel, the conductive current flowing through this plasma channel increases rapidly, resulting in intense Joule heating and thermalisation in the channel. The entire system, including the plasma channel and pulse driving circuit, can be described as an equivalent circuit using RLC-lumped elements. Kirchhoff's equation analysed the transient current *I(t)* flowing in the circuit for this RLC equivalent circuit. Thus, the Kirchhoff equation for the post-breakdown current oscillation is given by:

$$\frac{d^2I(t)}{dt^2} + \frac{1}{L}\frac{d}{dt}(I(t) \cdot R_{total}) + \frac{I(t)}{L \cdot C_0} = 0 \tag{7.17}$$

where R_{total} is the sum of the resistance of the circuit, the current shunt resistance, and the plasma resistance, $R_{total} = R_c + R_{sh} + R_s(t)$, C_0 is the capacitance of the circuit, and L is the sum of the inductance of the circuit and the plasma inductance, $L = L_0 + L_s(t)$. In addition, define R_{st} as the stray circuit resistance of the post-breakdown circuit where $R_0 = R_c + R_{sh}$.

By solving the Kirchhoff equation of the RLC equivalent circuit, the time-dependent plasma resistance $R_s(t)$ can be obtained. The Kirchhoff equation for $R_s(t)$ is given by:

$$R_s(t) = \frac{1}{I(t)}\left[U_{th} - \frac{d}{dt}LI(t) - \frac{1}{C_0}\int_0^t I(t)dt - R_0 I(t)\right] \tag{7.18}$$

where U_{th} is the voltage across the plasma channel when the plasma becomes thermal. At this moment, the conduction current starts to flow through the plasma; *I(t)* is the transient current in the circuit; C_0, L_0, and R_0 are the equivalent circuit capacitance, inductance and resistance, respectively.

7.3.5 Dimensionless Lumped RLC Circuit Model

The modelling described in the previous sections uses equations (7.17) and the various models described above to describe the plasma channel resistance. We can define dimensionless variables to describe the experimental current curve through an optimised fitting.

Making use of (7.13) and (7.15), we can re-write (7.17) in the form:

$$\frac{d^2I}{dt^2}+\frac{l}{\sigma\pi k^{\frac{1}{3}}}\frac{1}{L}\frac{1}{\int dtI^{\frac{2}{3}}}\frac{dI}{dt}-\frac{l}{\sigma\pi k^{\frac{1}{3}}}\frac{1}{L}\frac{I^{\frac{5}{3}}}{\left(\int dtI^{\frac{2}{3}}\right)^2}+\frac{R_{st}}{L}\frac{dI}{dt}+\frac{I}{LC_0}=0 \qquad (7.19)$$

Setting $k=\frac{4}{\pi^2\rho_0\xi\sigma}$. We define the dimensionless variables: $z=\frac{I}{I_0}$; $x=\frac{t}{\tau_0}$; $R_{STN}=\frac{R_{st}}{R_N}$. At the same time, we introduce normalised time, current, resistance and constant, P: $\tau_0=\sqrt{LC}$; $I_0=U_{\text{th}}\sqrt{\frac{C}{L}}$; $R_N=2\sqrt{\frac{L}{C}}$; $P=\frac{l}{\sigma\pi k^{1/3}}\frac{1}{LI_0{}^{2/3}}$. The z is the normalised current with I_0, the reference current, x is the normalised time with, τ_0, the reference timescale, and R_{STN} is the normalised stray resistance. Thus, the normalised dimensionless Kirchhoff equation can be obtained:

$$\frac{d^2z}{dx^2}+P\frac{1}{\int dxz^{\frac{2}{3}}}\frac{dz}{dt}-P\frac{z^{\frac{5}{3}}}{\left(\int dxz^{\frac{2}{3}}\right)^2}+2R_{STN}\frac{dz}{dx}+z=0 \qquad (7.20)$$

The time-dependent resistance and the channel radius can be calculated using experimentally obtained current oscillation expressed in dimensionless variables defined above. The initial conditions on the later channel expansion are required for the solution of (7.20). At *t = 0*, the current in the discharge channel is zero, and the capacitor has a maximum charge. We can solve this differential equation (7.19) with initial conditions at *t = 0*: $I(t)|_{t=0}=0,\frac{dI(t)}{dt}\Big|_{t=0}=\frac{U_{th}}{L}$. For the normalised dimensionless equation (7.20), the initial conditions at *x = 0*: $z(0)=0$, $\frac{dz(t)}{dx}\Big|_{x=0}=1$. The circuit parameters can be known through calculations and experiments. The

thermal voltage, U_{th}, across the plasma channel can be measured when the plasma channel in the gap between the electrodes forms a bridge. For the given parameters and initial conditions, the dimensionless equation can be solved using the Runge-Kutta method (in Appendix).

7.4 Results

In the analysis provided in the previous section, the plasma resistance was related to the current in the circuit. The dynamic resistance of the plasma channel can be obtained by dynamically solving Kirchhoff's equation of these lumped element circuits. Based on Braginskii's hydrodynamic model for plasma resistance, the dynamic radius of the plasma channel can obtain. The dynamic resistance of the plasma channel based on various models can be obtained by fitting the reconstructed current waveform obtained by the analysis with the experimental current waveform.

7.4.1 Comparison with Reconstructed Current and Experimental Data

As shown in Figure.7.4, the oscillatory behaviour of the current can be described by the underdamped oscillation in the RLC circuit. The reconstructed current waveform from the normalised dimensionless lumped model, as defined by (7.20), shows a good agreement with the obtained experimental current, especially in the first half of oscillation.

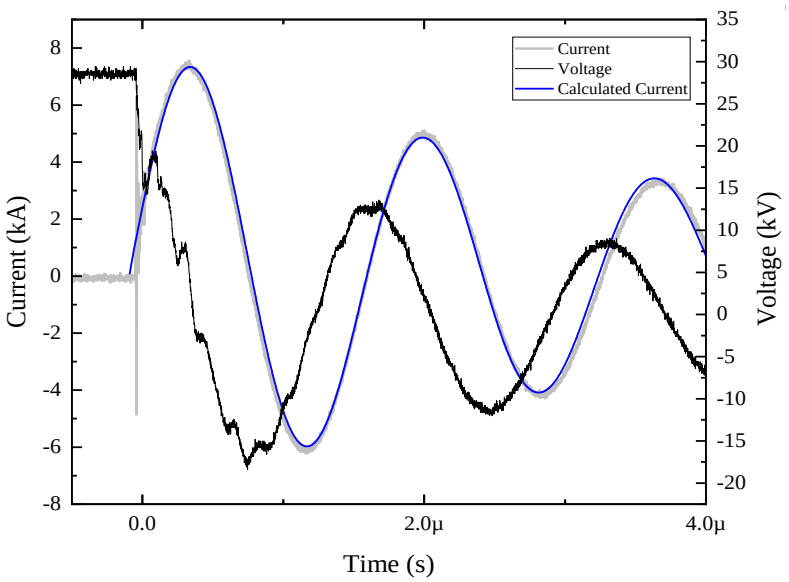

Figure. 7.4. Comparison of experimentally obtained post-breakdown current and the calculated current from the normalised dimensionless lumped model of breakdown in the air-filled switch at 6 bar.

7.4.2 Constant Resistance and Inductance of RLC Circuit

As mentioned previously, the analysis of the post-breakdown current waveform allows for its characteristics, such as the relative peak value of the current oscillation and the time difference between peaks. These parameters can be used to evaluate the dampening constant α (in 1/sec) and angular frequency ω (in rad/sec).

The total inductance of the *RLC* circuit formed during the breakdown can be calculated using equation (7.8). Then, by subtracting the inductance of the circuit, the inductance of the plasma channel is obtained. The nominal inductance of the capacitor is ~30 nH. The inductance of electrodes is ~60 nH obtained by the equations provided by (Grover 2004). The measuring circuit contains two stainless steel bars with a thickness of 3mm, the lengths of which are respectively 100mm and 200mm and two cables whose radius is 1.5mm with a length of 1500mm. The total inductance of the transmission line is ~750 nH, calculated using the equations provided by (Grover 2004), with topological parameters obtained from the experimental set-up. Once the inductance of the *RLC* circuit is obtained by using Equation (7.9), the total resistance of the *RLC* circuit during the transient post- breakdown process can also be evaluated.

Table 7-1 provides the inductance of the *RLC* circuit obtained by analysing the post-breakdown current waveform for all test gases within the test pressure range.

Table 7.1. The inductance of the RLC circuit for all tested gases

Pressure (Bar)	**Air**	**N_2**	**CO_2**	**90%/10% Ar/O_2**
1	867.5 ±1.20 nH	856.8±0.95 nH	868.7±1.38 nH	852.7±0.83 nH
2	863.8±1.08 nH	857.2±0.96 nH	865.3±1.54 nH	853.3±0.80 nH
3	862.2±1.15 nH	856.7±0.9 nH	866.2±1.50 nH	852.5±0.84 nH
4	865.3±1.18 nH	861.8±0.93 nH	865.3±1.56 nH	852.4±0.81 nH
5	857.0±1.15 nH	858.4±1.00 nH	862.0±1.48 nH	851.2±0.84 nH
6	856.9±1.08 nH	856.2±0.98 nH	861.4±1.45 nH	851.5±0.87 nH
7	852.5±1.00 nH	854.0±0.95 nH		852.2±0.85 nH
8		855.5±0.90 nH		850.7±0.82 nH
9		853.7±0.90 nH		850.4±0.83 nH
10		852.5±0.92 nH		850.5±0.87 nH

It can be seen from Table 7-1 that for all gases, the total inductance of the RLC circuit, which includes the plasma closing switch, is ~850 nH. This is two orders of magnitude larger than the inductance of the plasma channel obtained by equation (7.2).

Table 7-2 provides the resistance of the *RLC* circuit obtained for all tested gases within the test pressure range.

Table 7.2. Resistance of the RLC circuit for all tested gases

Pressure (Bar)	Air	N_2	CO_2	90%/10% Ar/O_2
1	0.823±0.07 Ω	0.837±0.05 Ω	0.825±0.11 Ω	1.133±0.09 Ω
2	0.785±0.05 Ω	0.795±0.05 Ω	0.772±0.10 Ω	0.907±0.07 Ω
3	0.707±0.03 Ω	0.718±0.04 Ω	0.720±0.09 Ω	0.781±0.07 Ω
4	0.658±0.04 Ω	0.630±0.05 Ω	0.653±0.09 Ω	0.698±0.05 Ω
5	0.620±0.05 Ω	0.606±0.04 Ω	0.668±0.07 Ω	0.680±0.06 Ω
6	0.587±0.03 Ω	0.623±0.03 Ω	0.607±0.07 Ω	0.647±0.06 Ω
7	0.543±0.04 Ω	0.644±0.04 Ω		0.624±0.05 Ω
8		0.587±0.04 Ω		0.636±0.06 Ω
9		0.541±0.03 Ω		0.593±0.04 Ω
10		0.524±0.03 Ω		0.564±0.04 Ω

It can be seen from Table 7-2 that for all gases, the total resistance of the RLC circuit gradually decreases as the pressure increases. The total resistance value for the 90%/10% Ar/O_2 mixture-filled gaps is higher under the same pressure as other tested gases.

7.4.3 Dynamic Radius of the Plasma Channel

According to the Braginskii model, the conductivity of the channel remains constant. At the same time, the radius will increase with the energy deposit as the current flows through the plasma channel during the discharge process. The reconstructed experimental post-breakdown current waveforms are used to numerically solve the equation (7.13) to obtain the corresponding time-dependent plasma channel radius.

Figure. 7.5 shows an example of the plasma channel radius calculated through the entire current oscillation period under dry air at a pressure of 4 bar. The first half cycle of the reconstructed current is ~900 ns, mainly because the frequency of the current oscillation is determined by the circuit capacitance and inductance in the model. In all test gases, the radius of the plasma channel reaches its first maximum in the first half of the current. It can be seen in Figure. 7.5. that the plasma radius of the plasma channel increases rapidly during the first half of the current oscillation, and after

several current oscillations, it tends to increase at a relatively gentle rate and finally tends to be constant. The plasma channel radius formed in the air can be estimated by light intensity measurements (X. Li et al. 2014; Castera 2015). This optical method confirms the dynamic behaviour obtained in the present analytical analysis.

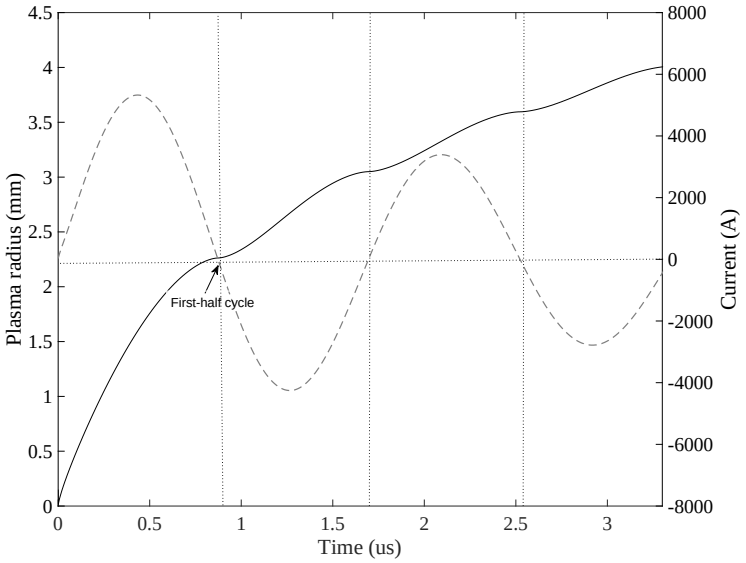

Figure. 7.5. The plasma channel radius obtained by (7.13) for breakdown in dry air at 4 bar; solid line: the plasma channel radius; dash line: post-breakdown current.

The obtained time-varying plasma channel radius for all the tested gases in the pressure range from 1 bar up to 10 bar is plotted in Figure. 7.6. Under each test condition, the current waveforms of 10 consecutive breakdown events were obtained, and the data from these waveforms were averaged. This average waveform is then used to calculate the time-dependent plasma channel radius using (7.13).

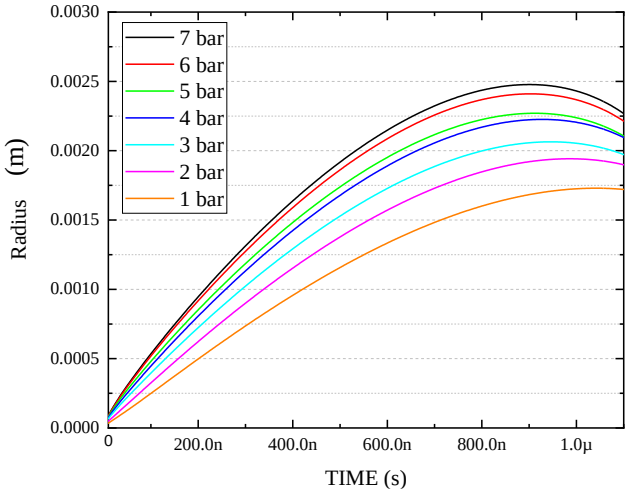
0.0030
0.0025
0.0020
0.0015
0.0010
0.0005
0.0000
Radius (m)
7 bar
6 bar
5 bar
4 bar
3 bar
2 bar
1 bar
0
200.0n
400.0n
600.0n
800.0n
1.0µ
TIME (s)

(a)

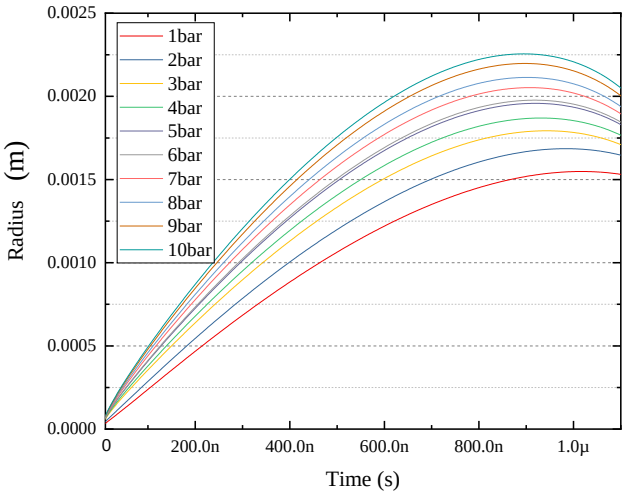
0.0025
0.0020
0.0015
0.0010
0.0005
0.0000
Radius (m)
1bar
2bar
3bar
4bar
5bar
6bar
7bar
8bar
9bar
10bar
0
200.0n
400.0n
600.0n
800.0n
1.0µ
Time (s)

(b)

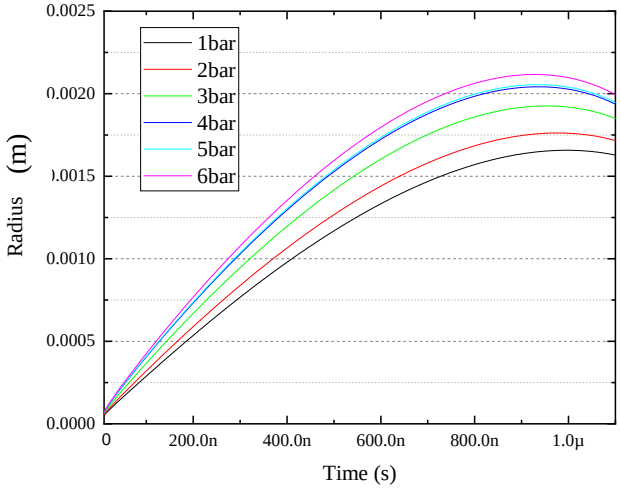
0.0025
0.0020
0.0015
0.0010
0.0005
0.0000
Radius (m)
1bar
2bar
3bar
4bar
5bar
6bar
0
200.0n
400.0n
600.0n
800.0n
1.0µ
Time (s)

(c)

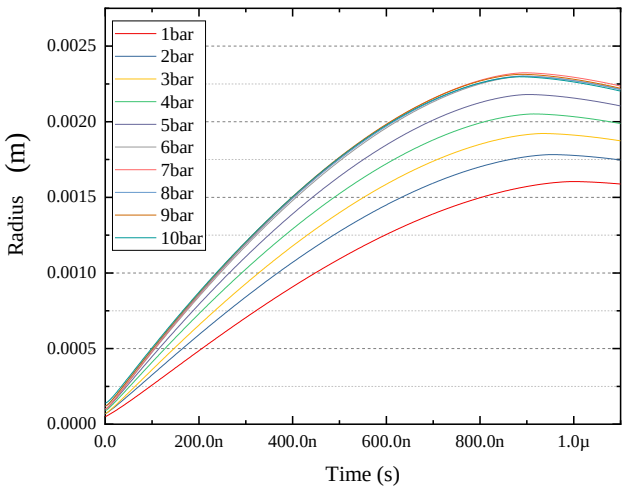

(d)

Figure. 7.6. Calculated time-varying plasma channel radius for different gas pressure within all the tested gases. (a): dry air; (b): N_2; (c): CO_2; (d): 90%/10% Ar/O_2.

Figure. 7.7 is a cumulative graph which includes plasma radii in all tested gases, demonstrating the time-varying plasma channel radii as functions of the gas pressure at the specific time after breakdown, 900 ns.

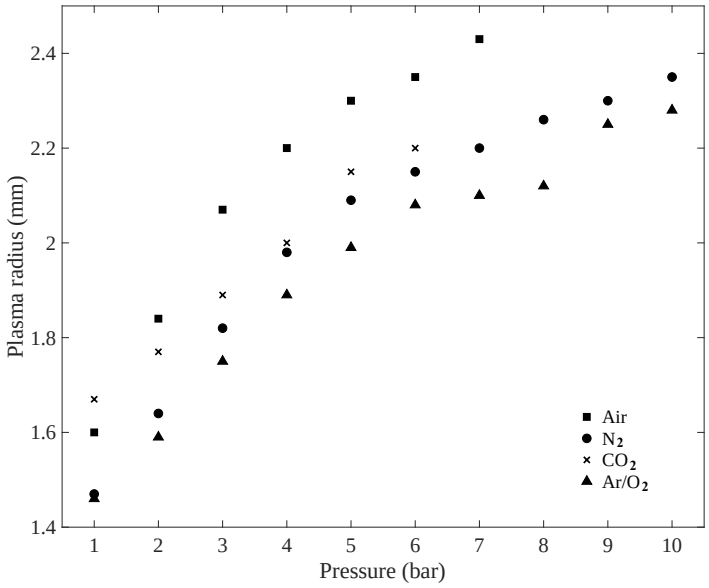

Figure. 7.7. Calculated time-varying plasma channel radii at 900 ns after a breakdown as a function of the gas pressure for all tested gases.

It can be seen in Figure. 7.7 that the time-varying plasma channel radius increases with the gas pressure increase. For all the test gases, the plasma channel radius of dry air is the largest under the same pressure, followed by CO_2 and N_2. At the same time, the 90%/10% Ar/O_2 mixture has the smallest time-varying plasma channel radius under the same conditions. In addition, it is found that there is almost no difference in the plasma channel radius when the pressure of 90%/10% Ar/O_2 mixture is above 6 bar. According to the analysis, the calculated plasma channel radius shows a functional dependence on the gas pressure, similar to the dependence of the self-breakdown voltage on the gas pressure in the previous chapter 4. This is mainly due to the higher breakdown voltage under higher pressure, and more energy is transferred to the plasma channel, leading to more significant Joule heating and channel expansion in the plasma.

7.4.4 Time-Dependent Inductance of the Plasma Channel

The transient inductance of the plasma channel is related to the size of the discharge channel. This inductance can be calculated using the equation (7.2) provided in (Grover 2004). The time-dependent plasma channel radius used in (7.2) can be calculated from Braginskii's equation (7.13) discussed in Section 7.3.2. Figure. 7.8 shows the time-dependent plasma inductance in the breakdown channel for all the tested gases over the pressure range from 1 bar up to 10 bar.

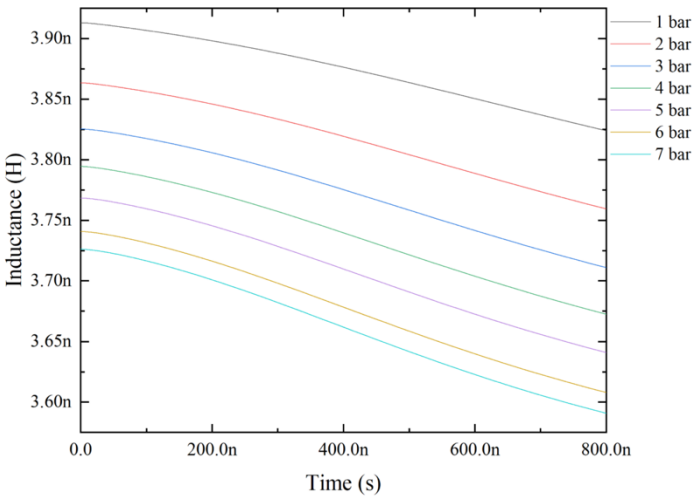

(a)

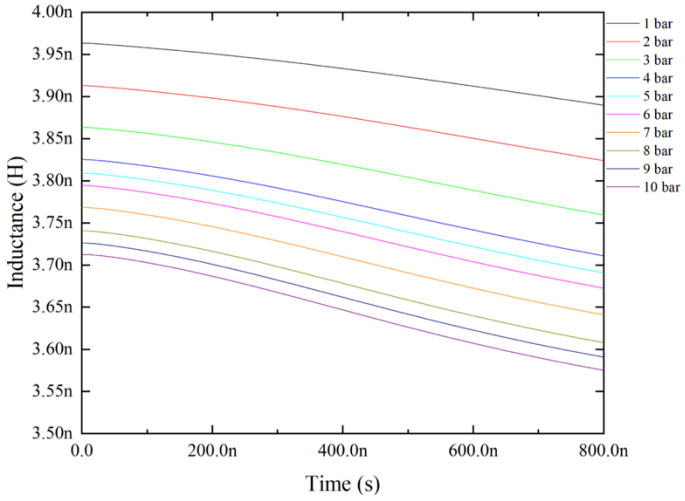

(b)

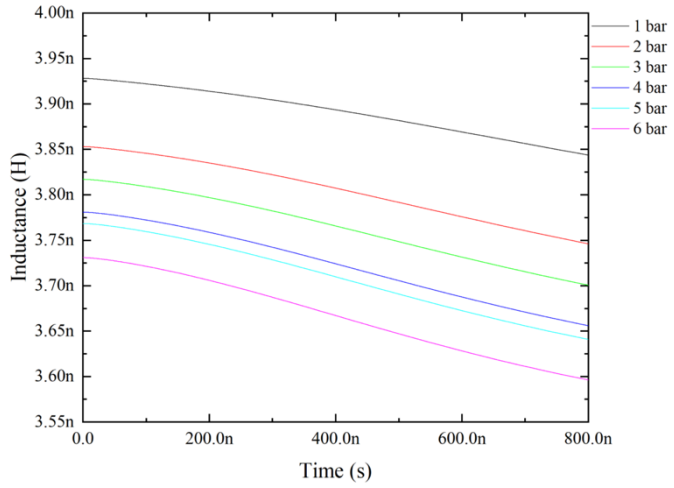

(c)

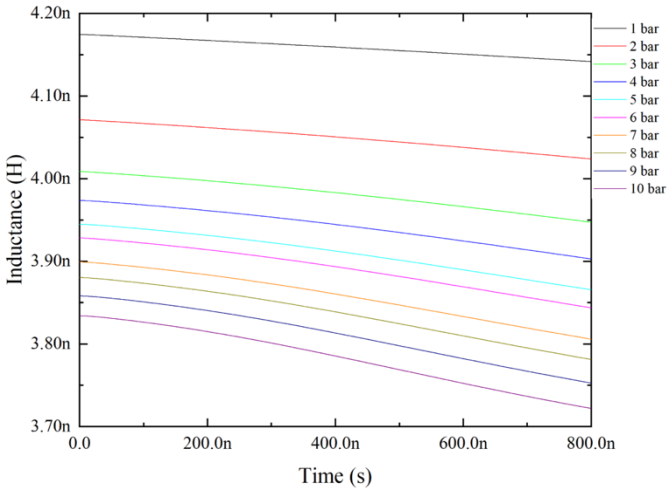

(d)

Figure. 7.8. The transient inductance of the plasma channel for different gas pressure. (a): dry air; (b): N_2; (c): CO_2; (d): 90%/10% Ar/O_2.

It can be seen in equation (7.2) that when the switch is stressed with a higher voltage, the current flowing through the plasma channel is higher, and more energy is transferred into the plasma channel, which will lead to more significant Joule heating and channel expansion in the plasma. As the arc cross-sectional diameter increases in the plasma channel, the transient inductance of the plasma channel will decrease. The value calculated by equation (7.2) is an order of magnitude but not very accurate to the actual arc inductance. The calculated transient inductance of the plasma channel is ~ (3.5-4) nH, which is significantly smaller than the inductance of the circuit and can be neglected.

7.4.5 Time-Dependent Resistance of the Plasma Channel

This chapter aims to study the time-dependent plasma resistance of the breakdown channel using different methods. When processing the experimental data, due to the noise in the observed current waveforms, the solution for $R_S(t)$ obtained by Kirchhoff's equation (7.18) also includes some "noise". Therefore, to minimise this effect and to facilitate the following analysis, the experimental current waveforms were processed in MATLAB to reduce the noise content before using them in (7.18). The denoising programme filter used was a fourth-order low-pass digital Butterworth filter.

Figure. 7.9 shows examples of the resistance of a plasma channel in the air at 1 bar obtained using different methods. In the initial stage of the transient process, the rapid rise of the current in the plasma channel and the plasma channel resistance obtained by the Braginskii model, Kushner model, and Kirchhoff's equation solution have a good consistency. The plasma resistance reduces to values smaller than 200 mΩ. After the initial stage, the resistance predicted by the Braginskii model continues to decrease. In contrast, Kirchhoff's equation and Kushner's model solutions show that as the current flowing through the plasma channel decreases, the plasma channel resistance in the channel begins to increase. In the Kushner model, after the second period of current oscillation, the channel resistance is much lower than the plasma channel resistance obtained by solving Kirchhoff's equation.

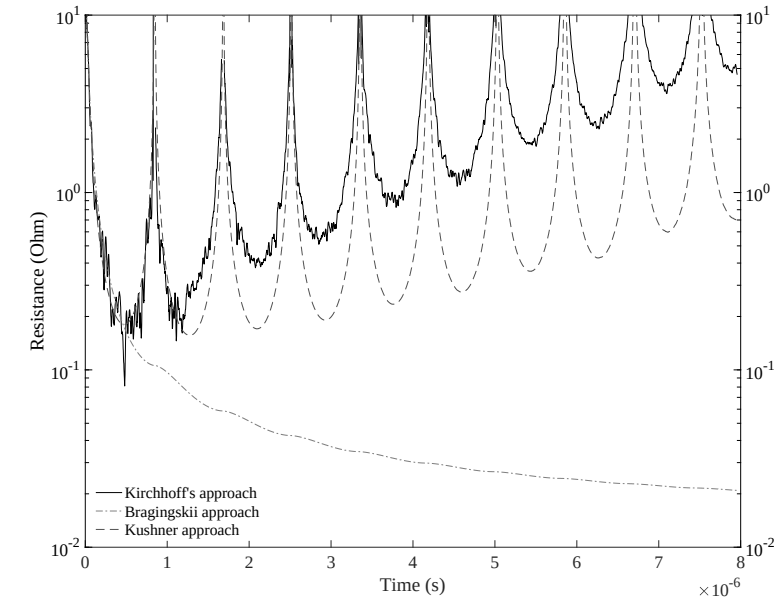

(a)

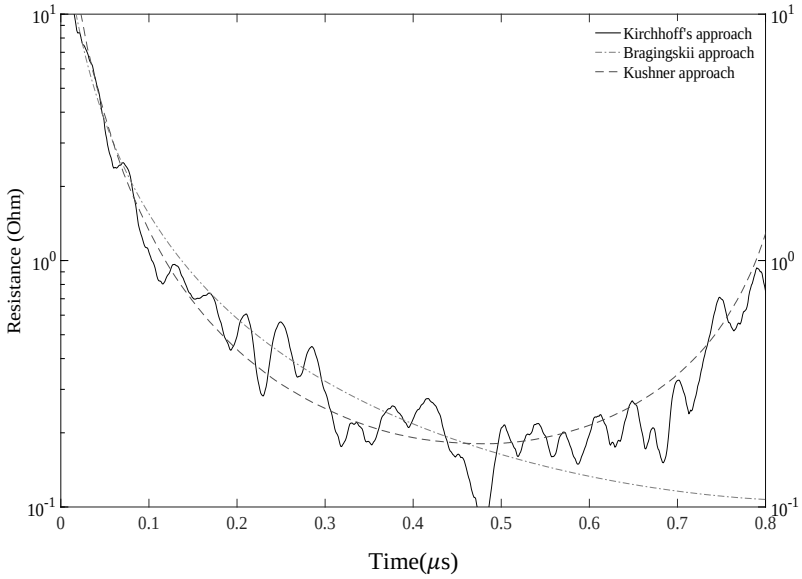

(b)

Figure. 7.9. The plasma channel resistance for air at 1 bar; (a) Calculated time-dependent plasma resistances for breakdown channel during several current oscillations; (b) Zoomed-in view of plasma resistance obtained by different methods during the first half of current oscillation. Solid line: Kirchhoff's approach; dot-dashed line: Braginskii model; dashed line: Kushner model.

The three methods demonstrate similar transient resistance functional behaviour at the initial stage for each tested gas in the test pressure range. When the current in the

plasma channel reaches the maximum, that is, in the first quarter of the current oscillation, the plasma resistance reaches the minimum.

Using all three models for all tested gases, air, N_2, CO_2, and Ar/O_2 mixtures, the minimum plasma resistance values were obtained under each specific test condition by averaging 10 consecutive breakdown events. Figure. 7.10 plots the plasma resistance in all tested gases within the experimental gas pressure range, demonstrating the time-varying resistance of the plasma channel as a function of the gas pressure at the first quarter of the current oscillation.

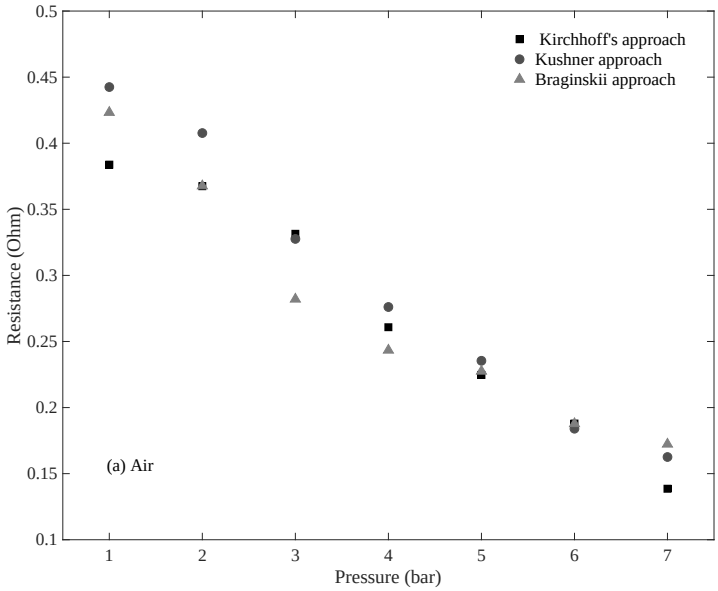

(a)

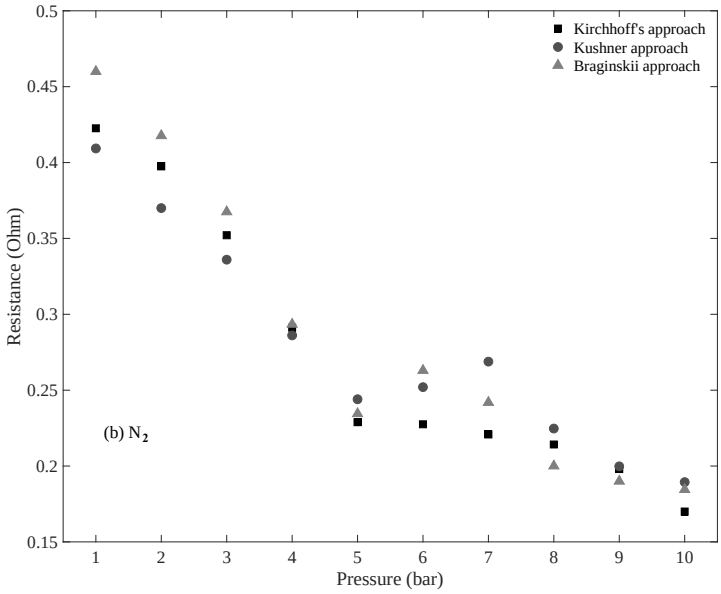
Kirchhoff's approach
Kushner approach
Braginskii approach
Resistance (Ohm)
Pressure (bar)
(b) N_2

(b)

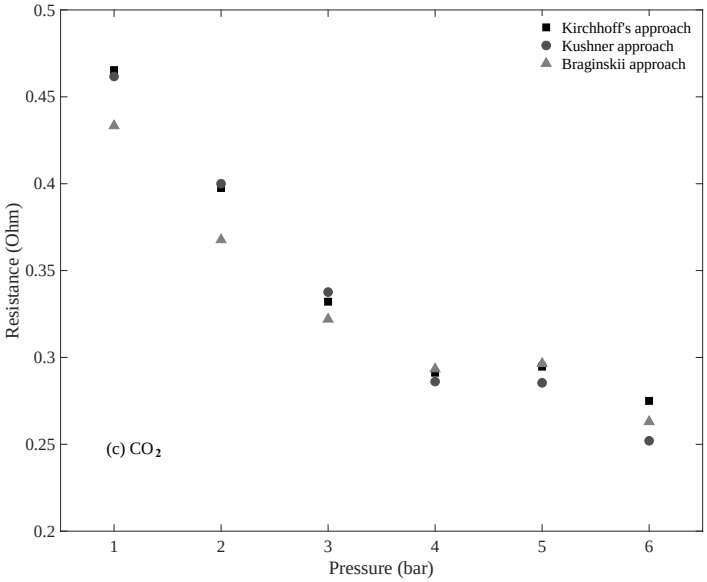
Kirchhoff's approach
Kushner approach
Braginskii approach
Resistance (Ohm)
Pressure (bar)
(c) CO_2

(c)

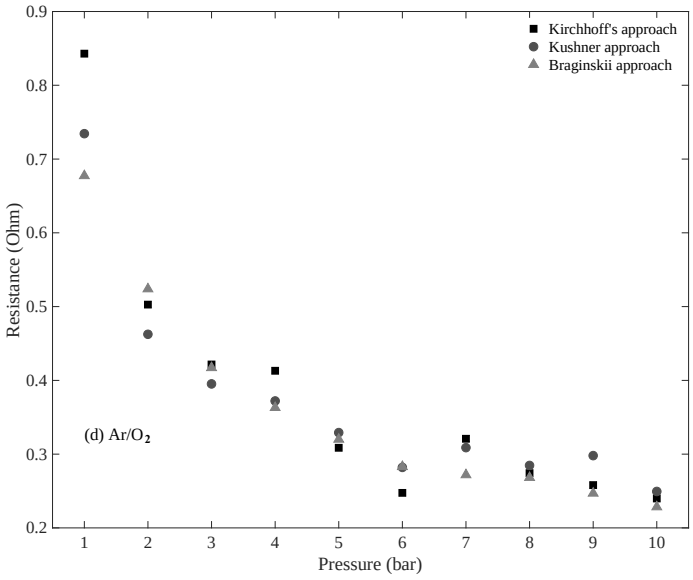

(d)

Figure. 7.10. The minimum value of plasma resistance as a function of the gas pressure at the first ¼ of the current oscillation for all investigated gases using all three models. (a) air; (b) N_2; (c) CO_2; (d) 90%/10% Ar/O_2.

Figure. 7.11 shows the obtained minimum plasma resistance for all tested gases as a function of the peak current. Each point in this graph was calculated as the average value of the resistance obtained by all three methods. The minimum resistance decreases with an increase in the peak current in the post-breakdown circuit. As Figure. 7.10 shows that there is no significant difference in the minimum resistance at the peak current for N_2 and the Ar/O_2 mixture; the resistance in the air is slightly higher than the resistance in these two gases, but the highest values for the plasma resistance as a function of current have been obtained in $CO2.$ The higher values of plasma resistance for a given peak current imply that there is considerably more energy dissipation in breakdown channels formed in CO_2 than those included in the other tested gases. This difference in the plasma resistance of CO_2 becomes higher with an increase in the peak current; for the highest observed peak current of 8.5 kA, the plasma resistance is 2.5-times higher than that in N_2 and air.

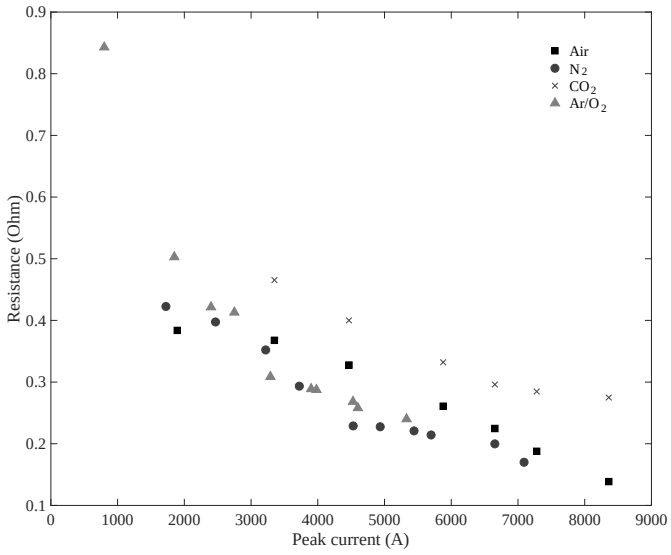

Figure. 7.11. The minimum plasma resistance of the plasma channel as a function of the maximum post-breakdown current for all tested gases.

7.4.6 Energy Deposited into the Plasma Channel

The total energy deposited in the plasma channel in the discharge is obtained by integrating the product of the transient plasma resistance and the square of the current:

$$E(t) = \int U(t)I(t)\,dt = \int R_s(t)I(t)^2\,dt \tag{7.21}$$

where $R_s(t)$ and $I(t)$ are the time-dependent resistance of the plasma channel and the transient current flowing in the plasma in the circuit, respectively.

Figure. 7.12 shows the energy deposited in the discharge as a function of gas pressure in the PCS. It can be seen in Figure. 7.11 that the energy increases with an increase in the pressure due to the higher breakdown voltage and the higher current flowing through the plasma channel. In addition, it was found that the energy deposited in the discharge is the largest in CO_2. The energy deposited in the plasma channel in the air is also significantly higher than the energy deposited in the plasma channel in the N_2 and Ar/O_2 mixture. This is because a higher breakdown voltage is observed in PCS

filled with CO_2 and air, which will cause the higher current in the discharge, resulting in higher discharge energy.

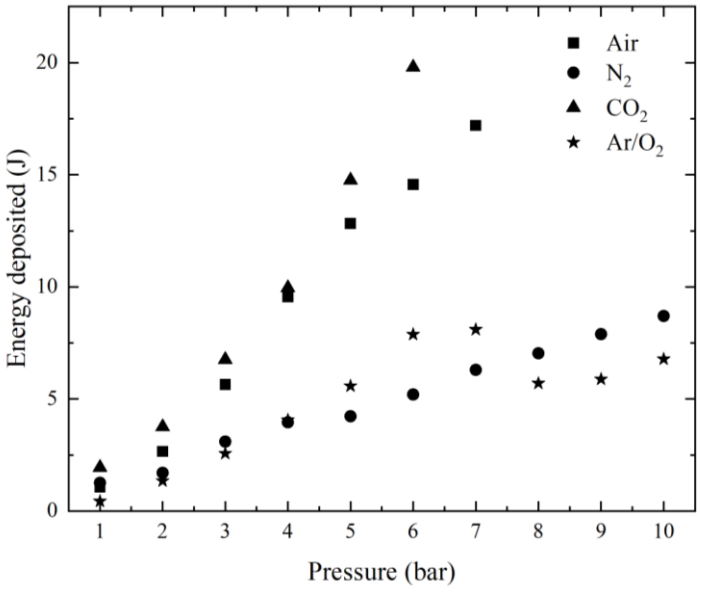

Figure. 7.12. The maximum energy deposited in the plasma channel for all tested gases as a function of gas pressure in the PCS.

7.5 Conclusions

In this chapter, three different time-varying resistance models (the RLC Kirchhoff lumped element circuit model, the Braginskii model and the Kushner model) were used to study the dynamic resistance of the plasma channel in the developed multi-electrode plasma closing switch topology filled with different tested gases.

The Braginskii model is based on the energy balance equation for the plasma channel. This approach assumes that when the current flows through the initial narrow plasma channel, the current heats the plasma channel. This process is characterised by the energy deposited into the channel. As the plasma temperature and pressure increase rapidly, the channel expands at supersonic speed and drives a strong cylindrical shock wave into the surrounding gas. At the same time, the plasma conductivity is assumed to be constant throughout this transient process. The time-dependent radius of the plasma channel was obtained using the Braginskii model, and it is in good agreement with the channel radius observed in optical experiments described in the literature.

The Kushner model assumes that the plasma in the plasma channel is in the local thermodynamic equilibrium, and the plasma channel expands hydrodynamically. The Kushner model can be used to obtain the dynamic resistance of the plasma channel from the current waveform and the analytical dynamic radius of the plasma channel.

When the plasma channel bridges the electrode gap, with the rapid expansion of the plasma channel, the conductive current flowing through the plasma channel increases rapidly, resulting in intense Joule heating and thermalisation of the channel. The entire system, including the plasma channel, can be described by constructing an equivalent circuit of RLC-lumped elements. Therefore, the plasma channel resistance can be obtained by solving Kirchhoff's equation.

This chapter also shows that the angular frequency and attenuation of the post-breakdown current waveform can be obtained using the experimentally obtained circuit oscillation. The inductance and resistance of the plasma channel formed in the gap between the electrodes can be estimated using the obtained values of the angular frequency and the attenuation parameter. During the breakdown event, the resistance and inductance of the plasma formed in the switch remain constant.

The constant inductance value estimated based on the experimental data is ~850 nH. This value is two orders of magnitude larger than the inductance of the plasma channel obtained by the theoretically calculated value. The constant plasma resistance range obtained by the waveform analysis is ~(0.4-0.7) Ω for all the tested gases within the test pressure range. The constant resistance of the plasma channel gradually decreases as the pressure increases. The plasma resistance of the 90%/10% Ar/O_2 mixture filled gaps is higher plasma as compared with other tested gases at the same pressure. The resistance and inductance values of the plasma channel obtained by the circuit's oscillation behaviour are not considered accurate. This is mainly due to the assumption that the plasma channel radius remains constant during the breakdown event, which is not the case. However, this method can reasonably estimate the plasma resistance (to the order of magnitude).

The results obtained and presented in this chapter show that all models predict a decrease in the plasma channel resistance, which is inversely proportional to a specific integrated power of the current flowing through the plasma channel. All three methods provide the same functional behaviour of time-dependent plasma resistance during the first quarter cycle of the current oscillation. That is, the resistance drops rapidly within the first 450 ns before reaching its minimum value. For extended periods, the Kushner model was found to be the most consistent with the results obtained by the Kirchhoff method. However, neither Kirchhoff nor Kushner's methods can accurately predict the expected resistance value when the current passes zero. The Braginskii model provides unrealistically low resistance values after the first quarter of the current oscillations. Therefore, it cannot be used to determine the channel behaviour in the case of underdamped current oscillations.

At the same time, it was found that the minimum resistance of the plasma channel is related to the current flowing through the channel and the type of gas used in the PCS. Under the same peak current value, the plasma resistance in CO_2 is higher than that in other gases. In addition, it has been determined that the maximum energy deposited in the plasma channel is the highest for the CO_2-filled switch. It was established that the energy deposited into the plasma channel is proportional to the time and the current flowing through the channel. Since the breakdown voltage is higher under higher gas pressure, and the current flowing through the channel increases when a breakdown occurs, the energy deposited in the channel increases with the increase of gas pressure. The energy deposited in the plasma channel in the air is also significantly higher than the energy deposited in the plasma channel in the N_2 and Ar/O_2 mixture. This is because a higher breakdown voltage is observed in PCS filled with CO_2 and air, which will cause more current to flow in the discharge, resulting in higher discharge energy.

This analysis will help in further understanding the dynamic characteristics of PCSs. The analysis method proposed in this chapter can be used to optimise the parameters of the plasma closing switches filled with environmentally friendly and lower environmental impact gases to improve their operating performance.

CHAPTER.8 RLC LUMPED CIRCUIT MODELS OF THE TRANSIENT PROCESS IN THE SWITCH

8.1 Introduction

In Chapter 7, the transient characteristics of the plasma channel obtained using the experimental breakdown waveforms in different gases were studied using analytical modelling of the plasma channel resistance. The theoretical analysis of the transient resistance and inductance of the plasma channel is based on the assumption that the plasma conductivity remains constant during the complete breakdown process. It was established that this modelling could provide a reasonable agreement with the experimentally obtained plasma channel characteristics and thus can be used to analyse the transient breakdown processes in the plasma closing switches to optimise their performance.

In this chapter, the plasma parameters in the switch will be coupled with the driving circuit in order to provide a method for analysis of the transient post-breakdown process in the complete pulsed power system.

The model used for this purpose was developed using PSpice software. In this software, the current and voltage in the modelled circuit gradually converge to an accurate solution through iterations starting from their initial states using the Newton-Raphson algorithm. PSpice provides a variety of circuit analysis methods and diagnostic output. Modelled circuits are based on the library of elements which include resistors, capacitors, inductors, transformers, independent voltage and current sources, control sources, lossless and lossy transmission lines, switches, and various standard semiconductor devices such as diodes and BJTs, JFETs, MESFETs, and MOSFETs.

It is common to use this software package to simulate pulsed power systems. However, the PSpice software library doesn't include many realistic elements of the pulsed power circuits, such as spark gap switches. Although simple switch models are available in the PSpice element library, these models can only approximate the

transient behaviour of practical plasma closing switches. This work focuses on developing a PSpice circuit model of the gas-filled PCS, which is based on realistic physical parameters. This chapter will use the PSpice circuit to model the dynamic plasma resistance. The transient plasma resistance model will be based on the approaches available in the literature (Toepler 1927; Rompe and Weizel 1944; Braginskii 1958; Barannik 1975; Kushner, Kimura, and Byron 1985). The results obtained by this model will be compared and verified with the theoretical calculations presented in previous chapters. The transient processes in the switch will be modelled using available experimental waveforms as initial parameters, which will provide a reliable basis for designing the plasma closing switches filled with environmentally friendly gases.

8.2 Constant Resistance and Inductance-based Circuit Model

A basic model simulating the breakdown process in the switch was developed using PSpice software. The plasma channel was represented as a lumped element circuit, as shown in Figure 8.1.

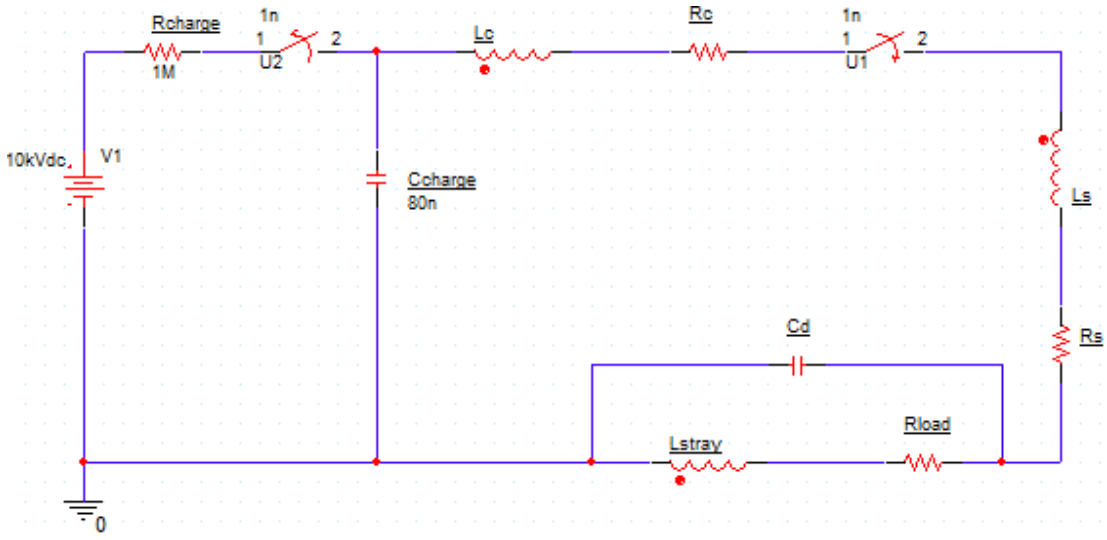

Figure. 8.1. The lumped circuit element model for simulation of the breakdown events

According to the practical circuit connection analysis presented in chapter 7, this circuit shown in Fig.8.1 has a 1 MΩ charging resistor, which acts as a current limiter to decouple the DC power supply from the plasma closing switch during the transient

event. The energy storage capacitor, C_{charge} used in the system has a capacitance of 80nF. This model uses the ideal switch available in PSpice (instead of a realistic PCS model). This ideal switch closure time is set to 1 ns, and its open-circuit and closed-circuit impedances are set to 1 MΩ and 0.01 Ω, respectively. The distributed capacitance of the PCS electrodes is 10 pF.

It can be seen from Figure 8.1 that when a breakdown event occurs, the plasma channel is described by a fixed-value lumped element circuit. The constant inductance of the channel has been calculated in sections 7.4.2 and 7.4.4. The total inductance of the RLC system formed during the breakdown event can be calculated using equation (7.8). The inductance of the capacitor is ~30 nH. The inductance of the PCS electrodes is ~60 nH as obtained by the formulation provided in (Grover 2004). The diagnostic circuit contains two stainless steel bars with a thickness of 3mm, the lengths of which are respectively 100mm and 200mm and two cables with radii of 1.5mm and a length of 1500mm. The total inductance of the transmission line is ~750 nH, calculated using analytical equations (Grover 2004), with topological parameters obtained from the experimental set-up. The calculated transient inductance of the plasma channel is (3.5 -4) nH.

In addition to the required inductance, in order to develop the lumped element circuit of the plasma closing switch, the resistance of the plasma channel during the breakdown event is required. The resistance of the two electrodes was calculated to be ~0.1mΩ. After measuring the experimental short-circuit current waveform, the total circuit resistance was obtained by fitting an exponentially decaying sinusoidal oscillation to the short-circuit waveforms. This procedure used ten independent short-circuit current waveforms, providing 0.35 Ω as an average value, with its standard deviation of 0.02 Ω. The constant resistance of the plasma channel for all test gases within the tested pressure range calculated in Section 7.4.2 is ~ (0.2-0.8) Ω.

In this section, the output voltage waveshapes across the load and the current waveforms in the circuit with the plasma switch are compared and analysed to establish the influence of the different characteristics of plasma switches and different

loads on these waveshapes. Figure 8.2 shows the voltage and current waveforms for different resistive loads under 10kV charging. The plasma resistance is set to 0.3Ω, the plasma inductance is set to 4nH, and the distributed capacitance and stray inductance of the system are set to values of 10pF and 10nH, respectively. In order to explore the influence of the matching resistance in the discharge circuit on the voltage and current waveforms, the PSpice parameter sweep function was used to simulate the pulse voltage and current when the resistance, inductance and capacitance changed.

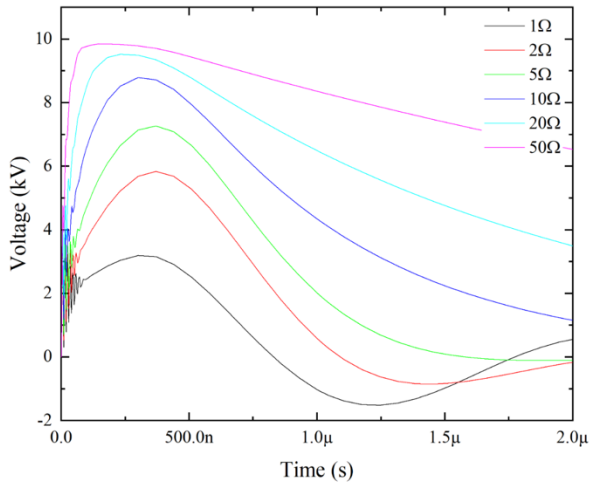

(a)

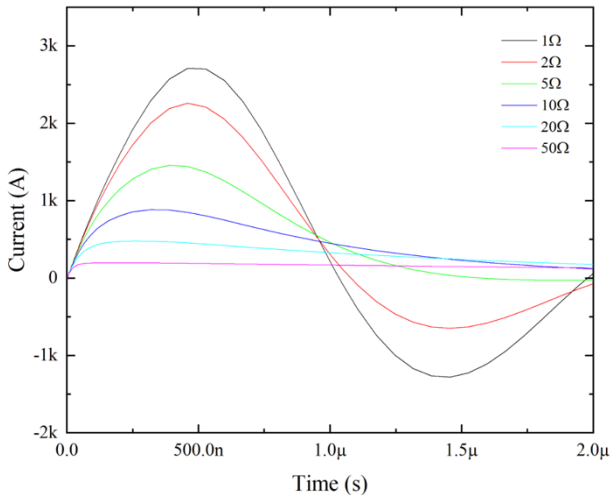

(b)

Figure. 8.2. The voltage across and current through a resistive load for different values of resistance, 10kV charging voltage: (a) voltage waveform; (b) current waveform.

It can be seen from Figure 8.2(a) that for different resistive loads, the peak voltage increases as the load resistance increases. Furthermore, the rate of rising of the voltage, dV/dt becomes higher as the load resistance increases. It can be seen from Figure 8.2(b) that as the load resistance increases the rate of rising of the discharge current, dI/dt, becomes faster. When the load resistance in the circuit decreases, the waveform period decreases, the peak current increases, and the total duration of the oscillation become longer.

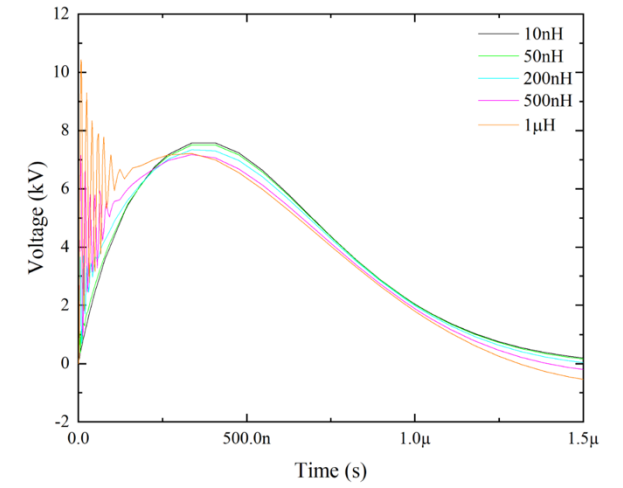

(a)

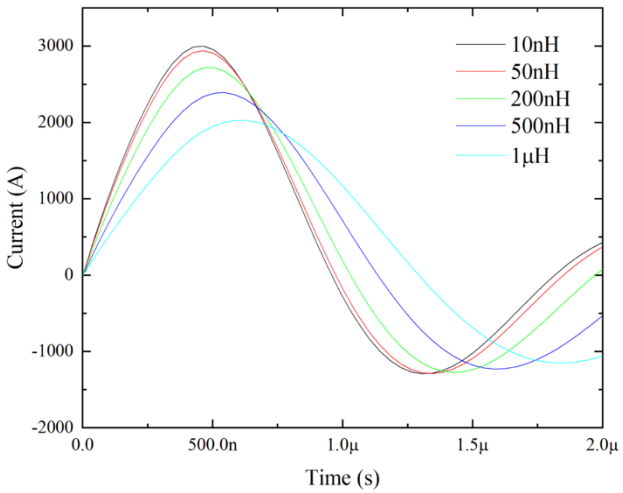

(b)

Figure. 8.3. The voltage waveforms across the load with different stray inductance values under 10kV charging voltage. (a) voltage waveform; (b) current waveform.

Figure 8.3(a) shows the voltage across the load with different values of the stray inductance under 10kV charging voltage. It can be found that the amplitude of the

voltage gradually decreases as the stray inductance increases. Additionally, the voltage rising rate, dV/dt becomes lower as the stray inductance becomes larger. It can be seen from Figure 8.3(b) that the rate of the current rise in the discharge current is related to the stray inductance value in the discharge circuit. dI/dt becomes lower as the stray inductance increases. The peak current gradually decreases as the stray inductance increases. The pulse width of the discharge current increases as the stray inductance increases.

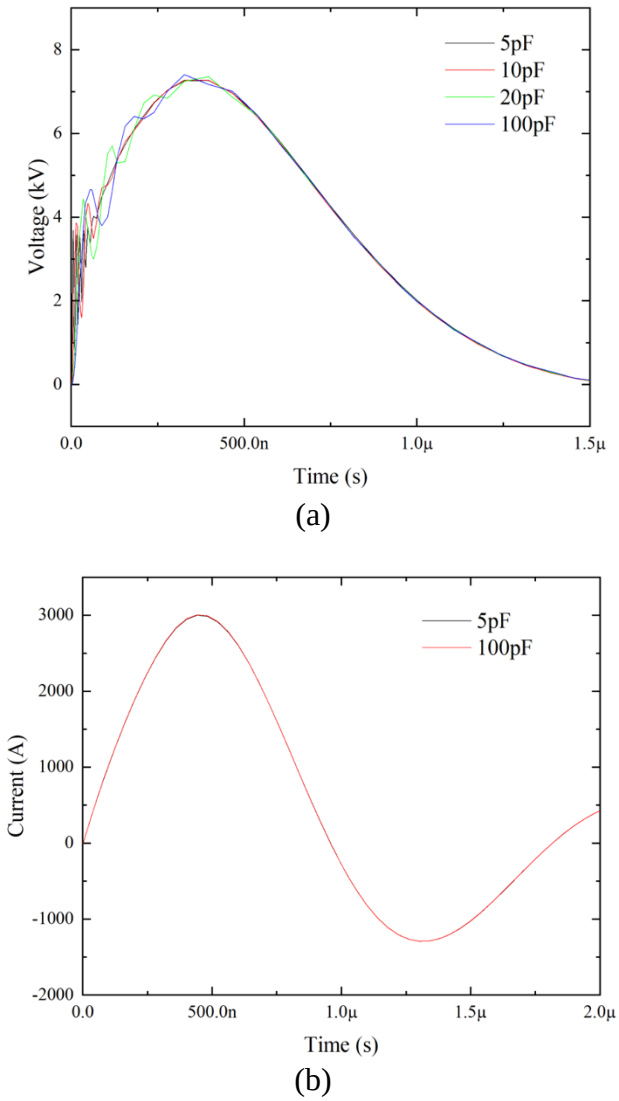

Figure. 8.4. The voltage waveforms across the load with different distributed capacitance values under 10kV charging voltage. (a) voltage waveform; (b) current waveform.

It can be seen from Figure 8.4(a) that the distributed capacitance does not significantly affect the voltage and current waveforms. The only observed effect is as follows:

when the distributed capacitance is smaller, the output waveform is smoother. Figure 8.4(b) shows that the distributed capacitance does not significantly affect the discharge current waveforms.

8.3 Dynamic Resistance Model

In the previous section, the analysis model of the transient plasma closing switch was realised by using the constant values of the resistance and inductance. In order to describe the performance of the gas-filled plasma closing switch more accurately, it is necessary to consider the time characteristics of the switch and to introduce the time-varying transient plasma resistance and inductance.

The lumped element circuits developed using the PSpice simulation software have been used to model pulsed power systems for a long time. Different components such as capacitors, inductors, and transmission lines can be easily placed into the model using the PSpice's element library. However, the plasma closing switch is not available in the PSpice library, so the realistic model of the PCS should be developed using other available circuit elements.

The plasma resistance in the circuit changes with time. However, there is no time-dependent resistor component in the PSpice element library. Nevertheless, the PSpice circuit model allows for the current to be modelled. The relationship between the time-varying plasma resistance can be obtained using the computational model in the ABM (analogue behavioural model) library in PSpice, thereby developing a computational model of the plasma closing switch.

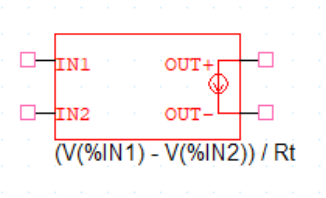

Figure. 8.5. Voltage-controlled current source.

Figure 8.5 shows a voltage-controlled current source with a voltage value proportional to the current in the circuit. Therefore, this component can represent the plasma resistance, represented by the variable function R_t. This time-varying function R_t can be based on the available models available in the literature (Toepler 1927; Rompe and Weizel 1944; Braginskii 1958; Barannik 1975; Kushner, Kimura, and Byron 1985).

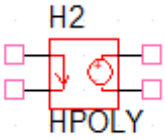

Figure. 8.6. Current-controlled voltage source.

To implement the expressions of these models in PSpice, it is necessary to express the relevant current(s) in terms of voltage(s). This requires a current-controlled voltage source component, which is represented by the icon shown in Figure 8.6. It is placed in the circuit in series to obtain the current signal, and its output is the voltage signal (of the same numerical value). Thus, this operation will not affect the current waveform.

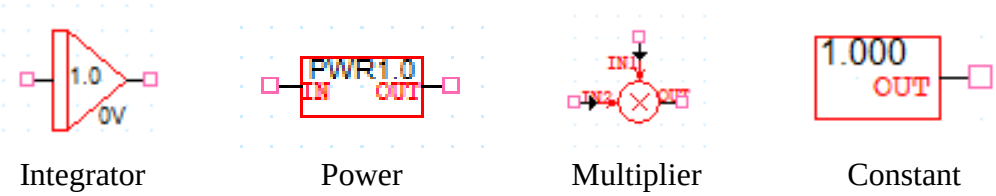

Figure. 8.7. ABM components used to model the time-varying resistance of plasma channels.

Figure 8.7 shows the mathematical components in the ABM library for integration, exponentiation, multiplication, and user-defined constants to solve the plasma resistance equation obtained from the literature.

The plasma resistance equation was solved by computing the voltage signal representing the current using the mathematical components described above. Figure 8.8 shows the solution of the plasma resistance equation for the Braginskii model (Equation (2.8)). According to the definition of the Braginskii model, the radius of the

plasma channel should be calculated first. The current expressed as a voltage signal should be integrated using the integrating power component. Then the output from this component should be multiplied by the Braginskii constant to get the radius of the plasma channel. Finally, the time-dependent plasma resistance is obtained by multiplying the output from the constant and power function components.

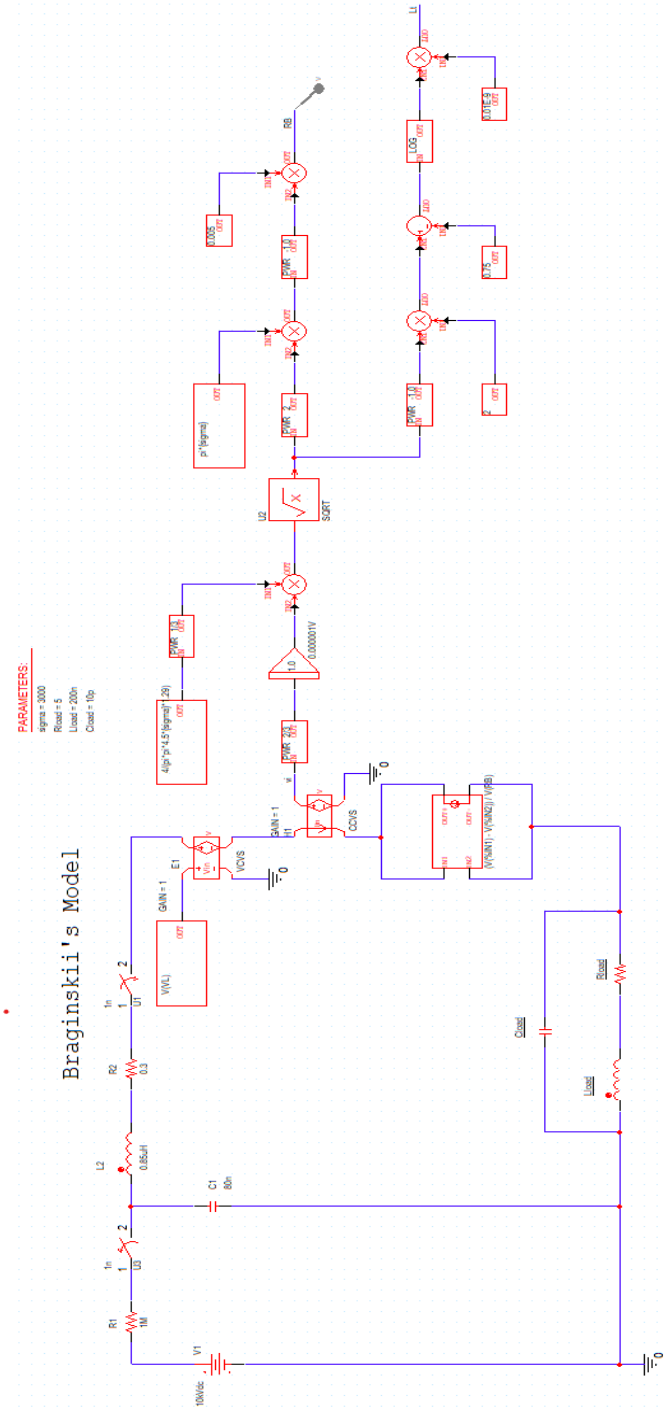

Figure. 8.8. The circuit diagram used to model dynamic plasma resistance by Braginskii's approach.

In the model, the current in the circuit is affected by the plasma resistance. When solving the model equations, the plasma resistance value is obtained using the current in the circuit. Therefore, it is necessary to import the control source component in Figure 8.5 to replace the plasma resistance value to simulate the self-consistent dynamic plasma resistance in this circuit.

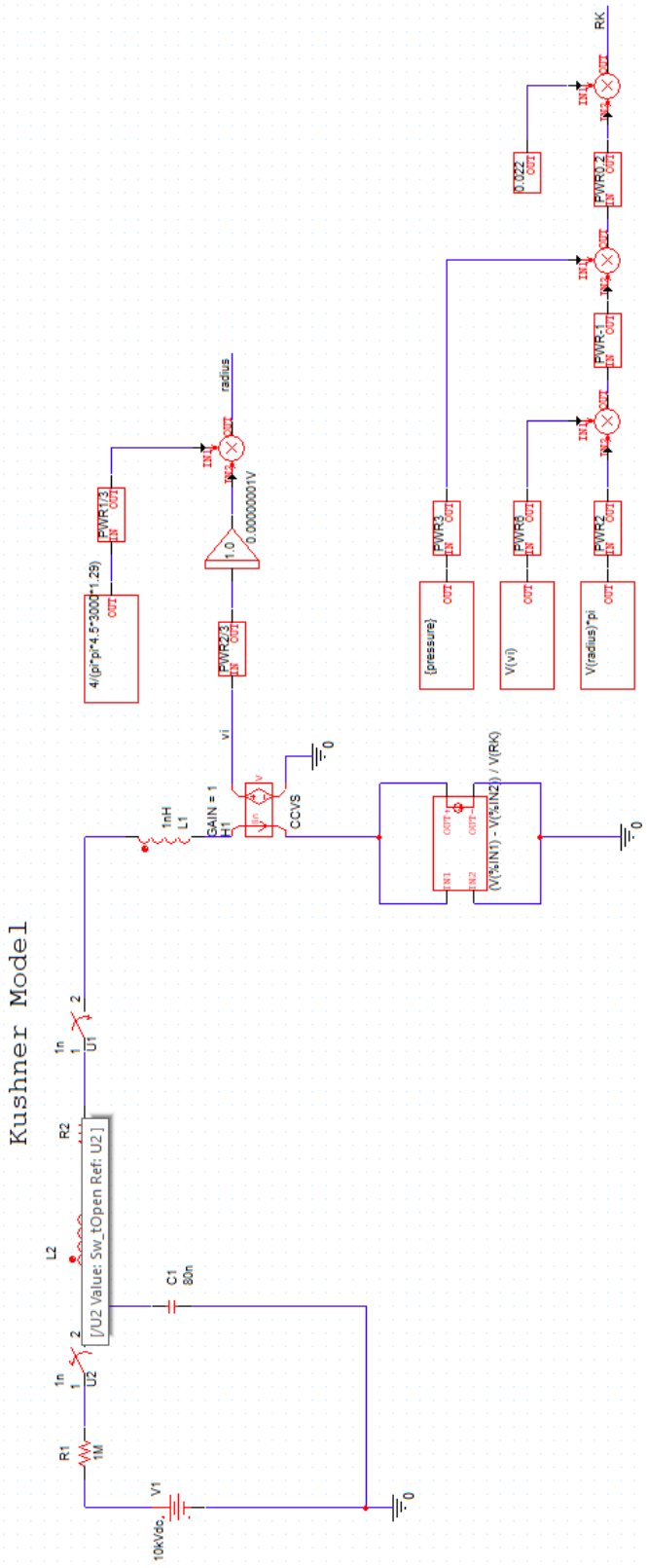

Figure. 8.9. The circuit diagram used to model dynamic plasma resistance by Kushner's approach

Figure 8.9 shows the model to the plasma resistance equation in the framework of the Kushner model (equation (2.15)). According to the definition of the Kushner model, the current expressed as a voltage signal should be integrated using the integral and power components and then multiplied by the output from the constant component to obtain the radius of the plasma channel. It is then multiplied by the sixth power of the current. Finally, the output from the constant component is multiplied by the power function component to obtain the dynamic plasma resistance.

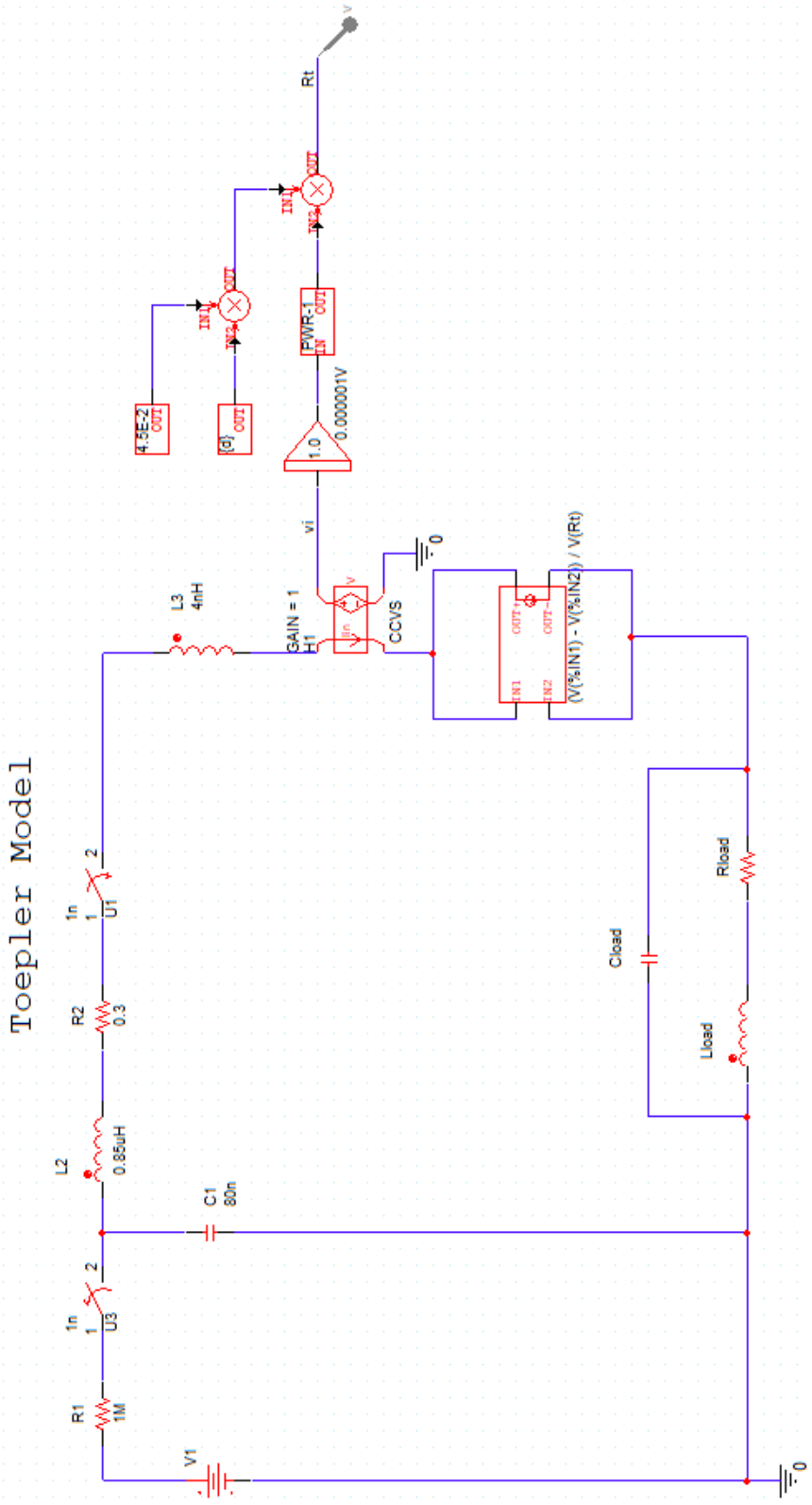

Figure. 8.10 The dynamic plasma parameters of the resistance in the Toepler model.

Figure 8.10 shows the model of the plasma resistance equation based on the Toepler approach (equation (2.9)). According to the Toepler model, the current expressed as a voltage signal is integrated by using the integral component, and then the reciprocal of the current is integrated using the power function component. Finally, the output is multiplied by the product of the two constant components (one for the distance and one for the Toepler constant) to obtain the dynamic plasma resistance.

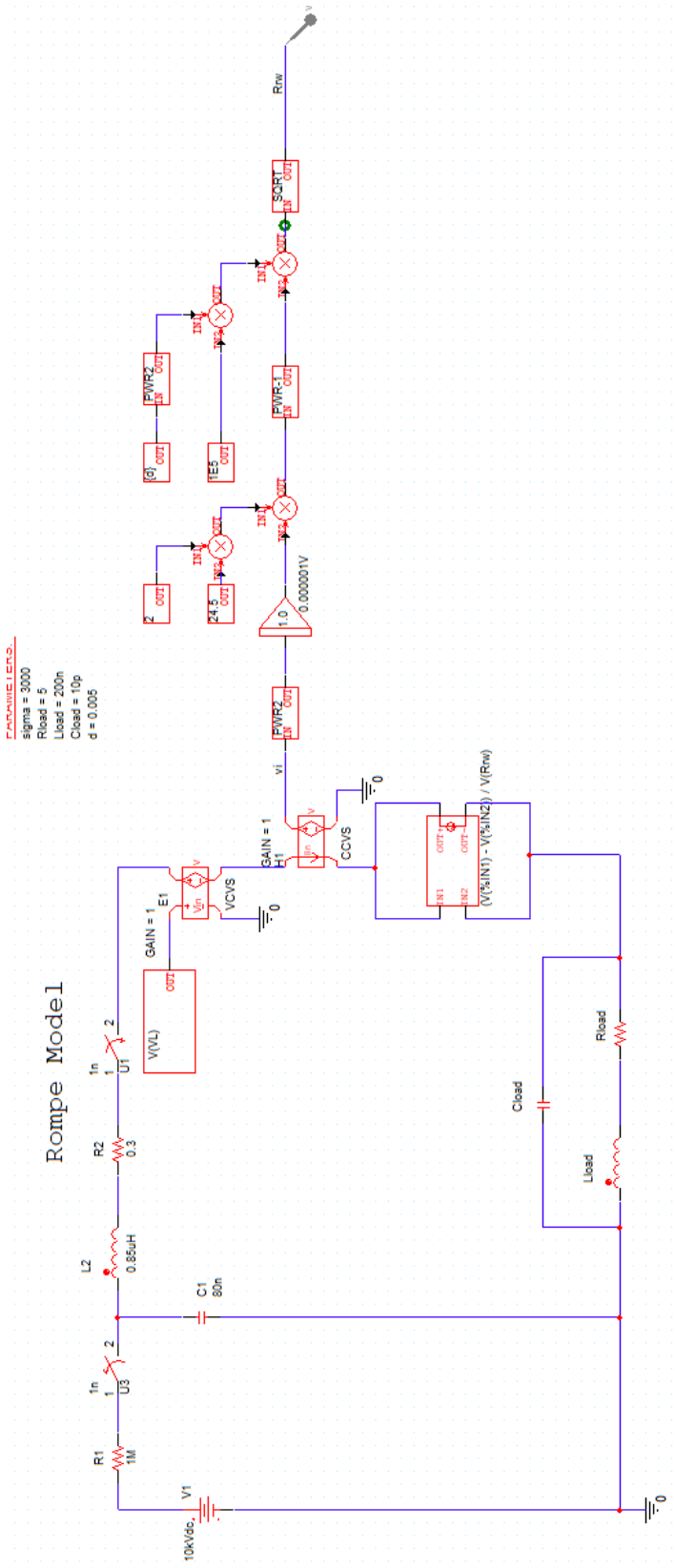

Figure. 8.11 The dynamic plasma parameters of the resistance in the Rompe and Weizel model.

Figure 8.11 shows the solution to the Rompe and Weizel model (equation (2.10)). According to the definition of the Rompe and Weizel model, the current expressed as a voltage signal is integrated by using the integral component, and then the reciprocal of the current is integrated using the power function component. Then the output is multiplied by two constant components (one for the pressure and one for the distance). Finally, the square root of the output value is calculated using the power function component to obtain the plasma resistance.

Figure 8.12 shows an example of the resistance of the plasma channel obtained using different methods. The plasma resistances obtained by each equation are plotted on the same graph for comparison. In the first quarter of the current oscillation, the plasma resistance reaches its minimum value at the current peak. In contrast, it was found that in Toepler's model, the plasma resistance reaches its minimum value, <100 mΩ, which is twice as minor as the minimum value obtained by Kirchhoff's approach using the experimental waveforms, ~200 mΩ. The hydrodynamic-based model by Braginskii, the Kushner model and the model of Rompe and Weizel provide a good match between the modelled plasma resistance and the measured resistance.

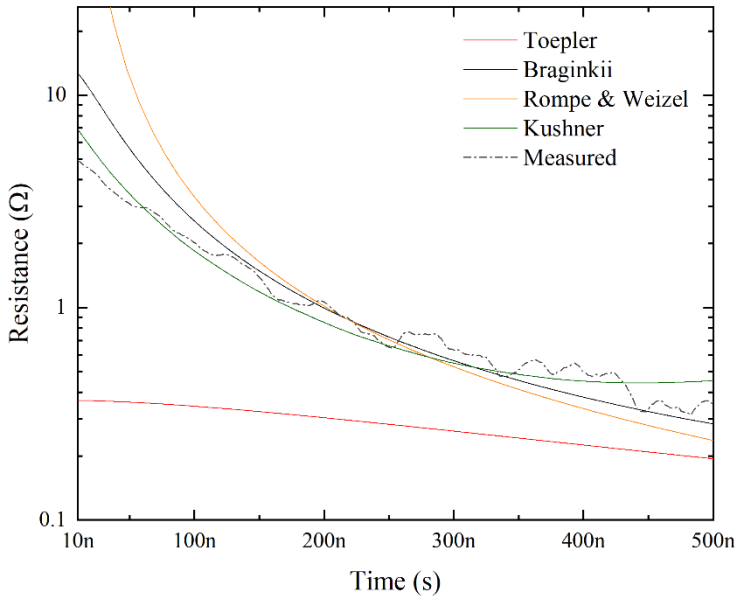

Figure. 8.12 The dynamic plasma resistance simulated using PSpice for different methods during the first quarter of current oscillation.

8.4 Conclusions

This chapter developed different models for modelling the transient plasma resistance using PSpice circuit simulation software. The obtained results were compared with the theoretical analysis presented in Chapter 7. This analysis and comparison determined the most suitable approach to modelling the plasma resistance and transient post-breakdown process. This approach provides a reliable basis for designing and optimising plasma closing switches filled with environmentally friendly gases.

This chapter describes the PSpice computational models for obtaining the resistance of the post-breakdown plasma channels developed in the PCS using constant plasma resistance and inductance. The model includes the distributed capacitance, stray inductance, and load resistance associated with the practical experimental system. The effect of the resistance on the voltage across the load and the current through the load has been investigated. By comparing the voltage and current waveform, the influence of the system parameters on the characteristics of the plasma switch and current and voltage waveform has been analysed.

It was observed that the peak output voltage across the load decreases as the stray inductance increases. Additionally, the rate of rising of voltage dV/dt becomes lower as the stray inductance increases. In contrast, the peak output voltage across the load increases as the load resistance increases. Furthermore, the voltage rising rate, dV/dt, becomes higher as the load resistance increases. The peak output voltages are not significantly different for loads with different distributed capacitance values. The smaller distributed capacitance(s) produces the smoother waveforms.

When the load resistance in the circuit increases, the pulse period and pulse width increase, and the peak current decreases. The rate of rising of the current is related to the stray inductance value in the discharge circuit. dI/dt becomes higher as the stray inductance decreases. The peak current gradually decreases as the stray inductance increases. The current pulse width increases as the stray inductance increases. It was

found that the distributed capacitance does not significantly affect the discharge current waveshape.

In order to simulate the parameters of plasma closing switches in the pulsed power systems more accurately, the dynamic parameters of the plasma channel should be obtained. This chapter used PSpice software to develop a self-consistent dynamic model of the plasma channel. The model can be successfully used to simulate the dynamic plasma resistance. By comparing the simulation results, it was found that Toepler's model provides the minimum plasma resistance of < 100 mΩ, which is twice lower than the measured resistance ~200 mΩ. In contrast, the hydrodynamic-based model developed by Braginskii, Kushner's model, and Rompe and Weizel's model provide values of plasma resistance which are in good agreement with the measured resistance values.

CHAPTER.9 CONCLUSIONS AND FUTURE WORK

9.1 Conclusions

The main objective of this thesis was to develop a novel two-stage triggered gas-filled plasma closing switch with corona electrodes and conduct a comprehensive and systematic study of its operational performance to establish its operational characteristics. The switch developed in the current project was filled with environmentally friendly gases in order to investigate their potential suitability for applications in PCSs.

Until recently, SF_6 gas was commonly used as a working gas in PCSs due to its high breakdown strength and excellent recovery properties. However, due to environmental concerns, there are requirements to replace SF_6 with gases with significantly lower GWP values. The developed PCS was filled with dry bottled air, N_2, CO_2 and the 90%/10% Ar/O_2 mixture in the present study. The switch performance and its operational characteristics were investigated over a wide gas pressure range from 1bar to 12bar (gauge).

The overall aim of this work is to study the operational performance of plasma closing switch(es) filled with environmentally friendly gases and to develop a novel two-stage triggered gas-filled plasma closing switch with specific operational characteristics.

The novelty of this research work includes the proposed two-stage switch topology, in which corona discharges are developed in both stages to improve the stability of its operation. The operational performance of the switch in the self-breakdown and triggered modes was thoroughly investigated.

Statistical analysis of the obtained experimental data was conducted to characterise the breakdown properties and operating characteristics of the switch.

Different analytical approaches have been developed and used to obtain the transient characteristics of the plasma channel formed during the breakdown of the plasma closing switch.

Chapter 2 provides the literature review of various aspects of the pulsed power technology, including the basic principles of generation of HV impulses, basic mechanisms and characteristics of gas discharges, different plasma closing switching topologies and their operational characteristics. Also, Chapter 2 provides an in-depth discussion of transient plasma resistance and a comprehensive review of different dynamic plasma resistance models available in the literature.

The insulating gases used in the plasma closing switches are reviewed in detail. It is shown that the growing environmental concerns have prompted the search for suitable alternatives to SF_6 gas. The literature review provides a detailed discussion of the critical operational characteristics of PCSs, which form the basis of the current research project.

During the course of this project, an advanced platform for the high-voltage breakdown tests has been designed and developed in order to investigate the operational characteristics of the plasma closing switch filled with different gases (air, N_2, CO_2 and the 90%/10% Ar/O_2 mixture).

A novel two-stage trigger gas-filled plasma closing switch with corona electrodes has been designed and developed. This switch can operate at high gas pressures (it was tested to withstand gas pressures up to 20 bar). Due to the symmetry in the switch topology, no breakdown polarity effects were observed. Thus, the switch can potentially be used in practical applications when stressed with either positive or negative high voltage. Another novel aspect of this work includes the test set-up in which the LabVIEW code was used to facilitate the control of the high voltage power supply (providing consistent and repeatable charging for the tested PCS), automatic measurements and data acquisition. The automated test system ensures that the experimental conditions are the same in each test and data are transferred for further

analysis in real-time, which is critical for practical work. This set-up was used to investigate the breakdown voltage and time to breakdown, to measure the voltage-current characteristics of corona discharges and to analyse impulse breakdown characteristics of the switch.

The self-breakdown performance of the plasma closing switch filled with air, CO_2, N_2, and the 90%/10% Ar/O_2 mixture has been investigated in the pressure range from 1 to 12 bar (gauge), and the breakdown voltage as a function of the gas pressure has been obtained.

It was found that at the specific critical pressure, the positive and negative breakdown voltages of the switch are the same (in the case of a breakdown occurring in the single (upper) gap of the switch). For the gas pressures lower than this critical pressure, the breakdown voltages for negative energisation were higher than positive breakdown voltages. For pressures above this critical pressure, the breakdown voltages for positive energisation significantly exceed the negative breakdown voltages.

It was found that the gas type and gas pressure directly affect the critical gas pressure. When breakdowns occurred in both gaps in the switch, no significant difference was found between the positive and negative breakdown voltages for all the tested gases. These voltages increase as the gas pressure increases. It was found that when the switch was filled with air and N_2. the self-breakdown voltage is a linear function of the gas pressure: the self-breakdown voltage increases as the gas pressure increases. Thus, these two gases provide a highly predictable operational behaviour of the switch. When the switch is filled with CO_2 and the 90%/10% Ar/O_2 mixture, the breakdown voltage demonstrates a significant corona stabilisation effect, typically observed in electronegative gases. The space charge generated by the corona discharges weakens the electric field near the point electrode(s), preventing the formation of streamer(s).

The corona discharges were generated in the switch, and their effect on the switching performance was investigated.

Due to the symmetrical topology of the switch, when positive DC voltage stresses the high voltage electrode, negative corona discharge occurs at the tips of the needle electrodes located in the upper gap, while positive corona discharge occurs at the tips of the needle electrodes located in the lower gap of the switch. When the high voltage electrode is negatively stressed, positive corona discharge occurs at the needle electrodes in the upper gap, while negative corona discharge occurs at the needle electrodes located in the lower gap. Therefore, positive and negative corona discharges are generated in both gaps regardless of the polarity of the applied voltage.

Following the study of the self-breakdown voltage and pre-breakdown corona discharge, the impulse breakdown characteristics of the developed switch were systematically investigated. The obtained results are essential for accurate control of the operation of the PCS. It was shown that the time to breakdown increases with an increase in the gas pressure for all DC voltages used in this study when the switch was filled with air, N_2, and CO_2. However, in the case of the 90%/10% Ar/O_2 gas mixture, the pre-breakdown time did not change significantly with the applied voltage. The pre-breakdown time fluctuates slightly and remains within the range between ~ 31ns and ~35 ns for all energisation levels.

It was also found that the jitter of the switch, when plotted as a function of the gas pressure, increases as the gas pressure increases for the 70% and 90% DC self-breakdown energisation levels when the switch is filled with the air, N_2, and CO_2. However, when the switch was filled with the 90%/10% Ar/O_2 gas mixture, the jitter had its minimum value as compared with the other tested gases. It was found that the jitter for this gas mixture was as low as ~1.2 ns and ~1.1 ns at 10 bar for the 70% and 90% DC self-breakdown energisation levels, respectively. It was also obtained that the jitter reduced to the sub-nanosecond level for the gas pressures above 11 bar when the switch was stressed with 90% of the DC self-breakdown voltage. The jitter reduces as the pressure of the 90%/10% Ar/O_2 gas mixture increases.

This research project also comprehensively investigates and analyses the post-breakdown plasma characteristics. Different analytical approaches to modelling the

post-breakdown plasma resistance in a plasma closing switch have been used to obtain the resistance of the plasma channel in the developed PCS. The analytical results show that all of these models predict a decrease in the resistance of the plasma channel at the early stage of the transient post-breakdown process in the switch. The resistance of the plasma channel is inversely proportional to the integral of the current (in specific power) flowing through the plasma channel.

At the same time, it was found that the minimum resistance of the plasma channel is related to the current flowing through the channel and the type of gas used in the PCS. At the same peak current value, the plasma resistance in CO_2 is higher than that in other gases. In addition, it has been shown that the maximum energy deposited in the plasma channel is the highest for the CO_2-filled switch. The energy deposited in the plasma channel in the air is significantly higher than the energy deposited in the plasma channels in the N_2 and the Ar/O_2 mixture. This study of the plasma resistance contributes to a further understanding the dynamic characteristics of gas-filled plasma closing switches. The developed methods can be used to optimise the parameters of plasma closing switches filled with environmentally friendly, low environmental impact gases to improve their operational performance.

Based on the dynamic resistance models presented in the literature, a new method for obtaining the transient plasma resistance in the multi-electrode plasma closing switching topology was developed using the PSpice circuit simulation software. This model includes distributed capacitances, stray inductance, and load resistance and allows for modelling of the transient processes in practical pulsed power experimental systems. The results obtained using the PSpice model have been compared with the analytical results. This PSpice method of simulation of the plasma resistance can be used to model the transient processes in complex pulsed power systems to predict and optimize the waveforms of the output impulses.

9.2 Future Work

In this project, a novel two-stage triggered gas-filled plasma closing switch with corona electrodes was designed, and its operational characteristics were investigated. It was shown that pre-breakdown corona discharge could improve the stability of the switch operation when filled with environmentally friendly gases. However, there are some aspects which require further investigation.

The switch used in this study is based on the corona-stabilisation topology, and its switching characteristics were investigated in a single-shot regime. Thus, the next step in this research direction could be focused on exploring the recovery performance and repetitive operation of this novel two-stage trigger gas-filled plasma closing switch when filled with different environmentally friendly gases.

It will be beneficial to investigate such characteristics as the maximum pulse repetition rate and voltage recovery that this switch can provide. These parameters have practical significance and will help to establish the potential applicability of the developed PCS in practical high pulse repetition rate systems.

Another aspect which will require further investigation is electrode erosion rates and the establishment of electrode materials which can improve the operating lifetime of the gas-filled plasma closing switch. In future, it would be beneficial to investigate the performance of larger-scale pulsed power systems such as Marx generators equipped with the developed PCSs. Also, further analytical analysis, which will be based on the modelling of entire pulsed power systems (for example, a Marx generator), will help in the optimization of the wave shapes of the output impulses. The analytical methods and approaches developed in this work provide the basis for this further work.

CHAPTER.10 PUBLICATIONS AND CONFERENCE PRESENTATIONS

Y. Yao, I. V. Timoshkin, S. J. MacGregor, M. P. Wilson, M. J. Given and T. Wang, "Post-breakdown Transient Characteristics of a Gas-Filled Plasma Closing Switch," in IEEE Transactions on Plasma Science, vol. 49, no. 2, pp. 942-951, Feb. 2021, doi: 10.1109/TPS.2021.3053097.

Y. Yao, I. V. Timoshkin, S. J. MacGregor, M. P. Wilson, M. J. Given, and T. Wang. 2018. "Breakdown Characteristics of Plasma Closing Switch Filled with Air, N_2, CO_2, and Ar/O_2." IEEE Transactions on Plasma Science 46 (10): 3574-3583. https://doi.org/10.1109/TPS.2018.2856306.

Y. Yao, I. V. Timoshkin, S. J. MacGregor, M. P. Wilson, M. J. Given, and T. Wang. "Dielectric performance of HFO-gas mixtures," 2017 IEEE 21st International Conference on Pulsed Power (PPC), 2017, pp. 1-6, doi: 10.1109/PPC.2017.8291272.

Y. Yao, I. V. Timoshkin, S. J. MacGregor, M. P. Wilson, M. J. Given, and T. Wang. “Modelling of Post-breakdown Characteristics of a Plasma Closing Switch in Air ” 7th Euro-Asian Pulsed Power Conference (EAPPC) and 22nd International Conference on High-Power Particle Beams (BEAMS), Changsha, China, 16th-20th September 2018.

Y. Yao, I. V. Timoshkin, S. J. MacGregor, M. P. Wilson, M. J. Given, and T. Wang. "Performance Optimisation of Plasma Closing Switch Filled With Environmentally Friendly Gases," 15th Technological Plasma Workshop, Coventry, 11th-12th October 2017.

CHAPTER.11 REFERENCES

K. Adamiak, K. and Atten, P. 2004. "Simulation of corona discharge in point–plane configuration." *Journal of Electrostatics* 61: 85-98. https://doi.org/10.1016/j.elstat.2004.01.021.

Akiyama, H., Kristiansen, M., Krompholz, H. and Maas, B. 1988. "Current-voltage characteristics of a high-current pulsed discharge in air." *IEEE Transactions on Plasma Science* 16 (2): 312-316. https://doi.org/10.1109/27.3830.

Alston, Liviu Leonard, ed. 1968. *High-voltage technology*. Oxford University Press.

Barannik, S.I., Vasserman, S.B. and Lukin, A.N. 1975. "Resistance and inductance of a gas arc." *Soviet Physics Technical Physics* 19: 1449-1453.

Bernstein, B. and Smith, I. 1973. "Aurora, An Electron Accelerator." *IEEE Transactions on Nuclear Science* 20 (3): 294-300. https://doi.org/10.1109/TNS.1973.4327104.

Beroual, A. and Haddad, A. 2017. "Recent Advances in the Quest for a New Insulation Gas with a Low Impact on the Environment to Replace Sulfur Hexafluoride (SF6) Gas in High-Voltage Power Network Applications." *Energies* 10 (8). https://doi.org/10.3390/en10081216.

Beveridge, J.R., MacGregor, S.J., Given, M.J., Timoshkin, I.V. and Lehr, J.M. 2009. "A Corona-Stabilised Plasma Closing Switch." *IEEE Transactions on Dielectrics and Electrical Insulation* 16 (4): 948-955. https://doi.org/10.1109/IPMC.2008.4743697.

Beverly, Robert. 2001. "Application Information for SG-Series Spark-Gap Switches."

Bluhm, H. 2006a. *Power Systems*. Springer.

Bluhm, Hansjoachim. 2006b. *Pulsed Power Systems: Principles and Applications.Power Systems*: Springer Berlin/Heidelberg.

Bondiou, A., and I. Gallimberti. 1994. "Theoretical modelling of the development of the positive spark in long gaps." *Journal of Physics D: Applied Physics* 27 (6): 1252-1266. https://doi.org/10.1088/0022-3727/27/6/024. http://dx.doi.org/10.1088/0022-3727/27/6/024.

Braginskii, S. I. 1958. "Theory of the Development of a Spark Channel." *Sov. Phys. JETP* 34: 1068-1074. https://ci.nii.ac.jp/naid/10019124452/en/.

Broadbent, T. E. 1957. "The breakdown mechanism of certain triggered spark gaps." *British Journal of Applied Physics* 8 (1): 37-40.

Brown, Sanborn Conner. 1966. "Introduction to electrical discharges in gases."

Burkes, T. R., J. P. Craig, M. O. Hagler, M. Kristiansen, and W. M. Portnoy. 1979. "A review of high-power switch technology." *IEEE Transactions on Electron Devices* 26 (10): 1401-1411. https://doi.org/10.1109/T-ED.1979.19621.

Cai, Li, Lee Li, Chaobin Bao, Liu Yunlong, Yu Bin, Ge Yafeng, Xie Longjun, and Fuchang Lin. 2013. "Study of characteristics and performance optimization of a three-electrode spark gap." *IEEE Transactions on Dielectrics and Electrical Insulation* 20 (4): 1032-1039.

Can, Guo, Zhang Qiaogen, Zhang Lingli, Ma Jingtan, Wu Zhicheng, and Chen Ming. 2017. "Influence of electric field non-uniformity on discharge characteristics in SF6/N2 gas mixtures under power frequency voltage." 2017 IEEE Electrical Insulation Conference (EIC), pp. 74-77. IEEE, 2017.

Carey, W. J., A. J. Wiebe, R. D. Nord, and L. L. Altgilbers. 2011. "Characterization of Paschen curve anomolies at high P*D values." 2011 IEEE Pulsed Power Conference, pp. 741-744. IEEE.

Cary, W. K., and J. A. Mazzie. 1979. "Time-resolved resistance during spark gap breakdown." *IEEE Transactions on Electron Devices* 26 (10): 1422-1427. https://doi.org/10.1109/T-ED.1979.19625.

Castera, Philippe. 2015. "Energy coupling mechanisms in pulsed surface discharges for flow control." Ecole Centrale Paris (2015ECAP0041). https://tel.archives-ouvertes.fr/tel-01225674.

Chang, J., P. A. Lawless, and T. Yamamoto. 1991. "Corona discharge processes." *IEEE Transactions on Plasma Science* 19 (6): 1152-1166. https://doi.org/10.1109/27.125038.

Chen, L., P. Widger, M. S. Kamarudin, H. Griffiths, and A. Haddad. 2017. "CF3I Gas Mixtures: Breakdown Characteristics and Potential for Electrical Insulation." *IEEE Transactions on Power Delivery* 32 (2): 1089-1097. https://doi.org/10.1109/TPWRD.2016.2602259.

Chen, Y. J., J. J. Mankowski, J. C. Dickens, J. Walter, and M. Kristiansen. 2008. "Low-Jitter Triggered Spark Gap With High-Pressure Gas Mixtures." *IEEE Transactions on Plasma Science* 36 (5): 2546-2553. https://doi.org/10.1109/TPS.2008.2004366.

Christophorou, Giannis, D. L. McCorkle, and Scott Hunter. 1987. "GAS MIXTURES FOR SPARK GAP CLOSING SWITCHES WITH EMPHASIS ON EFFICIENCY OF OPERATION." In *Gaseous Dielectrics V*, 381-388. Pergamon.

Chu, K. W., and G. L. Scott. 1999-02-01 1999. *A Comparison of High-Voltage Switches.* (United States). https://www.osti.gov/servlets/purl/3560.

Clough, S., K. Thomas, M. Williamson, A. Jones, I. Smith, V. Bailey, P. Corcoran, and H. Kishi. 2005. "Triggering of 1.5 MV SF6 Filled Blumlein Switches." *2005 IEEE Pulsed Power Conference*: 655-658. https://doi.org/10.1109/PPC.2005.300744.

Cobine, J. D. 1941. *Gaseous Conductors: Theory and Engineering Applications*. Vol. 27. McGraw-Hill book Company, Incorporated.

Coelho, R., and J. Debeau. 1971. "Properties of the tip-plane configuration." *Journal of Physics D: Applied Physics* 4 (9): 1266-1280. https://doi.org/10.1088/0022-3727/4/9/305. http://dx.doi.org/10.1088/0022-3727/4/9/305.

Cong, P., G. Zhang, L. Sheng, T. Sun, H. Wu, Z. Zeng, and A. Qiu. 2013. "Reproducibility of Microsecond Self-Breakdown Water Switch With Negative Field Enhancement." *IEEE Transactions on Plasma Science* 41 (2): 355-359. https://doi.org/10.1109/TPS.2013.2238255.

Cook, D. L., G. O. Allshouse, J. Bailey, G. W. Barr, J. D. Boyes, E. L. Burgess, W. B. Boyer, J. S. Cap, R. S. Coats, P. L. Dreike, H. G. Fifer, J. P. Furaus, R. A. Gerber, S. Goldsmith, S. A. Goldstein, R. A. Hamil, D. R. Humphreys, R. J. Leeper, D. H.

McDaniel, T. H. Martin, C. W. Mendel, P. A. Miller, L. P. Mix, E. L. Neau, J. N. Olsen, G. D. Peterson, K. R. Prestwich, J. P. Quintenz, G. E. Rochau, S. E. Rosenthal, D. C. Rovang, C. L. Ruiz, L. Schneider, L. O. Seamons, D. B. Seidel, T. N. Simmons, S. A. Slutz, R. W. Stinnett, W. A. Stygar, M. A. Sweeney, K. M. Tolk, B. N. Turman, J. M. Wilson, and J. P. VanDevender. 1986. "Progress in light ion beam fusion research on PBFA II." *Plasma Physics and Controlled Fusion* 28 (12B): 1921-1930. https://doi.org/10.1088/0741-3335/28/12b/004. http://dx.doi.org/10.1088/0741-3335/28/12B/004.

Craggs, J. D., M. E. Haine, and J. M. Meek. 1946. "The development of triggered spark-gaps for high-power modulators." *Journal of the Institution of Electrical Engineers-Part IIIA: Radiolocation* 93 (5): 963-976.

Cristina, S., G. Dinelli, and M. Feliziani. 1991. "Numerical computation of corona space charge and V-I characteristic in DC electrostatic precipitators." *IEEE Transactions on Industry Applications* 27 (1): 147-153. https://doi.org/10.1109/28.67546.

Crull, E., H. Krompholz, A. Neuber, and L. Hatfield. 2004. "Pulsed gas breakdown with high overvoltages in argon and air." *The 31st IEEE International Conference on Plasma Science, 2004. ICOPS 2004. IEEE Conference*: 273. https://doi.org/10.1109/PLASMA.2004.1339921.

Demenik, I. V. 1968. "Resistance of a xenon plasma in a large flash lamp." *Sov. Phys.-Tech. Phys.* 13: 829.

Dick, A. R., S. J. MacGregor, M. T. Buttram, R. C. Pate, L. F. Rinehart, and K. R. Prestwich. 2000. "Breakdown phenomena in ultra-fast plasma closing switches." *IEEE Transactions on Plasma Science* 28 (5): 1456-1462. https://doi.org/10.1109/27.901214.

Dougal, R. A., and G. Morris. 1992. "Closing/opening switch for inductive energy storage applications." *IEEE Transactions on Plasma Science* 20 (1): 42-46. https://doi.org/10.1109/27.120193.

Dougal, R. A., G. Morris, and G. D. Volakakis. 1991. "Low-loss, high-repetition-rate vacuum switching." *IEEE Transactions on Plasma Science* 19 (5): 976-988. https://doi.org/10.1109/27.108442.

Driga, M. D., and H. D. Fair. 1991. "Advanced concepts for electromagnetic launcher power supplies incorporating magnetic flux compression." *IEEE transactions on magnetics* 27 (1): 350-355.

Dutton, J., F. Llewellyn Jones, and R. W. Palmer. 1961. "Electrical breakdown of gases: ionization growth in air at high pressures." *Proceedings of the Physical Society (1958-1967)* 78 (4): 569.

Engel, A. V., and Max Steenbeck. 2013. *Elektrische Gasentladungen: ihre Physik und Technik*. Springer-Verlag.

Engel, T. G., A. L. Donaldson, and M. Kristiansen. 1989. "The pulsed discharge arc resistance and its functional behavior." *IEEE Transactions on Plasma Science* 17 (2): 323-329. https://doi.org/10.1109/27.24643.

Engel, Thomas G., William C. Nunnally, and Nathanial B. VanKirk. 1999. "Design and development of a novel flux compression generator for landmine detection applications." *IEEE transactions on Magnetics* 35 (1): 245-249.

Fridman, A., A. Chirokov, and A. Gutsol. 2005. "Non-thermal atmospheric pressure discharges." *Journal of Physics D: Applied Physics* 38 (2): R1-R24. https://doi.org/10.1088/0022-3727/38/2/r01.

Fridman, A., and L. A. Kennedy. 2004. *Plasma Physics and Engineering*. Taylor & Francis.

Gallimberti, I., J. K. Hepworth, and R. C. Klewe. 1974. "Spectroscopic investigation of impulse corona discharges." *Journal of Physics D: Applied Physics* 7 (6): 880-898. https://doi.org/10.1088/0022-3727/7/6/315. http://dx.doi.org/10.1088/0022-3727/7/6/315.

Gaudet, J. A., R. J. Barker, C. J. Buchenauer, C. Christodoulou, J. Dickens, M. A. Gundersen, R. P. Joshi, H. G. Krompholz, J. F. Kolb, A. Kuthi, M. Laroussi, A. Neuber, W. Nunnally, E. Schamiloglu, K. H. Schoenbach, J. S. Tyo, and R. J. Vidmar. 2004. "Research issues in developing compact pulsed power for high peak power applications on mobile platforms." *Proceedings of the IEEE* 92 (7): 1144-1165. https://doi.org/10.1109/JPROC.2004.829006.

Go, David B., and Daniel A. Pohlman. 2010. "A mathematical model of the modified Paschen's curve for breakdown in microscale gaps." *Journal of Applied Physics* 107 (10): 103303. https://doi.org/10.1063/1.3380855. https://doi.org/10.1063/1.3380855.

Greason, W. D. 1999. "Methodology to study the resistance of spark discharges." *IEEE Transactions on Industry Applications* 35 (2): 359-365. https://doi.org/10.1109/28.753629.

Grover, F. W. 2004. *Inductance Calculations: Working Formulas and Tables*.*Dover phoenix editions*: Dover Publications.

Gundersen, M. A. 1991. "Gas-phase pulsed power switches." *IEEE Transactions on Plasma Science* 19 (6): 1123-1131. https://doi.org/10.1109/27.125035.

Harrower, J. A., S. J. MacGregor, and F. A. Tuema. 1999. "Design considerations for corona-stabilized repetitive switches." *Journal of Physics D: Applied Physics* 32 (7): 790-797. https://doi.org/10.1088/0022-3727/32/7/007. http://dx.doi.org/10.1088/0022-3727/32/7/007.

Hogg, M. G., I. V. Timoshkin, S. J. Mcgregor, M. P. Wilson, and M. J. Given. 2015. "Polarity effects on breakdown of short gaps in a point-plane topology in air." *IEEE Transactions on Dielectrics and Electrical Insulation* 22 (4): 1815-1822. https://doi.org/10.1109/TDEI.2015.005029.

Hösl, A., P. Häfliger, and C. M. Franck. 2017. "Measurement of ionization, attachment, detachment and charge transfer rate coefficients in dry air around the critical electric field." *Journal of Physics D: Applied Physics* 50 (48): 485207. https://doi.org/10.1088/1361-6463/aa8faa.

Humphries, S. 1987. "Pulsed Power Opening Switch Research at the University of New Mexico." *IEEE Transactions on Plasma Science* 15 (6): 772-780. https://doi.org/10.1109/TPS.1987.4316790.

Husain, E., and R. S. Nema. 1982. "Analysis of Paschen Curves for air, N2 and SF6 Using the Townsend Breakdown Equation." *IEEE Transactions on Electrical Insulation* EI-17 (4): 350-353. https://doi.org/10.1109/TEI.1982.298506.

Hussain, Safdar, and M. Zakaullah. 2007. "Reliable Field Distortion Spark Gap for Plasma Focus." *Plasma Science and Technology* 9: 504. https://doi.org/10.1088/1009-0630/9/4/27.

Hussey, T. W., K. J. Davis, J. M. Lehr, N. F. Roderick, R. C. Pate, and E. Kunhardt. 1999. "Dynamics of nanosecond spark-gap channels." *Digest of Technical Papers. 12th IEEE International Pulsed Power Conference. (Cat. No.99CH36358)* 2: 1171-1174 https://doi.org/10.1109/PPC.1999.823730.

Jiang, J., J. Liu, M. Liu, and M. He. 2015. "Design and construction of a ±100 kV gas switch for linear transformer drivers." *IEEE Transactions on Dielectrics and Electrical Insulation* 22 (2): 1292-1297. https://doi.org/10.1109/TDEI.2015.7076833.

Jiasen, Chang, Wang Hu, Zhang Qiaogen, and Qiu Aici. 2011. "Multichannel Discharge Characteristics of Gas Switch Gap in SF6-N2 or SF6Ar Gas Mixtures Under Nanosecond Triggering Pulses." *Plasma Science & Technology - PLASMA SCI TECHNOL* 13: 719-723. https://doi.org/10.1088/1009-0630/13/6/16.

Ju, J., J. Zhang, T. Shu, and H. Zhong. 2017. "An Improved X-Band Triaxial Klystron Amplifier for Gigawatt Long-Pulse High-Power Microwave Generation." *IEEE Electron Device Letters* 38 (2): 270-272. https://doi.org/10.1109/LED.2016.2646679.

Judd, M. D. 2001. "Contact discharges as a source of sub-nanosecond high voltage pulses." *Journal of Physics D Applied Physics* 34: 2883-2893. https://doi.org/10.1088/0022-3727/34/18/323.

Katagiri, H., H. Kasuya, H. Mizoguchi, and S. Yanabu. 2008. "Investigation of the performance of CF₃I Gas as a Possible Substitute for SF₆." *IEEE Transactions on Dielectrics and Electrical Insulation* 15 (5): 1424-1429. https://doi.org/10.1109/TDEI.2008.4656252.

Kawamura, Tatsuo, Satoshi Matsumoto, Masahiro Hanai, and Yasufumi Murayama. 1998. "SF 6/N 2 mixtures for HV equipment and practical problems." In *Gaseous Dielectrics VIII*, 333-343. Springer.

Khalifa, M. 1990. *High-voltage Engineering: Theory and Practice*.*Clinical Guides to Medical Management*: M. Dekker.

Kim, A. A., B. M. Kovalchuk, V. V. Kremnev, E. V. Krumpjak, A. A. Novikov, B. Etlicher, L. Frescaline, J. F. Leon, B. Roques, F. Lassalle, R. Lample, G. Avrillaud, and F. Kovacs. 1997. "Multi gap, multi channel spark switches." *Digest of Technical Papers. 11th IEEE International Pulsed Power Conference (Cat. No.97CH36127)* 2: 862-867 https://doi.org/10.1109/PPC.1997.674501.

Kiyan, Tsuyoshi, Takeshi Ihara, Suguru Kameda, Tomohiro Furusato, Masanori Hara, and Hidenori Akiyama. 2011. "Weibull statistical analysis of pulsed breakdown voltages in high-pressure carbon dioxide including supercritical phase." *IEEE Transactions on Plasma Science* 39 (8): 1729-1735.

Kline, L. E., D. K. Davies, C. L. Chen, and P. J. Chantry. 1979. "Dielectric properties for SF6 and SF6 mixtures predicted from basic data." *Journal of Applied Physics* 50 (11): 6789-6796. https://doi.org/10.1063/1.325814. https://doi.org/10.1063/1.325814.

Koch, M., and C. M. Franck. 2015. "High voltage insulation properties of HFO1234ze." *IEEE Transactions on Dielectrics and Electrical Insulation* 22 (6): 3260-3268. https://doi.org/10.1109/TDEI.2015.005118.

Koutoula, S. G., I. V. Timoshkin, M. D. Judd, S. J. MacGregor, M. P. Wilson, M. J. Given, T. Wang, and E. I. Harrison. 2016. "A Study of Energy Partition During Arc Initiation." *IEEE Transactions on Plasma Science* 44 (10): 2137-2144. https://doi.org/10.1109/TPS.2016.2579312.

Kristiansen, M. 1993. "Pulsed power applications." *Ninth IEEE International Pulsed Power Conference* 1: 6. https://doi.org/10.1109/PPC.1993.512864.

Kuffel, J., and E. Kuffel. 2000. *High Voltage Engineering Fundamentals*. Elsevier Science.

Kunhardt, E. E., C. Sutton, and D. Danner. 1984. "DC Breakdown of C3F8/Ar and C3F8/N2 Mixtures." *IEEE Transactions on Plasma Science* 12 (3): 232-233. https://doi.org/10.1109/TPS.1984.4316325.

Kunhardt, Erich E. 1980. "Electrical breakdown of gases: The prebreakdown stage." *IEEE Transactions on Plasma Science* 8 (3): 130-138.

Kushner, M. J., W. D. Kimura, and S. R. Byron. 1985. "Arc resistance of laser-triggered spark gaps." 58 (5): 1744-1751. https://doi.org/10.1063/1.336023. https://aip.scitation.org/doi/abs/10.1063/1.336023.

Lama, W. L., and C. F. Gallo. 1974. "Systematic study of the electrical characteristics of the ``Trichel'' current pulses from negative needle-to-plane coronas." *Journal of Applied Physics* 45 (1): 103-113. https://doi.org/10.1063/1.1662943. https://doi.org/10.1063/1.1662943.

Larsson, A., D. Yap, J. Au, and T. E. Carlsson. 2014. "Laser Triggering of Spark Gap Switches." *IEEE Transactions on Plasma Science* 42 (10): 2943-2947. https://doi.org/10.1109/TPS.2013.2297161.

LeChien, K. R., W. A. Stygar, M. E. Savage, P. E. Wakeland, V. Anaya, D. S. Artery, M. J. Baremore, D. E. Bliss, R. Chavez, G. D. Coombs, J. P. Corley, P. A. Jones, A. K. Kipp, B. A. Lewis, J. A. Lott, J. J. Lynch, G. R. McKee, S. D. Ploor, K. R. Prestwich, S. A. Roznowski, D. C. Spencer, S. D. White, and J. R. Woodworth. 2010. "6.1-MV, 0.79-MA laser-triggered gas switch for multimodule, multiterawatt pulsed-power accelerators." *Physical Review Special Topics - Accelerators and Beams* 13 (3): 030401. https://doi.org/10.1103/PhysRevSTAB.13.030401. https://link.aps.org/doi/10.1103/PhysRevSTAB.13.030401.

Lee, H. W., S. K. Kang, S. K. Kwon, I. H. Won, H. Y. Kim, J. K. Lee, and H. W. Lee. 2013. "Enhancement of microwave plasma characteristics for biomedical applications using pulse modulation method." 2013 19th IEEE Pulsed Power Conference (PPC)

Lee, Woo-Young, Jang-Un Jun, Ho-Seok Oh, Jun-Kyu Park, Yeon-Ho Oh, Ki-Dong Song, and Hyun-Jae Jang. 2020. "Comparison of the Interrupting Capability of Gas Circuit Breaker According to SF6, g3, and CO2/O2 Mixture." *Energies* 13: 6388. https://doi.org/10.3390/en13236388. https://mdpi-res.com/d_attachment/energies/energies-13-06388/article_deploy/energies-13-06388-v2.pdf?version=1607390226.

Li, L., Z. Huang, and Y. Yang. 2020. "The Influence of Electric Field Inhomogeneity on Repetitive Performance of a Corona-Stabilized Switch." *IEEE Access* 8: 195515-195527. https://doi.org/10.1109/ACCESS.2020.3033327.

Li, X., X. Liu, F. Zeng, H. Yang, and Q. Zhang. 2014. "Study on Resistance and Energy Deposition of Spark Channel Under the Oscillatory Current Pulse." *IEEE Transactions on Plasma Science* 42 (9): 2259-2265. https://doi.org/10.1109/TPS.2014.2331346.

Lister, G. G., Y. -M Li, and V. A. Godyak. 1996. "Electrical conductivity in high-frequency plasmas." *Journal of Applied Physics* 79 (12): 8993-8997. https://doi.org/10.1063/1.362631. https://doi.org/10.1063/1.362631.

Liu, J. L., B. Ye, T. W. Zhan, J. H. Feng, J. D. Zhang, and X. X. Wang. 2009. "Coaxial Capacitive Dividers for High-Voltage Pulse Measurements in Intense Electron Beam Accelerator With Water Pulse-Forming Line." *IEEE Transactions on Instrumentation and Measurement* 58 (1): 161-166. https://doi.org/10.1109/TIM.2008.927195.

Liu, Jin-liang, Yi Yin, Tian-wen Zhan, Jia-huai Feng, Hui-huang Zhong, and Xin-xin Wang. 2008. "Application of a self-breakdown hydrogen spark gap switch on high power pulse modulator." *Journal of Applied Physics* 104 (8): 083307. https://doi.org/10.1063/1.3005902. https://doi.org/10.1063/1.3005902.

Liu, S., Y. j. Fan, and Lei Shi. 2008. "Experimental study on high pressure hydrogen gas switch breakdown." *2008 17th International Conference on High Power Particle Beams (BEAMS)*: 1-4.

Llewellyn-Jones, F. 1957. *Ionization and breakdown in gases*. Methuen.

Loeb, Leonard B. 1955. *Basic processes of gaseous electronics*. Berkeley: University of California Press.

Loeb, Leonard B., and Arthur F. Kip. 1939. "Electrical Discharges in Air at Atmospheric Pressure The Nature of the Positive and Negative Point-to-Plane Coronas and the Mechanism of Spark Propagation." *Journal of Applied Physics* 10 (3): 142-160. https://doi.org/10.1063/1.1707290. https://doi.org/10.1063/1.1707290.

Loeb, Leonard B., and John M. Meek. 1940. "The Mechanism of Spark Discharge in Air at Atmospheric Pressure. I." *Journal of Applied Physics* 11 (6): 438-447. https://doi.org/10.1063/1.1712792. https://doi.org/10.1063/1.1712792.

Maas, B. L. 1985. *Arc Current, Voltage, and Resistance in a High Energy, Gas-filled Spark Gap*. Texas Tech University.

MacGregor, S. J., S. M. Turnbull, F. A. Tuema, and O. Farish. 1996. "The application of corona stabilised breakdown to repetitive switching." *'96 IEE Colloquium on Pulsed Power*: 21/1-21/3. https://doi.org/10.1049/ic:19960395.

Mahdy, A. M. 2011. "Assessment of breakdown voltage of SF6/N2 gas mixtures under non-uniform field." *IEEE Transactions on Dielectrics and Electrical Insulation* 18 (2): 607-612. https://doi.org/10.1109/TDEI.2011.5739467.

Malik, N. H., and A. H. Qureshi. 1979. "A Review of Electrical Breakdown in Mixtures of SF6 and Other Gases." *IEEE Transactions on Electrical Insulation* EI-14 (1): 1-13. https://doi.org/10.1109/TEI.1979.298198.

Mardikyan, Kevork, Serhat Seker, and Emine Ayaz. 2000. "Breakdown strength estimation of air and a mixture of air+SF6 using artificial neural network approach." 43: 1-14.

Markins, D. 1971. "Command triggering of synchronized megavolt pulse generators." *IEEE Transactions on Nuclear Science* 18 (4): 296-302.

Martin, J. C. 1995. "The pre-history of pulsed power." *'95 IEE Colloquium on Pulsed Power*: 1/1-1/3. https://doi.org/10.1049/ic:19950284.

Martin, T. H. 1969. "Design and Performance of the Sandia Laboratories Hermes II Flash X-Ray Generator." *IEEE Transactions on Nuclear Science* 16 (3): 59-63. https://doi.org/10.1109/TNS.1969.4325178.

Martin, T. H., M. Williams, and M. Kristiansen. 2014. *J. C. Martin on Pulsed Power*. Springer.

McDonald, K., M. Newton, E. E. Kunhardt, M. Kristiansen, and A. H. Guenther. 1980. "An electron-beam triggered spark gap." *IEEE Transactions on Plasma Science* 8 (3): 181-185.

McGarvey, Caron. 2017. "Characterisation of plasma closing switches filled with different gases." University of Strathclyde.

Meek, J. M., and J. D. Craggs. 1954. *Electrical Breakdown of Gases*.*Electrical Breakdown of Gases*: Clarendon Press.

Mercer, S., I. Smith, and T. Martin. 1976. "A Compact, Multiple Channel 3 MV Gas Switch." In *Energy Storage, Compression, and Switching*, edited by W. H. Bostick, V. Nardi and O. S. F. Zucker, 459-462. Boston, MA: Springer US.

Mesyats, Gennady A. 2007. *Pulsed power*. Springer Science & Business Media.

Mizuno, A., J. S. Clements, and R. H. Davis. 1986. "A Method for the Removal of Sulfur Dioxide from Exhaust Gas Utilizing Pulsed Streamer Corona for Electron Energization." *IEEE Transactions on Industry Applications* IA-22 (3): 516-522. https://doi.org/10.1109/TIA.1986.4504752.

Morrow, R. 1985. "Theory of negative corona in oxygen." *Physical Review A* 32 (3): 1799-1809. https://doi.org/10.1103/PhysRevA.32.1799.

Morrow, R., and J. J. Lowke. 1997. "Streamer propagation in air." *Journal of Physics D: Applied Physics* 30 (4): 614. http://stacks.iop.org/0022-3727/30/i=4/a=017.

Ngoc, M. Nguyen, A. Denat, N. Bonifaci, O. Lesaint, W. Daoud, and M. Hassanzadeh. "Electrical breakdown of CF 3 I and CF3I-N2 gas mixtures." 2009.

Nijdam, Sander, Jannis Teunissen, and Ute Ebert. 2020. "The physics of streamer discharge phenomena." *Plasma Sources Science and Technology* 29 (10): 103001. https://doi.org/10.1088/1361-6595/abaa05.

Paschen, Friedrich. 1889. "Ueber die zum Funkenübergang in Luft, Wasserstoff und Kohlensäure bei verschiedenen Drucken erforderliche Potentialdifferenz." *Annalen der Physik* 273: 69-96. https://doi.org/10.1002/andp.18892730505.

Pedrow, P. D., K. O. Goyal, R. Mabalingham, and M. A. Osman. 1997. "Explosion model applied to an intense pulsed plasma source for thin film deposition." *IEEE Transactions on Plasma Science* 25 (1): 89-96. https://doi.org/10.1109/27.557490.

Peek, F. W., and H. K. Humphrey. 1915. *Dielectric Phenomena in High Voltage Engineering*. McGraw-Hill Book Company, Incorporated.

Peng, T., F. Jiang, Q. Q. Sun, Q. Xu, H. X. Xiao, F. Herlach, and L. Li. 2014. "Design and Test of a 90-T Nondestructive Magnet at the Wuhan National High Magnetic Field Center." *IEEE Transactions on Applied Superconductivity* 24 (3): 1-4. https://doi.org/10.1109/TASC.2013.2284273.

Peterkin, F. E., and P. F. Williams. 1989. "Triggering of trigatron spark gaps." *7th Pulsed Power Conference*: 559-562. https://doi.org/10.1109/PPC.1989.767547.

Pokryvailo, A., Y. Yankelevich, M. Wolf, E. Abramzon, S. Wald, and A. Welleman. 2004. "A high-power pulsed corona source for pollution control applications." *IEEE Transactions on Plasma Science* 32 (5): 2045-2054. https://doi.org/10.1109/TPS.2004.835952.

Popovic, M. M., S. S. Popovic, and M. M. Platisa. "Investigation of the beginning of high current discharges in pulsed arcs." 1974.

Protocol, Kyoto. 1997. "United Nations framework convention on climate change." *Kyoto Protocol, Kyoto* 19 (8).

Qin, Si, Igor Timoshkin, Michelle Maclean, Mark Wilson, S. J. MacGregor, Martin Given, John Anderson, and T. Wang. 2014. "Pulsed Electric Field Treatment of Microalgae: Inactivation Tendencies and Energy Consumption." *IEEE Transactions on Plasma Science* Accepted for publication. https://doi.org/10.1109/TPS.2014.2317522.

Rabie, Mohamed, and Christian M. Franck. 2018. "Assessment of Eco-friendly Gases for Electrical Insulation to Replace the Most Potent Industrial Greenhouse Gas SF6." *Environmental Science & Technology* 52 (2): 369-380. https://doi.org/10.1021/acs.est.7b03465.

Raether, Heinz. 1964. *Electron avalanches and breakdown in gases*. Butterworths.

Raizer, Y. P. 2017. *Spark Discharge*. CRC Press.

Raizer, Y. P., V. I. Kisin, and J. E. Allen. 2011. *Gas Discharge Physics*. Springer Berlin Heidelberg.

Rizk, Farouk A. M., and Giao N. Trinh. 2018. *High voltage engineering*. CRC Press.

Robledo-Martinez, A. 1993. "Characteristics of DC corona discharge in humid, reduced-density air." *Journal of Electrostatics* 29 (2): 101-111. https://doi.org/https://doi.org/10.1016/0304-3886(93)90099-S.

Rokunohe, Toshiaki, Yoshitaka Yagihashi, Fumihiro Endo, and Takashi Oomori. 2005. "Fundamental insulation characteristics of air; N2, CO2, N2/O2, and SF6/N2 mixed gases." *Electrical Engineering in Japan* 155: 9-17. https://doi.org/10.1002/eej.20348.

Rompe, R., and W. Weizel. 1944. "Über das Toeplersche Funkengesetz." 122 (9): 636-639. https://doi.org/10.1007/bf01330625. https://doi.org/10.1007/BF01330625.

Santamaria, F., and F. Román. 2013. "Experimental Study of a Submillimeter Spark-Gap." *IEEE Transactions on Plasma Science* 41 (4): 985-992. https://doi.org/10.1109/TPS.2013.2249531.

Schaefer, Gerhard, M. Kristiansen, and Arthur Henry Guenther. 1990. *Gas discharge closing switches*. New York, N.Y.: Plenum Press.

Schaefer, Gerhard, Magne Kristiansen, and Arthur Henry Guenther. 2013. *Gas discharge closing switches*. Vol. 2. Springer Science & Business Media.

Sharma, A., S. Kumar, S. Mitra, V. Sharma, A. Patel, A. Roy, R. Menon, K. V. Nagesh, and D. P. Chakravarthy. 2011. "Development and Characterization of Repetitive 1-kJ Marx-Generator-Driven Reflex Triode System for High-Power Microwave Generation." *IEEE Transactions on Plasma Science* 39 (5): 1262-1267. https://doi.org/10.1109/TPS.2011.2116809.

Sharma, D. K., R. N. Rajan, S. K. Srivastava, S. Dewangan, D. Jayaprakash, R. I. Bakhtsingh, S. Acharya, and L. M. Gantayet. 2014. "H.V. support structure of 3MVDC generator and its protection from HV discharges in vacuum and SF6 gas for DC electron Accelerator." *2014 International Symposium on Discharges and Electrical Insulation in Vacuum (ISDEIV)*: 649-651. https://doi.org/10.1109/DEIV.2014.6961766.

Singhasathein, A., A. Pruksanubal, N. Tanthanuch, and W. Rungseevijitprapa. 2013. "Dielectric strength of breakdown voltage of Nitrogen and Carbon-dioxide." *2013 10th International Conference on Electrical Engineering/Electronics, Computer, Telecommunications and Information Technology*: 1-5. https://doi.org/10.1109/ECTICon.2013.6559491.

Smith, I. 1991. "Pulsed Power In The United States." Eighth IEEE International Conference on Pulsed Power, 16-19 June 1991.

Sorensen, T. P., and V. M. Ristic. 1977. "Rise time and time-dependent spark-gap resistance in nitrogen and helium." *Journal of Applied Physics* 48 (1): 114-117. https://doi.org/10.1063/1.323311. https://doi.org/10.1063/1.323311.

Spitzer, L. 2006. *Physics of Fully Ionized Gases*.*Dover Books on Physics*: Dover Publications.

Spyrou, N., and C. Manassis. 1989. "Spectroscopic study of a positive streamer in a point-to-plane discharge in air: evaluation of the electric field distribution." *Journal of Physics D: Applied Physics* 22 (1): 120-128. https://doi.org/10.1088/0022-3727/22/1/017.

Timoshkin, I. V., J. W. Mackersie, and S. J. MacGregor. 2004. "Plasma channel miniature hole drilling technology." *IEEE Transactions on Plasma Science* 32 (5): 2055-2061. https://doi.org/10.1109/TPS.2004.835489.

Toepler, Max. 1927. "Zusammenhang zwischen Funken, Büschellichtbogen und Bogen." *Archiv für Elektrotechnik* 18 (6): 563-566. https://doi.org/10.1007/BF01656201. https://doi.org/10.1007/BF01656201.

Torres, C., P. G. Reyes, F. Castillo, and H. Martínez. 2012. "Paschen law for argon glow discharge." *Journal of Physics: Conference Series* 370: 012067. https://doi.org/10.1088/1742-6596/370/1/012067.

Townsend, J. S. 1915. *Electricity in Gases*. Clarendon Press.

Tran, V., T. Park, H. Choi, and J. Choi. 2015. "High efficiency and reliability pulsed power system for medical lasers with the digital controller." *2015 IEEE Pulsed Power Conference (PPC)*: 1-6. https://doi.org/10.1109/PPC.2015.7296860.

Trichel, G. W. 1939. "The Mechanism of the Positive Point-to-Plane Corona in Air at Atmospheric Pressure." *Physical Review* 55 (4): 382-390. https://doi.org/10.1103/PhysRev.55.382.

Turnbull, S. M., S. J. MacGregor, and J. Harrower. 1997. "The repeatability of sphere-sphere spark gap columns." *IEE Colloquium on Pulsed Power '97 (Digest No: 1997/075)*: 23/1-23/4. https://doi.org/10.1049/ic:19970410.

Uchii, Toshiyuki, Yoshikazu Hoshina, Hiromichi Kawano, Katsumi Suzuki, Tetsuya Nakamoto, and Mitsuru Toyoda. 2007. "Fundamental Research on SF 6-free Gas Insulated Switchgear Adopting CO 2 Gas and Its Mixtures." ISETS07.

VanDevender, J. Pace. 1978. "The resistive phase of a high-voltage water spark." *Journal of Applied Physics* 49 (5): 2616-2620. https://doi.org/10.1063/1.325205.

Veldhuizen, E. M. van, and W. R. Rutgers. 2002. "Pulsed positive corona streamer propagation and branching." *Journal of Physics D: Applied Physics* 35 (17): 2169-2179. https://doi.org/10.1088/0022-3727/35/17/313.

Vlastós, Antonios E., Rompe R., and Weizel W. 1972. "The Resistance of Sparks." 43 (4): 1987-1989. https://doi.org/10.1063/1.1661429.

Vorobev, G. A., and G. A. Mesyats. 1971. *Technique of Shaping High-Voltage Nanosecond Pulses.* FOREIGN TECHNOLOGY DIV WRIGHT-PATTERSON AFB OH.

Wang, H., Q. Zhang, J. Wei, X. Liu, and A. Qiu. 2012. "Research on Erosion Property of Field-Distortion Gas Switch Electrode in Nanosecond Pulse." *IEEE Transactions on Plasma Science* 40 (6): 1733-1742. https://doi.org/10.1109/TPS.2012.2191162.

Wang, Lijun, Xiaolong Huang, Shenli Jia, Yu Liu, Shaohuang Shang, and Tao Du. 2014. "Experimental investigation of electrode erosion of trigatron in microsecond arc discharge process." *IEEE Transactions on Plasma Science* 42 (5): 1393-1399.

Wei, Hao, Aici Qiu, Fengju Sun, Xiaofeng Jiang, Jiahui Yin, Jiangtao Zeng, Tianxue Liang, Zhigang Liu, Zhiguo Wang, and Peng Liu. 2012. "±100 kV three-electrode field-distortion gas spark switch." *High Power Laser and Particle Beams* 24 (4): 881-884. http://inis.iaea.org/search/search.aspx?orig_q=RN:45093414.

Weibull, Waloddi. 1951. "A statistical distribution function of wide applicability." *Journal of applied mechanics* 18 (3): 293-297.

Widger, P., H. Griffiths, and A. Haddad. 2018. "Insulation strength of CF<inf>3</inf>I-CO<inf>2</inf> gas mixtures as an alternative to SF<inf>6</inf> in MV switch disconnectors." *IEEE Transactions on Dielectrics and Electrical Insulation* 25 (1): 330-338. https://doi.org/10.1109/TDEI.2018.006932.

Widger, Phillip, Daniel Carr, Alistair Reid, Meirion Hills, Chris Stone, and A. Haddad. 2020. "Partial Discharge Measurements in a High Voltage Gas Insulated Transmission Line Insulated with CO2." *Energies* 13 (11). https://doi.org/10.3390/en13112891.

Wilkinson, K. J. R. 1946. "Some developments in high-power modulators for radar." *Journal of the Institution of Electrical Engineers-Part IIIA: Radiolocation* 93 (6): 1090-1112.

Williams, P. F., and F. E. Peterkin. 1989. "Triggering in trigatron spark gaps: A fundamental study." *Journal of applied physics* 66 (9): 4163-4175.

Woodworth, J. R., J. A. Alexander, F. R. Gruner, W. A. Stygar, M. J. Harden, J. R. Blickem, G. J. Dension, F. E. White, L. M. Lucero, H. D. Anderson, L. F. Bennett, S. F. Glover, D. Van DeValde, and M. G. Mazarakis. 2009. "Low-inductance gas switches for linear transformer drivers." *Physical Review Special Topics - Accelerators and Beams* 12 (6): 060401. https://doi.org/10.1103/PhysRevSTAB.12.060401.

Xian-qin, D., X. Peng, Z. Su, and Z. Hui. 2017. "Research on insulation characteristics and decomposition products of c-C<inf>4</inf>F<inf>8</inf>/N<inf>2</inf> mixtures in slightly non-uniform electric field." *2017 4th International Conference on Electric Power Equipment - Switching Technology (ICEPE-ST)*: 251-254. https://doi.org/10.1109/ICEPE-ST.2017.8188839.

Xiao, Dengming. 2016. "Insulation Characteristics of Sulfur Hexafluoride (SF6)." In *Gas Discharge and Gas Insulation*, edited by Dengming Xiao, 195-229. Berlin, Heidelberg: Springer Berlin Heidelberg.

Yamada, Kimio. 2004. "An empirical formula for negative corona discharge current in point-grid electrode geometry." *Journal of Applied Physics* 96 (5): 2472-2475. https://doi.org/10.1063/1.1775301. https://doi.org/10.1063/1.1775301.

APPENDIX A. FUNDAMENTALS OF THE GAS DISCHARGE

Although there are many different types of gas-filled plasma closing switches, their operation dependents on the formation of the conductive discharge channel in the insulating gas between the switching electrodes. In order to control the conduction process in the switch, it is necessary to understand the discharge mechanisms of gas-filled plasma closing switches.

The breakdown process in the gas-filled plasma closing switches is the process of gas discharge, that is, the process of transferring from non-self-sustained discharge to self-sustained discharge and then potentially to the streamer discharge with the formation of the plasma conductive channel. The discharge process of gas can generally be divided into three stages: (i) The generation of charged particles; (ii) Maintenance of the discharge process; (iii) Disappearance of charged particles. In practical plasma closing switches, gas discharge mainly includes: (i) Townsend discharge (based on the development of electron avalanches); (ii) streamer discharge (rapid ionisation wave propagating in the gas), or corona discharge (incomplete discharge in areas where the electric field is above the critical electric field value); and (iii) formation of the conductive plasma channel. The gas discharge theory mainly includes the Townsend discharge theory and the Streamer theory. In this section, the discharge mechanism in gases is discussed.

A.1 Breakdown in the uniform electric field

This section considers the basic mechanisms of a discharge in a uniform electric field.

As shown in Figure A-1, a variable DC voltage is applied to two parallel flat plates (the electric field between the electrodes is uniform, and the medium between the electrodes is air). At the moment, corresponding to point A in Figure A.1, the external UV light provides photons with energy sufficient for ionising gas molecules and initial electrons forming in the gap. When the voltage gradually increases from zero, the

evolution of the current in the gas as a function of the applied voltage can be obtained, that is, the voltage-current (U-I) characteristic curve of the gas.

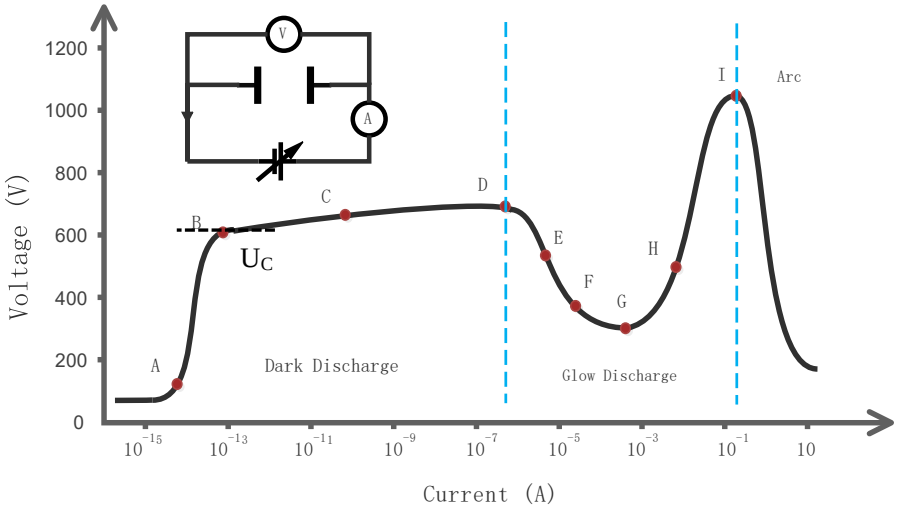

Figure A-1 Voltage–current (U–I) characteristics of electrical discharge under uniform field, in which point *A*: random pulses by radiation; *B*: saturation current; *C*: Townsend discharge; *D*: self-sustained discharge; *E*: corona discharge; *F*: sub-normal glow discharge; G: normal glow discharge; *H*: abnormal glow discharge; *I*: arc discharge.

As the voltage increases, the current will increase until it reaches its saturation value, point B. All the electrons emitted from the cathode and the electrons in the gas are attracted to the anode. The current does not increase with a further increase in the voltage. The current density in the saturated segment is minimal, typically of the order of $10^{-19}\,A/cm^2$, so the discharge gap still has a high resistance. This discharge is called dark discharge.

When the voltage increases further, the discharge is transformed into the glow discharge, and the current in the gap increases exponentially with the applied voltage. Thus, the discharge process reaches another phase, that is, the Townsend avalanche. Because the free electrons have accumulated sufficient kinetic energy to cause ionization when they collide with gas molecules in a sufficiently strong enough electric field and consequently produce additional electrons.

When the voltage continues to rise to a critical value of U_c, the current sharply increases, accompanied by distinct external characteristics, such as light emission. The medium in the gas gap suddenly becomes a good conductor. The experiment shows that when the applied voltage is less than U_c, the current through the gap is extremely small, and the gas gap has not yet lost insulation performance. The current will disappear if the external ionizing source (ultraviolet light) does not maintain. It is the non-self-sustained discharge. When the applied voltage increases to U_c, the ionization process in the gas can be maintained without any external ionization source. It is called the self-sustained discharge. *C* is the point of the boundary between the non-sustained discharge and the self-sustained discharge. The critical voltage U_c is called the breakdown voltage. However, in this phase, the discharge current ($< 10\mu A$) is minimal, and the light emission is very weak. Consequently, it is called a dark discharge. The current increases as the impedance decreases, and the discharge channel becomes smaller and brighter when the current increases to a specific value. The voltage across the electrodes decreases, indicating an increase in the electrical conductivity of the discharge channel. This type of discharge is called an arc discharge.

Different discharges can be formed in the gap depending on the gas pressure, electrode shape, and electrical power. A glow discharge is formed at lower electric power and gas pressure values. The glowing spark discharge can be formed at higher gas pressures in the gap. When the power is large enough and the circuit impedance is small, an arc discharge with a high current density and high temperature may occur. In the highly non-uniform electric field, a corona discharge with a thin ionisation layer around the electrodes can be formed.

A.1.1 Townsend electron avalanche theory

Due to external ionization factors, such as cosmic rays, radioactive radiation, ultraviolet light, etc., free electrons are generated near the cathode (Khalifa 1990). An electric field accelerates these initial electrons toward the anode, causing collisional ionization (by colliding with gas molecules) and producing additional free electrons. Those electrons (initial electrons and newly generated electrons) gain kinetic energy

in a significant electric field and continue to cause collisional ionization. This leads to a rapidly developing process of collisional ionization, in which the number of free electrons in the gap increases dramatically. The result of development is an avalanche multiplication or an electron avalanche (Townsend 1915). John Sealy Townsend discovered this phenomenon in 1897 at the Cavendish Laboratory, Cambridge. In the case of a non-self-sustained Townsend discharge, an external ionizing source should provide a sufficient number of seed electrons to develop the electron avalanche, as shown schematically in Figure A-2.

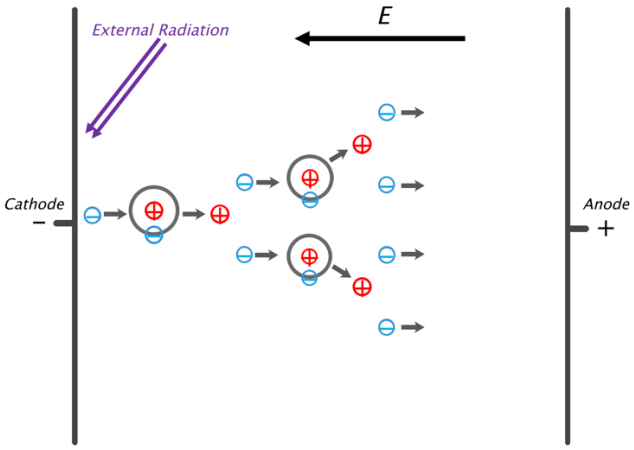

Figure A-2 The development of electron avalanche.

To describe the number of new ions (and electrons) produced on average by an electron travelling along the unit length in the direction of the electric field in the avalanche, Townsend's first ionization coefficient, α, is used (Brown 1966).

It is assumed that under the influence of external ionization factors (for example, photoionisation), n_0 electrons are generated near the cathode. In the external electric field, these electrons are accelerated and collide with gas atoms or molecules, causing collisional ionization in the process of moving towards the anode. After passing a distance *x*, the number of electrons becomes *n*, thus over a distance dx, the number of electrons increases, and becomes dn, so that

$$dn = \alpha n dx \qquad (A.1)$$

Integrating the above equation where α is the Townsend ionisation coefficient which is independent of *x* and the electrode gap is *d*, one can get the number of electrons reaching the anode is:

$$n = n_0 e^{\alpha d} \qquad (A.2)$$

alternatively, in terms of currents, the equation of the discharge current reaching the anode is:

$$i = i_0 e^{\alpha d} \qquad (A.3)$$

where i_0 is the initial current from the cathode by photoionizing the external source. The coefficient α is related to the field strength, *E*, and the gas conditions, including gas pressure *p* and temperature *T*. In principle and practice, α can be calculated in terms of *E* and *p* (Meek and Craggs 1954)

$$\frac{\alpha}{p} = Aexp\left(-\frac{Bp}{E}\right) \qquad (A.4)$$

where *A* and *B* are constant depending on the gas characters.

The above process only considers the collisional ionization in the gas between the electrodes. In fact, positive ions and photons with sufficient energy emit secondary electrons by bombarding the cathode surface and causing ionization on the cathode surface. To describe the number of emitted secondary electrons by an incident ion hitting the cathode surface, the second Townsend ionization coefficient γ was introduced. Experiments find that γ is related to gas properties, the electrode material and ion energy.

Let us suppose that n_0 electrons start to travel from the cathode to the anode, the number of electrons will be $n_0 e^{\alpha d}$ (including an initial electron) when they arrive at

the anode due to the electron multiplication process caused by collision ionization. Removing the initial electron, the number of new electrons or positive ions is $(n_0 e^{\alpha d} - 1)$. During a unit of time, $\gamma(n_0 e^{\alpha d} - 1)$ secondary electrons will be released from the cathode surface, due to Townsend's second ionization coefficient γ. The secondary electrons move to the anode in the electric field, forming a new sequence of ionisation events, thus supporting the development of the electron avalanche. The electron multiplication process continues. Finally, when the process is completed, the number of all electrons arriving at the anode is:

$$n_a = n_0 \frac{e^{\alpha d}}{1 - \gamma(e^{\alpha d} - 1)} \qquad (A.5)$$

The discharge current is (Llewellyn-Jones 1957; Fridman and Kennedy 2004):

$$i_a = i_0 \frac{e^{\alpha d}}{1 - \gamma(e^{\alpha d} - 1)} \qquad (A.6)$$

Therefore, to sustain the development of the electron avalanche without relying on any external ionization factors, at least one secondary electron is required to be released from the cathode surface; therefore

$$\gamma(e^{\alpha d} - 1) = 1 \qquad (A.7)$$

known as the breakdown criterion $e^{\alpha d} \gg 1$, so

$$\gamma e^{\alpha d} = 1 \qquad (A.8)$$

It is known as the Townsend breakdown criterion, which describes the condition of transformation from non-self-sustained to self-sustained discharge.

A.1.2. Paschen's breakdown law

Using the breakdown Townsend criterion, one can obtain:

$$d = \frac{1}{\alpha}\ln\left(1+\frac{1}{\gamma}\right) \qquad (A.10)$$

where d is the gap distance. α and γ are considered constants as a function of (E/p). The above equation can be rewritten as

$$d = \frac{1}{pf\left(E/p\right)}\ln\left(1+\frac{1}{\phi\left(E/p\right)}\right) \qquad (A.11)$$

In a uniform electric field: $E = V_b/d$, $where\ V_b$ is the breakdown voltage. Therefore, the breakdown criterion is

$$pd = \frac{1}{f\left(V_b/pd\right)}\ln\left(1+\frac{1}{\phi\left(V_b/pd\right)}\right) \qquad (A.12)$$

From the above equation, it can be seen that the breakdown voltage of a uniform electric field, V_b, is a function of pd. It is only related to the product of gas pressure and electrode spacing. Townsend's first ionization coefficient, $\alpha = Apexp(-Bpd/V_b)$, can be taken into the equation (Paschen 1889). So the breakdown voltage can be written as (Cobine 1941):

$$V_b = \frac{Bpd}{\ln Apd - \ln\left(\ln\left(1+\frac{1}{\gamma}\right)\right)} \qquad (A.13)$$

According to the equation, we can predict the breakdown voltage as a function of the *pd* product. The calculated breakdown voltage agrees with the experimental results. This functional dependency, $V_b(pd)$, is known as the Paschen breakdown law. Figure A-3 shows the Paschen curves of air, nitrogen (N_2), carbon dioxide (CO_2), and argon. The data plotted Paschen curves with corresponding coefficients *A*, *B* and γ were from

(A.V. Engel, and Max Steenbeck. 2013; Husain and Nema 1982; Raizer, Kisin, and Allen 2011; Torres et al. 2012).

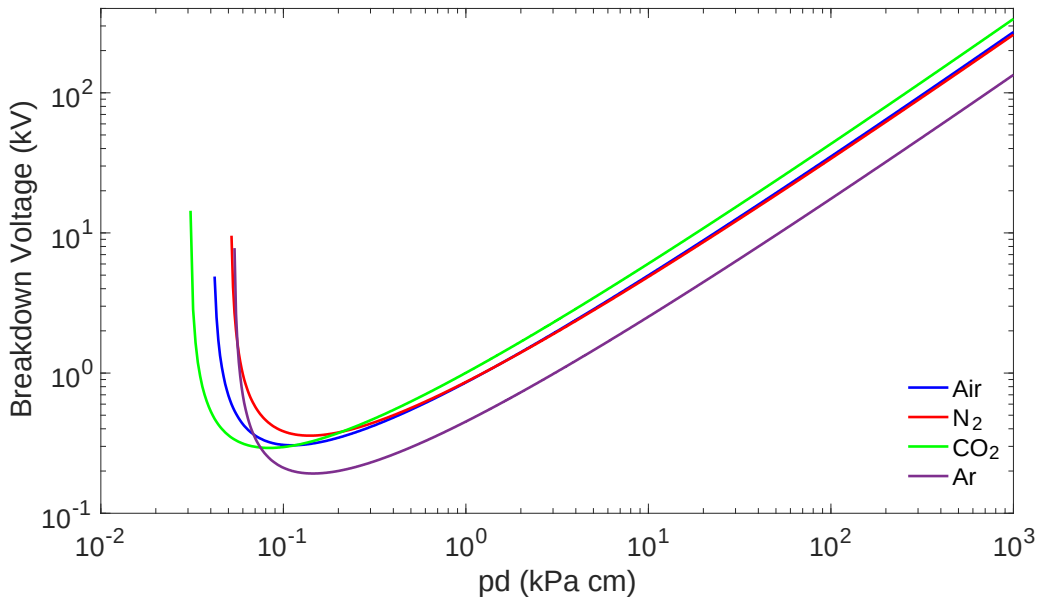

Figure A-3 Paschen curves obtained for air, nitrogen (N_2), argon and carbon dioxide (CO_2), using the Paschen's law expression, (A.13).

As can be seen from the Figure, the Paschen breakdown voltage curves are U-shaped curves. They have the Paschen minimum voltage, V_{bmin}, at a specific pd value and left and right voltage rising parts for larger and smaller pd values. The minimum breakdown voltage, V_{bmin}, and the corresponding pd_{min} are different for different gases. To get this minimum value, we can calculate the derivative of the equation (A.13) and set it equal to 0. The result is

$$\ln\frac{Apd}{\ln\left(1+\frac{1}{\gamma}\right)}=1 \qquad (A.14)$$

so,

$$pd_{min}=\frac{2.718}{A}\ln\left(1+\frac{1}{\gamma}\right) \qquad (A.15)$$

$$V_{bmin} = \frac{2.718B}{A} \ln\left(1 + \frac{1}{\gamma}\right) \qquad (A.16)$$

When the electrode spacing *d* stays the same, the gas pressure *p* changes. When *p* is increased, although the number of collisions between electrons and gas molecules is relatively high, the mean free path, $\bar{\lambda}$, is shortened. The kinetic energy accumulated by collisions is challenging to ionize the gas molecules at each collision, so V_b increases. Conversely, when *p* is reduced to a small value, although $\bar{\lambda}$ increases, the kinetic energy accumulated in each collision can cause the ionization of gas molecules. However, the probability of collision between electrons and gas molecules is significantly reduced, so V_b will also increase.

Assuming gas pressure *p* stays the same, just the electrodes spacing *d* changes, when *d* is increased, to obtain a sufficient electric field strength *E*, the applied voltage, V_b, must be increased. On the other hand, when *d* is reduced dramatically, the electric field strength *E* increases, but the probability of collision between electrons and gas molecules in the entire process decreases. The electrons may arrive at the anode with massive kinetic energy before colliding with the gas molecules. So V_b will also increase.

The Townsend discharge theory can describe discharge phenomena in a limited range of gas pressure and inter-electrode gap distances. Deviations from the predicted values of the breakdown voltage (Carey et al. 2011) occur when the gap distance between the electrodes is significantly reduced (~10μm and below) while the gas pressure remains constant at around 0.1 MPa (Go and Pohlman 2010). When the product *pd* value is very high, the electron avalanches occur to a certain extent and distort the local field by the space charge of electrons and positive ions, which cannot be explained by the Townsend theory (Judd 2001).

The first discrepancy is the breakdown time lag. The breakdown time obtained through experiments is much shorter than the theoretically calculated result. The second is the impact of the cathode material. According to the Townsend discharge theory, the

cathode material plays an essential role in the breakdown process. However, the experiment shows that the breakdown voltage of the gap is independent of the cathode material under atmospheric pressure. Besides, the theory does not consider the effect of space charges caused by electron avalanches. The density of positive ions produced by the electron avalanche is exceptionally high, which causes significant distortion of the initial electric field and strengthens the localized electron energy, intensifying the ionization. α is higher than that in the static electric field, which is important for the development of discharge. According to Townsend's theory, the discharge avalanche should be volumetric and propagates throughout the gap. However, in practice, the discharge channel was found to be filamentary.

A.1.3 Theory of the Streamer breakdown

The Townsend theory is based on the first and second ionisation coefficients (processes) α and γ to explain the discharge phenomenon when the *pd* values *are* relatively small. However, for more significant *pd*, as mentioned before, the discharge process and phenomenon have new changes. Therefore, based on the Townsend discharge theory, the Streamer theory was proposed by Raether, Meek, and Loeb based on multiple experimental observations (Loeb and Meek 1940; Loeb 1955; Raether 1964). The Streamer theory stipulates that the collisional ionization and photoionization processes are required to maintain the self-sustained discharge, and the space charge produced by the electron avalanche significantly distorts the electric field in the gap.

This field distortion process can be described as follow. If the electric field is sufficiently high, an initial electron created by external radiation develops collision ionization to cause an initial electron avalanche. Moreover, it triggers this electron avalanche, accelerating and travelling from the cathode to the anode. Since the mobility of electrons is much higher than that of the positive ions, most electrons are concentrated in the head of the electron avalanche. The avalanche builds up a cloud of electrons propagating rapidly towards the anode, while positive ions are considered relatively stationary. Due to the continuous diffusion of charged particles during the

development of the electron avalanche, the radius of the head of the electron avalanche will gradually increase.

As shown in Figure A-4, when the development of the electron avalanche reaches a particular stage, the electric field of the space charge formed by the electron avalanche will be significantly enhanced. As a result, the space charge field significantly distorts the original electric field, which intensifies the electric field at the head and tail of the avalanche. Meanwhile, it weakens the electric field between the positive ions and electrons charging areas in the avalanche. The space charge at the avalanche head is enhanced, and the ionization process is intense. The electric field distribution is affected by distortion, which causes the avalanche head to emit a large number of photons. The electric field is enhanced in front of the avalanche head, which underpins the excitation of gas molecules and ions. When the excited molecules and ions return to the ground state, they emit photons. In the region between the avalanche head (with a high concentration of electrons) and the avalanche body with a high concentration of ions, the electric field is reduced, which promotes the recombination process. It is easy for the excited molecules to return to the ground state. As a result of this process, photons will be emitted, leading to the photoionisation of gas molecules or atoms. This process is not very prominent when the external electric field is relatively weak. However, when the external electric field is strong enough, the electric field in the front of the avalanche head increases and the avalanche may transform into a fast-propagating streamer.

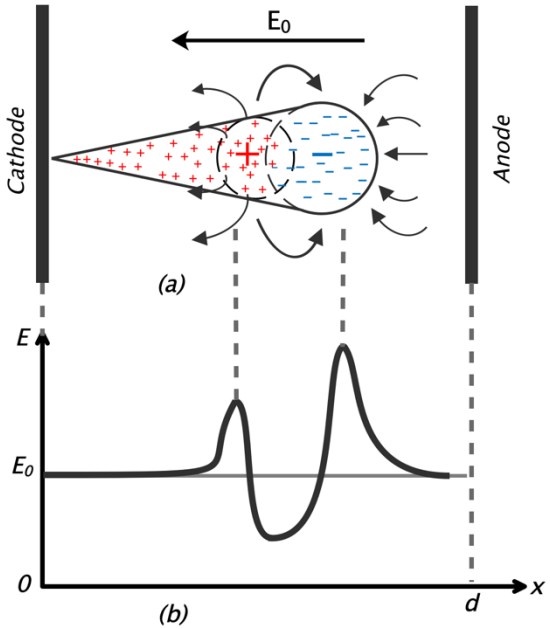

Figure A-4 The distortion of an external electric field by space charge in an electron avalanche

As Figures A-5 (a) and (b) show, when the applied external voltage exceeds the minimum value of breakdown voltage, the initial avalanche starting from the cathode reaches the anode. The electrons accumulated in the avalanche's head instantly swept into the anode. The positive ions are left behind to form a positive space charge at the anode and significantly enhance the external field in the tail of the initial avalanche. At the same time, photons are emitted into the gas. These photons cause photoionisation and produce photoelectrons in the surrounding gas. The newly formed photoelectrons are attracted by the positive space charge formed by the primary avalanche in the vicinity of the anode resulting in the generation of new secondary electron avalanches, as shown in Figure A-5 (c).

The positive space charge attracts the secondary avalanches, providing charges for the cathode-directed streamer. When the cathode-directed streamer reaches the cathode, the streamer channel is filled with positive ions, electrons and negative ions (in the case of electronegative gas). Thus, the streamer's “body” is electrically neutral.

As shown in Figure A-5, the positive cathode-directed streamer moves in the direction opposite to the initial avalanche. This streamer channel has high electrical conductivity (Nijdam, Teunissen, and Ebert 2020).

As shown in Figure A-5 (e), when the positive streamer crosses the gap, a conductive streamer channel is formed, and the streamer can be transformed into a spark.

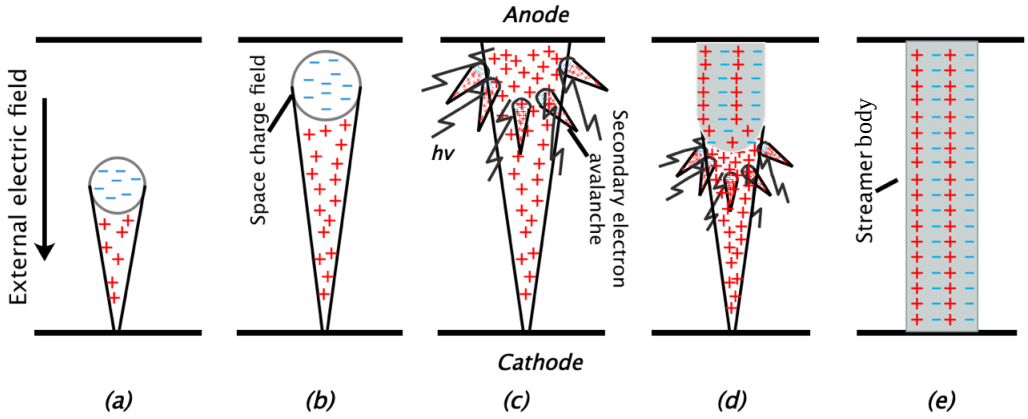

Figure A-5 A schematic diagram of the formation processes of the positive, cathode-directed streamer

Negative streamers propagate opposite the direction of the electric field, that is, in the same direction as electronic avalanches. As illustrated in Figure A-6, the propagation of the negative streamer is based on the successive avalanches around the streamer head. The newly formed electron avalanches rapidly rush into the anode and develop a negative streamer. During the propagation of a negative streamer, the movement of electrons is limited by positive charges left by electron avalanches. Therefore, the propagation velocity of negative streamers is smaller than that of positive streamers. Due to a negative space charge at the streamer head, the electric field enhancement in front of the negative streamer head is less than the field enhancement in the case of positive streamers. Therefore, negative streamers require higher electric fields for propagation than positive streamers.

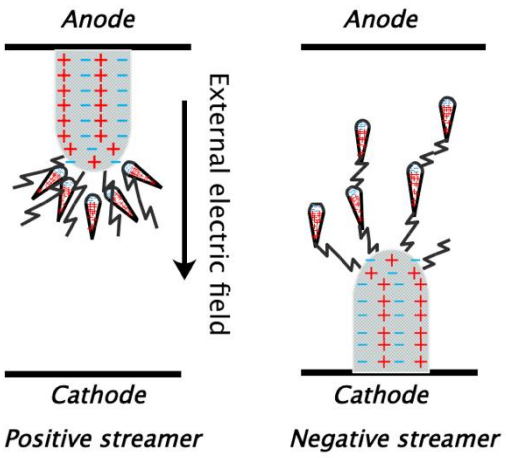

Figure A-6 Growth of the streamer

From the above analysis, it can be seen that the development of the streamer requires charge accumulation in the initial avalanche head. The space charge field can distort and strengthen the original electric field to generate photoelectrons to cause photoionization. Once the streamer crosses the gap, the higher current starts to flow through the conductive streamer body resulting in the spark breakdown (Morrow and Lowke 1997).

The Streamer breakdown theory complements the Townsend theory. It is generally believed that when $pd > 26\ kPa \cdot cm$, the discharge transitions from the Townsend discharge to the streamer discharge takes place. Therefore, the streamer theory can explain the discharge process in longer gaps and at high pressures.

A.2 Breakdown in non-uniform electric fields

In practice, in most plasma closing switches, the electric field is non-uniform. The geometry of the electrodes governs the electric field, for example, point-plane or point-point electrode geometry. When the ionisation process starts in a uniform electric field, it often results in a complete transition process and the establishment of a plasma

channel. However, in a highly non-uniform electric field, a non-complete corona discharge can be formed when the applied voltage is below the breakdown voltage.

In this case, the local electric field near the sharp energised electrode is strong, and the ionisation processes are limited by the local area where the field exceeds the ionisation level. If the radius of curvature of the electrode is small, the local field enhancement is high, and corona discharge may occur.

When the applied voltage is increased further, the corona discharge may transform into a spark/arc discharge (Chang, Lawless, and Yamamoto 1991).

In general, electrode geometry plays a vital role in the initiation and generation of the corona discharge. The non-uniformity of the electric field restricts the main ionisation processes near the electrodes with high local electric fields. The inhomogeneity of the electric field required to form a corona is considerably related to the type of gas. Corona discharges mainly occur in electronegative gases (air, oxygen or SF_6) due to the formation of volumetric negative space charge in the vicinity of the cathode.

The current in the corona discharge depends on the applied voltage, the electrode geometry, the distance between the electrodes, the gas properties and its pressure. The corona discharge is a self-sustained discharge that does not require an external ionising source. The polarity of the corona discharge depends on the polarity of the voltage applied to the corona electrode.

In heterogeneous electric fields, avalanches develop in the area where the electric field strength is maximum, that is, where the radius of curvature of the electrode is minimum. In order to generate the corona discharge, the coefficient of non-uniformity of the electric field *f* should be large enough. Moreover, experiments have shown that the threshold of corona discharge is related to the polarity of the electrode where the corona discharge is generated.

For the corona discharge formed in a coaxial electrode system filled with air, Peek and Humphrey found that the critical electric field for the corona ignition is related to the central conductor radius and air pressure (density). Peek and Humphrey obtained an empirical formula for the critical electric (Peek and Humphrey 1915).

$$E_c = E_0 m\delta\left(1 + {K}/{(\delta r)^{\frac{1}{2}}}\right) \qquad (A.17)$$

where, E_c is the critical electric field strength (corona inception); $E_0 = 31\,kV/cm$ which is equivalent to a uniform electric field strength at a gap of $1cm$ in air at atmosphere; m is a coefficient describing the surface state of the conductor ($0.6 < m < 1$); δ is the considerable air density; $K = 0.308cm^{1/2}$; r is the radius of the wire. This empirical formula is also applicable to other gases.

We can deduce the critical voltage with different electrode geometry from the above formula.

a) coaxial electrodes whose inner radius is r and the outer radius is R

$$V_c = E_c r \ln\frac{R}{r} \qquad (A.18)$$

b) coaxial spherical electrodes with inner radius r and outer radius R

$$V_c = E_c\left(\frac{r(R-r)}{R}\right) \qquad (A.19)$$

c) point-plane with tip's radius of r and gap distance of d

$$V_c = \frac{1}{2}E_c r \ln\frac{r+2d}{r} \qquad (A.20)$$

Positive and negative corona discharges are significantly different in their nature which affect the breakdown behaviour of the point-plane gap stressed positively or negatively. Before breakdown in the gap, the electric field strength near the point electrode should be high enough to cause ionisation. Significant space charge is developed around the HV electrode and distorts the external electric field. Due to the polarity effect, the effect of space charge in the discharge process is different when voltage stress of different polarity is applied to the sharp electrode.

First, let us consider the situation when the point electrode is the point anode. The corona discharge is initiated due to the intensive field near the point electrode. The electrons move quickly into the anode, and the positive ions move towards the negative electrode relatively slowly, so the positive space charge is accumulated surrounding the positive HV point electrode. Therefore, the electric field and ionisation near the point electrode are reduced, which makes the positive corona inception voltage relatively high. As the voltage gradually increases, streamer(s) may be formed in the ionisation zone of the corona discharge. The electric field in front of these streamer(s) head(s) is strengthened due to the positive space charge, which makes it easier to produce secondary electron avalanches. The development of this process is continuous and rapid, transforming the corona discharge into the spark discharge. Compared with the negative HV point electrode, the breakdown voltage is lower.

In contrast, in the case of the negative point electrode, the electron avalanche is easy to form, resulting in the development of the negative corona discharge. Therefore, the corona inception voltage is low. As the voltage gradually increases, the negative space charge builds up (in the case of electro-negative gases). It results in a reduction of the field in the vicinity of the corona electrode. Therefore, the breakdown voltage is higher than that of the positive point electrode, as shown in Figure A-7.

In summary, due to polarity effects, the positive sharp (point) electrode provides a higher corona inception voltage but lower breakdown voltage (voltage at which the

corona discharge transforms into the spark breakdown) as compared with the negative point electrode.

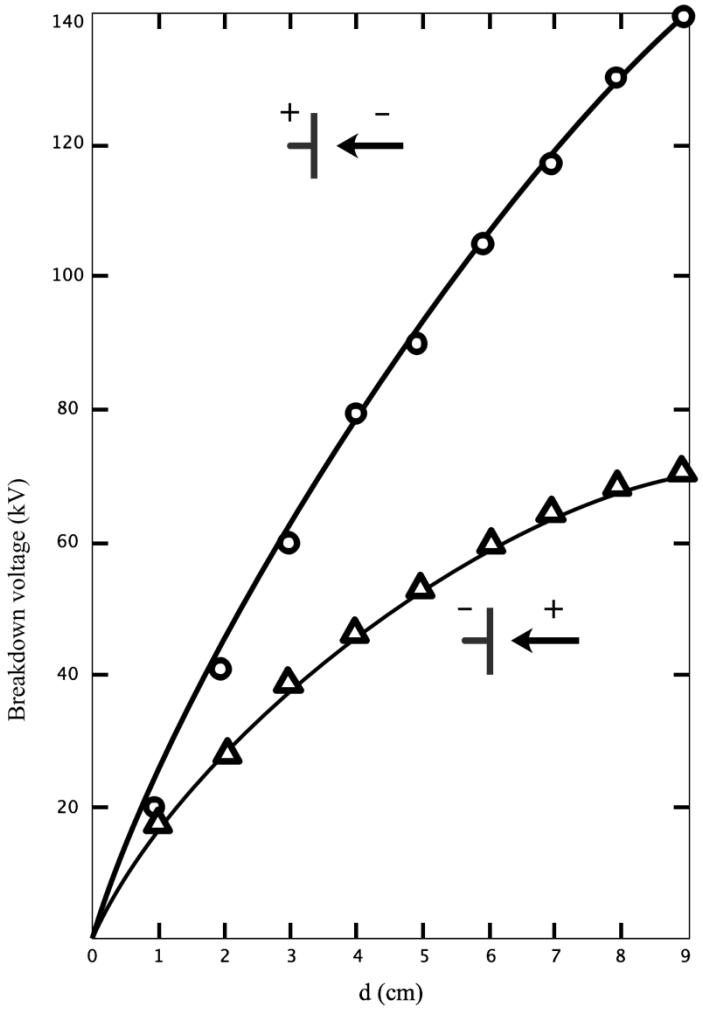

Figure A-7 The breakdown voltages of the air gaps under point–plate and point–point electrodes. Figure adapted from (Kuffel and Kuffel 2000)

APPENDIX B. LABVIEW FRONT PANEL AND DIAGRAM

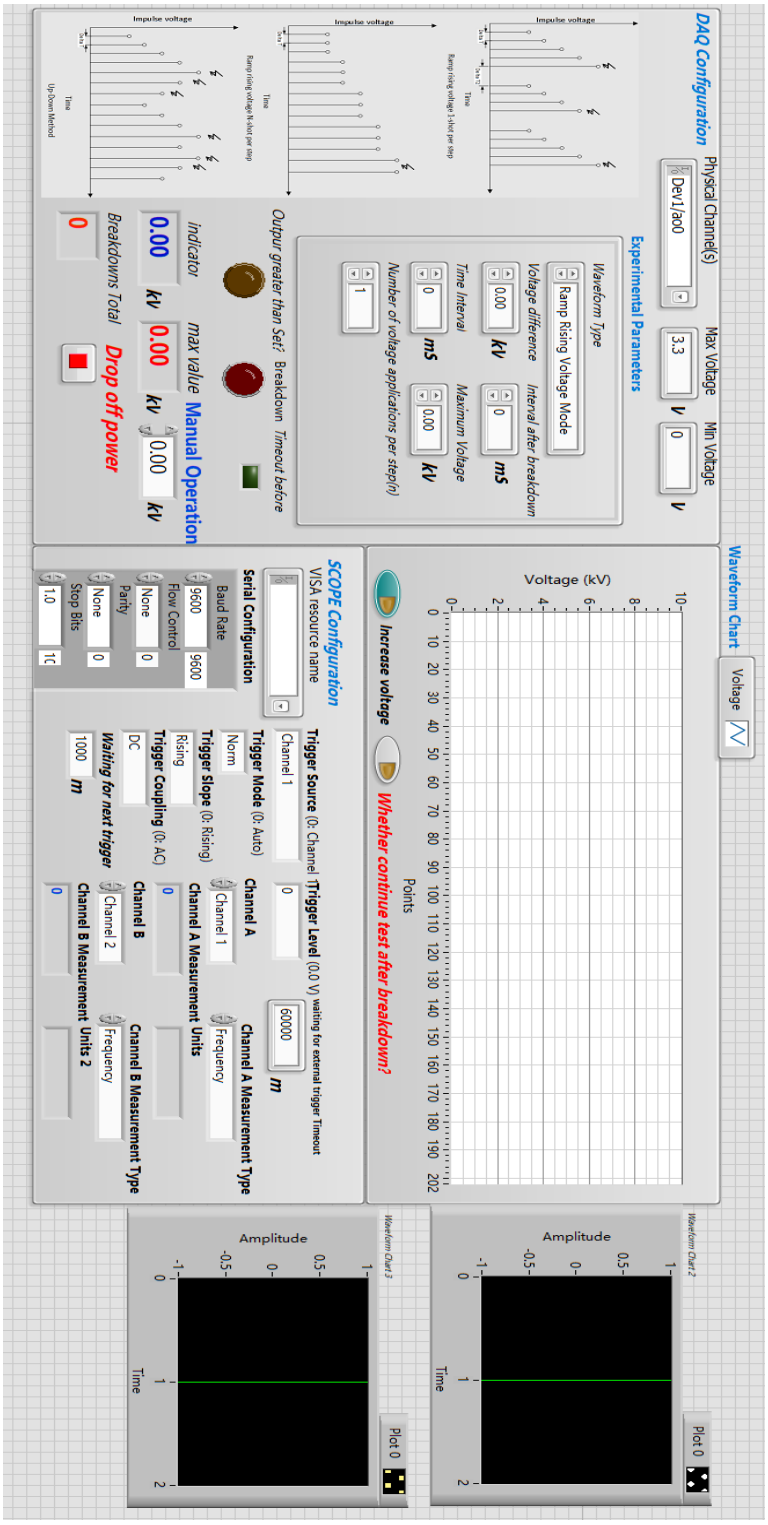

Figure B-1 The front panel of the LabVIEW control program

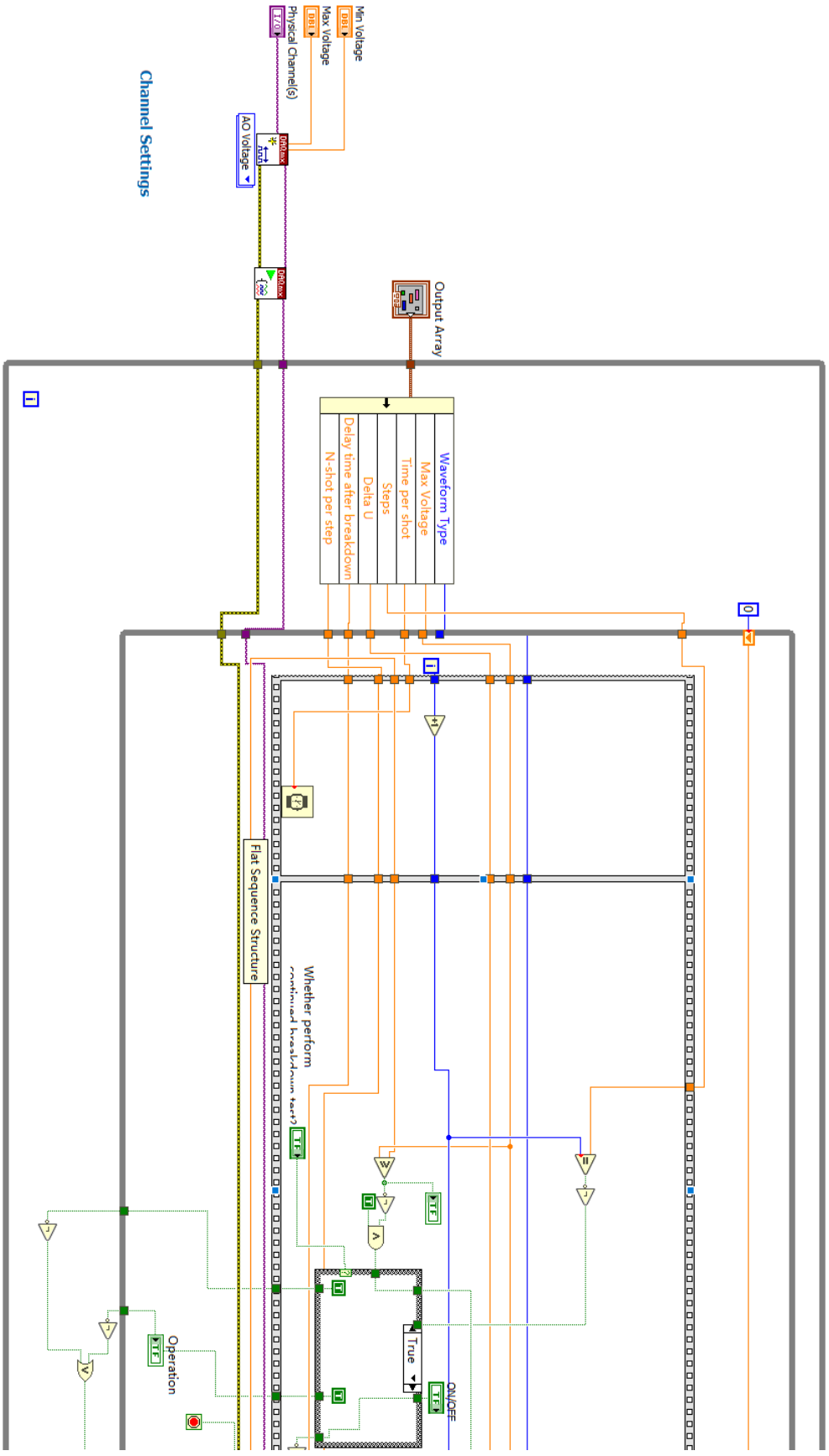
Channel Settings
Physical Channel(s)
Max Voltage
Min Voltage
AO Voltage
Output Array
Waveform Type
Max Voltage
Time per shot
Steps
Delta U
Delay time after breakdown
N-shot per step
Flat Sequence Structure
Whether perform
Operation
True
ON/OFF

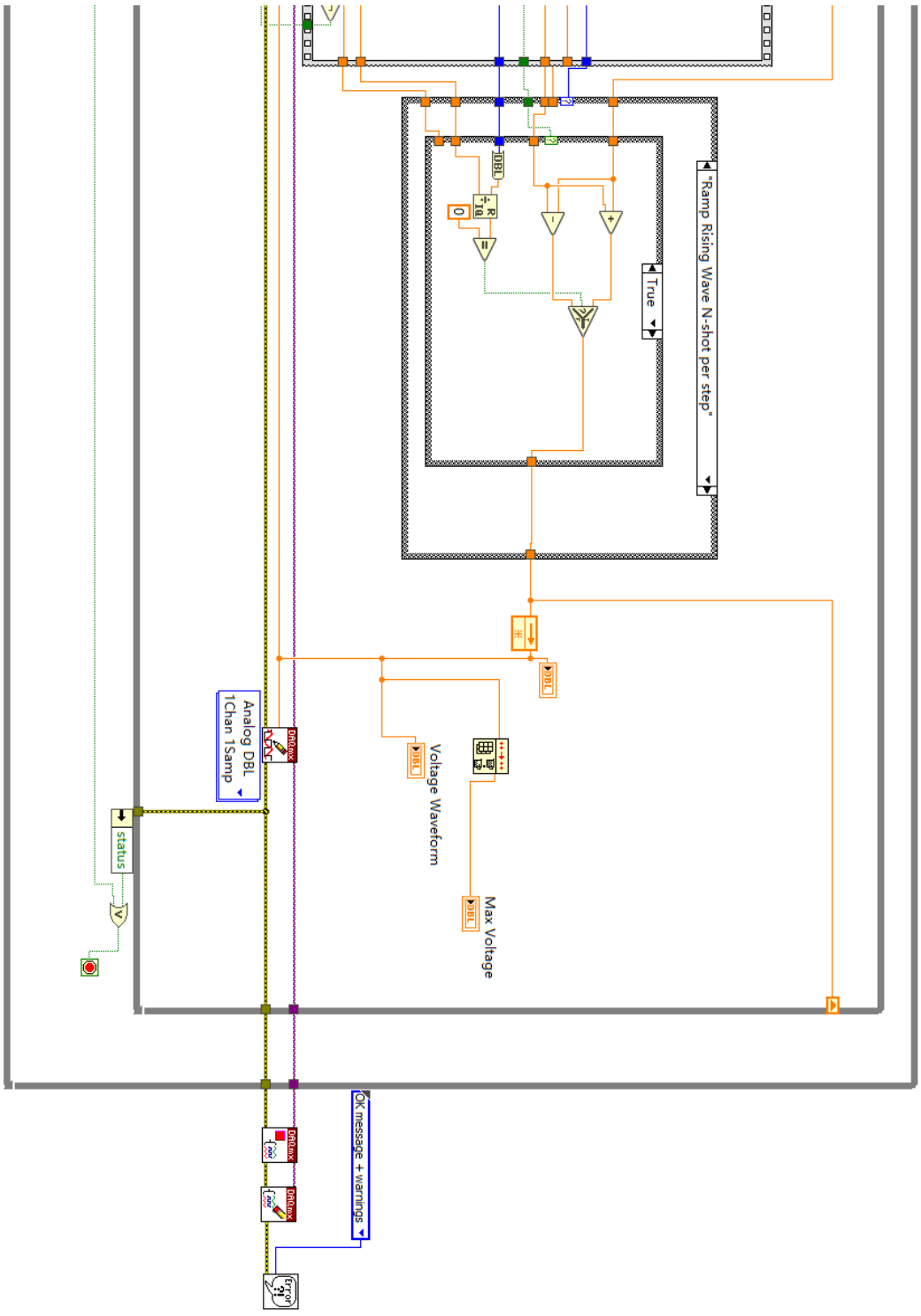

Figure B-2 The diagram of the LabVIEW control program

APPENDIX C MATLAB PROGRAMME FOR DIMENSIONLESS LUMPED RLC CIRCUIT MODEL

```
PI=3.14159;
U0=31.7*1000;
L=0.85*0.000001;   %78*0.000001;
C= 0.0807*0.000001;   %0.006*0.000001;

RAD0=0.00019; %0.00001*m+0.00012;  %Initial Radius of the channel,(M)
GAP=10*0.001;  %Inter-Electrode Gap,(M)
RSTRAY=0.4;   %Stray Resistance,(Ohm)
PSI=4.5;
DUND=1.25;    %Density of Gas,(KG/M^3)
COND=5000; %1.5E3+0.5E2*k;   %2.2E4*k; %     %Conductivity of
Gas,(1/(OHM*M))
I0=U0*(C/L)^(1/2);
RN=2*(L/C)^(1/2);
T0=(L*C)^(1/2);
RSTN=RSTRAY/RN;


K=4/(PI^2*DUND*PSI*COND);
M=GAP/(COND*PI*K^(1/3));
P=M/(L*I0^(2/3));
INT10=RAD0^2/(T0*I0^(2/3)*K^(1/3));

Z(1)=0;
Z(2)=1;

deltaT=3.8348E-3;

Length = 8000;

T = zeros(Length,1);
RAD = zeros(Length,1);
RAD1 = zeros(Length,1);
RAD2 = zeros(Length,1);
TOUT = zeros(Length,1);
IOUT = zeros(Length,1);
EN = zeros(Length,1);
IND = zeros(Length,1);
INT = zeros(Length,1);
PW = zeros(Length,1);

XI = zeros(Length,1);
```

```
RCH = zeros(Length,1);
INT1=INT10;
XI1=INT10^3;
FINT1=0;

for i=1:Length
   FINT1=Z(1)^(2/3);
   INT1=INT1+deltaT*FINT1;
   XI1=XI1+deltaT*FINT1^3;
   INT(i)= INT1;
   XI(i)= XI1;

   for J=1:2
      F(2)=P*(Z(1)*(Z(1)^(2/3))/INT1^2-Z(2)/INT1)-2*RSTN*Z(2)-Z(1);
      F(1)=Z(2);

      Z(J)=Z(J)+deltaT*F(J);
   end

   T(i+1)=T(i)+deltaT;

   TOUT(i)=T(i)*T0;
   IOUT(i)=Z(1)*I0;
   INT(i)= INT1*T0*I0^(2/3);
   RAD1(i)=sqrt(INT1*K^(1/3)*T0*I0^(2/3));
   %RCH(i)=GAP/(PI*COND*K^(1/3)*I0^(2/3)*T0)/INT1;
   %IND(i)=2E-7*GAP*log(0.03/RAD(i));

end

%     IO(k)=IOUT(400);
%     %RADINI(k)=RAD0;
%     CONDO(k)=COND;
%
% end
%
% plot(CONDO,IO);
% hold on;
% end
%
RAD=K^(1/6)*INT.^(1/2);% Radius of the channel
RCH=GAP./(PI*COND*RAD.^2);  % Resistance of the channel
% IND=2E-7*GAP*log(0.03./RAD);
% %EN=XI.*RCH;
PW=IOUT.^2.*RCH;      % Power of the channel
EN=cumtrapz(TOUT,PW); % Energy of the channel

% figure(1);
```

```
% plot(TOUT(1:950),RCH(1:950));
% hold on;
% figure(2);
% plot(TOUT(1:950),RAD(1:950));
% hold on;
subplot(5,1,1);       % add first plot in 2 x 1 grid
plot(TOUT(1:8000),IOUT(1:8000));
title('Current');
hold on;



subplot(5,1,2);
plot(TOUT(1:8000),RCH(1:8000));
title('Resistance');
hold on;
subplot(5,1,3);
plot(TOUT(1:8000),RAD(1:8000));
title('Radius');
hold on;
subplot(5,1,4);
plot(TOUT(1:8000),PW(1:8000));
title('POWER');
hold on;
subplot(5,1,5);
plot(TOUT(1:8000),EN(1:8000));
title('ENERGY');
hold on;
```

APPENDIX D WEIBULL GRAPHS

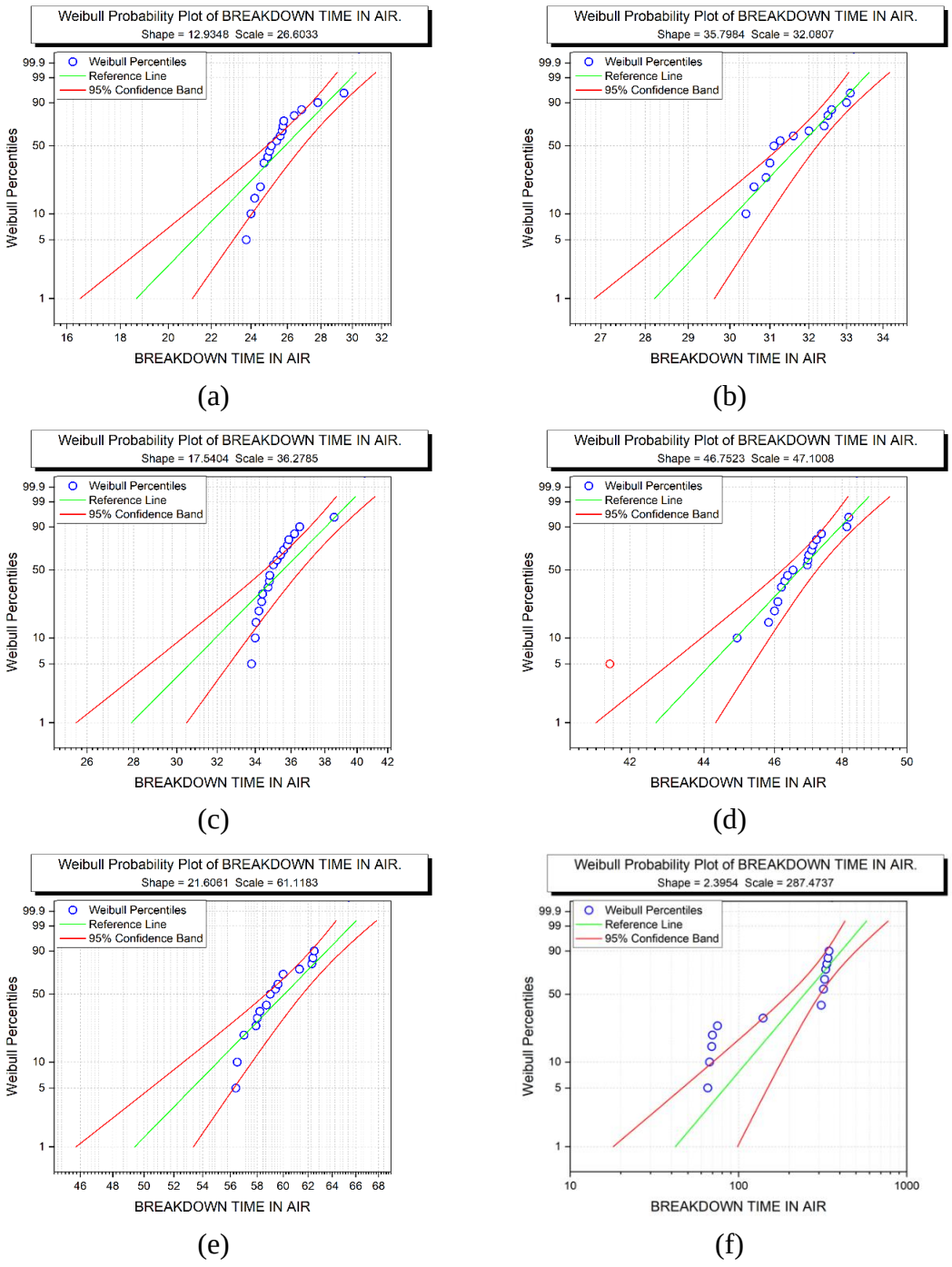

Figure D-1 Weibull distribution graphs for the time to breakdown in air at each of the tested gas pressure for 70% of the self-breakdown voltage level

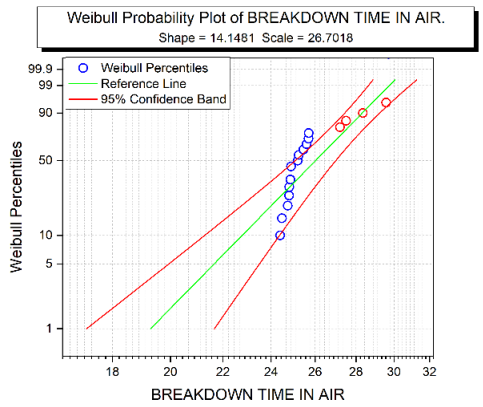
Weibull Probability Plot of BREAKDOWN TIME IN AIR.
Shape = 14.1481 Scale = 26.7018
Weibull Percentiles
Reference Line
95% Confidence Band
Weibull Percentiles
BREAKDOWN TIME IN AIR

(a)

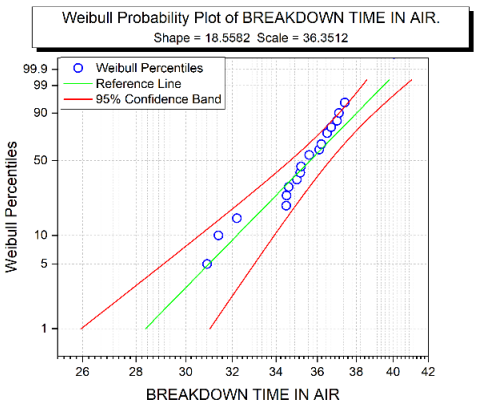
Weibull Probability Plot of BREAKDOWN TIME IN AIR.
Shape = 18.5582 Scale = 36.3512
Weibull Percentiles
Reference Line
95% Confidence Band
Weibull Percentiles
BREAKDOWN TIME IN AIR

(b)

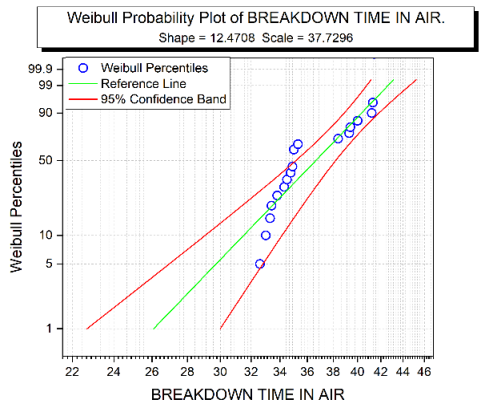
Weibull Probability Plot of BREAKDOWN TIME IN AIR.
Shape = 12.4708 Scale = 37.7296
Weibull Percentiles
Reference Line
95% Confidence Band
Weibull Percentiles
BREAKDOWN TIME IN AIR

(c)

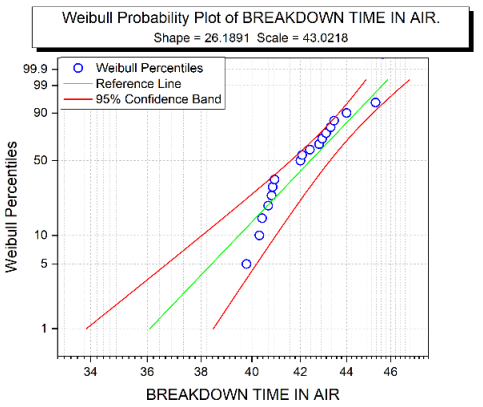
Weibull Probability Plot of BREAKDOWN TIME IN AIR.
Shape = 26.1891 Scale = 43.0218
Weibull Percentiles
Reference Line
95% Confidence Band
Weibull Percentiles
BREAKDOWN TIME IN AIR

(d)

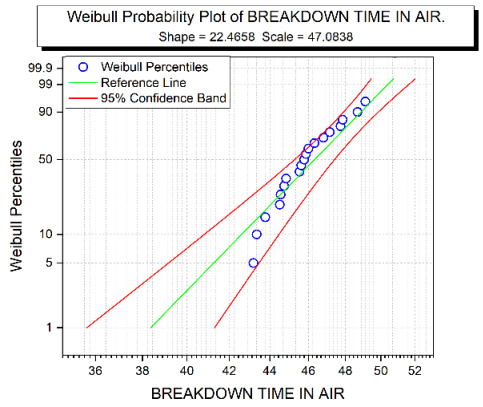
Weibull Probability Plot of BREAKDOWN TIME IN AIR.
Shape = 22.4658 Scale = 47.0838
Weibull Percentiles
Reference Line
95% Confidence Band
Weibull Percentiles
BREAKDOWN TIME IN AIR

(e)

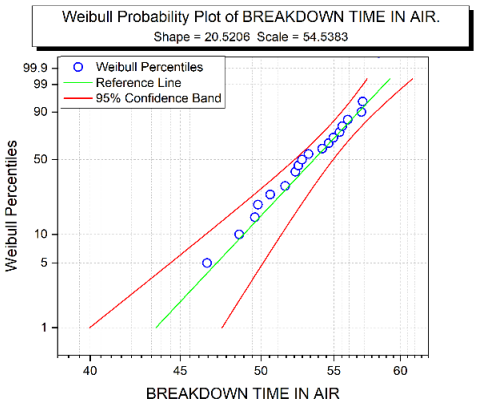
Weibull Probability Plot of BREAKDOWN TIME IN AIR.
Shape = 20.5206 Scale = 54.5383
Weibull Percentiles
Reference Line
95% Confidence Band
Weibull Percentiles
BREAKDOWN TIME IN AIR

(f)

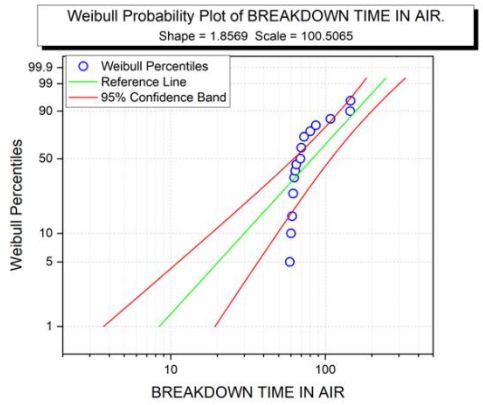

(g)

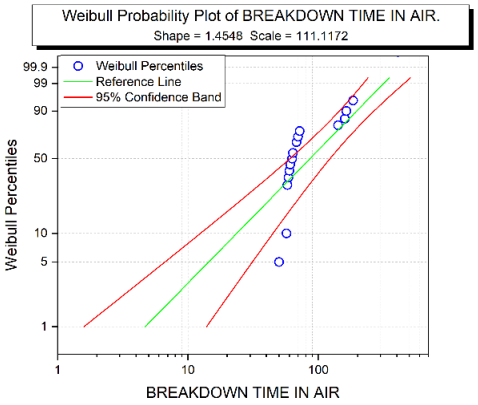

(h)

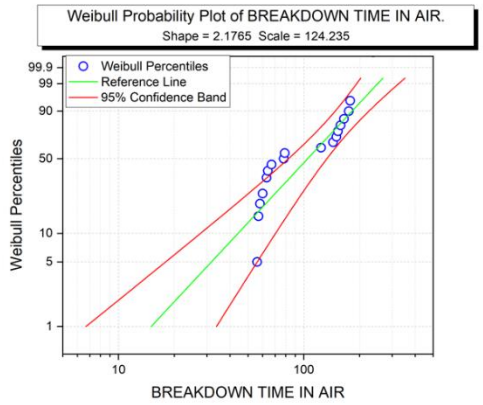

(i)

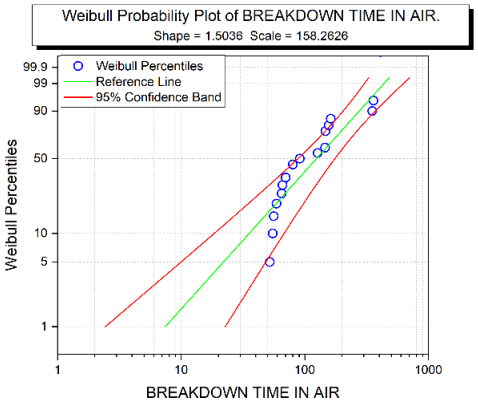

(j)

Figure D-2 Weibull distribution graphs for the time to breakdown in air at each of the tested gas pressure for 90% of the self-breakdown voltage level

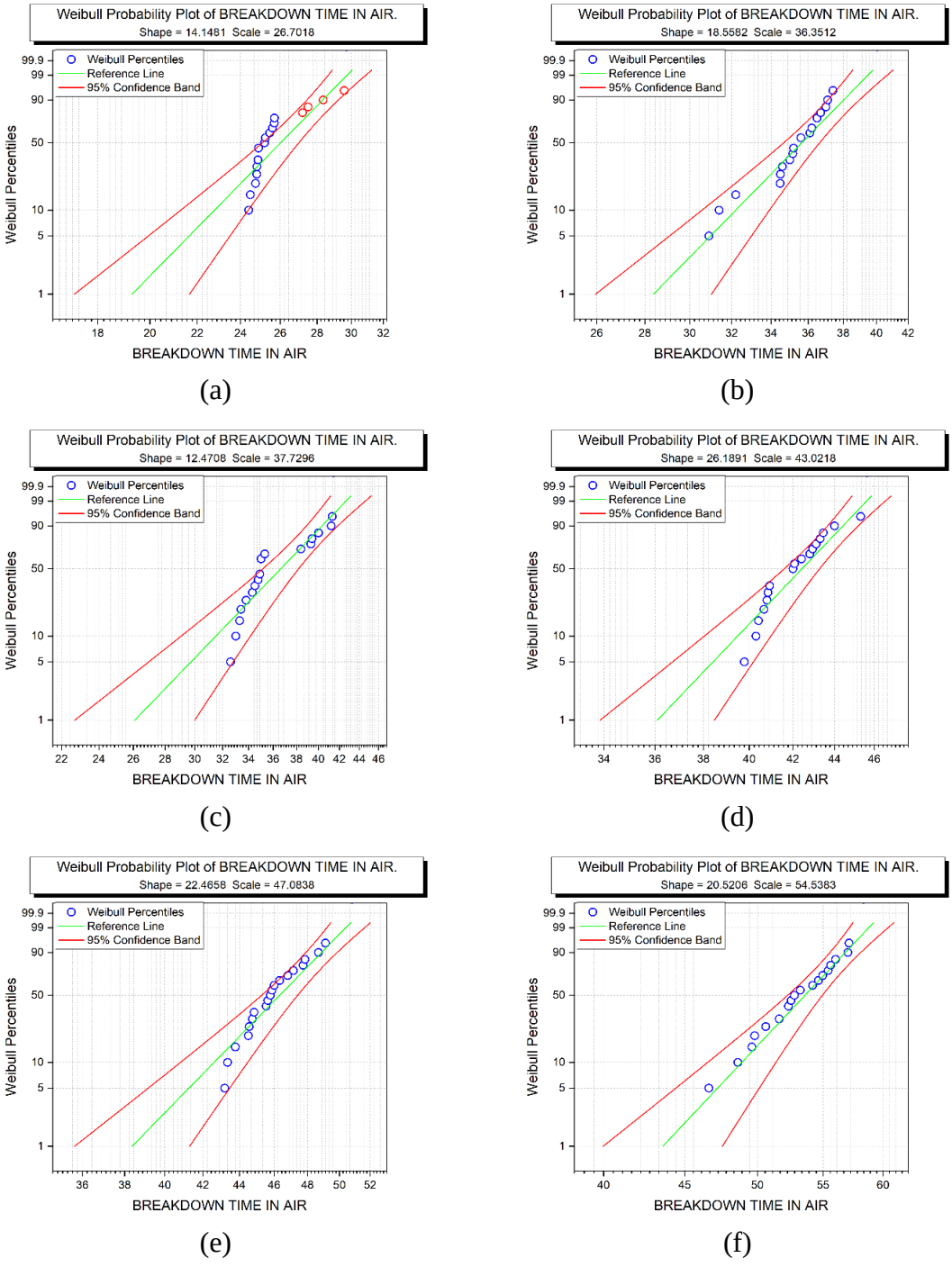

Figure D-3 Weibull distribution graphs for the time to breakdown in N_2 at each of the tested gas pressure for 70% of the self-breakdown voltage level

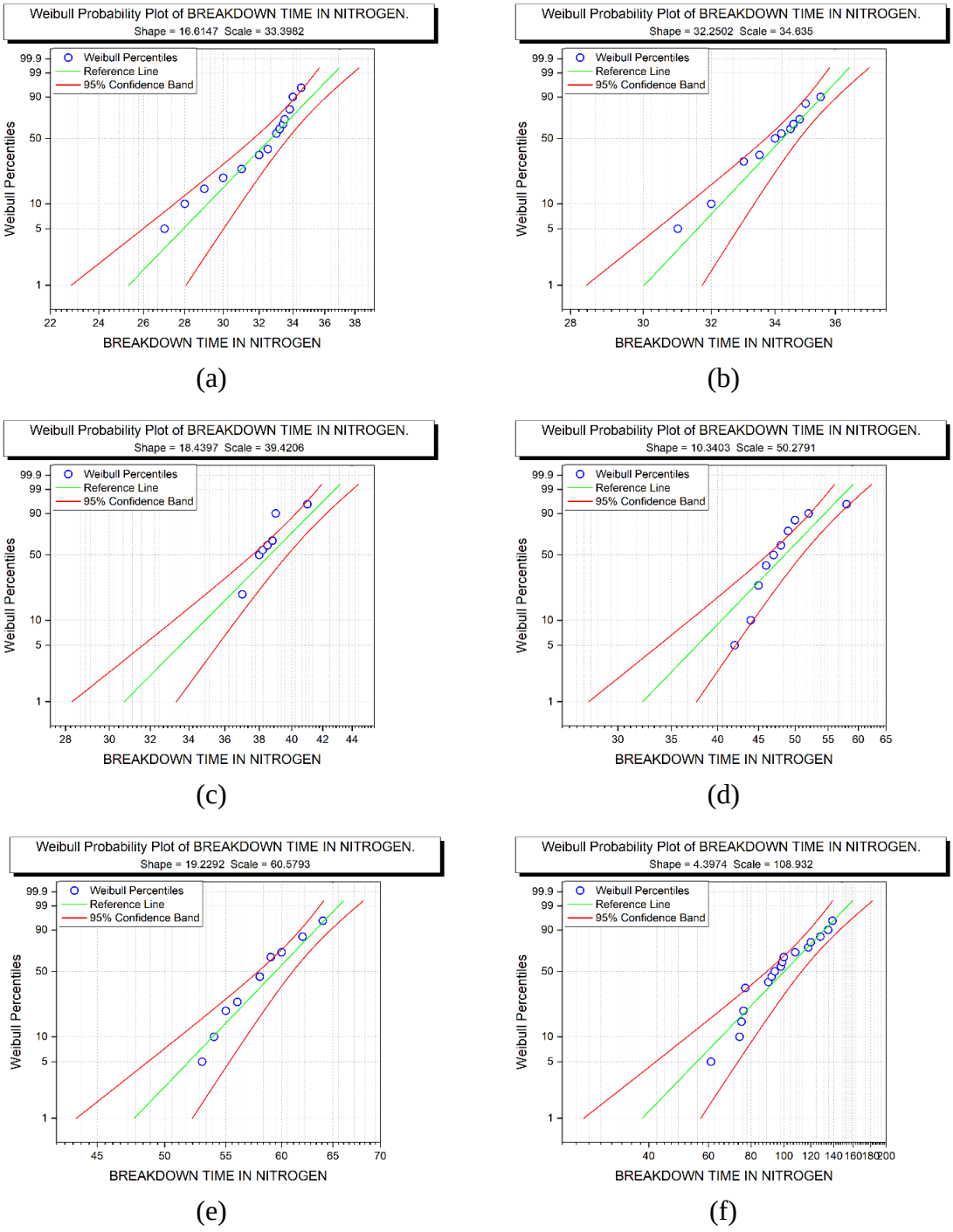

Figure D-4 Weibull distribution graphs for the time to breakdown in N_2 at each of the tested gas pressure for 90% of the self-breakdown voltage level

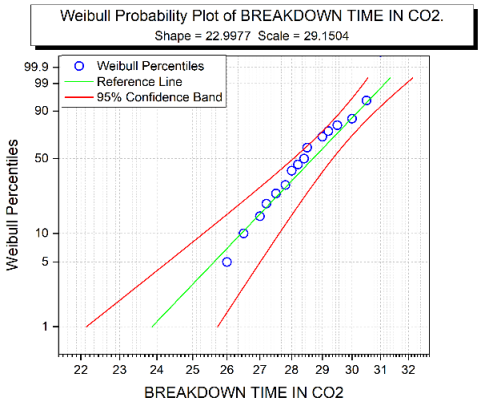
Weibull Probability Plot of BREAKDOWN TIME IN CO2.
Shape = 22.9977 Scale = 29.1504
Weibull Percentiles
Reference Line
95% Confidence Band
Weibull Percentiles
BREAKDOWN TIME IN CO2

(a)

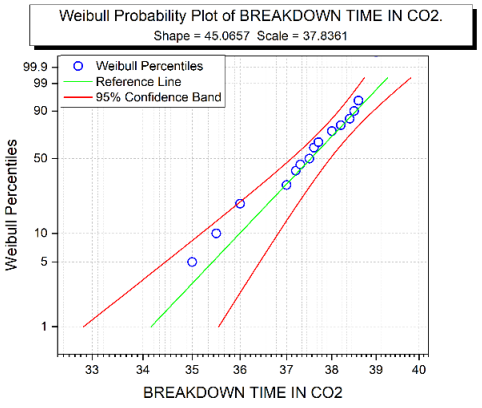
Weibull Probability Plot of BREAKDOWN TIME IN CO2.
Shape = 45.0657 Scale = 37.8361
Weibull Percentiles
Reference Line
95% Confidence Band
Weibull Percentiles
BREAKDOWN TIME IN CO2

(b)

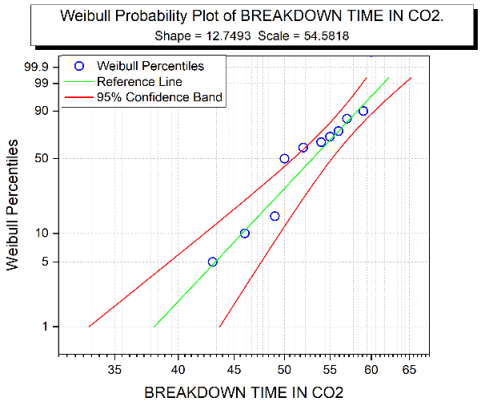
Weibull Probability Plot of BREAKDOWN TIME IN CO2.
Shape = 12.7493 Scale = 54.5818
Weibull Percentiles
Reference Line
95% Confidence Band
Weibull Percentiles
BREAKDOWN TIME IN CO2

(c)

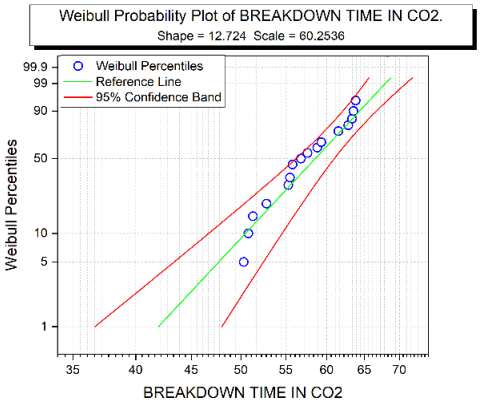
Weibull Probability Plot of BREAKDOWN TIME IN CO2.
Shape = 12.724 Scale = 60.2536
Weibull Percentiles
Reference Line
95% Confidence Band
Weibull Percentiles
BREAKDOWN TIME IN CO2

(d)

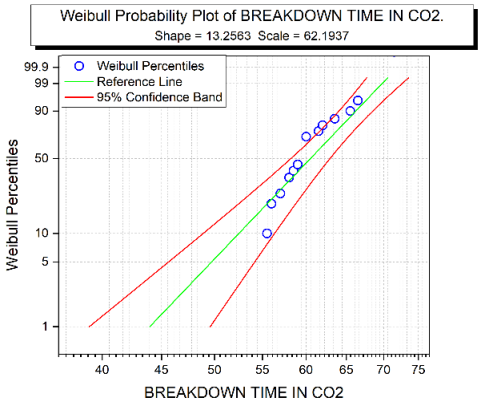
Weibull Probability Plot of BREAKDOWN TIME IN CO2.
Shape = 13.2563 Scale = 62.1937
Weibull Percentiles
Reference Line
95% Confidence Band
Weibull Percentiles
BREAKDOWN TIME IN CO2

(e)

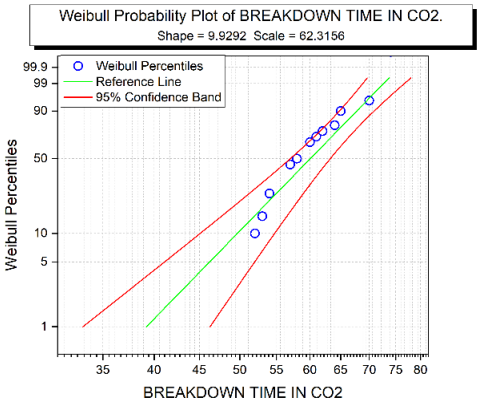
Weibull Probability Plot of BREAKDOWN TIME IN CO2.
Shape = 9.9292 Scale = 62.3156
Weibull Percentiles
Reference Line
95% Confidence Band
Weibull Percentiles
BREAKDOWN TIME IN CO2

(f)

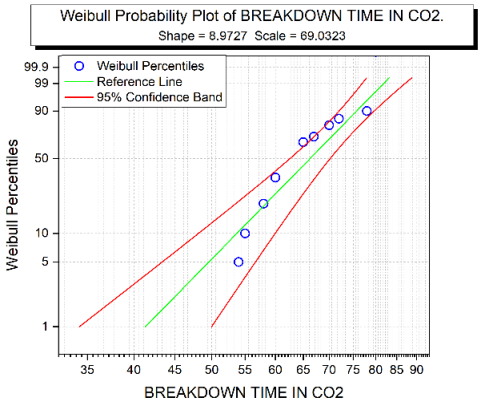
Weibull Probability Plot of BREAKDOWN TIME IN CO2.
Shape = 8.9727 Scale = 69.0323
Weibull Percentiles
Reference Line
95% Confidence Band
Weibull Percentiles
BREAKDOWN TIME IN CO2

(g)

Figure D-5 Weibull distribution graphs for the time to breakdown in CO_2 at each of the tested gas pressure for 70% of the self-breakdown voltage level

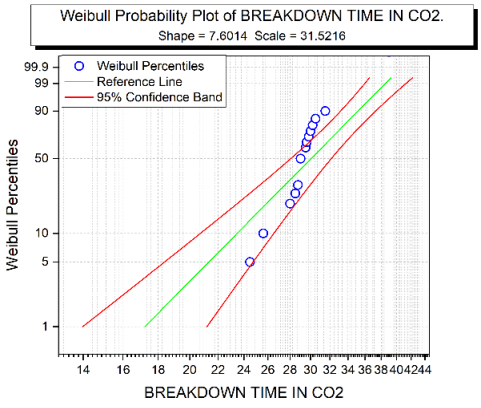
Weibull Probability Plot of BREAKDOWN TIME IN CO2.
Shape = 7.6014 Scale = 31.5216
Weibull Percentiles
Reference Line
95% Confidence Band
Weibull Percentiles
BREAKDOWN TIME IN CO2

(a)

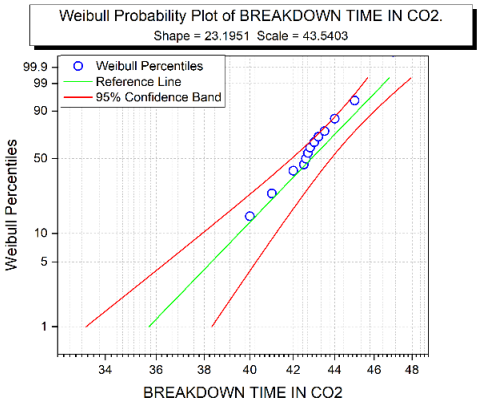
Weibull Probability Plot of BREAKDOWN TIME IN CO2.
Shape = 23.1951 Scale = 43.5403
Weibull Percentiles
Reference Line
95% Confidence Band
Weibull Percentiles
BREAKDOWN TIME IN CO2

(b)

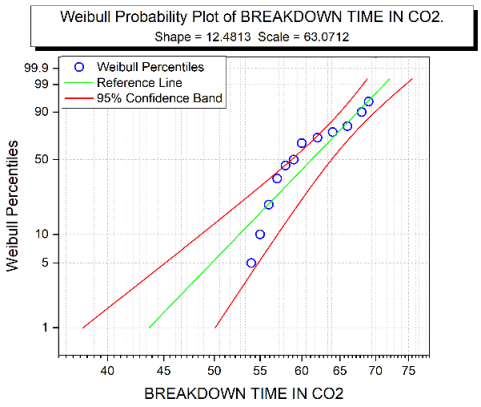
Weibull Probability Plot of BREAKDOWN TIME IN CO2.
Shape = 12.4813 Scale = 63.0712
Weibull Percentiles
Reference Line
95% Confidence Band
Weibull Percentiles
BREAKDOWN TIME IN CO2

(c)

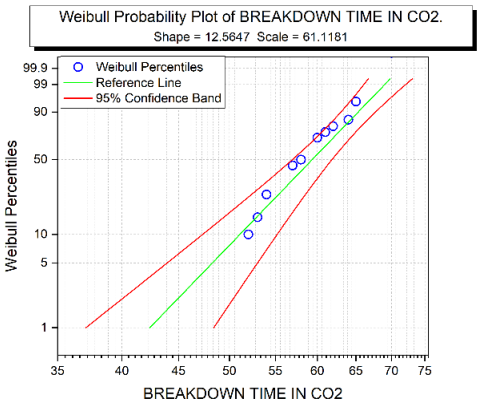
Weibull Probability Plot of BREAKDOWN TIME IN CO2.
Shape = 12.5647 Scale = 61.1181
Weibull Percentiles
Reference Line
95% Confidence Band
Weibull Percentiles
BREAKDOWN TIME IN CO2

(d)

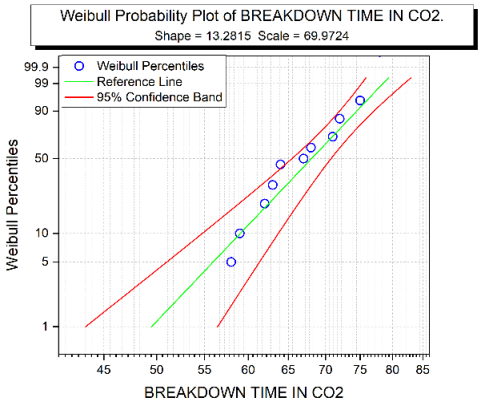
Weibull Probability Plot of BREAKDOWN TIME IN CO2.
Shape = 13.2815 Scale = 69.9724
Weibull Percentiles
Reference Line
95% Confidence Band
Weibull Percentiles
BREAKDOWN TIME IN CO2

(e)

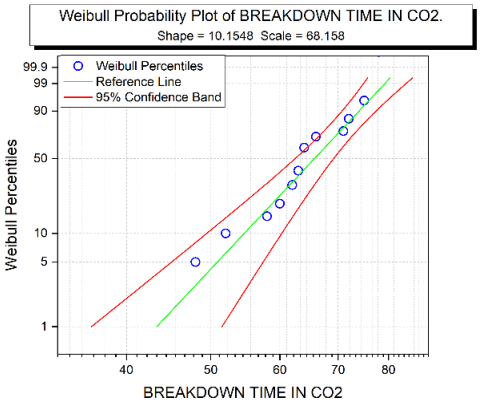
Weibull Probability Plot of BREAKDOWN TIME IN CO2.
Shape = 10.1548 Scale = 68.158
Weibull Percentiles
Reference Line
95% Confidence Band
Weibull Percentiles
BREAKDOWN TIME IN CO2

(f)

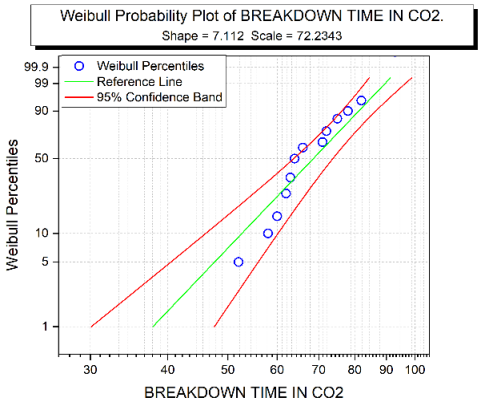
Weibull Probability Plot of BREAKDOWN TIME IN CO2.
Shape = 7.112 Scale = 72.2343
Weibull Percentiles
Reference Line
95% Confidence Band
Weibull Percentiles
BREAKDOWN TIME IN CO2

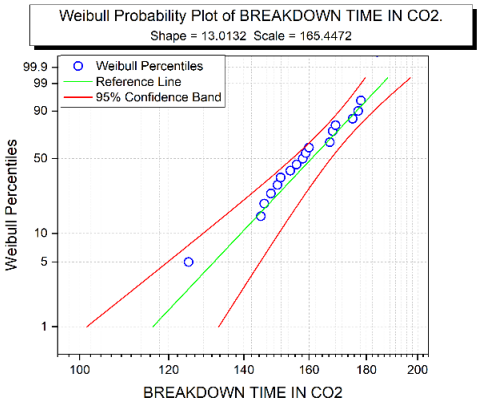
Weibull Probability Plot of BREAKDOWN TIME IN CO2.
Shape = 13.0132 Scale = 165.4472
Weibull Percentiles
Reference Line
95% Confidence Band
Weibull Percentiles
BREAKDOWN TIME IN CO2

(g) (h)

Figure D-6 Weibull distribution graphs for the time to breakdown in CO_2 at each of the tested gas pressure for 90% of the self-breakdown voltage level

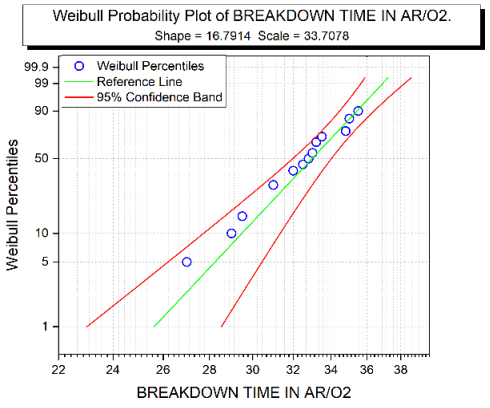
Weibull Probability Plot of BREAKDOWN TIME IN AR/O2.
Shape = 16.7914 Scale = 33.7078
Weibull Percentiles
Reference Line
95% Confidence Band
Weibull Percentiles
BREAKDOWN TIME IN AR/O2

(a)

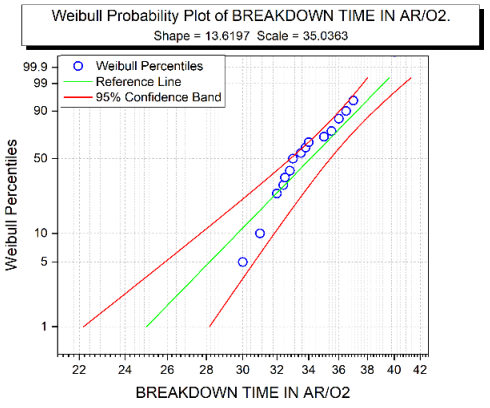
Weibull Probability Plot of BREAKDOWN TIME IN AR/O2.
Shape = 13.6197 Scale = 35.0363
Weibull Percentiles
Reference Line
95% Confidence Band
Weibull Percentiles
BREAKDOWN TIME IN AR/O2

(b)

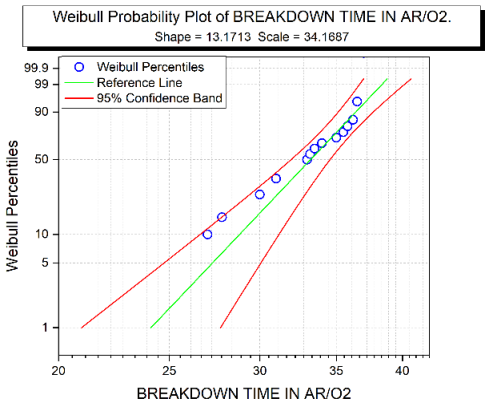
Weibull Probability Plot of BREAKDOWN TIME IN AR/O2.
Shape = 13.1713 Scale = 34.1687
Weibull Percentiles
Reference Line
95% Confidence Band
Weibull Percentiles
BREAKDOWN TIME IN AR/O2

(c)

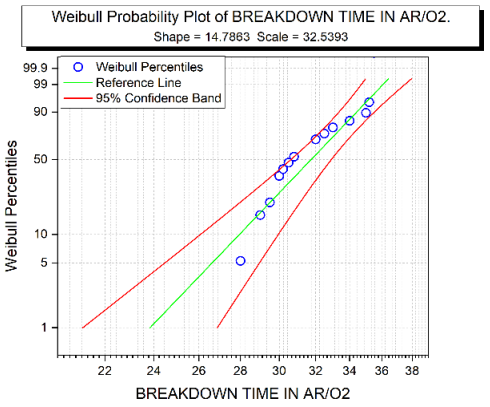
Weibull Probability Plot of BREAKDOWN TIME IN AR/O2.
Shape = 14.7863 Scale = 32.5393
Weibull Percentiles
Reference Line
95% Confidence Band
Weibull Percentiles
BREAKDOWN TIME IN AR/O2

(d)

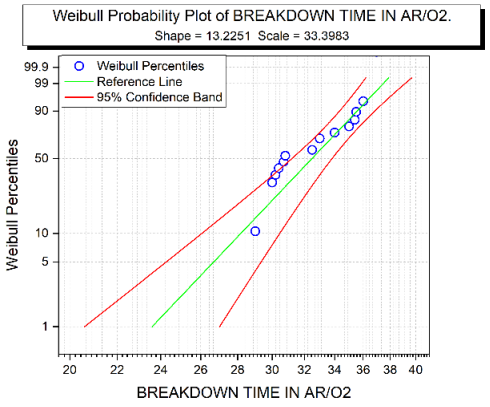
Weibull Probability Plot of BREAKDOWN TIME IN AR/O2.
Shape = 13.2251 Scale = 33.3983
Weibull Percentiles
Reference Line
95% Confidence Band
Weibull Percentiles
BREAKDOWN TIME IN AR/O2

(e)

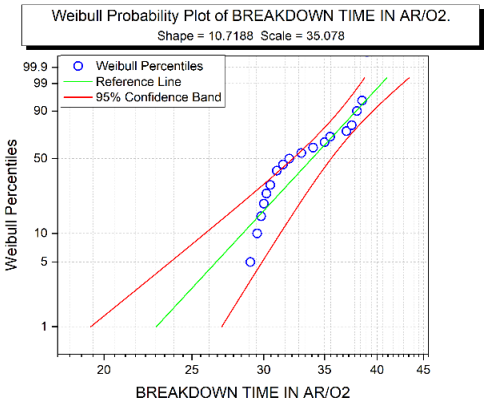
Weibull Probability Plot of BREAKDOWN TIME IN AR/O2.
Shape = 10.7188 Scale = 35.078
Weibull Percentiles
Reference Line
95% Confidence Band
Weibull Percentiles
BREAKDOWN TIME IN AR/O2

(f)

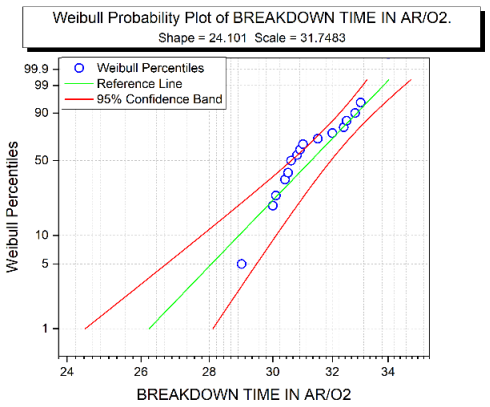
Weibull Probability Plot of BREAKDOWN TIME IN AR/O2.
Shape = 24.101 Scale = 31.7483
Weibull Percentiles
Reference Line
95% Confidence Band
Weibull Percentiles
BREAKDOWN TIME IN AR/O2

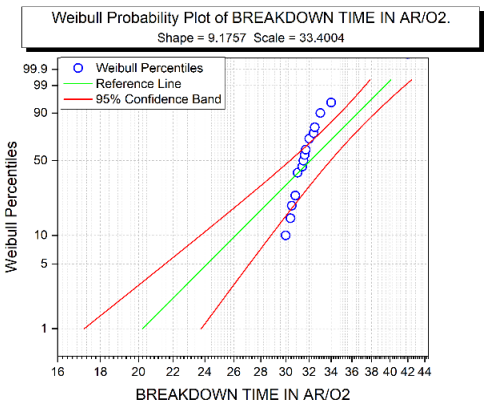
Weibull Probability Plot of BREAKDOWN TIME IN AR/O2.
Shape = 9.1757 Scale = 33.4004
Weibull Percentiles
Reference Line
95% Confidence Band
Weibull Percentiles
BREAKDOWN TIME IN AR/O2

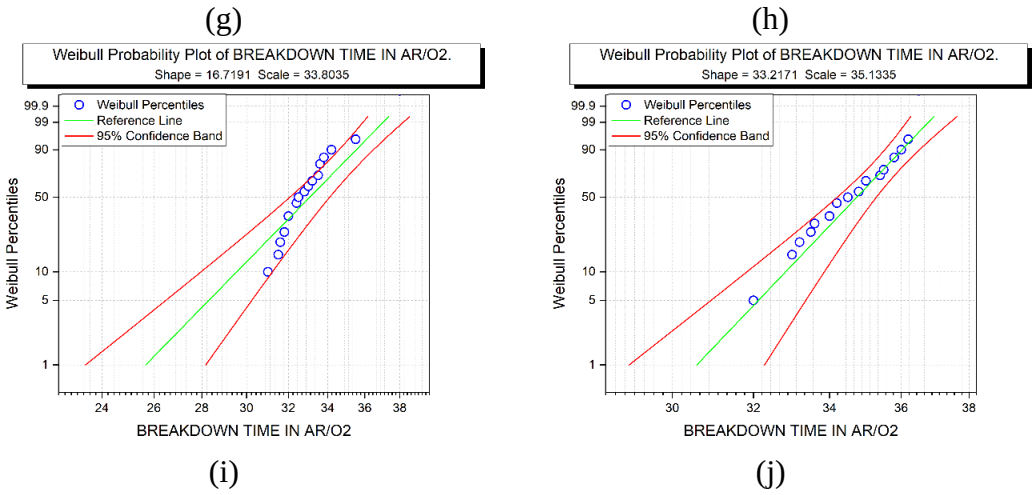

Figure D-7 Weibull distribution graphs for the time to breakdown in Ar/O_2 mixture at each of the tested gas pressure for 70% of the self-breakdown voltage level

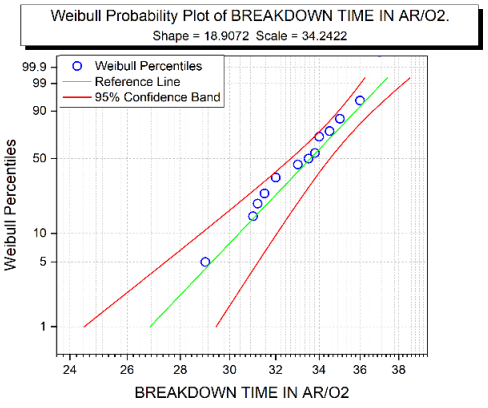
Weibull Probability Plot of BREAKDOWN TIME IN AR/O2.
Shape = 18.9072 Scale = 34.2422
Weibull Percentiles
Reference Line
95% Confidence Band
Weibull Percentiles
BREAKDOWN TIME IN AR/O2

(a)

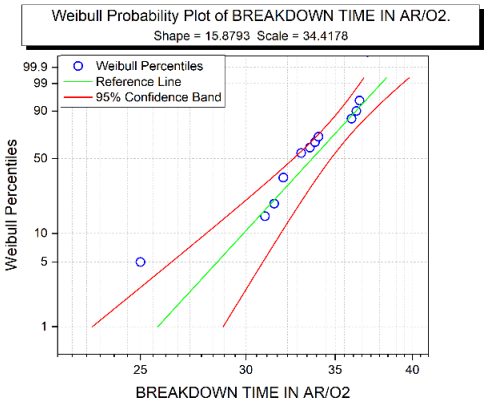
Weibull Probability Plot of BREAKDOWN TIME IN AR/O2.
Shape = 15.8793 Scale = 34.4178
Weibull Percentiles
Reference Line
95% Confidence Band
Weibull Percentiles
BREAKDOWN TIME IN AR/O2

(b)

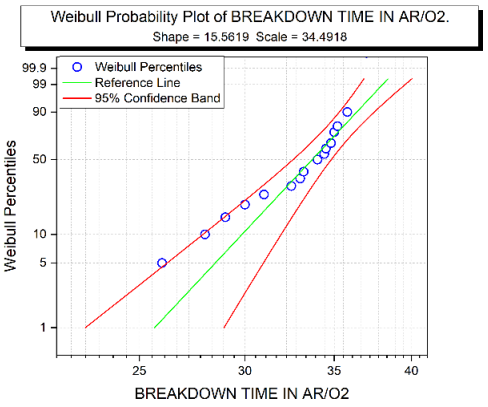
Weibull Probability Plot of BREAKDOWN TIME IN AR/O2.
Shape = 15.5619 Scale = 34.4918
Weibull Percentiles
Reference Line
95% Confidence Band
Weibull Percentiles
BREAKDOWN TIME IN AR/O2

(c)

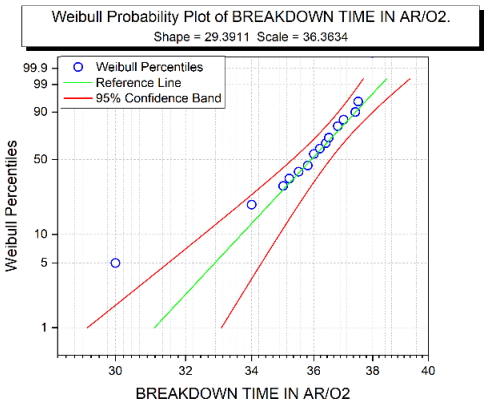
Weibull Probability Plot of BREAKDOWN TIME IN AR/O2.
Shape = 29.3911 Scale = 36.3634
Weibull Percentiles
Reference Line
95% Confidence Band
Weibull Percentiles
BREAKDOWN TIME IN AR/O2

(d)

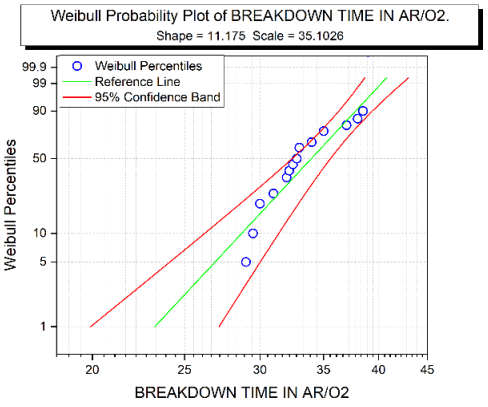
Weibull Probability Plot of BREAKDOWN TIME IN AR/O2.
Shape = 11.175 Scale = 35.1026
Weibull Percentiles
Reference Line
95% Confidence Band
Weibull Percentiles
BREAKDOWN TIME IN AR/O2

(e)

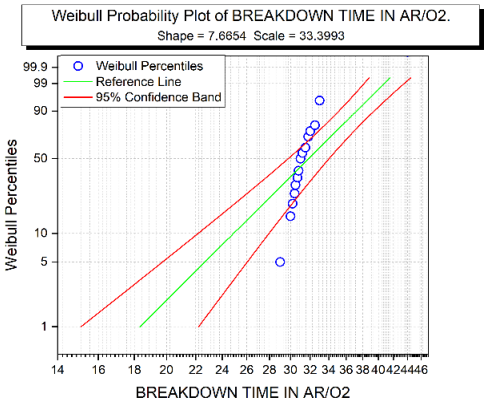
Weibull Probability Plot of BREAKDOWN TIME IN AR/O2.
Shape = 7.6654 Scale = 33.3993
Weibull Percentiles
Reference Line
95% Confidence Band
Weibull Percentiles
BREAKDOWN TIME IN AR/O2

(f)

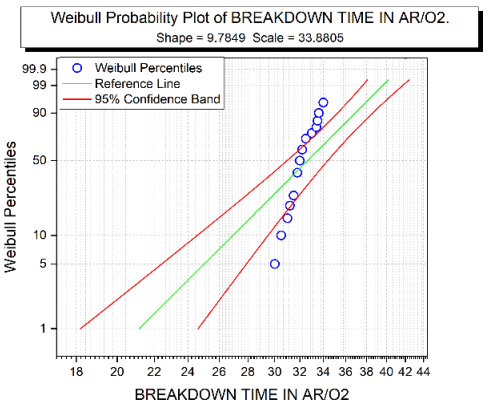
Weibull Probability Plot of BREAKDOWN TIME IN AR/O2.
Shape = 9.7849 Scale = 33.8805
Weibull Percentiles
Reference Line
95% Confidence Band
Weibull Percentiles
BREAKDOWN TIME IN AR/O2

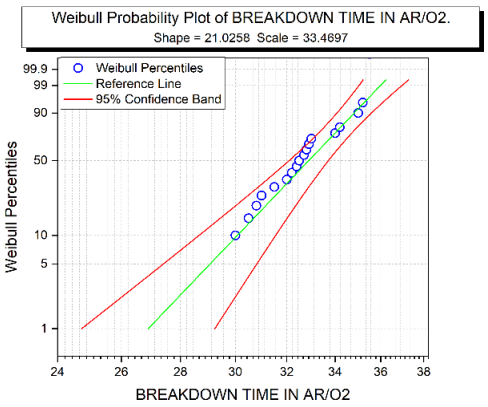
Weibull Probability Plot of BREAKDOWN TIME IN AR/O2.
Shape = 21.0258 Scale = 33.4697
Weibull Percentiles
Reference Line
95% Confidence Band
Weibull Percentiles
BREAKDOWN TIME IN AR/O2

(g)

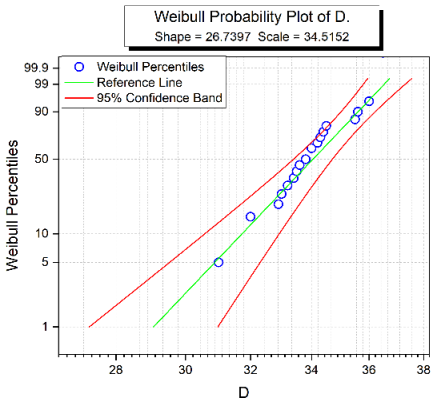

(h)

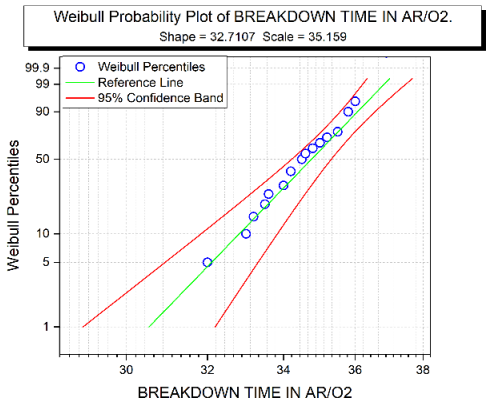

(i)

(j)

Figure D-8 Weibull distribution graphs for the time to breakdown in Ar/O_2 mixture at each of the tested gas pressure for 90% of the self-breakdown voltage level